Efficient two-photon water splitting photoelectrode

Bækbo, Martin Jesper

Publication date:
2018

Document Version
Publisher's PDF, also known as Version of record

Technical University
of Denmark

Efficient two-photon water splitting photoelectrode

Martin Jesper Bækbo

PhD thesis
Department of Physics
Technical University of Denmark
February, 2018

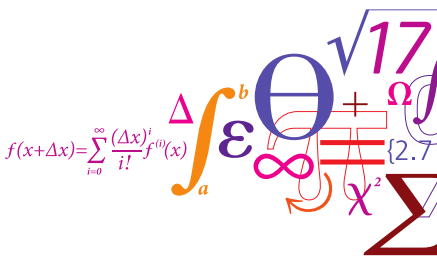

Efficient two-photon water splitting photoelectrode

PhD thesis by

Martin Jesper Bækbo

Supervisor: Associate professor Peter C. K. Vesborg

Co-supervisor: Professor Ib Chorkendorff

February 2018

Surface Physics and Catalysis (SurfCat)
Department of Physics
Technical University of Denmark

Preface

This thesis has been written in accordance with the requirements for obtaining the PhD degree at the Technical University of Denmark (DTU). The research was supported by grants from "Det Frie Danske Forskningsråd" (DFF-4005-00463) as well as Villum fonden (9455) and I would like to acknowledge their contributions. The work detailed within was supervised by associate professor Peter C. K. Vesborg and professor Ib Chorkendorff and carried out from the 1st of Marts 2015 to the 28th of February 2018. Most of the results were obtained at DTU in the Surface Physics and Catalysis (SurfCat) division though a substantial part were recorded at the Joint Center for Artificial Photosynthesis (JCAP) at Lawrence Berkeley National Laboratory (LBNL).

I would sincerely like to thank both of my supervisors for always providing guidance and ideas for new experiments. The experimental road to reach this point was sometimes rather bumpy and being able to draw on their considerable expertise has been a great support. I would also like to extend my gratitude to Francesca Toma and Ian Sharp for giving me the opportunity to spend my external stay at LBNL. Together with the rest of the terrific people at JCAP they made the experience extremely gratifying, both scientifically and personally. Writing a PhD at SurfCat has been a great experience due, in no small part, to the wonderful people that I have had the pleasure of working with. Not only have we had many interesting scientific discussions but they have also made the past three years very fun and I am going to miss each and every one of them. I would especially like to thank Erlend Bertheussen, Claudie Roy and Thomas Maagaard for proof reading the thesis and for always being ready for a cake run as well as Friday bar shenanigans.

A big thank you goes out to my parents for always supporting me over the years and for fanning my curiosity about the world from an early age. Finally I would like to say the greatest thank you to my wife Anne Mette for her unwavering faith in me, for always being able to make me laugh and for generally making my life wonderful.

Martin Jesper Bækbo

Abstract

This thesis presents work related to the development and fabrication of tandem photoelectrochemical (PEC) water splitting devices. These PEC cells have the potential to help mitigate the effects of solar power intermittency by converting sunlight into chemicals. The main focus of the work has been fabrication of high band gap cells intended to work in conjunction with Si devices. The materials employed as photoabsorbers have been methylammonium lead halide perovskites, which display a wide range of beneficial material properties. These include high absorption in the visible range, band gap tunability and high defect tolerance. The major shortcoming of the otherwise ideal class of material is their poor stability towards moisture and elevated temperatures. The projects included in the thesis are somewhat different in nature and range from device fabrication to the study of more fundamental material properties.

The first project focused on tandem solar cell deign and fabrication. Tandem cells have the potential to be much more efficient than single band gap absorbers and their use is thus desired. Monolithic tandem devices, employing a Si bottom cell, require a top cell with a band gap of around 1.7 eV to achieve maximum efficiency. The initial aim of the project was thus to fabricate single band gap perovskite absorbers with the appropriate band gap. This was achieved using the low pressure vapour assisted solution process (LP-VASP) perovskite deposition method and by varying the halide composition of the $CH_3NH_3PbI_{(3-x)}Br_x$ structure. The layers were subsequently utilized to fabricate devices, which reached a power conversion efficiency (PCE) of up to 15.2%, while using the normal cell architecture. Devices using the inverted configuration was also fabricated, although their performance was poorer. An atomic layer deposition (ALD) recipe for fabricating thin films of TiO_2 was furthermore developed and used to deposit thin layers on top of inverted perovskite devices. Inclusion of the ALD TiO_2 layers, as well as Ti contacts, was found to increase the open circuit voltages of the cells, yielding up to 1.15 V, while decreasing hysteresis. The ALD layers additionally increased the moisture resistance of the devices, although not to a sufficient degree. Further improvement of the lifetime of perovskite cells submerged in water was investigated by using a special encapsulation method. Although a functioning device was never produced, the method shows great promise. In addition to the protection schemes, sputtering

was utilized to deposit ITO layers to serve as transparent top contacts. The layers obtained showed good transmission in the visible range and featured sheet resistances down to 22.3 Ω/sq. Finally, attempts at improving the performance of the inverted configuration cells were carried out, unfortunately, without clear results.

The second project investigated evaporation of methylammonium iodide (MAI) using quartz crystal microbalance (QCM) measurements and mass spectrometry. Co-evaporation of MAI and $PbCl_2$ has been shown to be a possible route of perovskite deposition, though the resultant cell performance has generally been inferior. The origin of the issues have often been attributed to difficulties controlling the MAI deposition rate. From the QCM experiments it was found that the sticking of the MAI was extremely low, especially at elevated substrate temperatures. The sticking remained low, even when $PbCl_2$ was deposited on the QCM crystals. From the mass spectrometry it was found that MAI decomposes upon evaporation, primarily into CH_3NH_2 and HI. To form the perovskite from a $PbCl_2$ film high partial pressures of MAI are consequently needed to supply a net influx of the compounds. The results have consequences for the design of deposition chambers, and additionally, provide fundamental insights into the kinetics of perovskite deposition, as well as the nature of MAI evaporation.

The approach of using QCM sensors together with mass spectrometry was likewise used in the third and final project to study the thermal decomposition of various methylammonium lead halide perovskites. $CH_3NH_3PbI_{(3-x)}Br_x$ was deposited on a QCM crystal and by heating the sensor, the rate of reevaporation could be estimated. Using temperatures of 85 °C and 102 °C resulted in reevaporation rates of 2.44×10^{-4} nm/s and 1.42×10^{-3} nm/s, respectively. For the mass spectrometry investigations the pure $CH_3NH_3PbI_3$ was used, although $CH_3NH_3PbI_{(3-x)}Br_x$ was expected to yield similar mass spectra. The results of the experiments indicated that the organic part of the perovskite starts evaporating already at 100 °C, leading to the decomposition of the perovskite. The low thermal stability limits the possible protection layers that can be applied on top of the perovskite devices and lowers the lifetime of the cells.

Resumé

Denne afhandling præsenterer arbejde relateret til udvikling og fabrikation af tandem fotoelektrokemiske (PEC) celler til spaltning af vand. Disse PEC celler har potentialet til at afhjælpe den uregelmæssige energiproduktion, der er forbundet med solenergi ved at omdanne sollys til kemikalier. Arbejdets fokus har været fabrikation af højbåndgabsceller, som var tiltænkt at skulle arbejde sammen med Si-enheder. De udvalgte materialer til fotoabsorberne var metylammoniumblyhalid perovskiter, som besidder et bredt spektrum af nyttige materialeegenskaber. Disse inkluderer en høj absorption af synligt lys, mulighed for at tune båndgabet og en høj defekttolerance. Den altoverskyggende ulempe ved disse materialer er deres dårlige modstandsevne over for fugt og høje temperaturer. Projekterne inkluderet i afhandlingen er forholdsvis forskelligartede og spænder fra fabrikation af celler til undersøgelser af fundamentale materialeegenskaber.

Det første projekt havde design og fabrikation af tandemsolceller i fokus. Tandemenheder har potentialet til at være langt mere effektive end enkeltbåndgabsceller, hvilket gør dem attraktive. Monolitiske tandemenheder der benytter en Si-celle nederst, kræver at den øverste celle har et båndgab på 1,7 eV for at opnå maksimal effektivitet. Projektets første mål var derfor at producere perovskitabsorbere med et passende båndgab. Dette blev opnået ved at benytte den såkaldte "Low pressure vapour assisted solution process" (LP-VASP) deponeringsmetode samt ved at variere halogensammensætningen i $CH_3NH_3PbI_{(3-x)}Br_x$ strukturen. Disse lag blev efterfølgende benyttet til at fremstille solceller, der opnåede en effektivitet på op til $15,2\%$ ved at bruge den normale cellearkitektur. Enheder der anvendte den omvendte struktur blev også fremstillet, om end deres præstation var dårligere. En opskrift til atomar lags deponering (ALD) til fremstilling af tynde film af TiO_2 blev ydermere udviklet og benyttet til at deponere lag ovenpå inverterede perovskitenheder. Effekten af at inkludere ALD filmene, samt Ti kontakter, var en øget tomgangsspænding og op til 1,15 V blev opnået med en reduceret hysterese. ALD lagene øgede ydermere modstandsdygtigheden overfor fugt, om end ikke tilstrækkeligt. Muligheden for en bedre overlevelsestid af perovskitceller nedsænket i vand blev undersøgt ved at benytte en særlig indkapslingsmetode. Skønt en funktionsdygtig enhed aldrig blev produceret, var fremgangsmåden lovende. I tillæg til beskyttelsessystemerne blev sputtering benyttet til at deponere ITO, som

skulle tjene som gennemsigtige topkontakter. De producerede lag havde en god transmittans i det synlige spektrum og flademodstande ned til $22,3\ \Omega/\text{sq}$. Til slut blev der gjort forsøg på at optimere præstationen af de inverterede celler, desværre uden klare resultater.

I det andet projekt blev fordampning af metylammoniumiodid (MAI) undersøgt ved at benytte kvartskrystal mikrovægt (QCM) målinger samt massespektrometri. Det er tidligere vist, at co-fordampning af MAI og $PbCl_2$ er en deponeringsmulighed, selvom de resulterende cellers præstation generelt har været underlegne. Forklaringen på dette er ofte blevet tilskrevet problemer med at kontrollere deponeringsraten af MAI. QCM forsøgene viste, at MAIs klæbeevne var ekstremt lav selv når $PbCl_2$ var deponeret på krystallerne. Massespektrometriforsøgene viste, at MAI primært dekomponerer til CH_3NH_2 og HI når det fordampes. For at skabe perovskit fra en $PbCl_2$ film kræves der som konsekvens høje MAI tryk for at sikre en høj tilstrømning af reaktanter. Resultaterne har konsekvenser for design af deponeringskamre og giver i tillæg indsigt i perovskits fundamentale formeringskinetik samt omstændighederne ved MAI fordampning.

Fremgangsmåden med at benytte QCM sensorer og massespektrometri blev ligeledes benyttet i det tredje og sidste projekt til at studere termisk dekomponering af forskellige metylammoniumblyhalid perovskitter. $CH_3NH_3PbI_{(3-x)}Br_x$ blev deponeret på en QCM krystal og ved at opvarme sensoren kunne materialets fordampningsrate estimeres. 85 °C og 102 °C blev benyttet hvilet resulterede i de respektive fordampningsrater $2,44 \times 10^{-4}$ nm/s og $1,42 \times 10^{-3}$ nm/s. Til massespektrometriundersøgelserne blev den rene $CH_3NH_3PbI_3$ benyttet, selvom forventningen var at $CH_3NH_3PbI_{(3-x)}Br_x$ ville give lignende massespektre. Resultaterne indikerede, at den organiske del af perovskiten begyndte at fordampe allerede ved 100 °C, hvilket førte til at perovskiten dekomponerede. Den lave termiske stabilitet begrænser antallet af potentielle beskyttelseslag, der kan benyttes ovenpå perovskitenheder og sænker samtidig cellernes levetid.

List of publications

Deposition of Methylammonium Iodide via evaporation - combined kinetic and mass spectrometric study
Martin J. Bækbo, Ole Hansen, Ib Chorkendorff, Peter C. K. Vesborg
Under review

Contents

Chapter 1

Introduction

In this chapter I will outline the motivation for the work performed during my PhD studies as well as provide an overview of the contents of the thesis. As the thesis title suggests, the aim of the project has been to fabricate an efficient device which by absorbing sunlight can electrochemically split water into hydrogen and oxygen. To do so requires detailed knowledge about catalysis as well as photoelectrochemical cells and the chapter thus includes a brief introduction to these subjects. The primary focus of the work has, however, been on developing the photoabsorbing part of the device using organolead halide perovskites. A short overview of the materials and their use in solar cells is therefore included as an introduction to the field.

1.1 Motivation

Humanity is currently facing one of the most difficult problems we have ever encountered as a species, namely, the fact that our current way of life is in the process of destroying our habitat. The consequences of global warming have become ever more evident in recent years and weather that was previously described as extreme, has now become more likely [1]. The generally accepted cause for the phenomenon is emission of greenhouse gasses, such as CO_2, which are released during the burning of fossil fuels [2]. As seen in Figure 1.1a, which shows the atmospheric concentration of CO_2 measured at the top of the volcano Mauna Loa on Hawaii, the amount of CO_2 in the atmosphere has been steadily increasing during the last 55 years. The increase of about 120 parts per million is hard to put into context but if one compares it to the atmospheric content of CO_2 from a longer period of time, this changes. By analysing ice core samples one can estimate the CO_2 concentration in the atmosphere from the last 400,000 years which is shown in Figure 1.1b.

From the figure it is clear that the current level of CO_2 is unprecedented in the last 400,000 years and is about 25% higher than levels pre-dating 1950. The emission of CO_2 is driven by the ever increasing demand for energy, partly in the form of electricity, but also as fuel for the transportation sector.

As seen from Figure 1.2 the energy production today predominatly originates from various fossil fuels and only 3.2% was supplied by renewables in 2016. This is

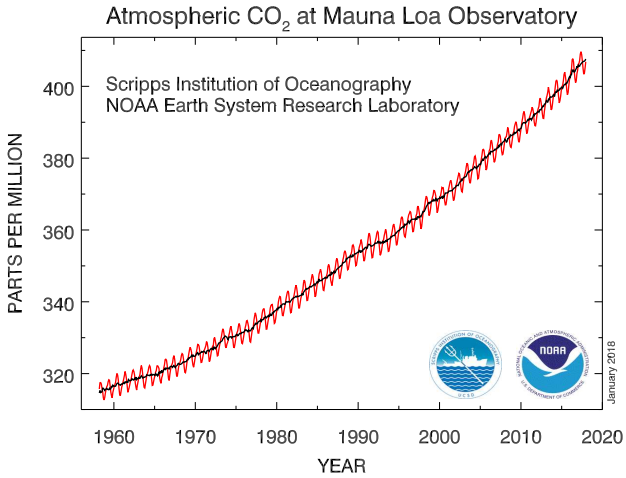

(a)

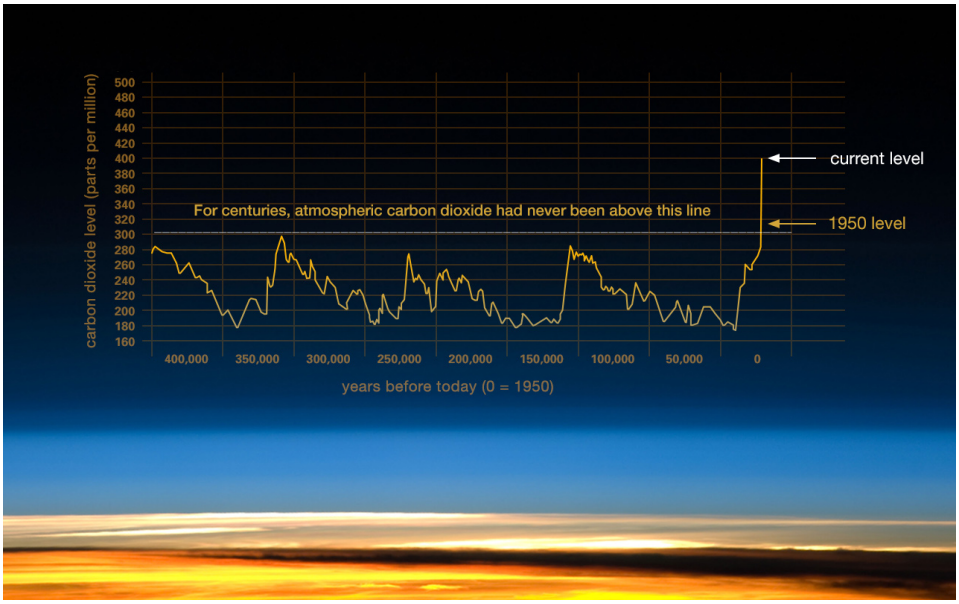

(b)

Figure 1.1: The development of the CO_2 concentration in the atmosphere over the years. **(a)** shows data measured at the Mauna Loa observatory on Hawaii acquired from [3]. **(b)** shows the CO_2 level of the last 400,000 years acquired from ice core samples as well as direct measurements. Figure from [4].

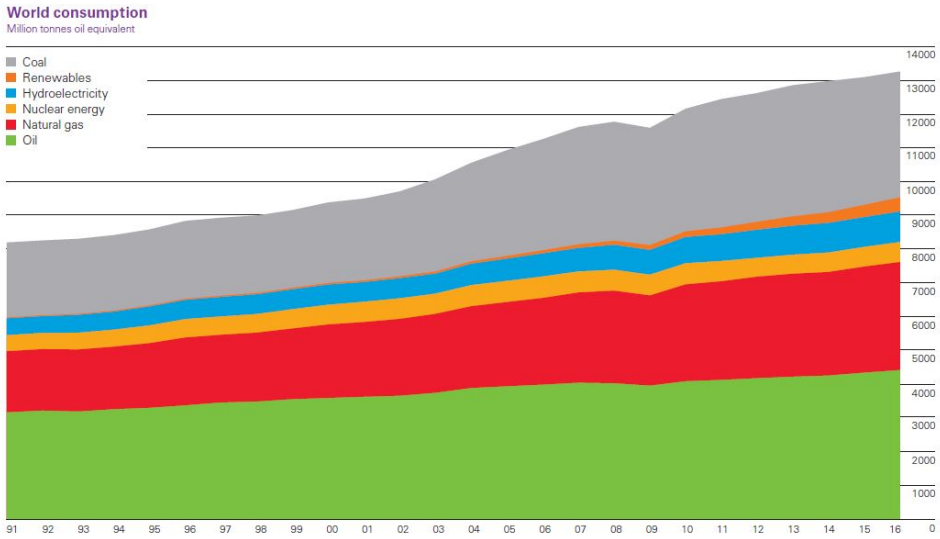

Figure 1.2: Overview of the worlds energy consumption from 1991-2016 divided into the various sources making up the whole. The orange sliver represents the renewable energy sources, not counting hydro power, and is seen to make up 3.2% of the total in 2016. The unit of y-axis is million tones oil equivalent (mtoe) where one mtoe equals 42×10^9 J. Figure from [5].

in spite of the fact that the largest energy reserve by far is solar radiation which has the potential to cover the Earth's current needs many times over [6]. With such a massive untapped energy source sitting outside our doorstep it might seem perplexing that solar power is not dominating the energy sector. The explanation for this is twofold, where the most immidiate restriction has been the higher price of solar power as compared to fossil fuels. In recent years the price per kWh produced by solar panels has, however, decreased and can in some parts of the world already meet the US Department of Energy's 2020 goal [7]. The second obstacle is the intermittency of sunlight imposed by the Earth's day and night cycle which complicates the use of solar power for base load supply. The problem with intermittency is naturally not limited to solar cells but is a common struggle for most reneweable energy sources, barring to some degree hydro power plants. To address this issue, storage technology is needed to save the energy from surplus production periods for the use during downtime. One approach is to use batteries and while they are very good for some applications, they do have some shortcomings. The most prominent of these is that the energy density of batteries is currently inferior to that of chemical fuels [8]. Rather than using batteries another possibility is to use the electricity generated by the renewable energy sources to produce chemical fuels using electrochemistry. Multiple approaches have been examined though the most studied in recent years have been CO_2 reduction and splitting of water into hydrogen and oxygen [7–14]. Though CO_2 reduction is certainly an interesting subject whose application is expected to have widespread effects in the energy sector

the focus of this thesis is on water splitting. Using hydrogen as an energy carrier offers many advantages as it features a high energy density per kg, high availability and a carbon free way of regaining the energy by using a fuel cell. Hydrogen is furthermore an integral component in many chemical processes such as hydrocarbon production from CO_2 and ammonia production using the Haber-Bosch reaction [9]. Though the storage of H_2 gas is not as easy as liquid fuels (currently the best way to store it is in high pressure tanks) its use has significant potential to help shift the world towards a more sustainable future.

1.2 The basics of catalysis

The common denominator of all the suggested chemical fuel production scheems is that they require efficient catalysts. A catalyst is a material that increases the rate of a chemical reaction by interacting with the reaction constituents without being consumed itself. Catalysts are found in almost all industrial chemical reactions and one of the most important ones is the iron based catalyst used in the before mentioned Harbor-Bosch process. This is due to the fact, that the current world population is sustained largely by the artificial fertilizer produced from the NH_3 created in the process [15]. Looking at a chemical reaction in terms of Gibbs free energy, a catalyst offers an alternative reaction path with a lower energy barrier between some, or all, of the reaction steps. This is visualized in Figure 1.3 where a schematic representation of the potential energy diagram of a simple reaction, $X \rightarrow Y + Z$, is shown.

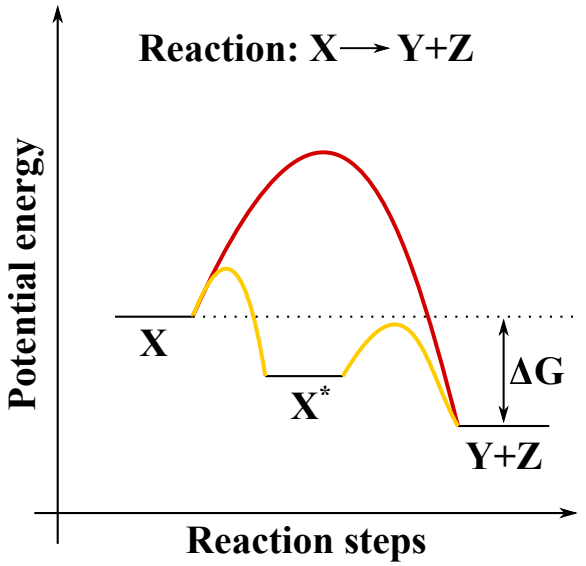

Figure 1.3: Schematic representation of a potential energy diagram of the reaction $X \rightarrow Y + Z$. The red curve shows a non-catalysed reaction path while the yellow shows a catalysed reaction which includes one or more additional reaction steps, X^*.

As the change in Gibbs free energy of the reaction is negative, the reaction will run and since the barriers encountered in the yellow (catalysed) reaction path are lower, it will progress faster than in the uncatalysed red reaction path. The field of catalysis can be divided into two general groups depending on how the energy needed to surpass the barriers, as well as make the reaction "down hill" in free energy, is supplied. In thermal catalysis the reaction is driven by elevated reaction pressure and temperature. In electrocatalysis a potential difference is applied between two electrodes submerged in an electrolyte, causing the reaction to run on the surface of the electrodes. The thermodynamically minimal reaction potential needed, the equilibrium potential E°, is related to the change in Gibbs energy, ΔG, by

$$\Delta G = -n_e F E^\circ, \tag{1.2.1}$$

where n_e is the number of electrons transferred in the reaction and $F = 96485$ C mol^{-1} is the Faraday constant. Due to barriers in the reaction path the reaction potential needed to achieve a significant reaction rate is almost always higher than E°. This extra potential is aptly named the overpotential, η_e, and depends, among other things, on the catalyst used. The overall reaction potential needed, E_a, therefore becomes $E_a = E^\circ + \eta_e$. Catalysts can only be optimized for one chemical reaction but fortunately the two half reactions of a redox reaction, namely the reduction and the oxidation, take place at the cathode and anode, respectively. This means that a catalyst, optimized for the appropriate reaction, can be applied to each of the electrodes. The best suited catalysts depend on many things such as the used electrolyte, price and stability. Though catalyst development is an intriguing and important scientific topic (a lot of the research performed at SurfCat is aimed at this), it is not the main topic of this thesis. Consequently the underlying mechanics of catalyst design and production will not be discussed in detail.

1.2.1 Photoelectrocatalytic water splitting

As described, electrochemistry, or more specifically, electrocatalysis enables one to transform electricity into chemicals by running a redox reaction. In principle the power supply of the electrochemical cell can be anything from a waterwheel to a nuclear power plant but as mentioned, it is also highly useful for mitigating the intermittency of solar power production. To split water one needs to run the redox reaction

$$\mathrm{H_2O} + E_a \rightarrow \frac{1}{2}\mathrm{O_2} + 2\mathrm{H_2}, \tag{1.2.2}$$

which can be split into the anode

$$\mathrm{H_2O} + E_{\mathrm{ox}} \rightarrow \frac{1}{2}\mathrm{O_2} + 2\mathrm{H^+} + 2e^-, \tag{1.2.3}$$

and cathode reaction

$$2\mathrm{H^+} + 2e^- + E_{\mathrm{red}} \rightarrow \mathrm{H_2}, \tag{1.2.4}$$

where E_{ox} is the oxidation potential, E_{red} is the reduction potential and e are electrons. The sum of E_{ox} and E_{red} naturally equals E_a. The best suited catalysts in acidic media are Pt and IrO_x used for the hydrogen evolution reaction (HER) and the oxygen evolution reaction (OER), respectively. Since Ir and Pt are, however, both precious and scarce metals, a well spring of other materials have been tested [16, 17]. Pt has, nevertheless, been shown to be a more scalable solution when comparing to more abundant catalysts due to its high activity [18]. In alkaline electrolytes other materials, such as Fe doped NiO, become good candidates for OER catalysts [16, 19].

The equilibrium potential for the water splitting reaction is 1.23 V but in practice one must apply around 1.7 V to overcome the various overpotentials, even when well optimized catalysts are used [14]. The easiest way to achieve this using solar power is to connect one or more photovoltaic (PV) modules to an electrolyzer whenever surplus energy is produced. The overall efficiency of this configuration depends on both the solar cell and the electrolyzer but solar to hydrogen (STH) efficiensies of up to 12% have been demonstrated [20]. Another approach, which is the focus of this thesis, is to combine the two devices in a single cell called a photoelectrochemical (PEC) cell. In such a device light is absorbed in a photoabsorber and rather than collecting the carriers in an external circuit, they are used to drive the redox reaction on the surface of the cell. Several different design concepts can be used which all have their strengths and weaknesses. The most straight forward approach is to use a semiconductor and a semiconductor-electrolyte interface to achieve the light absorption and charge separation, respectively. Upon submerging the semiconductor in the electrolyte the Fermi level of the semiconductor will equilibrate with the redox reaction by electron transfer [11]. This will cause the bands in the semiconductor to bend due to the electric field established between the localized atom nuclei in the semiconductor and the electrolyte. The direction of the band bending depends on the type of semiconductor and the correct type needs to be selected depending on whether the semiconductor acts as the anode (n-type) or cathode (p-type) in the device. In the simplest configuration, a single semiconductor cell (called a photoelectrode) is used in conjunction with a metal counter electrode. A schematic band diagram of such a device is seen in Figure 1.4a.

Like in a normal PV device the potential delivered by the cell equals the quasi Fermi level splitting of the electrons and holes during operation [21]. As previously shown in literature, this splitting will always be around 400 mV lower than the band gap of the semiconductor under 1 sun illumination due to the limitation imposed by light absorption and emission considerations [14, 22]. This restricts the size of the band gap as the potential produced by the semiconductor needs to be larger than the needed reaction potential. In case of water splitting, a band gap of at least 2.3 eV is needed due to various losses, which means that a substantial amount of the visible spectrum will not be absorbed [14]. Furthermore, the valance and conduction band of the semiconductor needs to be more anodic and cathodic than E_{ox} and E_{red}, respectively. If this is not the case, charge cannot flow in the electrochemical circuit, meaning that the reaction will not run. Due to the requirements single photoelectrode devices are generally not very efficient and as a consequence a two photoelectrode configuration is preferred [14]. A simplified

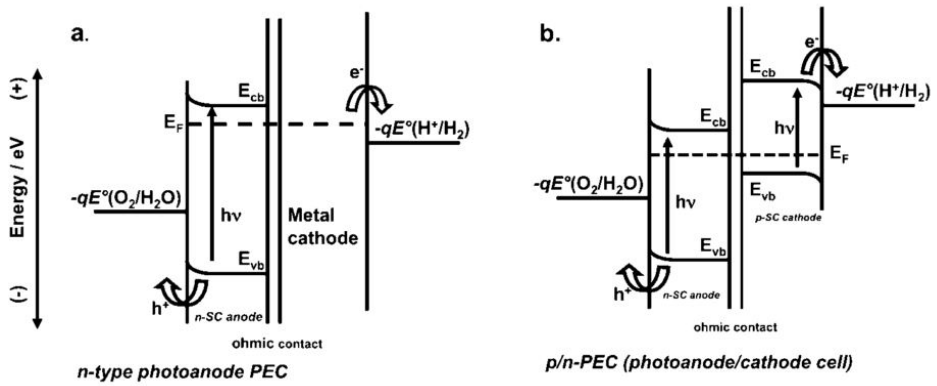

Figure 1.4: Schematic band diagrams of a single **(a)** and double **(b)** photoelectrode device. $-qE^{\circ}(\mathrm{O_2/H_2O})$ is the (OER) potential, $-qE^{\circ}(\mathrm{H^+/H_2})$ is the (HER) potential while E_{cb}, E_{vb} and E_F are the semiconductor conduction band, valance band and Fermi level, respectively. In the latter case the two half cells can either operate in a side by side configuration or on top of each other, in both cases connected by an ohmic contact. Figure from [11].

band diagram of one so-called tandem device can be seen in Figure 1.4b. Here a photocathode and photoanode work in unison to deliver the needed reaction potential. As a consequence lower band gap absorbers can be used, which results in much better utilization of the sunlight. Using the side-by-side configuration, where the two cells are placed next to each other, one can obtain a solar to hydrogen efficiency of 15.5% by using two absorbers with a band gap of 1.59 eV [8]. One can, however, obtain a substantially better result if the two photoelectrodes are placed on top of each other and STH efficiencies of up to 22.8% can be reached in this way [8]. As reported by Seger *et al.* [14] an optimum is reached if a large band gap (LBG) absorber is used in conjunction with a small band gap (SBG) absorber having a combined band gap of 2.7 eV. The calculations furthermore show that 1.7 eV should originate from the LBG absorber, while the remaining 1.0 eV should come from the SBG absorber.

Since light now have to pass through the front electrode to reach the underlying one, the amount of current that can be produced in the lower cell now also depends on the top cell. The large band gap cell should therefore be placed on top to absorb the high energy photons, while the SBG device absorbs the rest. When taking into account the inhomogeneous wavelength distribution of the solar spectrum the aforementioned distribution of band gaps between the SBG and the LBG, ensures that the devices are current matched. This is important since half of the carriers produced at each electrode (electrons from the anode and holes from the cathode) need to recombine with one another to avoid a charge build up. If this is not achieved the recombination rate in the device will increase, thus lowering the efficiency. This scenario can be visualised if one considers the J-V curves of the

anode and cathode shown in Figure 1.5.

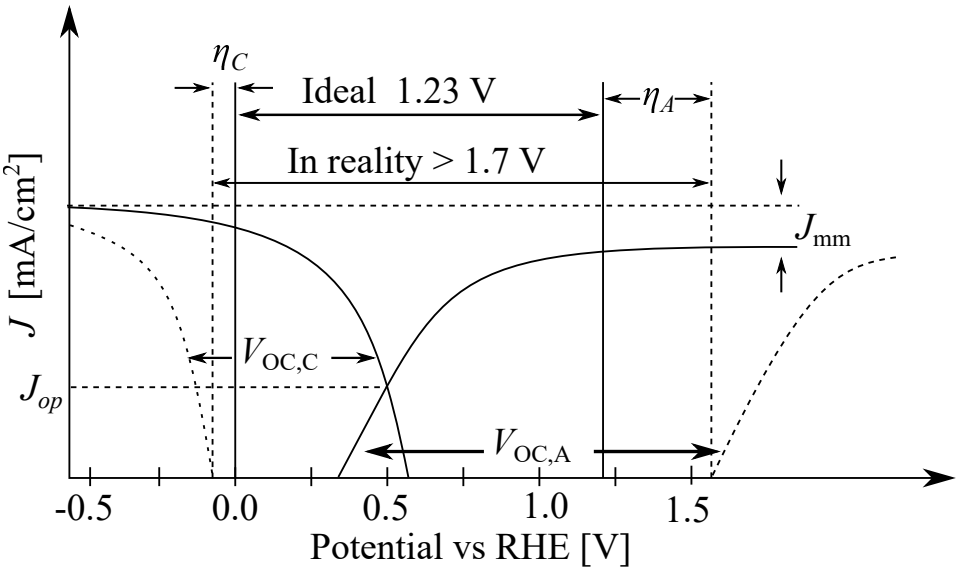

Figure 1.5: Schematic J-V curves of the photoanode and photocathode where the absolute of the current density has been used - i.e. the otherwise negative current of the reduction has been flipped. η_C and η_A are the overpotentials of the cathode and anode, respectively. Figure from [23].

In the dark no photocurrent is produced and no water splitting thus occurs. Upon illuminating the device photoexcited electron-hole pairs are produced causing the quasi Fermi levels to split, resulting in the generation of a photovoltage. The effect of this on the J-V curves is that the onset potential of the HER and OER are shifted by the open circuit potential of the photocathode, $V_{\mathrm{oc,C}}$, and photoanode, $V_{\mathrm{oc,A}}$, respectively. Due to the nature of the reactions the onsets are shifted in opposite directions towards 0 V vs a reversible hydrogen electrode (RHE) on the potential scale. If the curves are shifted to a degree where they intersect the device is able to perform unassisted water splitting, running at a current density given by the intersection of the two curves, J_{op}. If the currents are not matched, signified by J_{mm}, the saturation current densities of the two devices will be different. This means that even if the two cells are otherwise perfect, maximum efficiency cannot be achieved.

The monolithic tandem cell described above can in principle be used to split water but several improvements to the design can be made in order to increase the stability of the device. As mentioned, the band bending in the semiconductor originates from it equilibrating with the redox reaction taking place in the electrolyte. In case of water splitting the reaction potentials are dependent on the H^+ concentration in the electrolyte, which means that the produced photovoltage becomes a function of the pH of the system. To counter this issue one can use a so-called buried junction type device, where the charge separation is achieved using

a semiconductor pn-junction rather than a semiconductor/electrolyte interface. In this way the power supply of the device becomes independent of the electrolyte meaning that it can work in both acidic and alkaline conditions. Such a buried-junction device was used by Khaselev *et al.* [13] to obtain a STH of 12.4% using III-V semiconductors. The downside of this approach was the poor stability as well as the high price of the device. Poor stability in strongly acidic or alkaline environments is likewise a problem for other semiconductors used to form the pn-junctions, which means that they need to be protected. This can be achieved by depositing a transparent protection layer such as NiO or TiO_2 on top of the cells [19, 24, 25]. The final buried-junction device is thus a fairly complex thin film structure and as outlined by Seger *et al.* [14] a lot of effort needs to go into its design.

1.3 Perovskite solar cells

In this thesis a priviously developed Si photocathode has been envisioned to serve as the SBG device due to its near optimal band gap [26]. The focus of the work presented here is thus on the development of a suitable LGB device with a band gap close to 1.7 eV. Though this is slighly higher than the 1.6 eV suggested by the optimum overall band gap, the additional photovoltage produced by such a layer would result in a larger margin of error. The choice for the large band gap photoabsorber fell on a, in terms of solar cells, fairly novel group of materials, namely organolead halide perovskites. These materials have shown great promise as thin film solar cell absorbers and devices based on them have reached power conversion efficiencies (PCE) of up to 22.1% [27]. At the beginning of the project the only subclass of these materials which had been examined was the methylammonium lead halides and these are thus the focus of the work presented in this thesis. Other materials have, however, been introduced and today one of the most successful perovskite devices produced, used a so-called triple cation structure where formamidinium (FA), methylammonium (MA) and caesium were mixed with Pb, I and Br [28]. Methylammonium lead halides, with the chemical formula $CH_3NH_3PbX_3$ (MAPbX, X = I, Br, Cl), crystallize in the perovskite structure ABX_3 where A and B are cations and X is the anion, as shown in Figure 1.6. The best studied materials are the pure iodide material $CH_3NH_3PbI_3$ or the mixed halide configuration, $CH_3NH_3PbI_{(3-x)}Cl_x$, which both feature a high absorbtion in the visible range, long carrier diffusion lengths and high defect tolerance [29, 30]. The inclusion of Cl was initially reported as being pivotal for achieving high PCEs as it was found to increase the carrier diffusion length substantially [31]. The cause for this was improved crystal growth during the formation of the perovskite promoted by the chlorine, though it was itself not present in the final material [32–34].

The inclusion of Br into the structure introduced a beneficial feature of the perovskite solar cells, namely the ability to tune the band gap of the absorber [35, 36]. As shown by Noh *et al.* [35] one can achieve a band gap ranging from 1.57 eV of the pure I perovskite to the 2.28 eV of pure bromine perovskite by varying the Br content in the $CH_3NH_3I_{(3-x)}Br_x$ structure. This makes the perovskites ideal for tandem cell construction as a material with the required band gap of 1.7 eV can readily be obtained. In addition to tunability of the band gap a large amount of fabrication methods have been demonstrated in literature. These include among

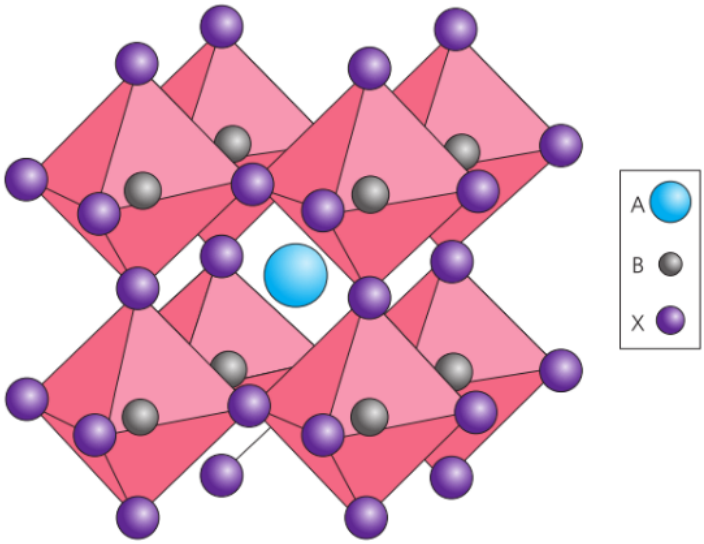

Figure 1.6: Visualization of the perovskite ABX_3 crystal structure. A is the MA, FA or Cs ion, B is the Pb ion while X is the halogen ion. Figure form [29].

others high vacuum deposition, chemical vapour deposition, spin coating and a wide variety of approaches for device production thus exist [21, 37–44]. In addition to the deposition technique the fabrication methods also differ when it comes to the number of steps involved in the perovskite preparation. Though the methods all introduce the Pb compounds through PbX_2 and the methylammonium halide as MAX, some do it in a single step deposition while others split the introduction into two separate processes. Both of these approaches have their merits and have been used with success [41, 45].

1.3.1 Device structure

Regardless of which perovskite is applied, two overall solar cell architectures are used, which have been dubbed the normal and the inverse design. Both of these configurations are based on using heterojunctions, rather than the homojunctions used in a Si pn-junction, to achieve the charge separation. A schematic band diagram of a basic perovskite heterojunction solar cell is shown in Figure 1.7. As indicated in the figure, the charge separation of the photogenerated holes and electrons happens at different interfaces in the device. The electrons are collected at the electron transport layer (ETL) which consists of a material with a lower conduction and valence band as compared to the perovskite. In this way electrons can freely move into the layer and be collected at the external contact while holes are blocked. The hole transport layer (HTL) works in a similar fashion but for holes. Throughout the thesis the terms electron and hole selective contact are used together with ETL and HTL when referring to these layers. Typical ETLs are TiO_2, Phenyl-C61-butyric acid methyl ester (PCBM[60]), ZnO and SnO while

common HTLs are N2,N2,N2′,N2′,N7,N7,N7′,N7′-octakis(4-methoxyphenyl)-9,9′-spirobi[9H-fluorene]-2,2′,7,7′-tetramine (Spiro-OMeTAD), NiO and poly(3,4-ethylenedioxythiophene) (PEDOT:PSS) [46–49]. Several of these layers were employed in the work described later in the thesis though many more exist. As detailed in Figure 1.7 metals or transparent conductive oxides (TCO) are usually used to form the front and back contacts, which are in turn, utilized to connect the solar cell to the external load. The optimal choice of material depends strongly on the situation and will be discussed in more detail in chapter 3.

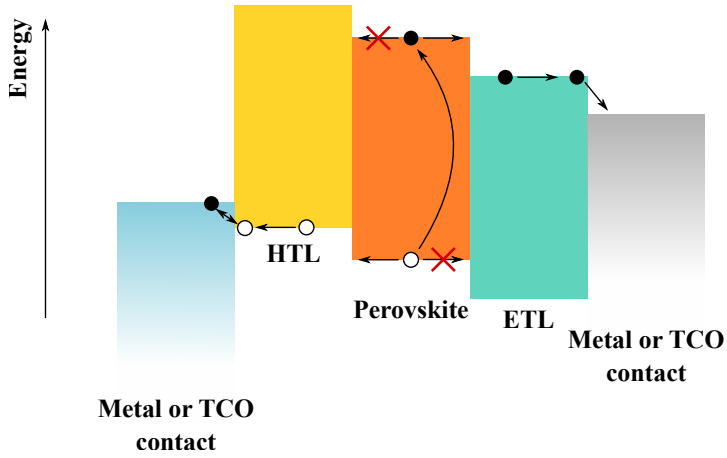

Figure 1.7: Schematic band diagram of a heterojuction perovskite solar cell under illumination. The filled out dots are electrons while the hollow ones are holes. HTL, ETL and TCO are abbreviations for hole transporting layer, electron transporting layer and transparent conducting oxide, respectively.

The most common structure is the normal configuration in which the ETL is deposited as the bottom layer of the junction stack, usually on top of a TCO covered glass substrate. In case TiO_2 is used as the ETL two different approaches have been investigated, namely the mesoporous and planar device structure. In the former case a mosoporous matrix of the metal oxide is prepared on top of a compact layer of TiO_2 [45]. The perovskite is then deposited onto the scaffold and infiltrates the porous structure. Afterwards, the HTL and back contact are deposited to finish the device. This device architecture has the advantage that the generated carriers do not have to diffuse very far to be collected by the mesoporous scaffold. The downside of this approach is that one risks having unconverted PbX_2 inside the scaffold, if the two step deposition method is applied. In case of the planar structure the perovskite and HTL layers are deposited on top of the compact TiO_2 after which the device is finished with the deposition of the back contact. This configuration has the advantage that it requires one less process step and that it is well suited for both types of deposition. The film layout of the normal configuration device can be seen in Figure 1.8a. In the inverse configuration the locations of the ETL and the HTL are switched as shown in Figure 1.8b. This allows for different choices with regards to which HTLs can be used. As an example, NiO usually

requires an annealing step over 200 °C which is incompatible with the perovskite. In the inverse configuration it is, however, deposited prior to the perovskite thus making it applicable.

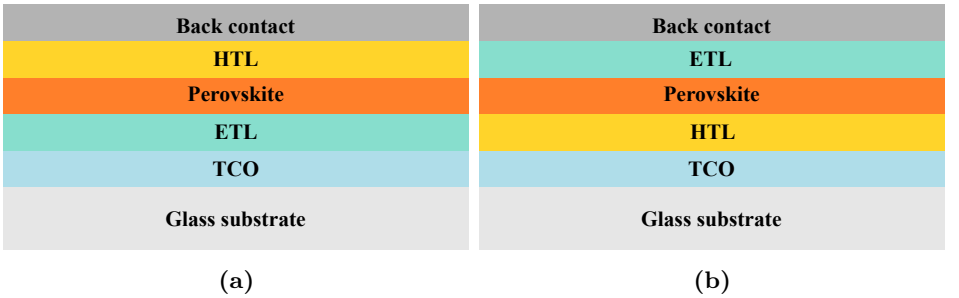

Figure 1.8: Schematic visualization of the **(a)** normal and **(b)** inverted configurations.

In addition to expanding the available ETLs and HTLs the choice of configuration also becomes important if the device is to be part of a tandem cell. Like with the PEC devices tandem cells have the potential to be substantially more efficient than a single band gap device. The maximal theoretical PCE of a single band gap cell can be shown to be 31% which is the so-called Shockley-Quessier limit [22, 50]. In comparison, a tandem device can theoretically reach up to 47% or 39% depending on whether a four or two terminal device, respectively, is used [50]. In the two terminal monolithically stacked device the LBG cell is deposited directly on top of the small band gap cell separated only by a suitable recombination layer. This device has the advantage that less contact layers are needed which results in a lower parasitic absorption. On the other hand the device requires well current matched subcells and is additionally more challenging to fabricate. In the four terminal configuration the two cells used are complete cells, each with a front and back contact. The high band gap cell is mechanically stacked on top of the SBG device and the devices are interconnected using wires. This approach has the advantage that it is easier to construct and does not suffer from rigorous requirements to current matching [50]. On the downside the structure is more prone to suffer from parasitic absorption and requires additional wiring.

Since the prevalent PV technology today is based on Si, much effort have gone into creating perovskite cells which could serve as top cell in a tandem device while using a Si cell as the bottom [51–54]. To this day the best performing device was a four terminal cell which displayed a PCE of 26.4%, which is very close to the efficiency of the best single band gap Si cell [53]. Perovskite-perovskite tandem cells have, however, also been demonstrated where incorporating Sn into the perovskite structure facilitated the production of low band gap (ca. 1.2 eV) devices [55, 56]. The produced PCEs were somewhat lower than the perovskite-Si devices though PCEs over 17% have been obtained [55, 56]. It should be mentioned that many of the above results have been achieved using either the triple cation approach

mentioned earlier or a combination of just FA and Cs.

Though the above mentioned properties of the methylammonium lead halides make them very suitable for PV cells they do have one major shortcoming, namely, their poor stability. In their relatively recent review paper Leijtens *et al.* [30] cover this issue and explain how the perovskites act under thermal and environmental stress. The major causes of $MAPbI_3$ degradation is found to be moisture and temperature. In the former case the moisture attacks the perovskite stucture and facilitates the removal of the organic compounds, leaving behind PbI_2 [57]. This transformation happens over time (tens of hours at 80 °C) if unprotected $MAPbI_3$ is exposed to atmospheric conditions [30]. In case the cell is submerged into water the degradation is almost instantaneous, making the prevention of moisture ingress paramount especially considering its intended use in this project. As introduced in chapter 3 several different approaches have been attempted in this thesis work, using either an epoxy coating or a layer of TiO_2 deposited by ALD to protect the perovskite. Inclusion of Br into the perovskite structure has furthermore been found to increase its moisture resistance [35].

Thermal decomposition is another stability challenge facing methylammonium lead halide solar cells. $MAPbI_3$ is found to undergo a structural change from tetragonal to cubic crystal structure at 60 °C though both faces are photoactive [30]. At 85 °C the $MAPbI_3$ is found to thermally decompose slowly into its constituents and considering that operation temperatures of PV modules can reach similar levels, this is naturally an issue [58, 59]. The thermal decomposition of $MAPbI_3$ was also studied during this thesis work as detailed in chapter 5. Leijtens *et al.* [30] explain that including a capping layer of ITO might serve to contain the volatiles (CH_3NH_2 and HI) which could increase the thermal stability of the layer. They do, however, strongly advocate the exclusion of MA from the perovskite structure owing to its inferior thermal stability as compared to structures containing only FA and Cs.

The final two causes for degradation are both induced by light. Oxygen has been found to readily photooxidise the perovskite, lowering their stability in atmospheric air [30]. Perovskite structures not containing MA have again been shown to be less susceptible to photooxidation which further favours the use of pure FA and Cs containing materials [30]. The effects of UV-radiation have also proven to be problematic if the common electron conductor TiO_2 is used. Due to the high energy of the photons the UV-light was found to introduce trap states in the TiO_2 conduction band which reduced the performance of the devices [60]. Fortunately this problem can be rectified by doping the TiO_2 with metal atoms and including 0.3% of Nd was found to increase the stability and PCE [61].

Though the stability challenges faced by the methylammonium lead halide are detrimental to the long term stability of the solar cells if not addressed properly, the benefits of $MAPbX_3$ certainly makes it worthwhile to study. If the cells can be properly protected from the environment and not heated unduly, this class of materials might have its place in the arsenal of renewable energy sources of the future.

1.4 Thesis outline

As initially mentioned the PhD work has mainly focused on the development of a suitable large band gap cell to include in an unassisted water splitting device. The results presented within the thesis all relate to the development of the perovskite cell though some of the studies are more fundamental in nature. The outline of the thesis is as follows

Chapter 2 introduces some of the more common experimental characterization and deposition methods used in the thesis.

Chapter 3 contains the projects related to perovskite solar cell and tandem device fabrication. The low pressure vapour assisted solution process (LP-VASP) deposition method is introduced and the performances of the solar cells it was used to produce, are presented. Devices including ALD TiO_2 layers along with the initial attempts at a perovskite photoelectrode are furthermore presented. Finally, details regarding the deposition of tin doped indium oxide (ITO) and aluminium doped zinc oxide (AZO) are presented. Though a final tandem device was never produced most of the individual projects showed great promise and could serve as the foundation for further investigations.

Chapter 4 details the work related to the evaporation of methylammonium iodide. The material was investigated using quartz crystal microbalance (QCM) experiments as well as mass spectrometry. Through the experiments insights into the fundamental nature of MAI evaporation and the difficulties relating to high vacuum deposition of $MAPbI_3$, were obtained.

Chapter 5 describes the work related to the thermal stability of $MAPbI_3$. QCM experiments, as well as mass spectrometry, were again employed to study the material. The experiments confirmed the low decomposition temperature of $MAPbI_3$ and provided kinetic and fundamental information about the degradation.

Chapter 6 gives a summery of the presented results and provides an overall conclusion of the thesis as well as an outlook detailing potential future work.

Chapter 2
Experimental methods

The main focus of this thesis has been characterization of materials as well as solar cell stack fabrication and in order to gauge the success of the endeavours several different characterization methods have been utilized. In this chapter a short introduction to the theory and application of the different methods will be given to help the reader gain insight into the general concepts before diving into the specific use in the later chapters. In addition brief introductions to the different thin film fabrication techniques used are included.

2.1 UV-visible spectroscopy

UV-visible spectroscopy, or UV-vis for short, uses monochromatic light to measure optical transmission or absorbance of a sample as a function of wavelength. From these several key parameters of a solar cell absorber material can be estimated, where the absorbance of the sample in the wavelength region of interest is the most important. The explanation for this is naturally that the absorbed photons is what drives the electron-hole pair generation of the PV device and a high absorbance of the absorber material is needed to achieve a high power conversion efficiency. The transmission T of a sample is given by

$$T = \frac{\Phi_t}{\Phi_i}, \tag{2.1.1}$$

where Φ_t and Φ_i is the transmitted and incident radiant flux, respectively. The transmission is correlated to the absorbance through

$$A = \log\left(\frac{\Phi_i}{\Phi_t}\right) = \log\left(\frac{1}{T}\right) = -\log(T), \tag{2.1.2}$$

where A is the absorbance. From this one gets that an absorbance of 1-2 means that $90\% - 99\%$ of the light is absorbed and being in this range is usually sufficient for efficient solar cell operation.

In the data presented in the thesis the UV-vis spectrometer was exclusively operated in a two beam configuration where the incident beam is split in two prior to hitting the sample. One part of the beam is let through the sample while the other is let through a reference, usually the sample substrate, which allows one to subtract the part of the absorbance not attributed to the active layer. In this way, one gains a better insight into the transmission of the absorber itself. The approach has one shortcoming, namely that one is not able to estimate the reflection of the sample. Consequently, the absorbance measured will most likely overestimate the amount of light absorbed in the active layer and one needs to use an integrating sphere set-up to get a more accurate measurement. One is, however, still able to get a lot of information from the two-beam experiment, depending on how the spectrum looks. The presence of a sharp increase in absorption (see e.g Figure 3.5) suggests a high amount of interband gap excitations in the sample. This is naturally what one would expect when irradiating a direct band gap semiconductor, like the perovskite, with photons more energetic than its band gap [29]. One can thus deduce that a large amount of the absorbance above this feature is caused by actual absorption in the sample.

A more quantitative piece of information obtainable from the absorbance spectrum is the band gap energy of the absorbing semiconductor. This parameter can be acquired by using what is known as a Tauc plot. It can be shown that

$$(\alpha h\nu)^{1/n_t} = B(h\nu - E_g), \tag{2.1.3}$$

where α is the absorption coefficient, h is Planck's constant, ν is the frequency of the light, n_t is equal to 0.5 or 2 for direct and indirect band gab transitions, respectively, B is a constant and E_g is the band gap energy of the absorber [62]. From Lambert-Beer's law

$$T = \frac{\Phi_t}{\Phi_i} = \exp(-\alpha d) = \exp\left(-A\ln(10)\right), \tag{2.1.4}$$

where d is the sample thickness, one gets that $\alpha = \frac{A\ln(10)}{d}$. Inserting this in equation (2.1.3) yields

$$\left[\frac{Ah\nu\ln(10)}{d}\right]^{1/n_t} = B(h\nu - E_g) \Leftrightarrow (Ah\nu)^{1/n_t} = B_1(h\nu - E_g), \tag{2.1.5}$$

where $B_1 = B[d/\ln(10)]^{1/n_t}$. From equation (2.1.5) one would expect that a plot of $(Ah\nu)^{1/n_t}$ vs $h\nu$ would yield a straight line where the intersection with the $h\nu$-axis would yield E_g. In reality non-linear effects dominate in certain parts of the spectrum as explained by Viezbicke *et al.* [62] and due to this a real Tauc plot looks more like the data shown in Figure 2.1. To estimate E_g one fits the linear region, where equation (2.1.3) does hold true, and uses that the fitted lines intersection with the $h\nu$-axis equals the band gap energy. The precision of E_g is dependent on the quality of the data and due to the implications of the sample reflectance the two beam experiments will only yield an estimation of the band gap. To measure

the data presented in the thesis a Shimadzu SolidSpec-3700 UV-Vis spectrometer was used. For the Tauc plot analysis a direct band gab was assumed ($n_t = 0.5$) in all cases.

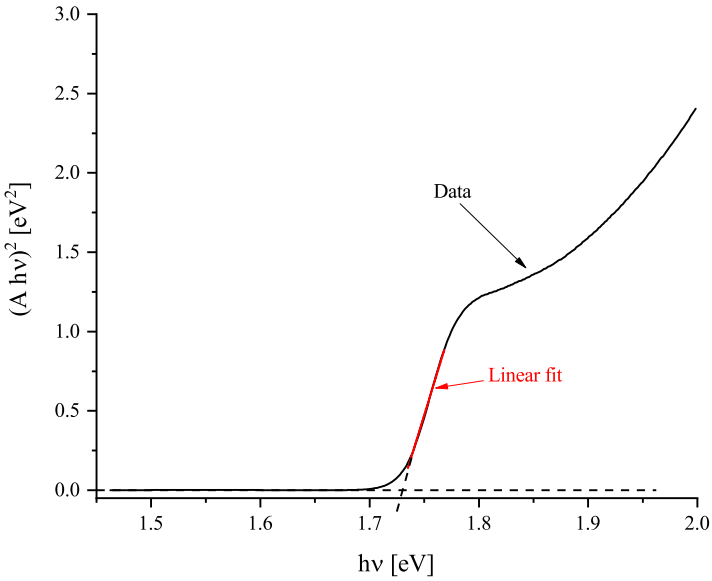

Figure 2.1: Tauc plot analysis of a perovskite absorption spectrum assuming a direct band gap. The black curve shows the data while the red curve shows the linear fit. The E_g is estimated to be around 1.73 eV.

2.2 X-ray diffraction

X-ray diffraction (XRD) patterning is widely used to analyse powders or thin films as the technique gives a large amount of insight into what different species constitutes the sample material, as long as they are reasonably crystalline. As the name suggests, the working principle behind XRD involves diffraction of X-rays or more precisely inelastic scattering off the atoms of the sample being examined [63]. The scattered X-rays will interfere with one another and since the amount of scatters is usually very large, and sitting in a well defined crystal lattice, one can show that constructive interference will almost exclusively occur if the so-called Bragg equation is observed. The Bragg equation is given by

$$\lambda n_B = 2d_{hkl} \sin(\theta_B), \tag{2.2.1}$$

where λ is the wavelength of the X-rays, n_B is the reflection order, d_{hkl} is the interlayer distance of the crystal planes and θ_B is the X-ray angle of incidence as seen in Figure 2.2.

The interlayer distance for the different crystal orientations are given from the Miller indices hkl as well as the interatomic distances of the material. For a simple

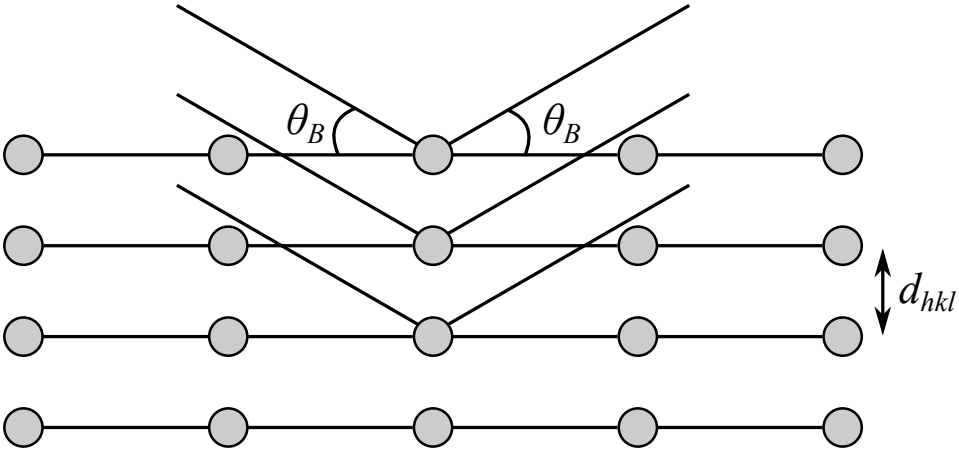

Figure 2.2: Schematic showing the interaction of X-rays with a crystal structure.

cubic crystal structure only one interatomic distance, a, is needed to define the structure, yielding the relationship

$$d_{hkl} = \frac{a}{\sqrt{h^2 + k^2 + l^2}}. \tag{2.2.2}$$

By scanning through θ_B and detecting the scattered X-rays one can generate a diffraction pattern of a material, which will be unique due to the interatomic distance being material specific. This feature allows one to detect different (crystalline) species composing a sample and thus gauge the success of ones fabrication process. The most commonly used technique is the $\theta/2\theta$ configuration, where the detector and the X-ray tube are both scanned through θ_B. The method usually yields good results for powders and reasonably thick thin film samples. For very thin samples, or in cases where the sample substrate gives rise to issues, one can use gracing incidence X-ray diffraction (GIXRD). Here the X-rays angle of incidence is kept constant allowing one to scan only the topmost part of the sample. In this thesis the presented patterns were recorded at LBNL and measured using a Rigaku SmartLab set-up in the GIXRD configuration.

2.3 Scanning electron microscopy

Scanning electron microscopy (SEM) is routinely employed to image structures with sizes down to tens of nanometres. Rather than using light as in a normal microscope SEM sweeps a high energy electron beam across the sample surface. The electrons interact with the material in different ways, which allows for a diverse range of characterization methods. The most immediate of these originates from analysis of secondary electrons (SEs) which is what is used to image a surface. Secondary electrons are generated when the primary beam of the microscope interacts with the material and will typically have an energy of 5-50 eV. Due to the low energy, their mean free path in the material will be limited to around a nanomater, which means,

that only electrons generated close to the surface of the sample can be detected [64]. In a SE image the parts of the sample closest to the detector will appear brighter and one is thus able to obtain the structure as well as the topography of the sample surface. As the microscope requires a low pressure to function, the samples need to be high vacuum compatible and additionally conductive enough to avoid charging.

The second imaging mode of a SEM microscope, the so-called backscatter mode, utilizes the electrons of the primary beam that scatter off the sample to give information of the sample composition. Since the scattering efficiency of the sample atoms increases with their Z number, heavier atoms will appear brighter in the image which allows one to discern between different materials incorporated into the sample. The composition of the sample can furthermore be investigated using another product of the primary beams interaction with the sample, namely X-rays. As the frequency of the emitted X-rays will depend on the energy levels of the atom generating them, they can be used to elucidate the chemical composition of the sample. This technique is aptly named electron dispersive X-ray analysis or EDX for short. In this project only the secondary electron imaging method has been employed to gauge the thickness and homogeneity of the various layers in the thin film stack. The images have all been captured using a Quanta FEG ESEM which is located at DTU CEN.

2.4 Ellipsometry

Ellipsometry is a non-destructive way of determining the complex refractive index, as well as the thickness, of a thin film sample by illuminating it with elliptically polarized monochromatic light. By measuring the polarization of the reflected beam one is able to deduce the refractive index, the extinction coefficient and the thickness of the film. In the simplest case possible (a single interface and a thick film) the material parameters can be obtained relatively easy from the change in polarization [65]. In thin film cases where multiple interfaces are present interpretation of the measurements become much more difficult and complicated modelling is required. The model used at LBNL was developed for TiO_2 thin films on top of SiO and Si prior to my arivel at LBNL. The creation of the model was thus not something I was involed in and the specifics are not known to me. Introductions to the general mechanics of the various fitting routines usually employed can, however, be found in literature [65,66]. In all cases the ellipsometry measurements were conducted using a J.A Woolam alpha-SE ellipsometer.

2.5 Mass spectrometry

Mass spectrometry is a widely used experimental technique which allows one to gauge the chemical composition of a sample. As the name suggests, this is done by observing the masses of the different constituents of the material as it is evaporated. By comparing the observed distribution of masses, called a mass spectrum, with reference spectra one can identify the different compounds included in the sample. This feature is naturally very useful and allows one to identify unknown compounds, detect gaseous products of a chemical reaction or analyse thermal fracturing patterns of materials. In the work presented in this thesis mass spectrometry is used for the latter as detailed in a later chapters.

Several different types of mass spectrometers exist such as quadropol mass spectrometers (QMS), time-of-flight mass spectrometers (TOFMS) or sector magnet mass spectrometers. The common factor for all of the approaches is that they require the particles under investigation to be charged in order to separate and detect them individually. To ionize the gaseous species they are let through a beam of electrons, which subsequently charge them. The difference between the different techniques lies in how they filter the ionized compounds. The QMS uses a time varying electric field while the TOFMS uses the time flight through the mass filter to select the mass per charge range to study. In this work a sector magnet type mass spectrometer has, however, been used and thus only this technique will be discussed in detail. As the name suggests a mass filter based on a magnetic field rather than an electric one, is used. The force, $\mathbf{F}$, on a charged particle moving in an electric and magnetic field is governed by the Lorantz force law

$$\mathbf{F} = z(\mathbf{E} + \mathbf{v} \times \mathbf{B}), \tag{2.5.1}$$

where z is the charge of the particle, $\mathbf{E}$ is the electric field, $\mathbf{v}$ is the velocity of the particle and $\mathbf{B}$ is the magnetic field. In the absence of an electric field, and in the case where the magnetic field only points in one direction, the magnitude of the force, F, becomes

$$F = zvB, \tag{2.5.2}$$

where v and B denote the magnitudes of $\mathbf{v}$ and $\mathbf{B}$, respectively. The particle will move in a circular fashion perpendicular to $\mathbf{v}$ and $\mathbf{B}$ where the centripetal force equals the magnetic force. From this one gets

$$zvB = m\frac{v^2}{R} \Leftrightarrow v = \frac{zBR}{m}, \tag{2.5.3}$$

where R is the radius of the circular trajectory and m is the mass of the particle. The speeds of the particles are controlled by the potential, V, applied in the ion source which yield the kinetic energy

$$zV = \frac{1}{2}mv^2. \tag{2.5.4}$$

By inserting this in equation (2.5.3) one gets

$$\frac{m}{z} = \frac{B^2R^2}{2V}. \tag{2.5.5}$$

In the mass spectrometer the value of R is fixed by the curvature of the magnetic zone and one can therefore filter the particles by their m/z ratio by varying B and V. For the experiments conducted in this project, a Waters VG AutoSpec was used which features a m/z range of 0-3000 AMU/e. The spectrometer furthermore featured an ionization source where the ionization energy could be varied. A schematic overview of the various slit and lens positions are shown in Figure 2.3

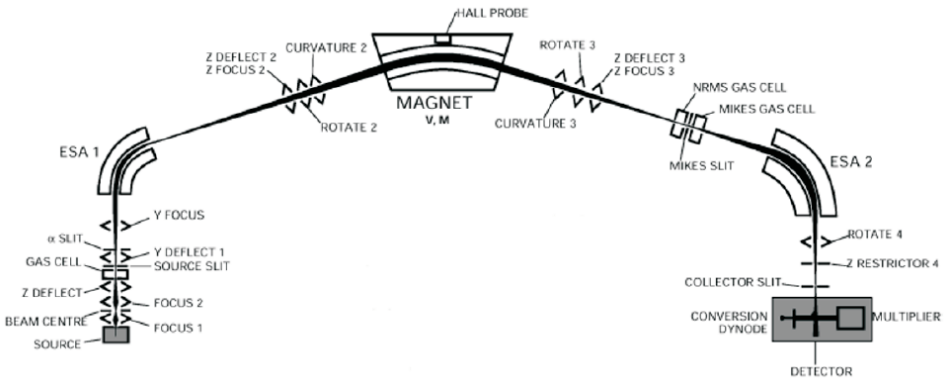

Figure 2.3: Schematic overview of the various slits and lenses included in the Waters VG AutoSpec. Figure from [67].

The mass resolution of the experiments depended on the slit and lens settings used during the experiment, which also controlled the signal intensity. Before a measurement was performed, the lens and slit setting were therefore calibrated to obtain optimal performance. For the experiments shown in the following chapters a mass resolution above 1500 was used in all cases. The hall probe usually used to gauge the size of B was, sadly, not operational. To calibrate the magnet current, and subsequently the m/z axis, the reference chemical Perfluorokerosene (PFK) was introduced through a septum. By recording a mass spectra of the compound and comparing it to a reference, the appropriate shift in the m/z axis could be determined and applied in the subsequent experiments.

2.6 *J-V* characterization

The main method for characterizing a perovskite solar cell utilized in the thesis was to measure the correlation between the voltage, V, applied to it and the current density, J, it produced, also known as the J-V characteristic. In essence, this is done by applying external contacts to the front and back contacts of the device, and subsequently sweep the potential while measuring the produced current. By knowing the device area one is able to convert the measured current into current density and obtain the J-V characteristics. From the curves one can deduce the PV performance of the device but also gain insights into possible issues. To do so one compares the cell characteristics with a model of the device. Most solar cells are based on one or more pn-junctions, which are formed when a n-type and a p-type semiconductor is brought into contact with each other. Given their difference in Fermi level the two materials will equilibrate by an exchange of holes and electrons. As with the semiconductor-electrolyte junction, the immobile nuclei will remain behind forming the so-called depletion region. The static charges give rise to an electric field and consequently band bending. Equilibrium is established when the electric field is of such a magnitude that it prevents further exchange of

charge carriers. The band bending introduced during equilibration is illustrated in Figure 2.4.

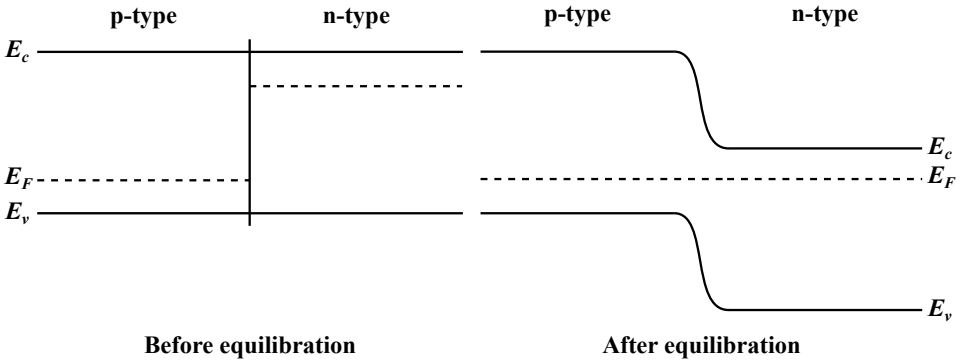

Figure 2.4: Schematic drawing of the band diagram of the pn-junction before and after the equilibration process. E_F is the Fermi level, E_c is the conduction band and E_v is the valance band.

Upon illuminating the device electron-hole pairs will be generated and due to the band bending photoexcited electrons in the p-type will be swept to the n-type while the opposite is true for the holes. In this way the generated electron-hole pairs are separated spatially which effectively prevents them from recombining radiatively with one another. Due to the constant injection of holes into the p-type and electrons into the n-type, a quasi-equilibrium is established in the two regions, yielding the quasi-Fermi level, $E_{F,n}$ and $E_{F,p}$, in the n-region and p-region, respectively. This splitting of the Fermi level will give rise to a potential difference between the two regions, which can be used to drive current through an external load. A schematic band diagram of a pn-junction under illumination is shown in Figure 2.5.

In case of the perovskite solar cell the band structure is slightly different from a regular pn-junction and more similar to a p-i-n junction, where an intrinsic semiconductor is included in-between the two doped layers. The inclusion of an intrinsic layer broadens the depletion region which consequently widens the region where charges are properly separated. The mechanises of the device, however, remain the same as in the regular pn-junction and thus the model of the J-V behaviour will not change. Due to this fact the model presented will be derived on the basis of a pn-junction diode following the steps detailed in [68]. The object of the model is to describe the dependence of the current, I, passing through the device on the potential difference across the junction, V. If the interface of the junction has the area A one obtains $I = JA$. In the dark the current density through the device comes from majority carriers surmounting the potential barrier or from minority carriers in the two regions (electrons in the p-type or holes in the n-type) being swept across the depletion region. By ignoring edge effects, the problem becomes one dimensional in nature (e.g. the x-dimension) and J thus equals

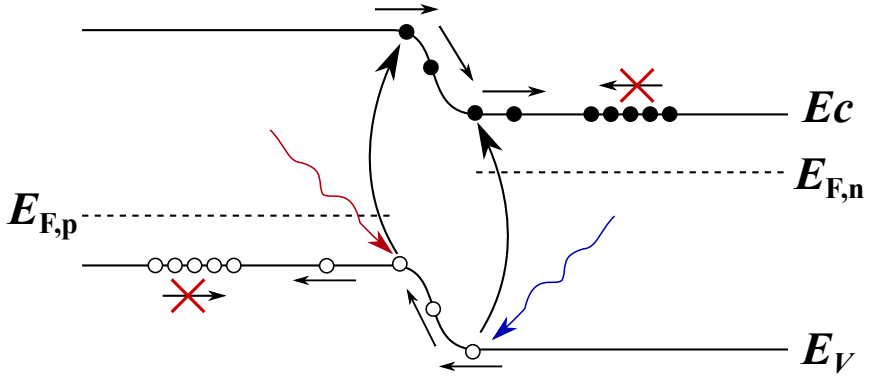

Figure 2.5: Schematic drawing of the band diagram of the pn-junction under illumination. E_c is the conduction band and E_v is the valance band while $E_{\mathrm{F,n}}$ and $E_{\mathrm{F,p}}$ are the Fermi levels in the n and p region, respectively.

$$J = J_n(x) + J_p(x), \tag{2.6.1}$$

where $J_n(x)$ is the current density attributed to electrons at x and $J_p(x)$ is the current density attributed to holes at x. At equilibrium J must naturally equal zero which means that J_n and J_p cancel exactly. Applying a forward bias to the device will split the Fermi levels in the same way as when illuminating the cell, which will cause a non zero current to run across the junction. When the carriers reach the opposite region they are now minority carriers and one can thus model the overall current through the device by deducing the minority carrier densities of the electrons in the p-type material and the holes in the n-type material. The transport of the carriers happens either by drift in an electric field or through diffusion. If one assumes that the potential drop happens entirely at the junction and that no electric field is thus present outside the depletion region, carriers arriving at its edge can only get there by diffusion. If one furthermore assumes that the thermal recombination and generation inside the depletion region is negligible, continuity demands that the current density flowing out of the region must equal what entered it [68]. If the depletion region extends $-x_p$ into the p-type region and x_n into the n-type region one thus arrives at

$$J = J_n(-x_p) + J_p(x_n). \tag{2.6.2}$$

Due to the absence of an electric field outside the depletion region

$$J_N = qD_N \frac{d\Delta n_p}{dx}, \tag{2.6.3}$$

and

$$J_N = -qD_P \frac{d\Delta p_n}{dx}, \tag{2.6.4}$$

where D_n, D_p, Δn_p, Δp_n, are the diffusion constants and change in minority carrier concentration of the electrons and holes, respectively, while q is the electron charge. By assuming that the quasi-Fermi level splitting inside the depletion region equals qV, the minority carrier concentrations at the junction edge can be found from the so-called law of the junction

$$np = n_i^2 \exp\left(\frac{qV}{k_B T}\right), \tag{2.6.5}$$

where n_i is the intrinsic doping level of the semiconductors (here assumed to be the same), k_B is the Boltzmann factor and T is temperature. The minority carrier concentrations of holes in the n-type layer and electrons in the p-type layer far from the junction equal n_i^2/N_D and n_i^2/N_A, respectively, where N_D is the doping density of the n-type material and N_A is the doping density of the p-type material. From this one can find the change in minority carrier concentrations and by assuming steady state conditions Pierret [68] shows that

$$J_n(-x_p) = q\frac{D_n\ n_i^2}{L_n\ N_A}\left[\exp\left(\frac{qV}{k_B T}\right) - 1\right], \tag{2.6.6}$$

and

$$J_n(x_n) = q\frac{D_p\ n_i^2}{L_p\ N_D}\left[\exp\left(\frac{qV}{k_B T}\right) - 1\right], \tag{2.6.7}$$

where L_n and L_p are the diffusion lengths of the electrons and holes, respectively. By inserting equations (2.6.6) and (2.6.7) into (2.6.2) one arrives at

$$I = JA = Aq\left(\frac{D_n\ n_i^2}{L_n\ N_A} + \frac{D_p\ n_i^2}{L_p\ N_D}\right)\left[\exp\left(\frac{qV}{k_B T}\right) - 1\right], \tag{2.6.8}$$

or

$$I = I_0\left[\exp\left(\frac{qV}{k_B T}\right) - 1\right], \tag{2.6.9}$$

where

$$I_0 \equiv Aq\left(\frac{D_n\ n_i^2}{L_n\ N_A} + \frac{D_p\ n_i^2}{L_p\ N_D}\right). \tag{2.6.10}$$

Equation (2.6.9) is called the ideal diode equation, while I_0 is called the reverse saturation current which is generally very small. For a real diode the assumption that the generation and recombination inside the depletion region can be neglected, is not always sound and a more realistic model is

$$I = I_0\left[\exp\left(\frac{qV}{nk_B T}\right) - 1\right], \tag{2.6.11}$$

where n is called the ideality factor [69]. As mentioned, illumination of the pn-junction will give rise to a photocurrent, I_L, which will flow in the same direction as the dark current. The equation for the diode under illumination thus becomes

$$I = I_0 \left[\exp\left(\frac{qV}{nk_BT} \right) - 1 \right] - I_L. \tag{2.6.12}$$

From this equation one can define the figures of merit generally used to describe the performance of a solar cell. The open circuit voltage, V_{oc}, is the potential at which no current is passed while the short circuit current, I_{sc}, is the current flowing in the absence of a bias. For good devices I_{sc} will equal I_L though this is not always the case as discussed later. The power produced by the cell is equal to the product of V and I, which reaches a maximum at the maximum power point $P_{\text{mp}} = V_{\text{mp}} I_{\text{mp}}$. From P_{mp} one can define the fill factor, FF, as

$$FF = \frac{V_{\text{mp}} I_{\text{mp}}}{V_{\text{oc}} I_{\text{sc}}}. \tag{2.6.13}$$

As stated previously one is generally interested in the current density rather than the current, as it makes the comparison of devices with different areas easier. Consequently the short circuit current density, $J_{\text{sc}} = I_{\text{sc}}/A$, and the maximum power point current density $J_{\text{mp}} = I_{\text{mp}}/A$ will be used throughout the thesis. The locations of J_{sc}, V_{oc}, J_{mp} and V_{mp} on a J-V curve are visualized in Figure 2.6.

The most important parameter of a solar cell is its power conversion efficiency (PCE) which is defined as its produced power density divided by the intensity of the sunlight. Under AM1.5 illumination the intensity equals 100 mW/cm^2 and the PCE thus becomes

$$\text{PCE} = \frac{J_{\text{mp}} V_{\text{mp}}}{100 \text{ mW/cm}^2}. \tag{2.6.14}$$

Equation (2.6.12) is a good model for the J-V behaviour of well optimized solar cells. Often devices, however, suffer from the effects of parasitic resistances which leads to reduced performance. In the modelling done so far it has been assumed, that the carriers that do not recombine radiatively, have to do so by travelling through the external load, to get to the opposite contact of the solar cell. If the interface, on the other hand, contains defects, recombination paths through the depletion region might be present. This phenomenon effectively shunts the cell either slightly or, in the worst case, completely. The overall resistance of the shunting paths is known as the shunt resistance, R_{sh}, which is very high for efficient cells.

To get to equation (2.6.12) it was, additionally, assumed that there is no potential drop outside the depletion regions or when the carriers move into the external contacts. This is naturally an idealized situation and in real devices some resistance, called the series resistance, R_s, will be present. In good solar cells the series resistance is very small. The effects of the shunting and series resistances can be deduced if one looks at the equivalent circuit diagram of a solar cell, shown in Figure 2.7, where R_{sh} and R_s are included.

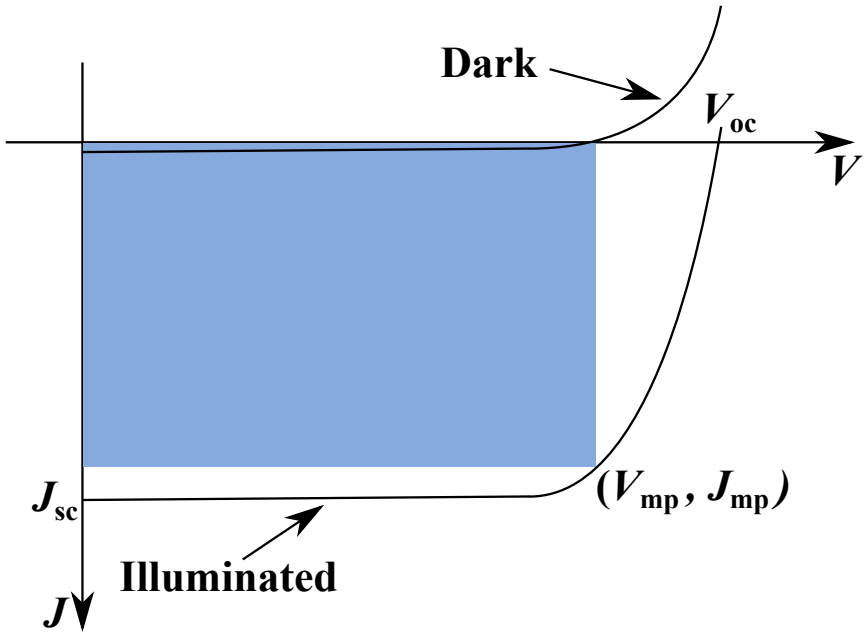

Figure 2.6: Schematic drawing of a J-V curve visualizing the locations of J_{sc}, V_{oc}, J_{mp} and V_{mp}. The maximum area of the blue square defines the maximum power point.

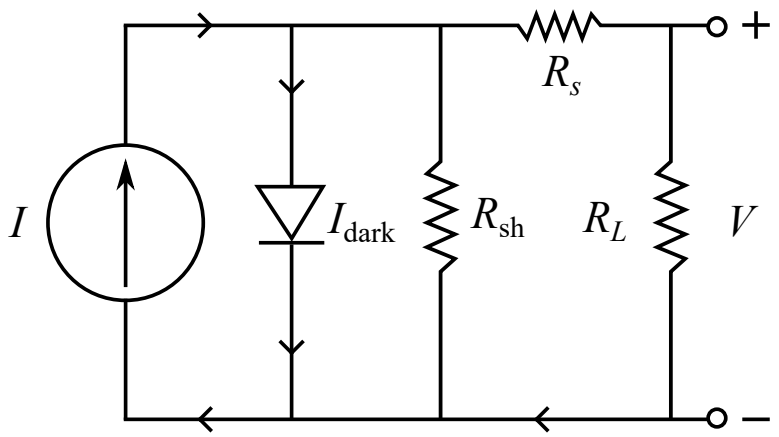

Figure 2.7: Schematic drawing of the equivalent circuit of a solar cell. I is the produced current, I_{dark} is the dark current running through the diode, while R_L is the external load.

From the circuit it is clear that the potential drop across the diode and R_{sh}, must equal $V + IR_s$ which means that the current flowing through R_{sh} is $(V + IR_s)/R_{\text{sh}}$. If these changes are included in equation (2.6.12) one arrives at

$$I = I_0 \left[\exp\left(\frac{q(V + IR_s)}{nk_BT} \right) - 1 \right] - I_L + \frac{V + IR_s}{R_{\text{sh}}}. \tag{2.6.15}$$

The qualitative effects that non-ideal parasitic resistances have on J-V curves are shown in Figures 2.8a and 2.8b [70]. A high series resistance is seen to lower the fill factor and additionally lower J_{sc}. A low shunt resistance will likewise decrease the fill factor and lower V_{oc}. A low shut resistance will furthermore give rise to a significant dark current. By comparing the measured curves to what one would expect from equation (2.6.12), one can therefore gain insight into the healthiness of the device and pinpoint which parasitic resistance is not optimal. A more quantitative estimation of R_s and R_{sh} is, however, also possible from the J-V curves. The shunt resistance can be estimated from the slope of the curve through J_{sc} while R_s can be found through a comparison of the light and dark J-V curves [69].

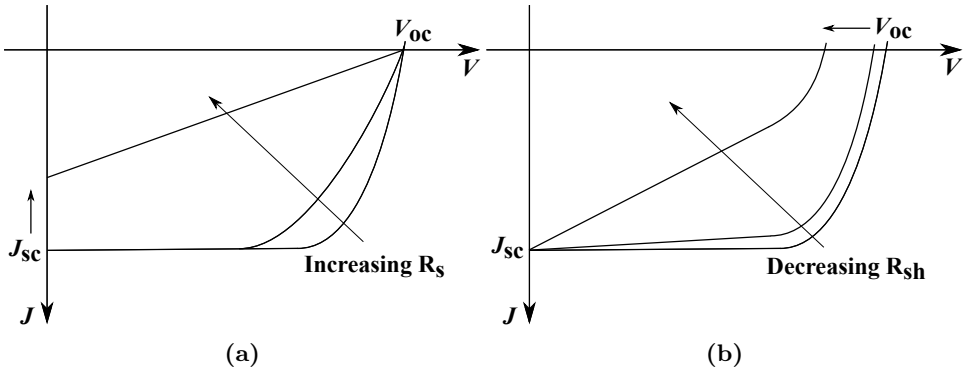

Figure 2.8: Qualitative visualization of the effects of sub-optimal parasitic resistances. **(a)** shows the effects of increasing R_s while **(b)** shows the effect of decreasing R_{sh}.

2.7 Quartz crystal microbalance measurements

A quartz cryskal microbalance (QCM) is based on a piezoelectric quartz crystal and is often used as a rate monitor due to its ability to detect the rate at which a film is being deposited on its surface. By applying an alternating potential to the crystal it will oscillate at harmonic frequencies which are dependent on the thickness of the crystal. By assuming that the film being deposited is an extension of the crystal, the shift in resonance frequency can be related to the change in deposited mass per area. The correlation is given by the Sauerbrey equation

$$\Delta f = -C_f \Delta m, \tag{2.7.1}$$

where Δf is the frequency change, C_f is the so-called sensitivity factor and Δm is the change in mass per area [71]. By measuring the rate of frequency change, one can determine the rate of mass per area change and ultimately the increase of the film thickness. C_f depends on the crystal used and can be shown to equal

$$C_f = \frac{2n_q f_0^2}{(\rho_q \mu_q)^{1/2}}, \tag{2.7.2}$$

where n_q is the number of the harmonic at which the crystal is driven, f_0 is the resonant frequency of the fundamental mode of the crystal, $\rho_q = 2.648 \ \frac{\text{g}}{\text{cm}^3}$ is the density of quartz, $\mu_q = 2.947 \times 10^{-11} \ \frac{\text{g}}{\text{cm s}^2}$ is the shear modules of quartz [72]. Assuming that $n_q = 1$ and using that $f_0 = 6 \times 10^6$ Hz for all the crystals used in this work, yields $C_f = 8.15 \times 10^7 \ \frac{\text{cm}^2 \text{ Hz}}{\text{g}}$. This means that a frequency change of 1 Hz is equivalent to 12.3 ng/cm^2 being deposited, thus making a QCM a very sensitive scale.

2.8 4-point probe measurements

4-point probe measurements can be used to accurately measure the sheet resistance, ρ_s, of materials by using different probes to measure current and potential individually. A sketch of the 4-point probe measurement configuration is shown in Figure 2.9.

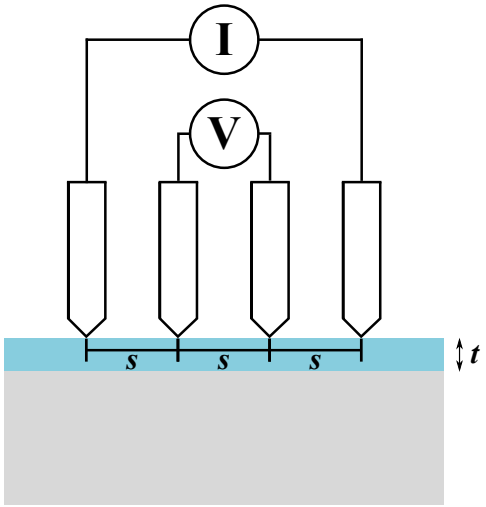

Figure 2.9: Schematic drawing of a 4-point probe measurement of a thin film with thickness t using probes with equal spacing s.

The current is forced through the outer leads while the resulting potential is measured between the inner probes without passing any current. If the probes are in-lined while the spacing, s, between them is the same, the interpretation of the results is considerably easier. If the ratio between the sample thickness, t, and

the probe spacing (t/s) is, furthermore, below 0.5 one can show that the sheet resistance is given by [70, 73]

$$\rho_s = \frac{\pi}{\ln 2}\frac{V}{I}. \tag{2.8.1}$$

The 4-point probe measurements were conducted using a commercial 4-point probe and a Keithley multimeter which allowed for 4-way sensing.

2.9 Physical vapour deposition methods

To fabricate the thin film solar cell stack discussed previously, a series of different deposition methods were used. In this section a short introduction to some of the more common physical vapour deposition (PVD) methods used is included. The common factor in all the methods is that they employ a beam of the material intended for deposition to fabricate the thin films. To ensure a high cleanliness of the procedures, they are all performed in high vacuum chambers using background pressures below 6.7×10^{-4} Pa. The differences in the methods relate to the way they create the material beam which gives rise to both advantages and drawbacks.

2.9.1 Thermal evaporation

The simplest PVD process is thermal evaporation, where the energy needed to sublimate the material is supplied by heating it. In practise this is often done by placing the material in an evaporation "boat" made from a highly thermally stable material such as W. A large current is then applied to the boat, which subsequently heats resistively. Another approach is to run the current through a rod of the material itself. The advantage of the thermal evaporation approach is that the evaporated species are mostly not very energetic and thus cause minimal impact damage when hitting the sample. The downside of this approach is that many of the materials used have a high evaporation temperature and need to be compatible with the boat materiel. Thermal evaporation is thus not applicable in some cases. In this project thermal evaporation was used to deposit Au and Ag from a W boat, while Ti was evaporated by running a current through the material itself. $PbCl_2$ and MAI were furthermore deposited using effusion cells, which in the latter case was homemade. The evaporation rate of a material, m_e, can be shown to be related to its vapour pressure, p, by

$$m_e = \sqrt{\frac{M}{2\pi RT}} \times p, \tag{2.9.1}$$

where M is the molar mass of the material, R is the gas constant and T is the evaporation temperature [74]. The vapour pressure itself is exponentially dependent on T, as well as the sublimation enthalpy of the material, and the evaporation rate is thus expected to increase strongly with increasing evaporation temperatures [75]. Except for the MAI case, which will be discussed further in chapter 4, a deposition pressure around 6.7×10^{-4} Pa was used.

2.9.2 Sputter deposition

In case of sputtering, material is released from the sputtering target by bombarding it with ions. The standard sputtering gas is Ar, where the ions are supplied by generating a plasma inside the chamber. By applying a strong bias to the target, the Ar ions are accelerated towards it and subsequently sputter the surface. To better confine the plasma to the surface of the sputter target, permanent magnets are often used which increase the deposition rate substantially. By introducing O_2 or N_2 together which the Ar one can furthermore deposit oxides and nitrides. The drawback of sputter deposition is that high energy particles are released from the target, which can cause considerable damage to the sample surface. This unfortunate feature limits the use of sputter deposition to samples which are sufficiently durable to withstand the bombardment. On the other hand, sputtering the sample with Ar is a good way of cleaning it, and offers a way to remove any native oxide that has formed on its surface. In addition, sputtering is very suitable for deposition of materials with high evaporation temperatures. To generate a plasma the deposition pressure of a sputtering process is usually around 0.4 Pa. This causes the mean free path of the particles escaping the target to be lower than in the thermal evaporation case. This feature leads to better step coverage which might be attractive in some cases but also complicates the use of shadow masking. In this project reactive sputtering of Ti, Ni and ITO was used to deposit TiO_2, NiO as well as ITO itself using two different AJA sputtering systems.

2.9.3 E-beam evaporation

The final PVD method used in this thesis was electron beam evaporation or E-beam for short. As with the thermal evaporation method the material is deposited by supplying thermal energy to the evaporation target. In case of E-beam evaporation the heat is, however, delivered by bombarding the target with high energy electrons (10-20keV). The electrons are generated from a filament and guided towards a crucible containing the material to be deposited using a magnetic field. By varying the magnetic field the electron beam can be swept across the target and subsequently heat the material. The advantage of E-beam is that materials with a high evaporation temperature can readily be deposited at high rates and with substantially less sputter damage. The downside of E-beam evaporation is that the high energy electrons might produce X-rays (through bremsstrahlung) which could damage the sample. In the project E-beam evaporation was exclusively used at LBNL to deposit Au and Ti back contacts.

2.10 Atomic layer deposition

Atomic layer deposition (ALD), as the name suggests, allows one to deposit films of material one atomic layer at a time by using sequential deposition of self terminating gas-solid reactions [76]. In the simplest scheme two different gasses are used which react and from the desired thin film material. A normal ALD cycle progresses as shown schematically in Figure 2.10. Initially the first reactant gas, "A", is lead into the reaction chamber where it adsorbs on the sample surface. Given the self-terminating nature of the gas it will cover the entire surface in a highly conformal

way, which results in a superb step coverage. Following the first reactant phase, the gas is purged by evacuating the reaction chamber. The remaining reactant, "B", is then introduced into the chamber where it reacts with species "A" and forms a layer of the film. The cycle finishes with the purge of by-products of the reaction as well as unreacted chemical "B". The cycle is repeated as many times as needed to reach the desired film thickness. During the deposition the substrate temperature can be changed to promote better growth as well as good crystallization. The ALD depositions were, in all cases, performed using a GEMStar XT thermal ALD system.

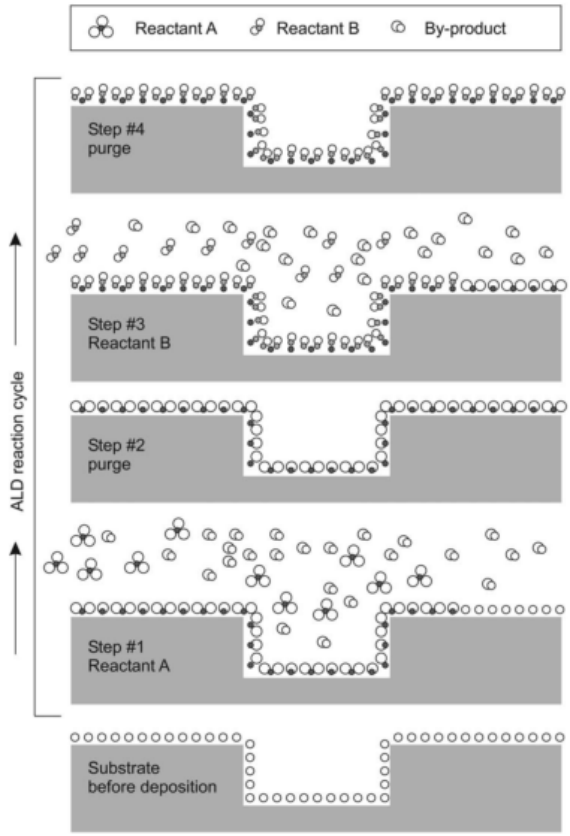

Figure 2.10: Schematic overview of an ALD proccess using the two reactant gases A and B. Figure from [76].

2.11 Spin coating

Spin coating is a commonly used technique in the microelectronics industry where it, among other things, is applied to deposit thin films of photoresist. The working principle of a spin coating process is, conceptually, very simple. The substrate is placed on a stub and affixed using a vacuum after which the solution, containing

the thin film material, is introduced. The sample is then spun rapidly and due to the centripetal force the solution will form a thin film, while excess solution is spun off the sides of the substrate. A the same time the solvent used in the solution will start to evaporate, which causes the film to become increasingly viscous, until it finally solidifies. In some cases an annealing step is included following the spin process to drive out any remaining solvent. Modelling the spin process is generally difficult due to the many factors involved, but the resulting film thickness, h_f, can be shown to roughly depend on the spin speed, ω, and the initial viscosity of the film, η_0, in the following way [77]

$$h_f \propto \eta^{1/3}\omega^{-1/2}. \tag{2.11.1}$$

As discussed by Hall *et al.* [77] the model will underestimate the film thickness in certain cases and thus only serves as a rule of thumb. The introduction of the deposition solution can happen either prior to spinning the sample or during, depending on the situation. As shown in detail in the following chapters, spin coating was used extensively during the fabrication of the perovskite devices.

Chapter 3

Low pressure vapour assisted solution processed solar cells for tandem devices

The low pressure vapour assisted solution processed (LP-VASP) fabrication method was developed at Lawrence Berkeley National Laboratory (LBNL) as a further development of the regular VASP method which was described by Chen *et al.* [41, 78]. The deposition scheme, which will be described in further detail in section 3.2, uses a sequential approach to fabricate $CH_3NH_3PbX_{(3-x)}Y_x$ (X, Y = I, Br, Cl) perovskite solar cells with good efficiency and relatively small hysteresis. It has furthermore been demonstrated that LP-VASP may be used to tune the band gap of the perovskite, by varying the ratio of MAI to MABr used in the process [36]. This made the LP-VASP method highly applicable for monolithically stacked tandem cell fabrication as absorbers with the ideal band gab of 1.7 eV could be fabricated on top of Si devices. The work presented in this chapter focused on fabricating a fully functioning tandem cell to which appropriate protection layers could be applied. Initially this involved finding the correct MAI/MABr ratio and fabricating single band gap devices to serve as a starting point for the continued investigations. After having established an appropriate fabrication scheme, which yielded fairly efficient solar cells, the work branched out in three different directions relating to either tandem stack production or device protection. Most of the results shown in this chapter were obtained during my external stay at LBNL though a section detailing work performed at DTU is included as well. The experiments carried out at DTU ran in parallel with the B.Sc and M.Sc thesis work of two students (Tor A. Elmelund and Lukas Spanier, respectively). Some of their results influenced the approach that I adopted with the device optimization, especially with regards to the AZO and BCP layers.

3.1 Tandem cell designs

The envisioned devices were, as mentioned, based on buried-junction Si photoelectrodes optimized for tandem cell operation, which had previously been developed at DTU [26]. Initially, the aim was to incorporate the cells in the tandem structure as cathodes and electrons thus needed to be transported to the surface of the device. Consequently the cells consisted of a p-type Si base while the emitter was a thin layer of n^+ Si. In order to protect the Si from being corroded by the electrolyte the n^+ layer was capped with 100 nm of TiO_2 which has been shown to be an excellent photocathode protection layer [24, 25, 79]. Later in the process it, however, became apparent that it might be easier to have the Si device fill the role of anode. The protection layer would in this case have to conduct holes to (or electrones away from) the electrolyte, which can be achieved by using NiO or, suprisingly enough, TiO_2 [19, 24]. In either case the junction needs to be relatively close to the electrolyte interface to ensure that the appropriate carriers reach the surface and carry out half of the redox reaction. In the single band gap case this is not an issue as the cell is simply illuminated from the side presented to the electrolyte (the front side). In tandem operation the Si cell, however, needs to be illuminated from the dry side (the backside) after the light has passed through the high band gap absorber. Since Si is an indirect band gap absorber the thickness of the device needs to be some micrometers for it to absorb a sufficient fraction of the incoming light [26]. This poses a challenge when it comes to collecting the generated charge in the back illuminated device as the diffusion length of the charge carriers is not infinite. A fraction of the electrons consequently recombines in the device base before they can reach the junction area and be captured. In order to minimize this loss Bae *et al.* [26] showed that thinning down the Si base could alleviate the problem without sacrificing too much light absorption. The Si-devices described above, were all produced by Dowon Bae and Thomas Pedersen, in a similar manner as described in the paper by Bae *et al.* [26].

The initial object was as mentioned to fabricate a tandem cell that worked purely as a solid state device, in order to gauge and optimize the cell performance without having to worry about electrolyte corrosion. This meant that a transparent conducting top contact was needed to facilitate proper charge collection, without obscuring the light-coupling into the device. Several groups have worked on this challenge and have almost exclusively employed tin doped indium oxide (ITO) as both recombination layers and contacts [51, 53, 55, 56, 80]. Other materials are, however, also available such as aluminium doped zinc oxide (AZO), thin metal layers, silver nanowires and graphene [50]. ITO was, nevertheless, selected as the contact to be used, which yielded the schematic layer configurations seen in Figure 3.1a and 3.1b

In both schemes an AZO layer is included as a recombination layer between the two solar cells though ITO could fill this role as well. Deposition of the ITO layer is usually done using sputtering, which has the unfortunate consequence that the perovskite layer is subjected to ion bombardment if it is not protected. Bush *et al.* [80] used nanoparticles of ZnO and AZO as a barrier layer before the ITO sputtering which showed good results. The same group later employed ALD to fabricate ultrathin (4 nm) SnO and zinc doped tin oxide barrier layers with an

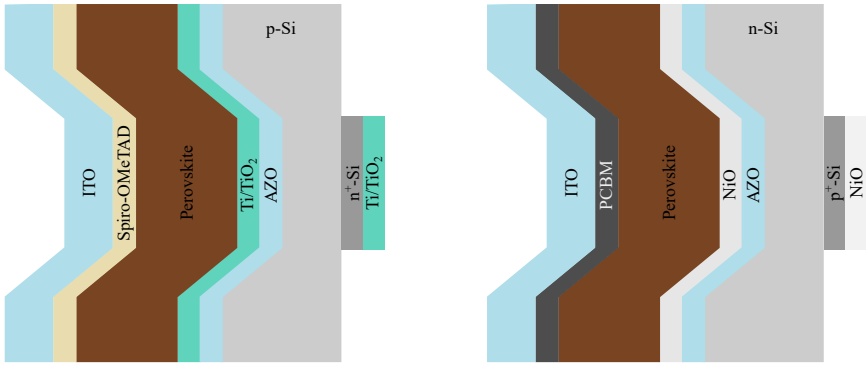

Figure 3.1: Schematic layout of the layers in the two different tandem designs. **(a)** shows the configuration where the Si cell acts as the cathode and the anode is a normal configuration perovskite cell. **(b)** shows the configuration where the Si cell acts as the anode while the cathode is now an inverse configuration perovskite cell.

improved coverage [55]. This approach has the advantage that very thin layers can be used and since the layers cannot be properly annealed, due to the thermal instability of the perovskite, the recombination losses in the otherwise defect prone layers can be reduced. Inspired by this, the intention was to use plasma-enhanced ALD to deposit thin SnO layers to protect the underlying perovskite layers before depositing the ITO. SnO is, however, routinely used as an electron contact and its valence band position is thus unsuited for use in conjunction with the normal configuration perovskite cell, where holes need to be collected at the ITO contact (see Figure 3.1a) [48]. As a consequence the SnO approach can only be used in the inverted perovskite scheme (see Figure 3.1b) whereas ALD deposition of NiO might enable the normal configuration.

3.2 The LP-VASP fabrication method

As mentioned previously, the LP-VASP method is a sequential fabrication scheme in which the Pb containing compounds and the methylammonium halides (MAI and MABr) are deposited in separate steps. The process proceeds as shown schematically in Figure 3.2.

The Pb containing compounds were introduced almost exclusively by spin coating a 0.8 M/0.2 M $PbI_2/PbBr_2$ in N,N Dimethylformamide (DMF, SigmaAldrich anhydrous) onto the substrate. The reason for using a mixed Pb solution rather than a pure PbI_2 one was that increased stability had been observed using this approach. Prior to deposition the solution was placed on a hotplate and heated to 110 °C. Following this, the solution was deposited on the substrate while the latter was spun at 500 rpm for 5s to reduce the formation of "coffee rings". To finish the

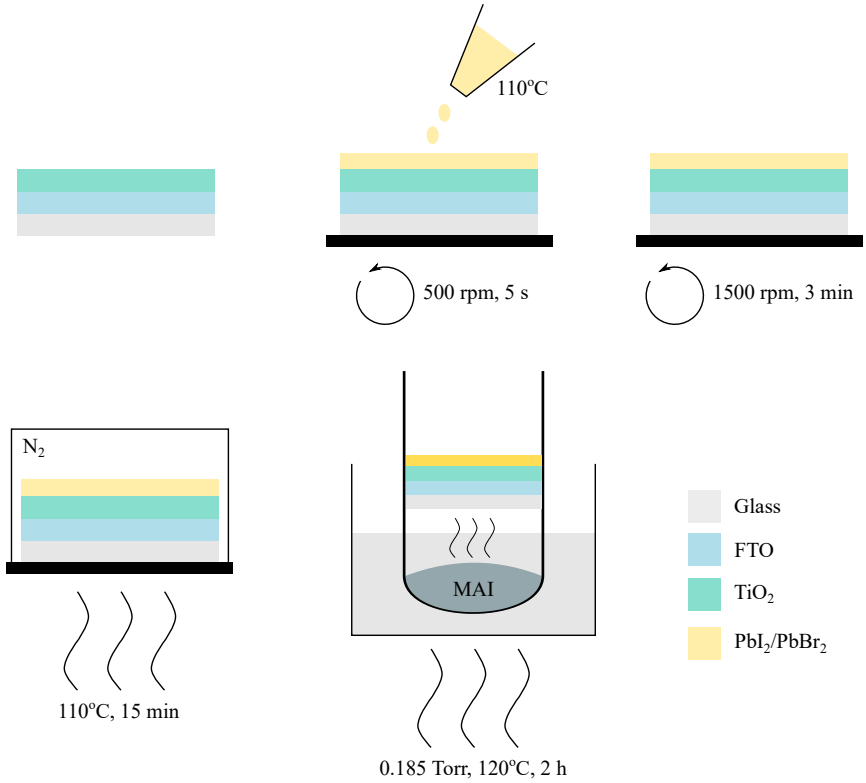

Figure 3.2: Step-by-step schematic showing the different process steps in the LP-VASP fabrication method. The substrate displayed is the one used in the normal cell configuration with the TiO_2 predeposited on the fluorine doped tin oxide (FTO). The process is here shown using pure MAI but mixtures of MAI and MABr were routinely used as well.

Pb film the substrate was subsequently spun at 1500 rpm for for 3 min and finally annealed at 110 °C for 15 min. Both the spin coating and the annealing was done in an inert atmosphere (N_2 or Ar) to reduce the effects of moisture, as well as the escaping solvent, on the film. To complete the conversion into $CH_3NH_3PbI_{(3-x)}Br_x$ the sample was placed in a glass tube containing the desired ratio of MAI and MABr. Following this, the tube was evacuated to 40 - 24 Pa using a rotary pump, submerged in a mineral oil bath held at 120 °C and left there for 2 h. During the initial 15 min the samples would start to change color from the bright yellow $PbI_2/PbBr_2$ films into the brown or reddish perovskite films, indicating the successful conversion. After 2 h the samples were finally washed in pure isopropanol to remove any leftover MAI/MABr before the next steps of the solar cell fabrication.

A total of 4 tubes could run in parallel and to control the pumping of the individual tubes they were connected to a Schlenk line through a glass stopper with a tube fitting. To ensure that a sufficiently leak tight connection could be made

the stopper was wrapped in Teflon tape. To calibrate the pressure the stopper was pressed into the tube, while the system pressure was observed using an attached pressure gauge. Though the glass stopper approach was, from a vacuum scientist's point of view, a rather crude way of adjusting the pressure, it proved effective. To improve the set-up one could replace the Schlenk line and tubing with high vacuum valves and steel tubing. This would allow one to make proper leak tight, VCR or CF, connections and consequently much better control of the atmosphere in the system. The low pressure atmosphere of atmospheric air that was needed could be introduced through a leak valve. This approach would make it substantially easier to control the pressure as compared to pressing the stopper more or less into the tube. The glass system, however, worked and ultimately none of the changes were implemented due to time considerations. When multiple tubes were used the pressure was set individually in each tube by isolating all other tubes from the pumping line. By doing the pressure calibration in this way one ensured that the leak size at each stopper was comparable as opposed to there being one big leak. In this way, the process would run under comparable conditions in each tube and thus yield similar results. A schematic of the LBNL LP-VASP set-up is shown in Figure 3.3.

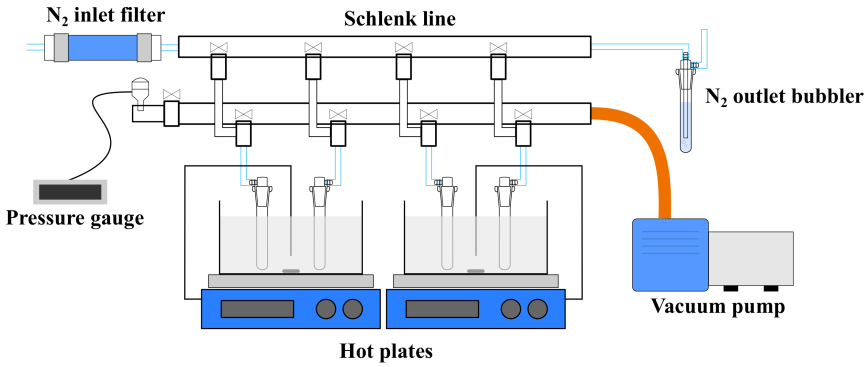

Figure 3.3: Schematic drawing of the set-up at LBNL. The entire construction was placed inside a fume hood to contain any toxic fumes developed during the process. The N_2 line was connected to the lab gas supply system.

The quality of the MAI and MABr turned our to be paramount for the performance and reproducibility of the produced absorbers and special attention was given to the synthesis and recrystallization of the compounds. MAI and MABr was synthesised by cooling 100 mL of pure ethanol to 0 °C using an ice bath. Following this 16.5 mL of CH_3NH_2 ($40_{wt.\%}$ in H_2O) was added after which 10 mL of HI ($51_{wt.\%}$ in H_2O) or 8.6 mL of HBr ($48_{wt.\%}$ in H_2O) was added dropwise while the solution was stirred vigorously. While keeping it at 0 °C the solution was left stirring for 2 h to finish the conversion into MAI or MABr. The powder was recovered using a rotary evaporator and recrystallized from pure ethanol and diethyl ether. Finally the powders were dried overnight at 70 °C in a vacuum oven held at 6.3 kPa. Each tube used was loaded with a cumulative mass of 0.1 g of MAI/MABr and preconditioned by running a deposition without any sample prior to it being

used for perovskite preparation.

Though the LP-VASP is an excellent deposition method for methylammonium lead halide perovskite it does have some shortcomings. Given that the MAI/MABr powder is placed in the same vessel as the sample the temperature used to evaporate the powder becomes the same as the annealing temperature. As the optimal evaporation and annealing temperature are most likely not the same it would be beneficial to be able to control these individually like in a two zone CVD chamber [81–83]. Furthermore, the method is not, in its current form, well suited for depositing double or triple cation perovskites. This is due to the fact that the evaporation temperatures of the FAI and MAI/MABr are somewhat different, which makes the single tube approach suboptimal [81, 82]. The triple cation perovskites have, as mentioned previously, been shown to be more stable and efficient as compared to pure $CH_3NH_3PbI_3$ and the lack of compatibility with the LP-VASP method is thus a substantial drawback [28]. This could, however, be rectified by introducing separate compartments for the FAI and MAI/MABr, which could be heated individually. As demonstrated by Jiang *et al.* [83] the Cs could later be introduced through cation exchange, although precise control of which cation gets swapped might be an issue [83]. The work presented in this thesis solely concentrates around methylammonium lead halide perovskites and consequently the LP-VASP method was well suited for the task at hand.

3.3 Band gap tuning

The first experiments were carried out to determine the ratio of MAI to MABr that was needed to yield the band gap of 1.7 eV. To do so, perovskite samples were fabricated using various fractions of MAI and MABr and their resulting band gaps, measured. Inspired by the results reported by Sutter-Feller *et al.* [36], a ratio of 70/30 MAI/MABr was used for the first batch of samples. As seen from the black trace in Figure 3.4a this yielded a strong absorption edge at around 780 nm. By applying the Tauc plot method this corresponds to an estimated band gap of 1.59 eV, which was some way from what was desired. As a small deviation from the optimal band gap results in a less than optimal tandem cell, several samples were made in which the Br content was increased, in order to achieve to the ideal absorption edge. The results are shown in Figure 3.4a and 3.4b. From the measurements the band gaps of the absorbers were estimated, again using the Tauc plot method, and yielded the results summarized in Table 3.1. From Figures 3.4a and Figure 3.4b it is clear that strong absorption edges are produced in all cases, which suggests that the perovskite has formed and that the quality is decent. Furthermore, the band gap energies are seen to increase in the expected manner, i.e. to increase with an increasing amount of Br. Finally a ratio of 20/80 MAI/MABr is seen to yield a band gap closer to the target value. Looking at Table 3.1 an issue is however apparent, namely that the produced band gap is very sensitive to the MAI/MABr ratio. This is clearly exemplified with the 20/80 and 15/85 samples where a relatively small difference in composition give rise to a discrepancy of 0.15 eV in their band gap energy. This unfortunate feature meant that reproducibility was an issue. Furthermore, the resulting band gaps as a function of the MAI/MABr ratio shown here were different than the one observed in literature [36].

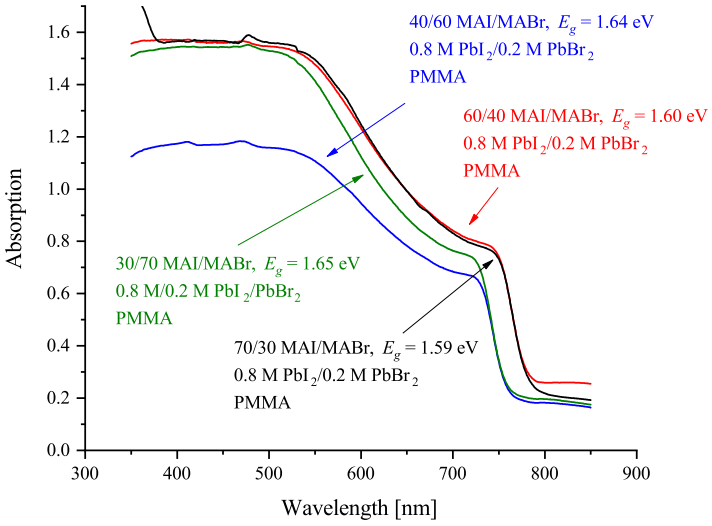

(a)

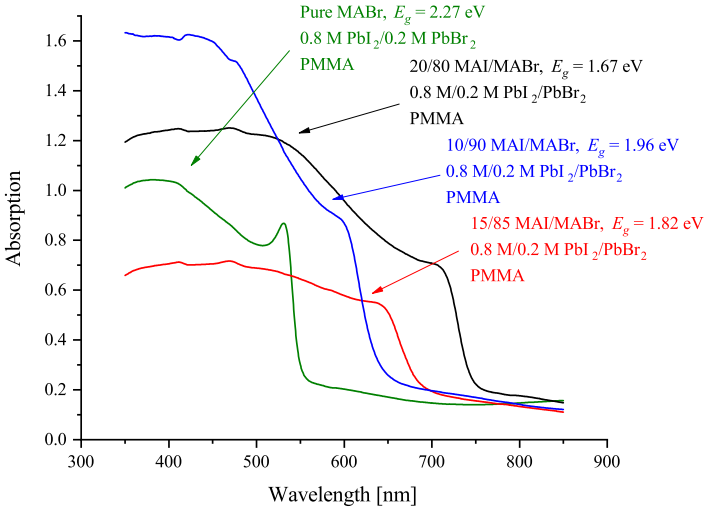

(b)

Figure 3.4: The absorption spectra of the different perovskite MAI/MABr composition samples. **(a)** shows the 70/30, 60/40, 40/60 and 30/70 spectra while **(b)** shows the 20/80, 15/85, 10/90 and 0/100 spectra. The band gaps were estimated using the Tauc plot method and in all cases the films were covered by a layer of PMMA to increase their resistance to moisture.

In addition to the UV-vis measurements, XRD patterns of the samples featuring different MAI/MABr ratios were measured to ensure that the Br was intercalated into the perovskite structure. Zoom ins of the area around a major perovskite peak in the resulting patterns, are shown in Figure 3.5. The large peaks observed between 14.2° and 14.6° are attributed to the perovskite (110) phase and clearly indicate that the desired compound has been formed [36]. The fact that only one peak is present indicates that perovskite has formed the mixed halide structure rather than crystallizing in separate Br and I domains. The shift of the peaks to higher angles with increasing Br content is as one would expect from literature but also from equation (2.2.1), where the comparably smaller Br should give rise to a larger diffraction angle than I [35,36]. By comparing the peak locations to the ones provided by Sutter-Fella *et al.* [36], one can further explain why the band gaps of the films are not as expected. In all cases the peaks are seen to be at a too low diffraction angle when considering the Br fraction that the used MAI/MABr ratio suggests. This indicates that a large part of the Br is not properly incorporated into the films. The peak seen clearly at 12.8° in the blue plot, but also faintly in the black, is attributed to PbI_2, which indicates that the conversion to perovskite had not been complete. It has, however, been reported that small amounts of PbI_2 could be beneficial as it might passivate the crystal boundaries in the film and thus suppress interface recombination [84–86]. On the other hand, Liu *et al.* [87] showed that the adverse effect PbI_2 had on photostability outweighed the benefits and that increasing the perovskite crystal size yielded a similar effect. It thus seems preferable to minimize the PbI_2 as much as possible and rather reduce the interface recombination by optimizing the perovskite fabrication process.

Table 3.1: Table showing the estimated band gaps resulting from different ratios of MAI and MABr.

MAI/MABr ratio	Estimated band gap [eV]
70/30	1.59
60/40	1.60
40/60	1.65
30/70	1.65
20/80	1.67
15/85	1.82
10/90	1.96
0/100	2.27

The encountered problems indicated that something in the fabrication procedure was not working properly, but since the MAI and MABr used for the initial experiments had not been recrystallized the compounds were identified as the likely culprits. Following the recrystallization the experiments were repeated, yielding the

results shown in Figure 3.6. From these several things are apparent. A band gap of around 1.7 eV is now achieved using either a 50/50 or a 40/60 MAI/MABr ratio and equally importantly the sensitivity to the MAX composition is seen to be less of an issue. This is further supported by the fact that producing 3 additional 40/60 samples yields an average band gap of 1.71 ± 0.02 eV (see Figure B.1). A relatively large discrepancy in the band gap energy as a function of MAI/MABr ratio between results presesnted here and literature was, however, still observed [36]. This indicated that a substantial part of the Br was not being incorporated properly, but since the process was reproducible and provided the needed absorption edge, it was decided to proceed to solar cell fabrication using the 40/60 procedure. The difficulties reproducing the literature values, even though the used set-up was the same, indicated that the origin of the differences were the MAX compounds. One should therefore take great care to employ high quality chemicals and even if this is the case some calibration of the MAI/MABr ratio might still be needed.

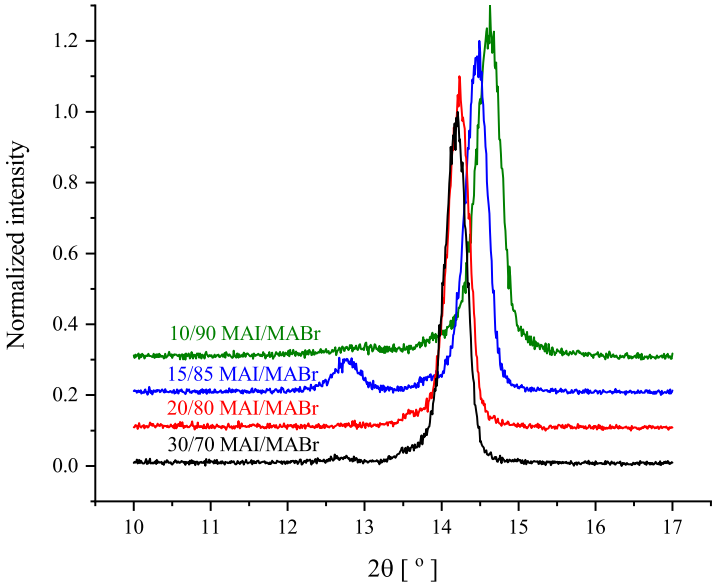

Figure 3.5: XRD patterns of the 30/70, 20/80, 15/85 and 10/90 samples in the $10° - 17°$ region. The plots have been normalized to the most dominant peak and the red, blue and green plot have been shifted upwards by 0.1, 0.2 and 0.3, respectively, to increase the readability.

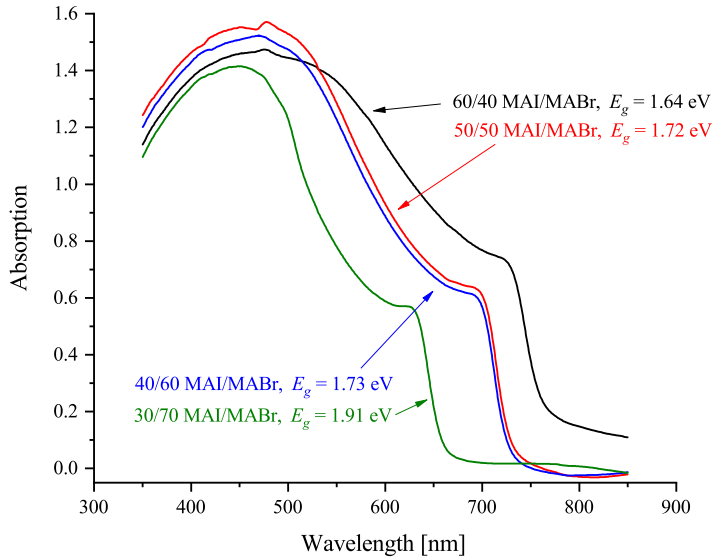

Figure 3.6: The absorption spectra of the 30/70, 40/60, 50/50 and 60/40 MAI/MABr composition perovskite samples following the recrystallization process. The band gaps were estimated using the Tauc plot method and in all cases the films were covered by a layer of PMMA to increase their resistance to moisture.

3.4 LP-VASP solar cells

3.4.1 Normal configuration devices

Having established the proper MAI/MABr ratio needed to produce the desired band gap of around 1.7 eV, the next task at hand was to produce full solar cells to gauge the efficiency of the absorbers. The initial devices were all produced in the normal configuration using TiO_2 as the electron contact while Spiro-OMeTAD was used as the hole collecter. The layers were deposited in a bottom-up type production scheme starting from flourine doped tin oxide (FTO) substrates, on which the PV stack and finally the Au top contacts were prepared, as shown in Figure 3.7. The TiO_2 film was produced using E-beam evaporation from a TiO_2 target and deposited under high vacuum conditions ($< 6.7 \times 10^{-4}$ Pa) using a substrate temperature of 350 °C. Prior to the TiO_2 deposition the pre-patterned FTO glass was cleaned by ultrasonication for 15 min, initially in an Alconox solution followed by acetone and finally isopropanol. The Spiro-OMeTad was deposited by spin coating and the solution was again introduced while the sample was spinning at 500 rpm for 5 s and subsequently spun at 3000 rpm for 30 s to finish the film. The solution consisted of 10 mg of N2,N2,N2′,N2′,N7,N7,N7′,N7′-octakis(4-methoxyphenyl)-9,9′-spirobi[9H-fluorene]-2,2′,7,7′-tetramine (Spiro-OMeTAD, Lumtec, 99%), 2.188 μL of lithium-bis(trifluoromethanesulfonyl)imide (Li-TFSI, SigmaAldrich, 99.95%) solution and 3.563 μL of 4-tert-butylpyridine (TBp, SigmaAldrich, 96%) dissolved in 125 μL of chlorobenzene (SigmaAldrich, anhydrous). The Li-TFSI solution con-

sisted of 520 mg Li-TFSI dissolved in 1 mL acetonitril (SigmaAldrich, anhydrous). Like the perovskite, the Spiro-OMeTAD film was prepared while flushing the spin coater with an inert gas. Before depositing the top contacts the samples were stored in a desiccator over night to dope the Spiro-OMeTAD further with air, which has been shown to have a positive effect on device performance [88]. Following this the Au contact was deposited through a shadow mask again by using E-beam evaporation in a high vacuum chamber ($< 6.7 \times 10^{-4}$ Pa). By using a shadow mask the area of the cells at LBNL could be defined to be 0.065 cm^2 and since each sample was 16×14 mm^2, 8 individual cells could be placed on each sample. This feature was allowed due to the poor lateral conduction of the Spiro-OMeTAD and the TiO_2 which meant that each cell was isolated from one another. This deposition scheme would naturally not have worked on a conducting surface like highly doped Si where each cell would have been shorted to the others. Having 8 cells on each sample increased the likelihood that a functioning device could be found and additionally gave insight into the homogeneity of the samples. The latter is obviously very important for up-scaling of the cells which need to be at least 10×10 cm^2 to be useful for commercial applications.

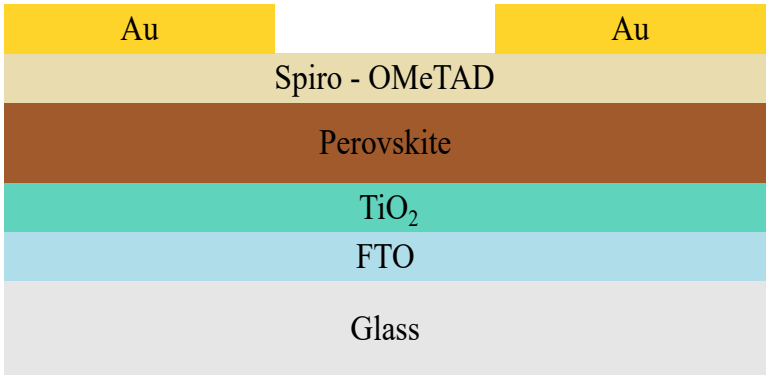

Figure 3.7: Schematic visualization of the thin film stack used in the normal configuration cells.

To perform the *J-V* characterization the cells were loaded into a glove box and placed in gas tight sample holders, meaning that the samples could be kept under inert atmosphere while being tested. Though this meant that the effects of illuminating the cell in ambient conditions could not be gauged it ensured that the maximum efficiency of the cell could be observed. Furthermore, this situation mimicked that of an encapsulated cell which is generally accepted as being a prerequisite for obtaining long term stability for perovskite solar cells [89]. To illuminate the devices a calibrated Newport solar simulator (100 mW/cm^2) was used. Before running the illuminated *J-V* sweep a dark measurement was conducted to gauge the rectifying quality of the cells, by establishing the amount of dark current produced. Following this the cells were light soaked for 20 min as this had previously been observed to increase the produced PCE. The theory was that a portion of the photo-excited carriers would passivate trap states in the TiO_2 and thus yield better

results. This procedure did, however, also have another advantage, namely that it yielded the steady state performance of the cell which more closely resembles the working condition of a commercial PV device.

The illuminated cells were finally characterized by running two linear sweeps, one going from 0 V to the vertex (forward) and one from the vertex to 0 V (reverse) using a scan speed of 20 mV/s. The vertex used was usually 1.2 V, which was found to be an appropriate number as V_{oc} could be observed without scanning excessively cathodic or anodic. The *J-V* curves of the best 40/60 MAI/MABr and pure MAI cells can be seen in Figure 3.8a and 3.8b, respectively, and yield the figures of merit summarized in Table 3.2. Looking at the dark *J-V* sweep seen in Figure 3.8a it is clear that very little current is passed before approximately 0.9 V at which point the built in potential of the diode is surpassed, allowing majority carriers to run through it. The low dark current indicates that the shunting resistance, R_{sh}, is high and suggests that the junction separates the charge carriers properly. The dark current is seen to reach a maximum at around 1.16 V after which it drops off. This feature is believed to be an artefact of the way the measurement was done and had a cyclic potential (e.g going from J_{sc} to V_{oc} and back to J_{sc}) rather than two linear sweeps been used, it would not have been observed. For the 40/60 sample only the V_{oc} to J_{sc} dark sweep was recorded but looking at the J_{sc} to V_{oc} sweep seen in Figure 3.8b it appears to be similar to its reverse sweep. The only difference is the artificial maximum discussed and there is thus no reason to expect that the corresponding J_{sc} to V_{oc} sweep of the 40/60 cell would hold any additional information.

Moving on to the illuminated *J-V* curves it is evident that the 40/60 MAI/MABr device is highly photoactive as a clear shift in the produced photocurrent is observed. In both sweep directions J_{sc} is seen to be equal to 18.8 mA/cm^2 which is decent when comparing to literature and considering the size of the band gap [53]. Some hysteresis is observed and the J_{sc} to V_{oc} sweep is seen to perform somewhat worse than the reverse, which has also been observed previously [41]. The produced open circuit voltages are, however, seen to be above 1.05 V in both directions while both the FF and the PCE (0.65, 13.1% for the forward and 0.74, 15.2% for the reverse) are comparable to what was observed by Li *et al.* [41], when they used $CH_3NH_3PbI_3$. When comparing these results with the ones for the pure MAI cell seen in Figure 3.8b some differences, but also some similarities, can be seen. The sample is again seen to be very photoactive yielding a $J_{sc} = 23.4$ mA/cm^2 for both sweep directions. The open circuit voltages are seen to be 0.97 V and 1.03 V for the forward and return sweep, respectively. These discrepancies are to be expected given the band gap differences between the two samples and clearly illustrate the optimization task that one is faced with when designing single band gap solar cells. In case of the pure MAI sample the hysteresis is seen to be slightly different when comparing it to that of the 40/60 sample, as the difference between the forward and return V_{oc} is seen to be larger (0.06 V vs 0.02 V). The difference in fill factor is, however, smaller in the pure MAI case and no clear correlation between the Br content and the detrimental effects of hysteresis can thus be established. Regardless of the differences in the forward and return sweeps, the pure MAI cell is seen to perform well and reaches a best case PEC of 17.8%, which is slightly better then what was obtained by Li *et al.* [41] who reached 16.8%. Though more optimiza-

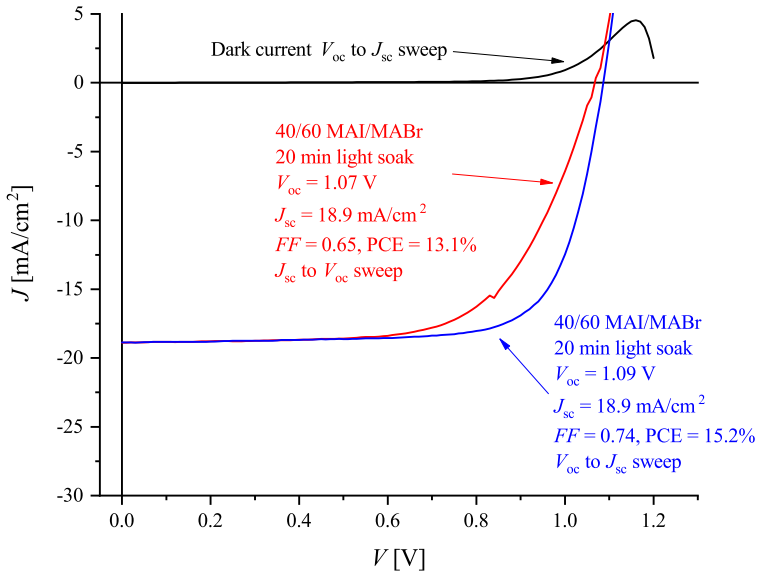

(a)

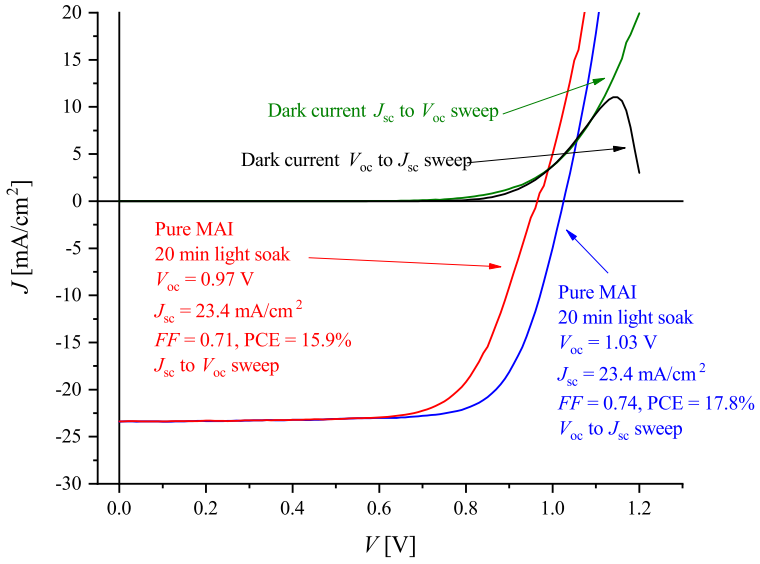

(b)

Figure 3.8: Plot showing the champion J-V curves of: **(a)** the 40/60 MAI/MABr device and **(b)** the pure MAI device. J_{sc} is the short circuit current density, V_{oc} is the open circuit potential, FF is the fill factor and PCE is the power conversion efficiency. The area of each cell was 0.065 cm^2 as defined by the Au shadow mask.

tion of the involved fabrication processes could have let to even better results (the lab record PCE was over 19%), it was decided that the current procedure yielded results which were sufficiently good and that the devices could serve as basis for subsequent investigations.

3.4.2 Inverted configuration devices

Having established that the perovskite fabrication approach yielded efficient solar cells the fabrication of the inverted device, was investigated. Patterned FTO covered glass was again used as the substrate and cleaned as described in the previous section. In addition to the chemical cleaning the substrates were sputter cleaned in an Ar plasma for 10 s using a table top plasma cleaner. The roles of hole and electron transport layer were filled by NiO and Phenyl-C61-butyric acid methyl ester (PCBM[60], 99% Solene BV), respectively. Both layers have been used previously in literature, either as they were or together with additional layers [49, 55, 90–93]. The NiO was deposited by spin coating a 1 M solution of nickel nitrate hexahydrate in ethyleneglycol mixed (1:1 wt.%) with ethylenediamine at 500/5000 rpm for 5/45 s. Like the previous instances the solution was introduced during the first 5 s while the sample spinning was slow. Following the spin coating the samples were annealed at 300 °C for 1 h under ambient conditions by placing them on a hotplate. The 40/60 MAI/MABr perovskite was then deposited using the same procedure as established with the normal configuration cells. The PCBM[60] layer was deposited by spin coating a solution consisting of PCBM[60] dissolved in chlorobenzene (25 mg/mL) at 500/3000 rpm for 5/30 s. Following the deposition the samples were annealed at 90 °C in a N_2 atmosphere. Finally a top contact of Au was deposited through a shadow mask yielding the device structure seen in Figure 3.9.

Figure 3.9: Schematic visualization of the thin film stack used in the inverse configuration.

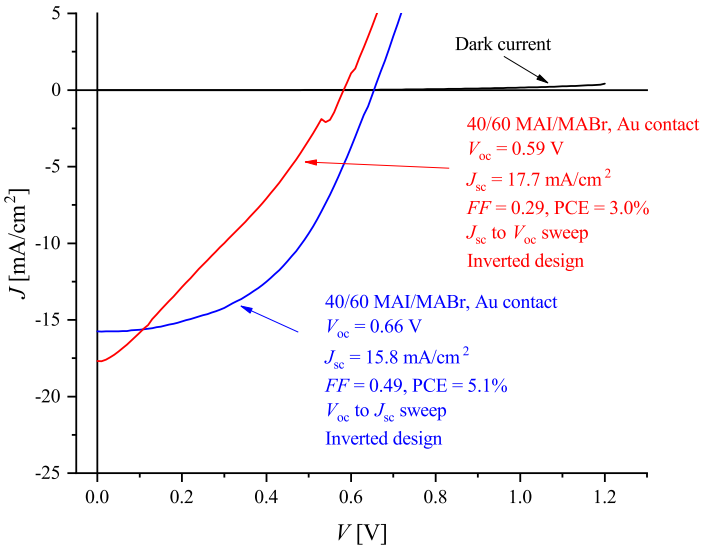

Figure 3.10: The champion *J*-*V* curves of the inverted device produced at LBNL using 40/60 MAI/MABr perovskite. J_{sc} is the short circuit current density, V_{oc} is the open circuit potential, *FF* is the fill factor and PCE is the power conversion efficiency cells.

Table 3.2: Table showing the figures of merit obtained from the *J*-*V* curves of the 40/60 and the pure MAI champion cells seen in Figures 3.8a - 3.10.

MAI/MABr ratio	J_{sc} [mA/cm^2]	V_{oc} [V]	*FF*	PEC [%]
Normal configuration				
40/60 forward	18.4	1.07	0.65	13.1
40/60 reverse	18.4	1.09	0.74	15.2
100/0 forward	23.4	0.97	0.71	15.9
100/0 reverse	23.4	1.03	0.74	17.8
Inverted configuration				
40/60 forward	17.7	0.59	0.29	3.0
40/60 reverse	15.8	0.66	0.49	5.1

The cells were tested in a similar manner as described in the previous section, yielding the results shown in Figure 3.10 and Table 3.2. In the best sweep a J_{sc} of

15.8 mA/cm^2, a $V_{\mathrm{oc}} = 0.66$ V a FF of 0.49 and a PCE of 5.1% was obtained. From the J-V curves it is clear that the inverted design fares much worse than its normal configuration counter part seen in Figure 3.8a. The short circuit current density is seen to be slightly worse which suggests that the perovskite is still very photoactive. The V_{oc} and the fill factors are, however, diminished which indicate that the cells have a high amount of shunts. The reason for this could be that Au is simply incompatible with the PCBM[60] and diffuse through the layer. Such a behavior has been reported when heating cells using Au on top of Spiro-OMeTAD to 70 °C [94]. Au has, however, been used in conjunction with PCBM[60] several times in literature, yielding PCEs of up to 18.1%, which suggests that it should at least work short term [95, 96]. A more likely explanation is thus that the PCBM[60] coverage was poor, which would allow the Au to directly interface with the perovskite and consequently reduce the charge separation. This lowering of the shunt resistance would lead to a reduction of the open circuit voltage without reducing J_{sc}, as described in chapter 2.

3.4.3 ALD TiO_2 covered devices

Even though the inverted cells were far from optimized it was decided to continue with deposition of ALD layers on top of them. Due to practical limitations it was unfortunately not possible to use the plasma enhanced ALD machine to deposit the protective SnO layers prior to ITO sputtering. As a consequence deposition of TiO_2 layers was examined. Though it is most likely less ideal to use TiO_2 instead of SnO underneath the ITO, it is an electron contact and a well known protection layer [25, 97]. It was therefore expected to be able to collect the electrons from the inverted cell and additionally provide some moisture protection. ALD deposition of TiO_2 has previously been used in conjunction with perovskite solar cells though the use has primarily been focused on forming pin-hole free contact layers [98, 99]. A month after the completion of the work presented underneath, Kim *et al.* [100] did publish work where TiO_2 was used as a protection layer. A discussion of their results in relation to the ones presented here, is included at the end of this section. To produce the TiO_2 Tetrakis(dimethylamido)titanium (TDMAT) was used as the Ti supply while ozone was employed as oxidizer. Using ozone rather than water to oxidise the Ti precursor meant that the perovskite was not subjected to moisture and the hope was that less degradation would occur as a consequence. It has, furthermore, been shown in literature that O_3 and TDMAT can be used at low substrate temperatures, which is an advantage considering the low thermal stability of the perovskite [101, 102]. The first task at hand was to establish the growth per cycle, r_g, for the fabrication process when a substrate temperature of either 40 °C or 60 °C was used. To do so, Si was used as a test substrate while the resulting thickness was estimated using ellipsometry. Each deposition cycle consisted of four phases, namely, a TDMAT pulse phase, followed by a purge phase, then an O_3 pulse phase and finally an ozone purge phase lasting for t_{TDMAT}, $t_{\mathrm{p,1}}$,$t_{\mathrm{O_3}}$ and $t_{\mathrm{p,2}}$, respectively. Several different pulse and purge durations were tested where $t_{\mathrm{TDMAT}} = 250$ ms, $t_{\mathrm{O_3}} = 500$ ms and $t_{\mathrm{p,1}} = t_{\mathrm{p,2}} = 25$ s were found to yield a growth rates of $r_{g,40\ ^\circ\mathrm{C}} = 0.6$ Å/s and $r_{g,60\ ^\circ\mathrm{C}} = 0.55$ Å/s. The TiO_2 thickness as a function of number of cycles can be seen in Figure 3.11. Though a low number of initial samples were prepared the results proved to be reproducible when the ALD

layers were used on the perovskite cells. Consequently, the growth rates might not be correct outside the range indicated in Figure 3.11 but should be accurate within.

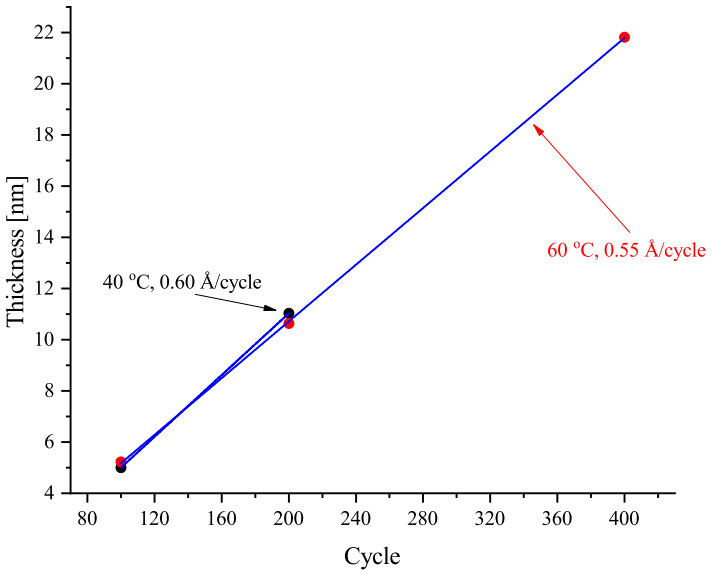

Figure 3.11: The TiO_2 film thickness as a function of ALD cycle number when using a substrate temperature of 40 °C or 60 °C.

Initially the deposition of the TiO_2 on the perovskite was attempted at 60 °C but the samples visually appeared to be degraded post-process. As a consequence 40 °C was used instead, in which case no apparent change could be observed. To further verify this an XRD pattern of a 40/60 MAI/MABr layer was recorded before and after the TiO_2 deposition, yielding the results shown in Figure 3.12. From the figure it is clear that no significant difference in the crystal structure can be detected, which suggests that no bulk degradation is taking place. It is, however, not possible to detect what has transpired at the interface between the two layers using XRD. Since a defect-riddled interface would severely hamper the functionality of the devices, the next step was examine whether or not this was the case. To gauge the healthiness of the interface several inverted 40/60 MAI/MABr solar cell stacks (up to the PCBM[60]) were prepared, on which 5 nm of ALD TiO_2 was deposited. The TiO_2 thickness was verified using ellipsometry on Si samples included in each deposition. To finalize the cells Au back contacts were deposited in a similar manner as described in the previous section. Following this, the *J-V* characteristics of the devices were recorded using the same test parameters as described above. The resultant *J-V* curves of the best cell are shown in Figure 3.13a while its figures of merit are summarized in Table 3.3.

Comparing the curves with the ones of the inverted cell without ALD TiO_2 several things are apparent. The hysteresis is seen to be smaller and since the hysteresis effect in perovskite solar cells have been attributed to defect movement during the potential sweeps, it suggests that the TiO_2 layer serves to passivate

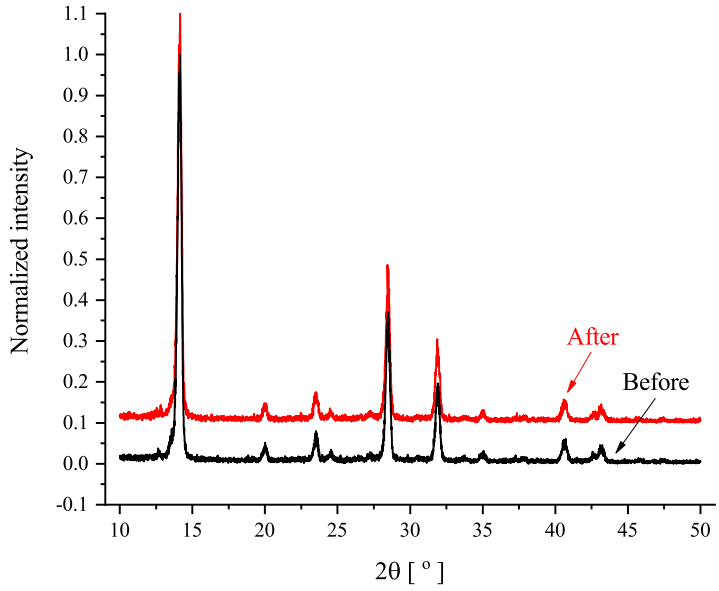

Figure 3.12: XRD pattern of 40/60 MAI/MABr perovskite sample before and after ALD TiO_2 deposition. The patterns have been normalized to the highest peak and the red pattern have been shifted upwards by 0.1 to increase the readability.

interface defects [103]. Likewise, the open circuit voltages are observed to be somewhat better than the previous cells (0.80 V vs 0.66 V in the best case), which indicates that the TiO_2 layer reduces shunting. On the other hand the short circuit current densities are seen to be diminished and the TiO_2 covered sample only delivers $0.3 - 0.4$ mA/cm^2. The consequence of this is very low FFs (0.12 and 0.10), which results in a PCE of 0.03% in the best case. The origin of the very low current is most likely a high series resistance being introduced by the TiO_2 layer. The most immediate explanation to this is that the TiO_2 is expected to be amorphous unless it is annealed above 200 °C and is therefore a less then optimal conductor [101]. Upon more close examination of the energetics of the Au/TiO_2 interface another possible cause, however, becomes apparent. From literature it is known that Au deposited on TiO_2 forms a Schottky barrier with a barrier height of around 0.9 eV, which severely hampers the electron collection [104, 105]. With this in mind the Au was replaced with a layer of Ti which is known to form ohmic contacts with TiO_2 [24, 25]. The Ti was deposited using E-beam evaporation in a similar manner as the Au contact. The resulting J-V curves of the best cell can be seen in Figure 3.13b while the J_{sc}, V_{oc}, FFs, and PCEs are summarized in Table 3.3. The use of Ti contacts is seen to vastly improve the device on all parameters yielding $J_{sc} = 4.4$ mA/cm^2, $V_{oc} = 1.12$ V, $FF = 0.34$, and PCE = 1.7% in the best case. The short circuit current densities are especially seen to be much better while the open circuit voltages, reaching over 1.1 V, are very good. The magnitude of the hysteresis is furthermore seen to be smaller though some difference in the short

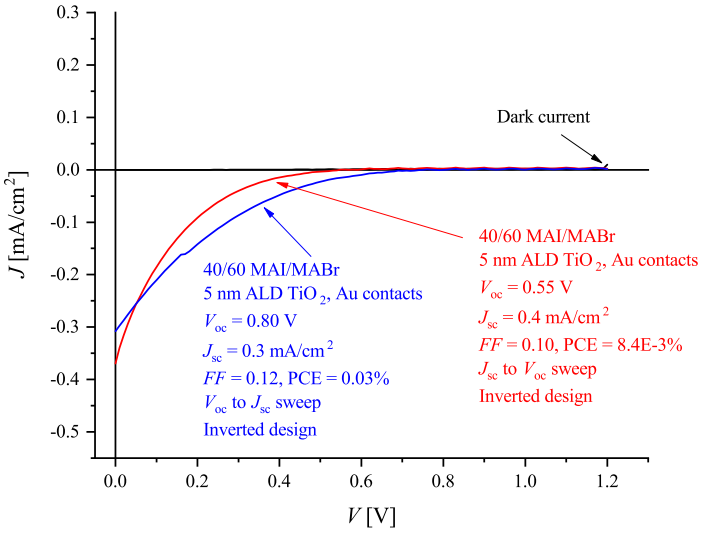

(a)

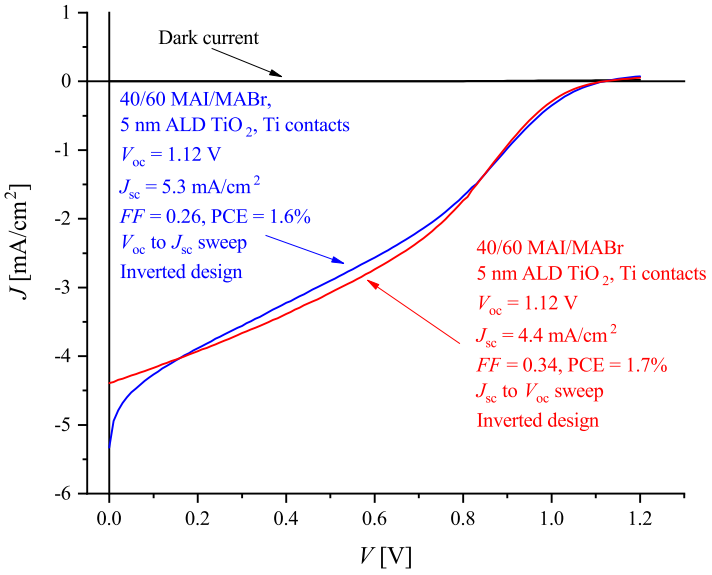

(b)

Figure 3.13: The champion J-V curves of the 40/60 MAI/MAbr inverted devices with 5 nm ALD TiO_2. **(a)** shows the best cell produced with Au contacts while **(b)** shows the best cell produced with Ti contacts. J_{sc} is the short circuit current density, V_{oc} is the open circuit potential, FF is the fill factor and PCE is the power conversion efficiency.

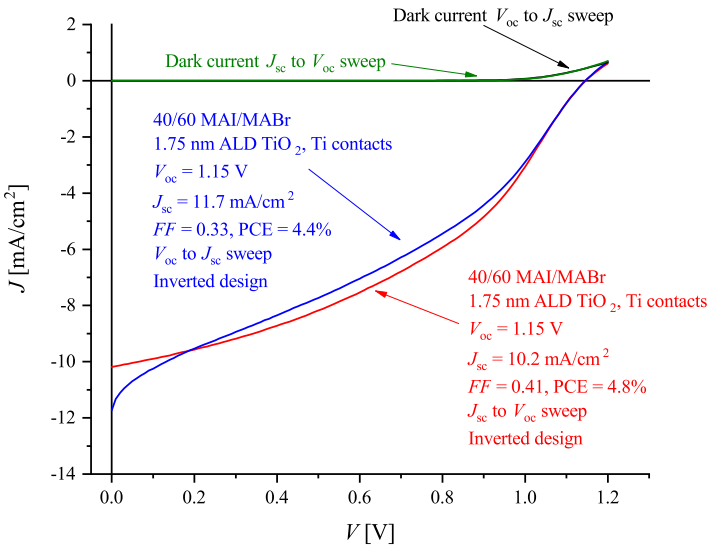

Figure 3.14: The champion J-V curves of the 40/60 MAI/MAbr inverted devices with 1.75 nm ALD TiO_2 and Ti back contacts. J_{sc} is the short circuit current density, V_{oc} is the open circuit potential, FF is the fill factor and PCE is the power conversion efficiency.

circuit current densities still persists. The current densities are, additionally, still somewhat lacklustre compared to the device without TiO_2 which indicates that some carriers are lost in the layer. To improve this, the TiO_2 thickness was decreased down to 1.75 nm which yielded the results shown in Figure 3.14 and Table 3.3. The thinning of the TiO_2 had the desired effect and the J_{sc}'s are seen to now be above 10 mA/cm^2 without compromising the improved open circuit voltages and the FFs. The resultant PCEs of $\geq$ 4.4% are, however, still not better than the maximum value seen in the device without TiO_2. The improved hysteresis, FFs as well as the very high open circuit voltages could, nevertheless, make this trade-off worthwhile in some instances. This would be the case with unassisted PEC devices where a high photocurrent is useless, if the cell does not deliver the photovoltage required to run the desired reaction.

Having established the beneficial effects that including a thin ALD TiO_2 had on the electrical characteristics of the perovskite devices, the protective properties of the TiO_2 were examined. To do so, 40/60 MAI/MABr perovskite was prepared on patterned FTO substrates onto which 6 nm or 12 nm of TiO_2 was deposited, again using a substrate temperature of 40 °C. The stabilities of the samples were tested by submerging them into water and measuring the time it took for them to turn bright yellow which signified complete degradation into PbI_2/$PbBr_2$. In case of the 6 nm sample the complete failure time was observed to be 30 s while the 12 nm film prolonged it to 90 s. The degradation was observed to begin from the part of the substrate where the FTO had been removed. This suggests that there might

Table 3.3: Table showing the figures of merit obtained from the *J-V* curves of the 40/60 champion cells including ALD TiO_2 layers seen in Figure 3.13a - 3.14.

Contact metal	J_{sc} [mA/cm^2]	V_{oc} [V]	FF	PCE [%]
5 nm ALD TiO_2				
Au forward	0.3	0.55	0.10	8.4×10^{-3}
Au reverse	0.4	0.80	0.12	0.03
Ti forward	4.4	1.12	0.34	1.7
Ti reverse	5.3	1.12	0.26	1.6
1.75 nm TiO_2				
Ti forward	10.2	1.15	0.41	4.8
Ti reverse	11.7	1.15	0.33	4.4

be a step coverage issue even though ALD is one of the most conformal deposition methods available. Another issue might be the sides of the sample, which could also introduce step coverage issues and subsequent water ingress. To test this, the edges of a 12 nm TiO_2 sample were covered with a UV cured epoxy. Though this effectively removed the sides as a path of attack for the water the degradation time was not improved noticeably and the main ingress points thus appeared to be through pin holes in the TiO_2. Pin holes might be caused by dust particles present on the sample and are a major issue when depositing protective layers. To counter the dust particle issue one needs to either remove the particles through a cleaning process or fabricate the cells in a high class clean room. The ALD layers employed here were fabricated in a low class clean room which reduced the amount of dust but, more than likely, it did not alleviate the problem completely.

Though the TiO_2 layers were nowhere near able to protect the perovskite films when the samples were submerged in water it was still interesting to examine their durability in atmospheric air. To do so, a 12 nm TiO_2 capped perovskite sample was left in a fume hood and inspected visually on a daily basis. This yielded the results shown in Figure 3.15a-3.15e. As seen from the images the sample appears unchanged for the first 2 days but already on day 3, signs of degradation start to appear along the edges of the FTO patch in the middle of the substrate. After 6 days the perovskite is seen to have been almost entirely converted into $PbI_2/PbBr_2$, which is naturally a far from sufficient lifetime when considering real world solar cell applications. The protective abilities of even a relatively thick layer of TiO_2 (1.75 nm were used in the best solar cell shown above) thus leave something to be desired and more effort needs to be applied if this approach is to be a viable solution to the stability challenge.

As mentioned in the beginning of the section, Kim *et al.* [100] published work very

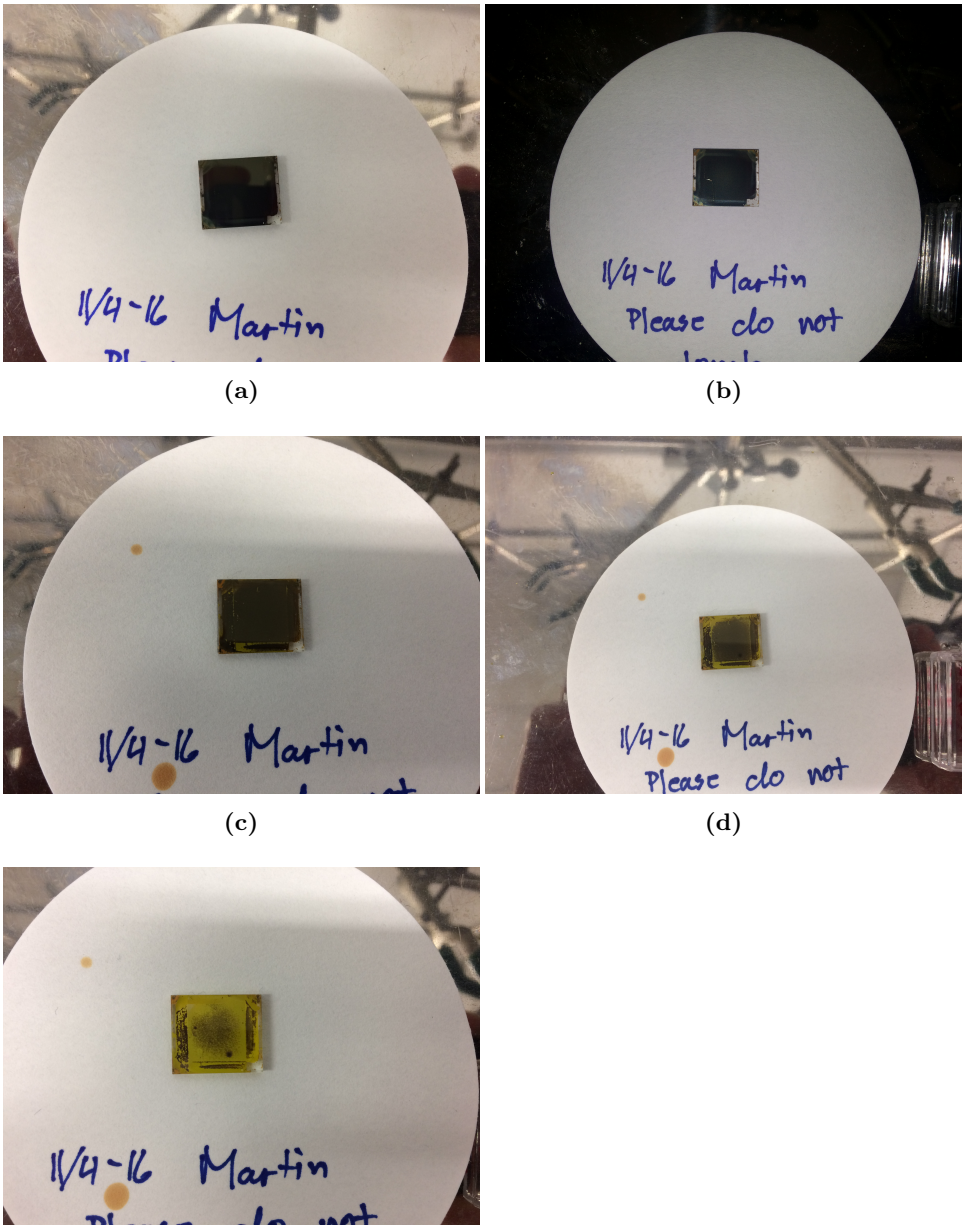

(a) **(b)**

(c) **(d)**

(e)

Figure 3.15: Images of the perovskite sample covered with 12 nm ALD TiO_2. **(a)** shows the sample after 1 day, **(b)** after 2 days, **(c)** after 3 days, **(d)** after 5 days and **(e)** after 6 days.

similar to what has been presented here. They used an inverted device consisting of NiO, $CH_3NH_3PbI_2$, PCMB[60] deposited on ITO rather than FTO. On top of this they deposited approximately 10 nm of ALD TiO_2 by employing a non-hydrolytic ALD approach in which acetic acid is used as the oxidizing species [100, 106]. To finish their device they deposited an Al/Au back contact. Using this approach they obtain a J_{sc} of 19.7 mA/cm^2, a V_{oc} of 0.93 V, a FF of 0.48 which yields a PCE of 8.8%. Comparing this to the results in Figure 3.14 it is clear that their short circuit current density is far superior to what was obtained here. It is, however, worth noting that their control device (i.e. a similar device without the TiO_2 layer) was also significantly better than what was used in this study. Where the inverse device employed here at best yielded $J_{sc} = 15.8$ mA/cm^2, $V_{oc} = 0.66$ V, $FF = 0.49$ and a PCE of 5.1% they measured $J_{sc} = 21.8$ mA/cm^2, $V_{oc} = 0.88$ V, $FF = 0.42$ and a PCE of 8.1%. Consequently, it is not unlikely that the short circuit current density of the TiO_2 devices presented could have been improved if a higher quality inverse stack had been used. The difference in current density is naturally also caused by the difference in perovskite band gap and the normal configuration device results suggests that a maximum J_{sc} of only 18.9 mA/cm^2 can be expected. The open circuit voltage presented here is, nevertheless, significantly higher which to some degree compensates for the lack of current. This difference is again, to some degree, caused by the difference in band gap, although a more optimal work function of the metal contact might also be a factor. From the above it is not immediately clear which ALD approach is superior but as Kim *et al.* [100] measure a much smaller current loss when using a film that is over 5 times as thick they most likely come out on top. Post annealing of the samples was, however, not investigated in depth here and even a slight annealing, e.g. at 100 °C, might improve the charge transport through the TiO_2.

3.5 Devices produced at DTU

3.5.1 Normal configuration devices

The endeavours to improve the inverse design were continued at DTU where several parameters were altered such as NiO fabrication method and thickness, electron selective contact, hole selective contact stack as well as back contact material. As with the cells produced at LBNL, the optimization process of the inverted devices began with producing normal configuration stacks, to gauge the quality of the produced perovskite. The set-up used at DTU was similar to the one used at LBNL though the Schlenck line was slightly different and Ar rather than N_2 was used to flush the system. Where the FTO substrates used at LBNL had been purchased with a pre-patterned film the substrates used at DTU were etched in-house. To do so 16×14 mm^2 samples were first cut from a 30×30 cm^2 FTO glass sheet with a sheet resistance of 7 Ω/sq. The center 14×12 mm^2 was then masked using kapton tape which defined the area not etched. To remove the exposed FTO a combination of Zn powder and HCl was used. Following the FTO patterning the samples were cleaned in the same manner as described in section 3.4. The solar cell stack was the same as the one seen in Figure 3.7. The 100 nm thick TiO_2 layer was produced by reactive sputtering of Ti in a 30:5 Ar:O_2 (0.4 Pa) atmosphere using 230 W DC and a substrate temperature of 400 °C. Prior to the film deposition the substrates

were sputter cleaned for 2 min in 2.7 Pa Ar at 35 W to remove any remaining contaminations. The area covered with TiO_2 was defined using a shadow mask.

For the initial test the MAI used was purchased from Lumtec (lot number LT-S9126) and used as delivered in an effort to save time. During the MAI preconditioning in the reaction tubes it was observed that the MAI changed color from white to brown, which indicated that it was decomposing. The Lumtec MAI was thus subjugated to the same recrystallization process used at LBNL which appeared to solve the issue. Another problem was encountered when depositing the $PbI_2/PbBr_2$, namely that the films would appear hazy both before and after the annealing. This was in stark contrast to the films produced at LBNL, which were transparent. The origin of the shortcoming turned out to be lack of flushing of the spin coater which meant that DMF was not removed properly from the films during the spin coating process. Upon rectifying this issue the films became transparent and the remainder of the VASP process ran as described above, without incident. The Spiro-OMeTAD solution was likewise prepared as described previously although the solution was ultrasonicated slightly longer to ensure that the powder was properly dissolved. A slight change in the spin coating procedure was also introduced as the same chuck was used for all processes, as opposed to using a dedicated Spiro OMeTAD chuck which was the case at LBNL. A 100 nm thick Au top contact was deposited from a W boat using thermal evaporation at pressures below 5×10^{-4} Pa. Using pure recrystallized Lumtec MAI this procedure resulted in decent devices, where the best sample yielded the results shown in Figure 3.16 and Table 3.4.

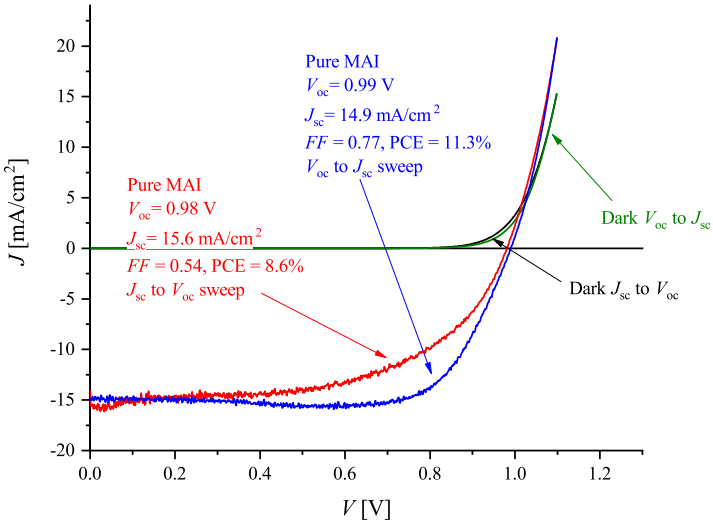

Figure 3.16: The champion J-V curves of the pure MAI normal configuration cells produced at DTU. J_{sc} is the short circuit current density, V_{oc} is the open circuit potential, FF is the fill factor and PCE is the power conversion efficiency.

From Figure 3.16 it is clear that the cell is still featuring the hysteresis in the

J-V characteristics which was also present in the LBNL cells. Nevertheless the best sweep (the reverse) yields a J_{sc} of 14.9 mA/cm^2, a V_{oc} of 0.99 V, a FF of 0.77 and a PCE of 11.3%. Comparing this with the best pure MAI cell produced at LBNL (Figure 3.8b and Table 3.2) the fill factors and the open circuit voltages are seen to be comparable. The short circuit current density is, on the other hand, seen to be much smaller, which causes the overall efficiency to be worse than the LBNL cells. The explanation for this is not clear, but it suggests that there is a difference between the perovskite layers and that optimization is still needed in the DTU set-up. One prime candidate for scrutiny is the quality of the MAI which was found to be very important for the device performance. Later in the process of optimizing the inverse configuration cells, the recrystallized Lumtec MAI was replaced with MAI synthesised in a similar way to the powder used at LBNL. New normal configuration devices were, however, not produced but a clear improvement was not observed with the inverse cells, though the lack hereof might have other explanations. In addition to the poorer perovskite quality, there were some differences in the testing procedure employed at LBNL and DTU which might partly be an explanation to the problem. Rather than running two linear sweeps, a single continuous sweep ran from J_{sc} to V_{oc} and back to J_{sc} at a rate of 20 mV/s. As indicated earlier, this had the effect that the artificial maximum in both the dark and light curves was no longer present. In addition to the difference in electrical characterization the cells tested at DTU were not light soaked. The reason for this was that they could not be held under inert atmosphere while being tested. The results obtained using light soaking were, furthermore, observed to be sub-par to the ones not subjected to this precondition. The cause for the deteriorating efficiency due to the light soaking was not investigated, but a likely explanation is that the lamp would heat the cell over time and thus accelerate the environmental decomposition of the perovskite. It is therefore possible that the expected increase in extracted photocurrent was suppressed by the increase in the number of defect sites. A final difference in the test conditions was the light source used. As mentioned, the illumination at LBNL was provided by a calibrated solar simulator while a Newport Xe lamp with an AM1.5 filter was used at DTU. Prior to measuring the *J-V* curves the Xe lamp was calibrated by measuring the light intensity using a Ocean Optics USB4000 spectrometer and varying the distance from the lamp to the optical fiber of the spectrometer . When an intensity of 68.4 mW/cm^2 in the 300 to 900 nm wavelength range was reached, the distance was measured and subsequently used in the *J-V* measurements. An example of a calibrated spectrum can be seen in Figure B.2. Due to this difference in light source the illumination of the cells was most likely not identical and interpreting the difference in J_{sc}, consequently, becomes more difficult.

3.5.2 Inverted configuration devices

Though the normal configuration cells were inferior to their LBNL counterparts they were still decent and it was therefore decided to continue with the inverted cells. Initially some changes were made to the device structure and fabrication method. Since plasma enhanced ALD was not possible at DTU the thin layer of SnO could not be deposited as intended. Instead a layer of solution processed AZO was envisioned to serve as the protection layer. As a starting point for the investigations

the work of Savva *et al.* [107] was used. Rather than employing PCBM[60] as their electron conductor they used the slightly different [6,6]-Phenyl-C71-butyric acid methyl ester (PCBM[70]). As a consequence the initial samples were fabricated using this material. The concentration, solvent, spin coating parameters as well as post annealing conditions, however, remained the same as with the PCBM[60]. The NiO layer was the other major change as it was, initially, deposited using reactive sputtering from a Ni target in a 0.4 Pa 35:10 Ar:O_2 atmosphere using a substrate temperature of 200 °C and a power of 140 W DC. The reason for this change in procedure was the expectation that sputtering would yield superior films as compared to spin coating. The sputtering parameters had furthermore previously been shown to yield good layers [19]. Prior to the film deposition the samples were again sputter cleaned (2 min in 2.7 Pa Ar at 35 W). Originally a film thickness of 50 nm was intended, but it became apparent that the tooling factor of the deposition was wrong, and thus the correct film thickness was closer to 120 nm.

The initial devices were thus made with 120 nm of NiO as the hole contact, pure recrystallized Lumtec MAI LP-VASP perovskite, PCMB[70] (> 99%, Solenne BV) as electron contact and Au as back contact. The *J-V* curves of the best resultant cell can be seen in Figure 3.17 and yield the J_{sc}, V_{oc}, FF and PCE seen in Table 3.4. Like with the LBNL cells, some hysteresis is observed and the best sweep is again the one from V_{sc} to J_{sc}. From the return sweep one gets a J_{sc} of 6.3 mA/cm^2, a V_{oc} of 0.65 V, a FF of 0.39 and a PCE of 1.6%. Comparing these results with the ones from LBNL (Figure 3.10) it is clear that the short circuit current density is substantially smaller. The rest of the metrics are, however, seen to be similar in good agreement with what was observed with the normal configuration cells. The reproducibility of the inverted cells was in general poor, which made the optimization process detailed below difficult. As a consequence some of the variations in the device composition did not yield any clear indication as to whether they improved or deteriorated the efficiency. The results presented in the following are thus only the ones where a relatively clear conclusion could be reached. The variation of the device structure included changing the back contact material, varying the NiO thickness and oxygen contents, varying the hole conductor thickness, concentration and material as well as adding layers of bathocuproine (BCP).

In the first attempt to improve the results the Au contacts were replaced with Ti ones, in the hope that a similar effect as with the ALD TiO_2 layers would be observed. The Ti contacts were deposited using a thermal evaporator (a Ti sublimation pump) placed roughly 10 cm away from the substrates. For the evaporation a background pressure below 2.7×10^{-3} Pa was used. A comparison between the return sweeps of cells using the two contact types can be seen in Figure 3.18a. The full *J-V* characterization of the Ti cells can be seen in Figure B.3 while the metrics are shown in Table 3.4.

From the curve one can observe a slight decrease in J_{sc} going from 6.3 mA/cm^2 in the Au case to 5.5 mA/cm^2 in the Ti case. The Ti contacts, however, provide a much higher V_{oc} (0.88 V vs. 0.65 V) though with a reduced FF. The overall PCEs therefore end up being comparable, with only a 0.1% advantage of using Au contacts. The improved open circuit voltage suggests that the cells are either less shunted, or that the Ti work function might be better suited than that of Au. The

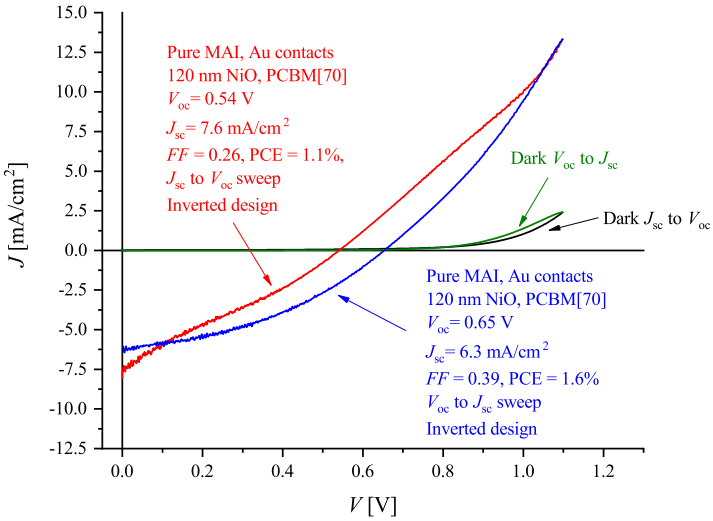

Figure 3.17: The J-V curves of the best performing initial inverse configuration cell produced at DTU. J_{sc} is the short circuit current density, V_{oc} is the open circuit potential, FF is the fill factor and PCE is the power conversion efficiency.

latter explanation is supported by the fact that the PCBM[70] has a conduction band edge located between -3.8 eV and -4.2 eV compared to vacuum [46]. Assuming that the PCBM[70] is n-type in nature like the PCBM[60], its Fermi level should lie above -5.1 eV vs vacuum as its valence band is located at -6.0 eV vs vacuum [46, 108]. Since Au has a work function between -5.1 eV and -5.47 eV it could introduce a barrier [68]. As mentioned the Au has, however, been shown to work with PCBM[60], which speaks against this hypothesis [95,96]. The reduced current density could be explained by an increase in interface defect concentration induced by the Ti deposition, compared to that of Au. As the melting temperature of Ti is much higher than that of Au (1668 °C vs 1064 °C) the Ti evaporation process will generate a lot more radiation which will heat the samples further. A higher degree of thermal decomposition is therefore expected from the Ti deposition process.

The next component that was varied was the thickness of the NiO. By halving the deposition time, 60 nm rather than 120 nm was deposited and used as hole contact. A comparison of the return sweep of the resultant J-V curves to that of the Ti experiment, seen in Figure 3.18a, is shown in Figure 3.18b. The full J-V curves are included in Figure B.4 while the metrics are shown in Table 3.4. From the curves it is clear that thinning the NiO appears to have a detrimental effect on the current density as J_{sc} is seen to drop to 2.8 mA/cm^2 while the V_{oc}, the FF and the PCE are 0.80 V, 0.25 and 0.6%, respectively. The much reduced FF furthermore suggests that the reduced efficiency is caused by an increase in series resistance. The results could in principle also be caused by a large decrease in shunt resistance but as the V_{oc} is seen to be only slightly smaller, this cannot be the dominant effect. The fact that the series resistance is increased when the NiO thickness is decreased

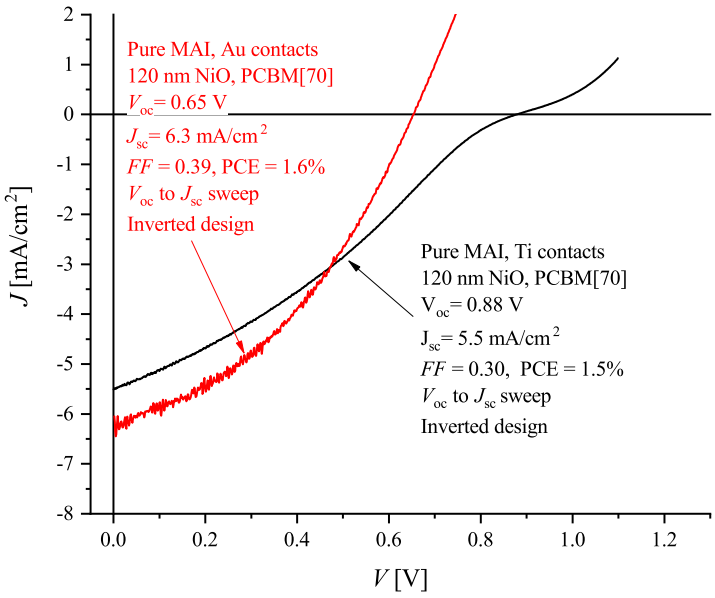

(a)

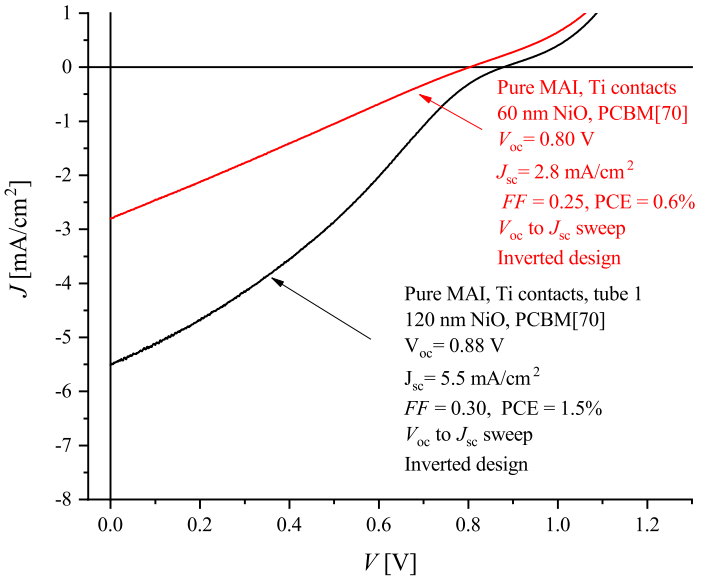

(b)

Figure 3.18: Return sweep J-V curves co-plotted compare the effects of different changes to the device structure. **(a)** shows the effect of replacing the Au contacts with Ti ones while **(b)** shows the effect of thinning the NiO. J_{sc} is the short circuit current density, V_{oc} is the open circuit potential, FF is the fill factor and PCE is the power conversion efficiency.

is somewhat counter-intuitive, as one would expect the opposite behaviour. That NiO layers of 30-150 nm have been successfully used in literature suggests that something have gone wrong with the thin NiO samples [49, 90].

In an effort to reduce the parameter space slightly it was decided to employ one of the more conventional back contacts used with the inverted configuration, namely Ag [46]. The Ag layers were deposited by thermal evaporation from a W boat under high vacuum conditions ($< 5 \times 10^{-4}$ Pa). This yielded the results shown in Figure 3.19a and Table 3.4. From the return curve one gets a J_{sc} of 4.1 mA/cm^2, a V_{oc} of 0.71 V, a FF of 0.57 yielding a PCE of 1.7%. Compared to the best Ti and Au contact cells the fill factor is seen to be substantially better though the short circuit current density is slightly lower. The V_{oc} is observed to be in between those of the Au and Ti cells while the PCE is better. The higher FF suggests that one of the parasitic resistances is lower. Since the open circuit voltage is diminished as compared to the Ti cell, it indicates that the improvement stems from a lower R_s. This is, however, in contradiction to the fact that one would expect a higher J_{sc} for decreasing series resistance and no clear conclusion can thus be reached. To further improve on the Ag samples a layer of BCP (0.5 mg/mL in ethanol) was deposited on top of the PCBM[70], as it has previously been used in conjunction with the PCBM[60] to increase device efficiency [109–111]. Though Yoon *et al.* [112] have in contrast suggested that BCP has no positive effects (at least when C_{60} is used as electron contact) the addition of the layer is seen to improve the results, as shown in Figure 3.19b and Table 3.4. The J_{sc} is seen to increase to 6.5 mA/cm^2 while the V_{oc} reaches 0.91 V in the best case (forward sweep). The fill factors decreased slightly which limits the increase in PCE to a maximum of 2.4%. The increase in short circuit current density can be explained by an increased hole blocking facilitated by the low valence band of the BCP (-7.0 eV vs vacuum) [112]. BCP's conduction band is, however, higher than that of PCBM[70] (laying at -3.5 eV vs vacuum) and the charge transfer thus happen by tunnelling. This leads to an increase in series resistance which consequently lowers the FF and potentially increases the hysteresis, in good agreement with what is observed here. A similar effect was reported by Yoon *et al.* [112] when using BCP together with C_{60}. For both of the Ag contact cells a slightly lower concentration of PCBM[70] solution (15 mg/mL) was used, as previous results indicated that better results could be obtained by doing so (see Figure B.5 and B.6).

The current density still remained unsatisfactorily low and as a consequence the PCBM[70] was replaced by PCBM[60] (99%, Solenne BV) as the latter is by far the most commonly used [113]. This did, however, not initially have the desired effect and as a consequence several things were attempted. The first alteration was the PCBM[60] layer thickness, which was varied by changing the spin speed of the deposition process. Following this, the O_2 content of the atmosphere in which the NiO was deposited was changed in an attempt to vary the oxygen content, and consequently the doping level, of the NiO [114, 115]. The hope was that any energetic barrier at the NiO/perovskite interface could be removed in this way. The endeavours did not have clear results as the overall cell quality was poor. The resulting J-V curves are shown in Figure B.7-B.12 for completeness. In an attempt to rule out that the perovskite was the problem J-V curves of a standard cell were measured using different intensities of light. To vary the light intensity an OD0.5,

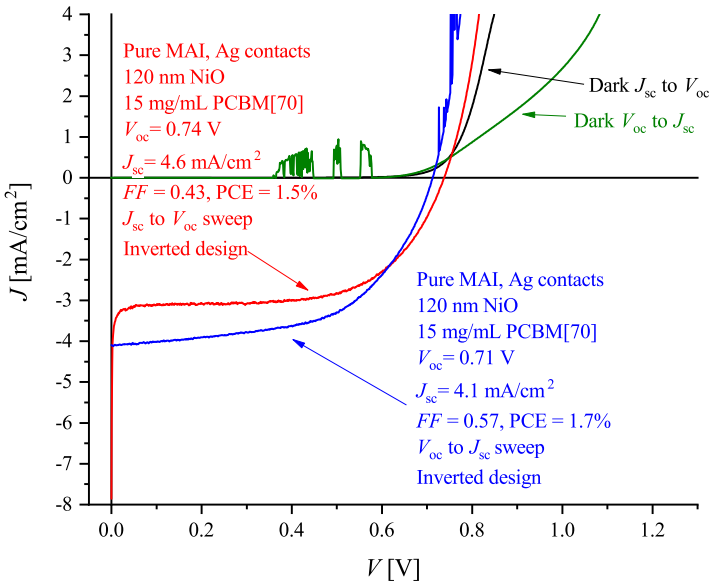

(a)

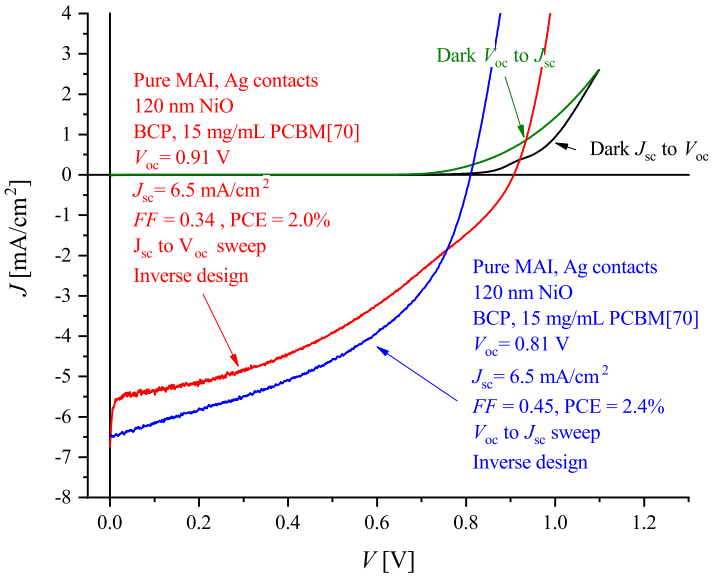

(b)

Figure 3.19: The initial J-V curves of the pure MAI inverse configuration cells using Ag as back contact. **(a)** shows the curves of the basic device whereas **(b)** shows the curves of the device where BCP had been included. J_{sc} is the short circuit current density, V_{oc} is the open circuit potential, FF is the fill factor and PCE is the power conversion efficiency.

an OD1 and an OD2 filter was inserted between the light source and the cell. By scaling the curves by the ratio between the light intensity using the filters and the case where no filter was used (OD0), one can say something about the quality of the absorber. The resultant scaled return J-V curves can be seen in Figure 3.20 while the unscaled data and the full OD0 J-V curves of the cell are shown in Figures B.13 and B.14, respectively.

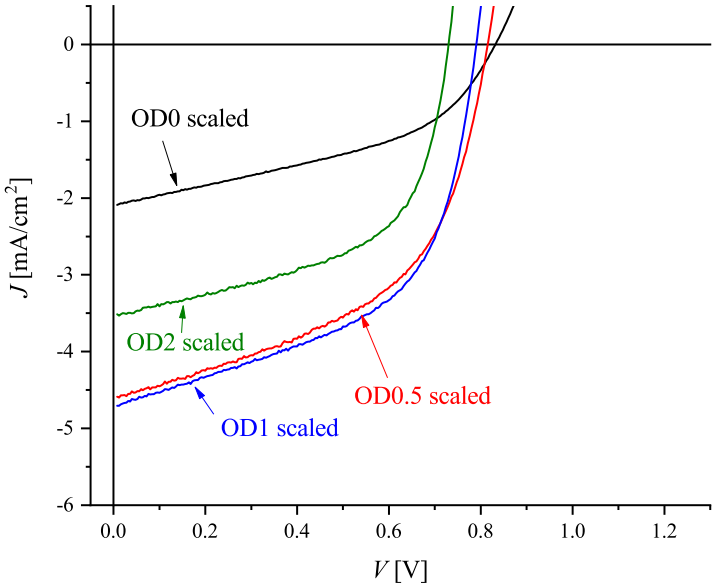

Figure 3.20: The scaled return J-V curves from the light intensity experiments recorded using OD0 (black curve), OD0.5 (red curve), OD1 (blue curve) and OD2 (green curve) filters.

If the device was limited by the photoabsorber one would have expected the scaled curves to lay on top of each other as the fraction of the absorbed light should not be intensity dependent. What is on the contrary observed, is that the devices appear to be more efficient at lower light intensities. The perovskite does therefore not seem to be the major limitation in the device. The issue appears to be one that strongly reduces the amount of current that is collected without introducing a massive series resistance. This suggests that the problem should be attributed to intensity sensitive defect recombination or a non-linear barrier. In the case of the latter one could imagine a situation where the channel that conducts through an otherwise massive barrier has a maximum capacity. An electron-hole generation rate higher than the conduction rate of this channel would consequently not lead to an increase in collected current. If the resistance through the channel is small, the magnitude of R_s would likewise remain indifferent as it would predominately come from the rest of the device. Whether or not this explanation is correct is, however, not clear and more intensity experiments, possibly coupled with external quantum efficiency (EQE) measurements, would have to be conducted to verify the theory. The final

three optimization paths that were examined were to replace the sputter deposited NiO with spin coated NiO or poly(3,4-ethylenedioxythiophene)(PEDOT:PSS) and to replace the Lumtec MAI with in-house synthesised MAI. The NiO was deposited by spin coating a similar NiO solution to the one used at LBNL, employing the same spin parameters. Variations in the annealing step were also carried out where a muffle furnace and an annealing temperature of 400 °C was used. Like before the results were not very conclusive (as detailed in Figures B.15-B.16) though the 400 °C sample appear to be slightly worse than the one prepared at 300 °C. Ultimately the best NiO device was produced by using the same procedure as used at LBNL, yielding the results detailed in Figure 3.21a and Table 3.4.

From the return sweep one obtains a J_{sc} of 7.7 mA/cm^2, a V_{OC} of 0.90 V, a FF of 0.58 and a PCE of 2.7%. Comparing the initial NiO cell (see Figure 3.17) to the final device, the latter appears less shunted as the open circuit voltages, and to some degree the fill factors, are seen to increase. This suggests that the coverage of the PCBM was better, most likely due to increased experience working with the solutions. Another factor is the different back contact which might have improved V_{oc} as well. The current density is, however, still substantially lower than what was obtained at LBNL though this was also the case with the normal configuration devices. For the final device the recrystallized Lumtec MAI was replaced with MAI synthesised in a similar manner as at LBNL though slightly different chemicals were used (the HI was 57% in water while the CH_3NH_2 was 33% in ethanol, both from SigmaAldrich). Additionally, the powder was dried under an Ar flow rather than under vacuum. The NiO was furthermore replaced with PEDOT:PSS which is a commonly used hole contact [113]. The layer was deposited by spin coating a PEDOT:PSS solution (Lumtec lot number LT-PS001) at 500/4000 rpm for 5/30 s. The PEDOT:PSS solution was, sadly, seen to have severe problems wetting the substrate surface and as a result the coverage was poor. A similar thing was observed when depositing the NiO by spin coating if the samples were not plasma cleaned before the deposition. As the substrates used with the PEDOT:PSS lacked this treatment a much improved layer homogeneity might be achieved by doing so. The results of the best PEDOT:PSS sample can be seen in Figure 3.21b and Table 3.4. From the J-V curves shown in Figure 3.21b it is clear that the open circuit voltages are slightly worse than the ones of the spin coated NiO sample (Figure 3.21a). This could be caused by the poor PEDOT:PSS coverage and no clear conclusion about which material is superior can thus be reached. The short circuit current densities and the fill factors are seen to be similar. Further experiments using PEDOT:PSS were sadly not conducted due to time limitations but the results were, nonetheless, promising and would serve as a good starting point for further investigations.

As is clear from this section the optimization process of the inverted devices was not very successful and the poor reproducibility meant that it was difficult to establish a proper baseline result to improve upon. Though this was naturally rather frustrating, especially in light of the good results obtained from LBNL, the presented results still have some value. The endeavours clearly exemplify that the gap between having a good photoabsorber and a good solar cell can sometimes be surprisingly wide. It furthermore underlines the importance of controlling as many aspects of the fabrication process as possible, as even small variations in

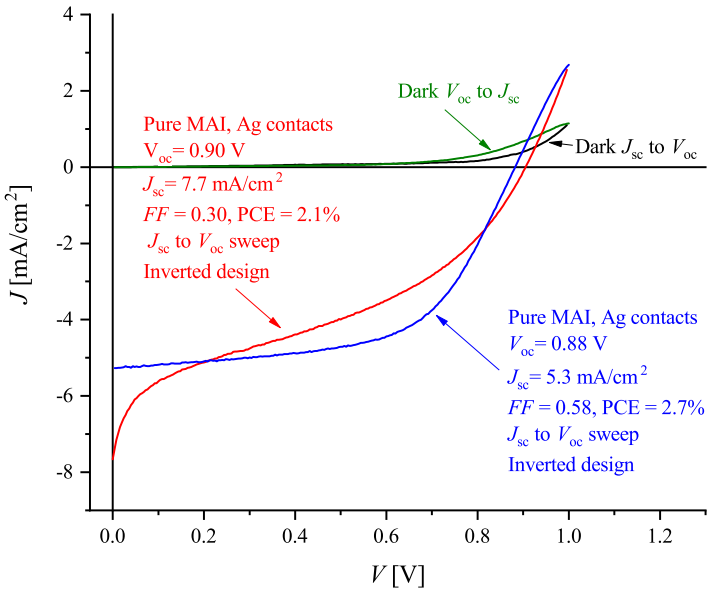

(a)

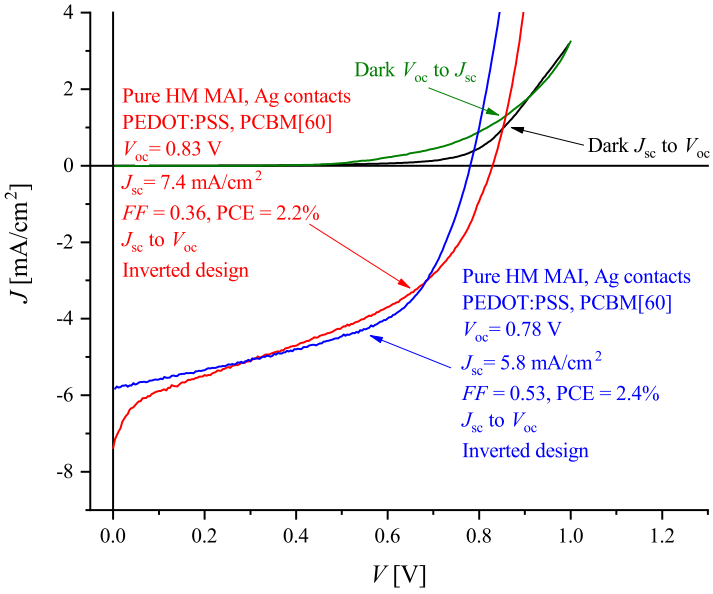

(b)

Figure 3.21: The *J-V* curves of the pure MAI inverse configuration cells using various hole conductors as back contact. **(a)** shows the curves of the soulution processed NiO device whereas **(b)** shows the curves of the device where PEDOT:PSS was used. J_{sc}, V_{oc}, FF and PEC are as defined earlier.

Table 3.4: Table showing the figures of merit obtained from the J-V curves of the pure MAI champion cells seen in Figures 3.16 - 3.19b, 3.21a and 3.21b.

Cell type	J_{sc} [mA/cm^2]	V_{oc} [V]	FF	PEC [%]
Normal configuration				
Best cell forward	15.6	0.98	0.54	8.6
Best cell return	14.9	0.99	0.77	11.3
Inverted configuration				
Initial NiO cell forward	7.6	0.54	0.26	1.1
Initial NiO cell reverse	6.3	0.65	0.39	1.6
Ti contact forward	7.2	0.81	0.19	1.1
Ti contact reverse	5.5	0.88	0.30	1.5
Thinned NiO forward	4.2	0.77	0.12	0.4
Thinned NiO reverse	2.8	0.80	0.25	0.6
Best NiO cell forward	7.7	0.90	0.30	2.1
Best NiO cell return	5.3	0.88	0.58	2.7
PEDOT:PSS cell forward	7.4	0.83	0.36	2.2
PEDTO:PSS cell return	5.8	0.78	0.53	2.4

the conditions could have profound effects on the results. The current state of the project finally serves as a point of entry for further investigations and the results help narrow the very wide parameter space.

3.5.3 AZO covered devices

During the opimization process of the inverse devices described above, AZO was tested as a buffer to be used in conjunction with ITO. As mentioned, the work of Savva *et al.* [107] served as a starting point for these investigations. After several attempts at using their proposed deposition method it, however, became apparent, from measurements done by Tor Elmelund, that the resultant layers were much thicker than what was expected from the article. Instead the method proposed by Bush *et al.* [80] was adapted with small variations. To deposit the layers a solution consisting of 12 nm AZO nanoparticles suspended in isopropanol (2.5 wt.%, Avantama lot number N-20X) was spin coated onto an inverted stack at 500/4000 rpm for 5/45 s. Inspired by the article two subsequent depositions of either 90 μL or 180 μL were conducted, which was expected to yield a layer thickness of around 50 nm [80]. This was confirmed from SEM images of a representative sample, which are shown in Figures 3.22a and 3.22b. To finish the layers the samples were annealed at 75 °C for 5 min to dry out the solvent.

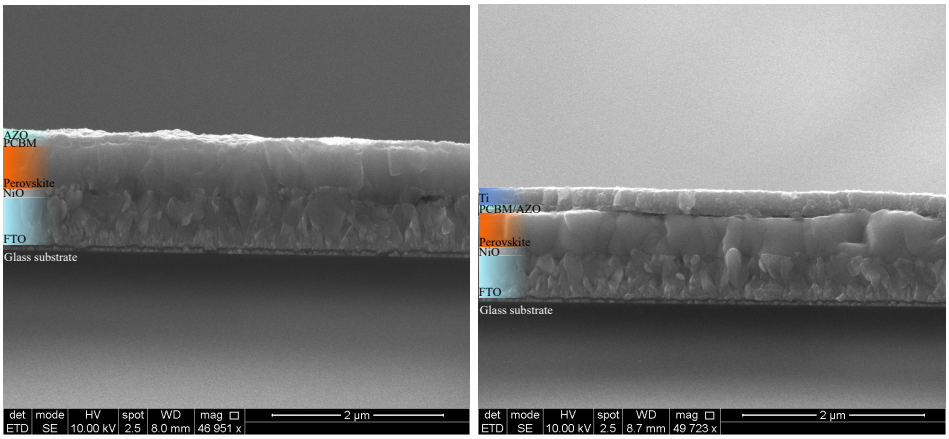

(a) **(b)**

Figure 3.22: SEM images of a 2 × 90 μL inverted device using 60 nm of NiO, perovskite, PCMB[70] and Ti contacts. **(a)** shows an area without the Ti back contact while **(b)** shows an area with the Ti layer.

The inverted stacks consisted of 60 nm or 120 nm of NiO, pure Lumtec MAI perovskite, PCBM[70] and Ti contacts. The initial devices were made using 2 × 90 μL and 120 nm of NiO which yielded the results seen in Figure 3.23a. From the best sweep one obtains a J_{sc} of 2.6 mA/cm^2, a V_{OC} of 1.01 V, a FF of 0.36 and a PCE of 0.95%. As can be seen from the curves the hysteresis effect is small and is much reduced compared with the device without the AZO (see Figure B.3). Like with the ALD TiO_2 layers discussed in Section 3.4.3, this indicates that the AZO serves to passivate surface defects. The open circuit voltages are likewise observed to improve by the addition of the blocking layer (1.01 V vs 0.88 V), again suggesting that the shunting is reduced. Finally, the short circuit current densities as well as the fill factors are seen to decrease, in good agreement with the fact that the R_s of the AZO is most likely not negligible. The homogeneity of the AZO films left some to be desired and as a consequence the amount of solution was increased to 180 μL per deposition. The increased amount of solution yielded the results shown in Figure 3.23b and from the return sweep a J_{sc} of 5.0 mA/cm^2, a V_{OC} of 0.98 V, a FF of 0.24 and a PCE of 1.2%, is obtained. The device is seen to retain the positive effects of the AZO while the short circuit current density is increased slightly as compared to the 90 μL sample. The higher J_{sc} can be explained by a small variation in the thickness of the AZO layer and subsequently in R_s.

The series resistance of the device is, nevertheless, still seen to be detrimentally high and a solution would have to be found before the layers would be truly useful as boundary layers. One way of reducing the resistance of the layer would be to thin it down further, which could most likely be achieved by increasing the deposition spin speed. Bush *et al.* [80] did, however, show that good results can be obtained using a 50 nm film so there might be a different explanation to the high resistance

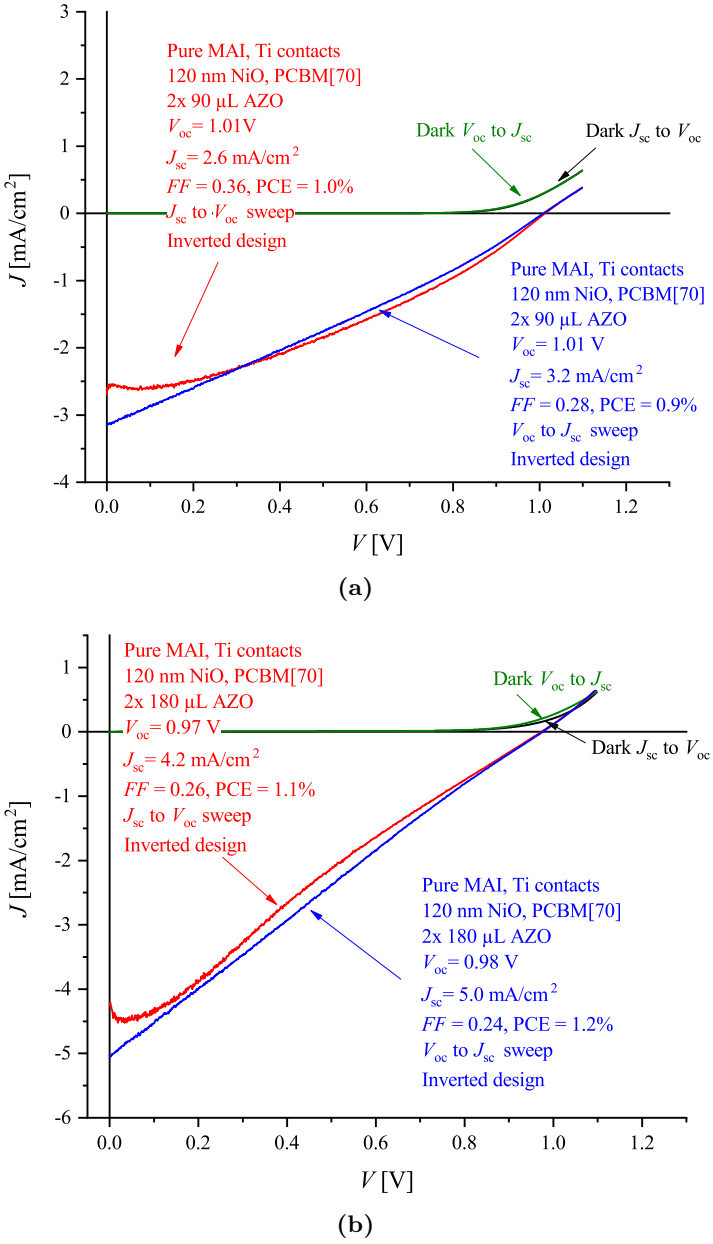

Figure 3.23: The *J*-*V* curves of the AZO layer experiments. **(a)** shows the curves of the device where 2 × 90 μL was used while **(b)** shows the curves for the cell where 2 × 180 μL was deposited. In both cases a NiO layer of 120 nm was used as hole conductor and the AZO films were annealed at 75 °C.

observed in the devices. Samples using 60 nm of NiO rather than 120 nm were, as mentioned, also fabricated using the 180 μL recipe. In good agreement with what was observed earlier, the performance of these cells were inferior to the ones using the thicker NiO layer (see Figure B.17).

3.6 ITO contact layers

As described earlier, the ITO was envisioned as the transparent conducting top electrode. Inspired by the work of Bush *et al.* [80] sputtering was used as the deposition method and parameters similar to those presented in the article, were used. More precisely the sputtering was done from an ITO target using a DC power of 40 W in a 0.33 Pa atmosphere consisting of a $5\% - 7\%$ O_2 in Ar gas mixture. The partial pressures of the gases were calibrated individually, using a combination of flow controllers and a gate valve for the chamber turbo pump. By doing so partial pressures of 0.27 Pa of Ar could be maintained while the lowest obtainable stable partial pressure of O_2 was 1.9×10^{-2} Pa. The lack of control of the latter gas was attributed to the flow controller and using a more precise one would most likely remedy this shortcoming. Several different deposition times (30 min, 60 min and 90 min) were used which resulted in various layer thicknesses. Furthermore, samples were in some cases subjected to an annealing step at 100 °C or 150 °C for either 15 min, 30 min or 60 min. In all cases the ITO was deposited on cleaned glass samples, using room temperature as substrate temperature. To test the success of the depositions, UV-Vis spectroscopy was used to gauge the transparency while 4-point probe measurements were utilized to measure the sheet resistance, $R_\square$, of the layers. The resultant UV-Vis spectra can be seen in Figure 3.24 while the sheet resistances are shown in Table 3.5.

Table 3.5: The sheet resistances of the different ITO samples measured using a 4-point probe.

Layer deposition time [min]	Annealing	Sheet resistance [Ω/sq]
30	-	186×10^3
60	-	114
90	-	27.7
90	100 °C, 15 min	24.0
90	150 °C, 30 min	22.8
90	150 °C, 60 min	22.3

All of the samples are observed to have a transparency of above 70% throughout most of the visible range. The sharp decrease in transmission observed in the blue and red spectra (90 min and 60 min samples) around 400 nm is caused by interband absorption in the ITO and is in good agreement with what have been observed in literature [80,116]. The absorption edge is not observed in the 30 min sample (black spectrum) until 360 nm, which suggests that the film is either very thin or patchy.

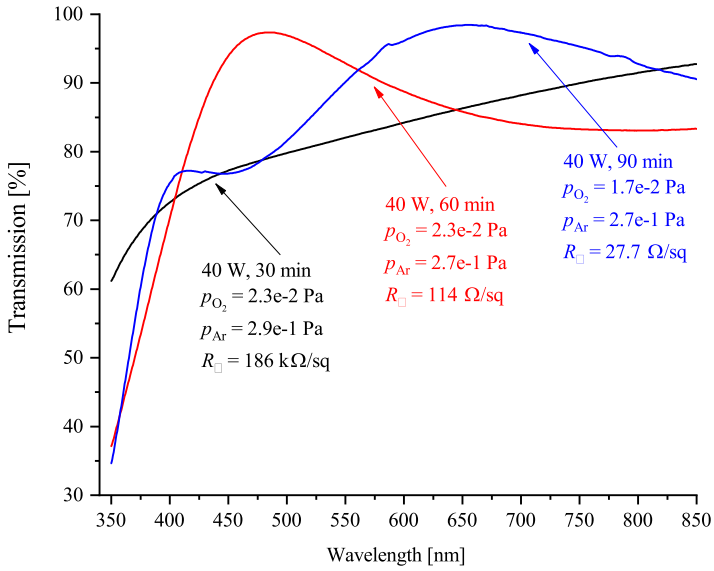

Figure 3.24: The transmission spectra of the various ITO samples. p_{O_2} is the partial pressure of O_2, p_{Ar} is the partial pressure of Ar and $R_□$ is the sheet resistance. The power and deposition time are noted in the curve labels.

This hypothesis is supported by the film's high sheet resistance of 186 kΩ/sq. A patchy film, or worse, profound island growth, would mean that the electron conductance was limited to a few corridors, thus severely limiting the transport. To further confirm this theory one could look at the sample using SEM which was, however, not done. The reason for this was that the $R_□$ of the 60 min and 90 min samples were much lower (114 Ω/sq and 27.7 Ω/sq, respectively), where the latter is similar to commercial ITO glass. In both the 60 min and the 90 min case waves appear in the transmission spectrum which are believed to be caused by interference phenomena between the films and the glass substrate. In good agreement with literature annealing the samples is seen to reduce the sheet resistance of the 90 min film down to 22.3 Ω/sq. Annealing time or temperature does not appear to have a large effect after 15 min or 100 °C as the improvement observed is only 1.7 Ω/sq. The best sheet resistance of 22.3 Ω/sq is still poorer than what was found by Bush *et al.* [80] who achieved an $R_□$ of 10.2 Ω/sq with an average transparency of 82.2%. From literature it is known that the conductivity of the films depend on the oxygen content in the way that a high oxygen content yields a higher $R_□$ [117]. Further optimization of the process might therefore be possible by varying the fraction of O_2 included in the deposition atmosphere. A lower oxygen content in the film will, however, reduce the transparency so several samples would have to be made before an optimum could be found. Guillen *et al.* [117] furthermore reports that an annealing temperature of 350 °C is needed to convert amorphous ITO to a crystalline phase. Though the perovskite would not sustain being heated to these temperatures the authors additionally show, that

annealing in vacuum rather than in air yields superior sheet resistances. Annealing perovskite in vacuum conditions does increase the risk of it decomposing as the MAI is more likely to reevaporate, but since the VASP perovskite is produced at reduced pressures it might be feasible to anneal the samples at 120 °C at roughing pump pressures. Due to a faulty power supply the ITO layers were sadly never properly tested on the perovskite cells, though the layers were expected to work well if a proper buffer layer was applied.

3.7 Photoelectrochemical perovskite devices

As described in the introduction, the overall objective of the work presented in this chapter was to fabricate a two photon tandem photoelectrochemical device for water splitting. During the stay at LBNL the very initial tests of a perovskite based device that was compatible with an electrolyte were conducted. As previously explained, one of the major problems with perovskite solar cells are their poor resistance towards moisture degradation. The challenge was therefore to make a completely ingress free vessel in which the perovskite cell could be placed or to coat it in a protective layer. As shown in Section 3.4.3 the quality of the ALD TiO_2 protective layers were not sufficient as the devices at best survived for 90 s in water. This lifetime would most likely decline during a PEC test as one would risk corroding the perovskite electrochemically as well. As a consequence another protection scheme was explored using the same approach as was presented by Walczak *et al.* [118]. In their work they used a corrosion stable epoxy resin in conjunction with a metal mesh in order to ensure that the electrolyte was separated from their III-V triple junction cell. To build their device they placed the cell in an acrylic chassis on top of the metal grid. The mesh was then pressed against the solar cell to ensure a good electrical contact while the voids in between the metal wires was filled in with the epoxy. After the epoxy had cured the cell was completely isolated from the electrolyte while the metal grid, sticking out of the epoxy, facilitated the charge transfer through the protective coating. In an attempt to replicate this approach, where the III-V cell was replaced by a normal configuration perovskite cell, the device design sketched in Figure 3.25 was envisioned.

Before the full device was produced the feasibility of using a macroscopic Au plated Ni mesh to contact the mechanically valuable thin film solar cell was investigated. The experiments used a normal configuration 40/60 MAI/MABr cell which was fabricated as described in Section 3.4. Rather than filling in the voids of the grid with epoxy the grid was placed inside a chassis and connected with Cu tape. The solar cell was then placed with the Au contacts facing the mesh and pressed gently against it using a back plate and screws. The circuit was completed with a piece of Cu tape connected to the FTO front contact. To test the device it was connected to a Bio-Logic potentiostat and illuminated from the FTO side using a calibrated AAA-rated Newport Oriel Sol3A equipped with a Xe lamp and an AM1.5 filter. Each of the eight solar cells defined on the sample had an area of 0.065 cm^2 like previously (see section 3.4). It was, however, not obvious which of the eight cells was in contact with the mesh and consequently 0.52 cm^2 was used to define the device area. To measure the *J-V* characteristics of the device two linear sweeps going form 0-1.1 V and 1.1-0 V using a scan speed of 10 mV/s.

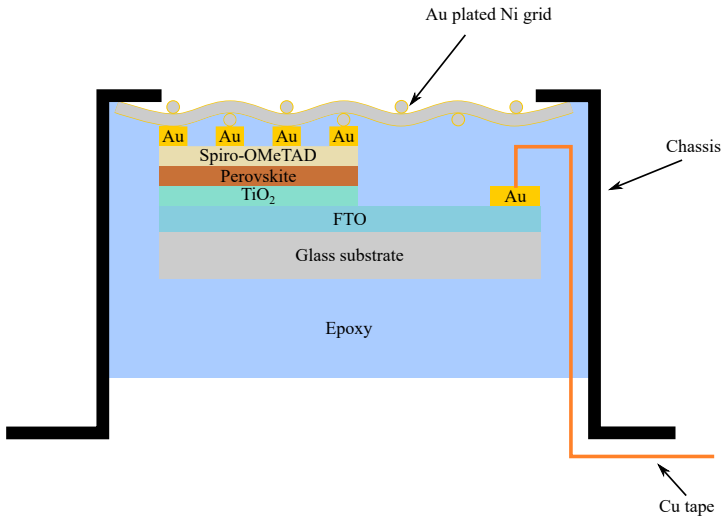

Figure 3.25: A sketch of the PEC device layout where a normal configuration perovskite solar cell would be used. The Cu tape was needed to connect to the FTO while the back contact was facilitated by the metal mesh-electrolyte junction. Pictures of the metal grid and chassis from different angles can be seen in Figures 3.27a and 3.27b

In contrast to the remainder of the LBNL cells discussed, the samples were not light soaked as initial tests indicated that doing so had a detrimental effect on the performance. Like the cells tested at DTU the likely cause for this was that they were not encapsulated in an inert atmosphere. The resultant J-V curves are shown in Figure 3.26.

Assuming that the contact area is correct one gets a J_{sc} of 12.5 mA/cm^2, a V_{oc} of 0.97 V, a FF of 0.31 and a PCE of 3.8% for the best sweep (forward). Comparing the results to what was obtained previously using pogo pins rather than the metal mesh as external contact (see Figure 3.8a), it is clear that the former is superior. The likely cause for this is that the metal grid slightly shunts the cell by causing a larger amount of mechanical damage. This has the effect that the V_{oc} observed here becomes smaller as compared to what was measured earlier. Though this is regrettable the fact that the cells are not completely shunted does, however, mean that the approach is feasible. Encouraged by this a full encapsulation of a cell was attempted using Epotek 302-3M epoxy (Epoxy Technologies, Billerica, MA) which was also employed by Walczak *et al.* [118]. This epoxy had a low viscosity which provided the advantage that the metal mesh could be placed on top of the cell and very gently affixed before the epoxy was poured on top. Due to the low viscosity the epoxy would readily flow into the voids of the mesh and by controlling the amount of sealant used one could ensure that the mesh was not completely covered. The curing temperature of the epoxy was furthermore only 65 °C, which was compatible with the perovskite cells. During the initial attempt it, however, became clear that the epoxy itself, or more likely the solvent used in it, dissolved the solar cell completely

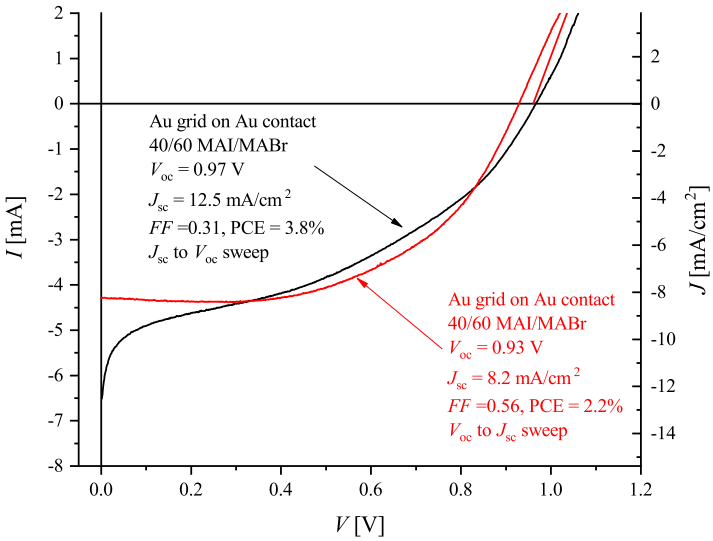

Figure 3.26: The *J-V* curves of the normal configuration 40/60 MAI/MABr cell contacted with the Au coated Ni mesh. The area used for calculating the current density was the total area of the 8 cells on the sample which equals 0.52 cm^2. The left y-axis shows the measured current while the right one shows the resulting current density. J_{sc}, V_{oc}, FF and PEC are as defined previously.

and it thus had to be abandoned. Instead a DP 105 clear epoxy (3M Scotch-Weld) was used which proved to be compatible with the perovskite cell. The downside of using the DP 105 was that it was far more viscous than the Epotek 302-3M which meant that a slightly different sealing method had to be adopted. Rather than weighing down the grid on the cell and filling in the epoxy the grid was taped to the chassis using kapton tape (see Figure 3.27a). The epoxy was then applied to the topside of the solar cell after which the chassis and grid was placed on top of the cell. Finally the construction was dried at 40 °C to cure the epoxy. Following the sealing of the front side the back side was filled in with epoxy to completely encapsulate the solar cell.

Two types of devices were sealed in this way, both of them using the normal configuration thin film stack. The difference was in the back Au contact which in one case was the 8 isolated cell configuration and in the other one single large cell as seen in Figure 3.27b. In the end neither of the devices were photoactive either due to shorting of the cell or due to insufficient contact to the Au contacts. As is evident from Figure 3.27b the issue of the adapted sealing approach was that the grid might not fully contact the Au, which is the case in the lower right corner of the device. Although the rest of the mesh appears to have achieved a good contact, it is difficult to confirm from the image. It should, however, be mentioned that the procedure was only attempted two times and more optimization could solve the issue. Another approach would be to use the Epotek 302-3M on a solar cell which had been capped with either ITO or the ALD TiO_2, which should provide some

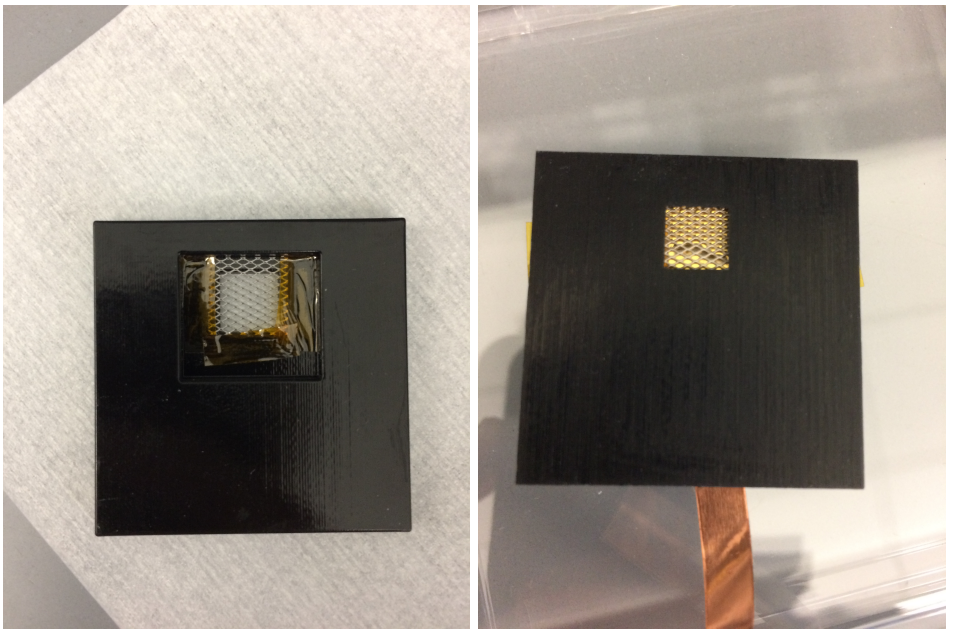

(a) **(b)**

Figure 3.27: Photos of the cell mounting into the chassis of the PEC cell. **(a)** shows the Au covered Ni grid mounted in the holder using kapton tape. **(b)** shows the front side of the device after a cell using one single Au back contact had been mounted. Contact to the front (FTO) contact was made using Cu tape.

protection from the solvents. Due to time restrictions these solutions were, sadly, never attempted but would naturally be rather interesting future work.

Though the approach of protecting the perovskite cells from the electrolyte presented here had a reasonable chance of succeeding it does, however, have one drawback, namely that the metal mesh will inadvertently shadow the solar cell. This naturally cannot be avoided in the current configuration which means that maximal performance of the encapsulated device will be lower than that of the unobstructed cell. This problem is well known in the PEC field and is one of the reasons why transparent protection layers like TiO_2 and NiO are so successful [19, 24]. An approach that could alleviate the issue would be to replace the metal mesh with a patterned ITO grid which could be fabricated using a shadow mask. The film would, however, need to be at least 1 mm thick which suggests a substantial deposition time. Furthermore, the increase in series resistance might also be problematic as ITO is a worse conductor than a metal. It is thus not clear if this solution is viable and further investigations would have to be performed to provide clarification on the matter.

3.8 Conclusion and outlook

In this chapter I have presented our work aimed at fabricating a functioning tandem device of Si and methylammonium lead halide perovskite. The LP-VASP method, and how it can be used to fabricate the perovskite, has been introduced. By varying the content of Br one can alter the band gap of the layers and by using a 40/60 MAI/MABr ratio together with 0.8 M/0.2 M PbI_2/$PbBr_2$, one can obtain the desired band gap of 1.7 eV. As detailed, the method can be used to produce efficient solar cells, in the normal configuration, with high open circuit voltages though hysteresis is still an issue. The inverse configuration is more troublesome and even after substantial effort a good, and in the case of the DTU experiments, reproducible fabrication protocol has not been achieved. Good results were nevertheless obtained with the ALD TiO_2 where I have shown how to grow layers from TDMAT and O_3 at 40 °C, that are compatible with the perovskite. Coupled with Ti contacts the TiO_2 was found to have many positive effects though the most interesting result was the very high V_{oc} of 1.15 V that was obtained. This work was never published due to a lack of time at LBNL but I firmly believe that this could be achieved if a few supporting experiments were carried out. First of all better uncertainty of the cell performance would need to be established by producing more samples. Furthermore, EQE measurements would need to be carried out to confirm the validity of the observed J_{sc}. Finally one should do XPS measurements on the TiO_2 films to confirm the formation of the compound and to estimate the coverage. The problems reproducing the LBNL results at DTU highlights the difficulties producing perovskite solar cells and that it requires good control of all aspects of the fabrication. A glove box environment, or a vacuum chamber, would therefore be beneficial to allow control of the atmospheric conditions throughout the process and not just during the perovskite fabrication.

In addition to the work concerning the fabrication of the perovskite solar cells, I have presented several smaller projects which relate either to the tandem or to the PEC aspect of the overall project. From the experiments with the ITO, I can conclude that reasonably transparent and conductive layers can be deposited by sputtering ITO in an oxygen and argon atmosphere. The need for a buffer layer to protect the perovskite solar cell from impact damage, however, meant that the ITO was never tested on an actual solar cell. Though SnO, deposited by plasma enhanced ALD, was the preferred choice of protection layer spin coated AZO could serve as a first step provided that the quality can be increased. Finally the work relating to the fabrication of a perovskite PEC using the metal mesh/epoxy approach was shown. From the results it seems likely that the endeavours could be successful with further optimization of the fabrication process or with the introduction of an ITO layer. As mentioned time restrictions sadly prevented the continuation of the experiments but the results obtained are exciting and provide an excellent starting point for further investigations.

Chapter 4

Thermal evaporation of methylammonium iodide

In this chapter I present the results of a project concerning the fundamental aspects of MAI evaporation and the implications it has on perovskite fabrication. The project started out with the intention of being a couple of quick experiments, aimed at explaining some curiosities regarding evaporative deposition of MAI. As detailed below, the initial experiments turned into a rather elaborate study involving the use of quartz crystal micro balances (QCMs) as well as mass spectrometry. The culmination of the project was the submission of the article *Deposition of Methylammonium Iodide via evaporation-combined kinetic and mass spectrometric study* to Energy and Environmental Science. The paper in its current form is appended to the thesis. Most of the data presented in the chapter is also found in the paper although additional comments and background have been included. To help future researchers interested in studying MAI using mass spectrometry, I have included some additional mass spectra in Appendix B. However, these will not be discussed in detail.

4.1 Introduction

As presented in the previous chapters, methylammonium lead halides can successfully be employed to fabricate fairly efficient solar cells. While the LP-VASP method has proven to be an effective fabrication method when an optimized system is used, another vacuum based approach was employed in the early stages of the PhD. Rather than roughing pump vacuum and the small glass tube reactors that the LP-VASP utilizes, a full physical vapor deposition (PVD) chamber, which could be evacuated down to $< 1 \times 10^{-4}$ Pa, was used. Here, $PbCl_2$ and MAI could be evaporated from separate effusion cells, either sequentially or at the same time, while the temperature of the sample could be controlled independently. The system was thus a lot more flexible than the LP-VASP set-up. Additionally, the system had the advantage that the entire fabrication of the cell could in principle be carried out without breaking vacuum. Given the moisture sensitivity of the

perovskites, the expectation was that high quality devices could be produced as a result. From the initial experiments it, however, became apparent that high partial pressures of MAI (around 1×10^{-2} Pa) were needed to produce perovskite, when it was deposited together with $PbCl_2$ in a co-evaporation scheme. An evaporation temperature above 220 °C was needed to reach these high pressures, which meant that entire grams of MAI were expended per hour of deposition. This indicated that massive incident flux densities of MAI were needed to form the perovskite, in stark contrast to what would be expected from a PVD process. The MAI was furthermore observed to deposit on all surfaces of the chamber. Given that the mean free path of the evaporated MAI at the used background pressure exceeds the chamber dimensions, this phenomenon was peculiar. Both of these findings, nevertheless, agreed well with what has later been reported in literature and with the deposition pressure used in the LP-VASP method [119].

In spite of the expected high quality films, the reported performance of devices deposited by co-evaporation have been poor compared to those where sequential evaporation or spin coating have been used [37, 41, 119, 120]. In a review paper from 2016, Ono *et al.* [119] explain that the cause for this was often difficulties controlling the MAI deposition. The usual approach for monitoring a physical vapour deposition process is to use a calibrated QCM which, as explained, allows one to gauge deposition rates. The observed rates have, however, been found to fluctuate wildly. This makes process optimization difficult, resulting in poor reproducibility [119]. To address this issue, deposition schemes using the partial pressure of MAI to control the process, have been sucessfully employed [121, 122]. The underlying cause for the difficulties, as well as the need for high deposition pressures, were not well understood or described in literature, which is what prompted the investigation presented in this chapter.

QCM measurements were employed to elucidate the nature of MAI deposition and its effect on perovskite growth. The latter was investigated by depositing thin films of $PbCl_2$ on the QCM crystals prior to running a deposition experiment. Mass spectrometry was used to further investigate the evaporating MAI and to gain insight into the chemical structure of the evaporating species.

4.2 QCM experiments

In the experiments, two separate QCM sensors, connected to an Inficon SQM-160 control box, were installed in a small vacuum chamber, pumped by a diffusion pump. To evaporate the MAI, a custom built effusion cell made from Cu was used. In addition to a thermocouple for monitoring the cell temperature, the effusion cell was equipped with a mechanical shutter which allowed one to block its exhaust. A schematic of the experimental set-up is shown in Figure 4.1

As seen in the figure, one sensor was installed facing the effusion cell while the other faced away from. In this way the direct and indirect deposition rates could be observed. Since the direct rate would be angle dependent, the QCMs were placed at an equal distance from the effusion cell center line, as detailed in Figure C.1. As the perovskite is often deposited using elevated substrate temperatures, both rate monitors were connected to a circulating water bath allowing them to be heated to various temperatures. Finally, the distance from the effusion cell to the two sensors

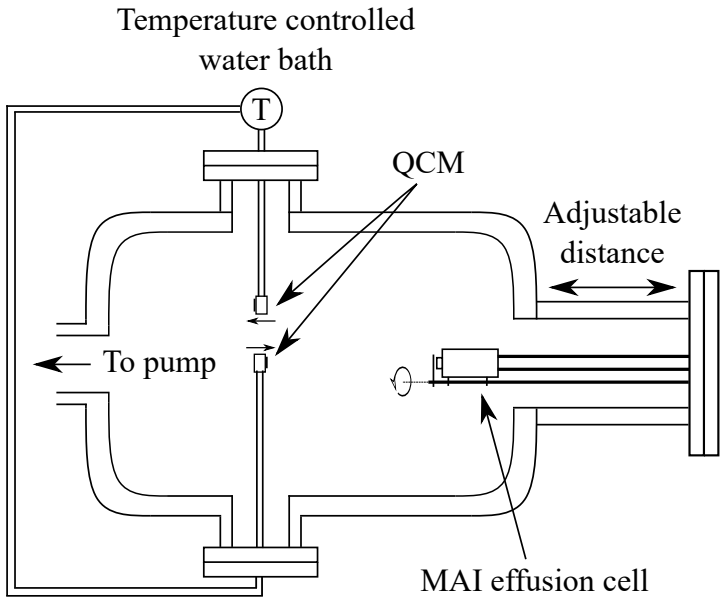

Figure 4.1: Schematic drawing of the QCM experimental set-up. One QCM faces the effusion cell while the other is rotated 180° facing directly away from it. Both sensors were connected to a circulating heat bath, while the distance from the effusion cell to the QCMs could be varied by inserting a spacer.

could be changed. The experiments were all carried out using a background pressure below 5×10^{-3} Pa, an effusion cell temperature of 130 °C and using MAI from Solaronix (lot number 24115). The $PbCl_2$ films were prepared in a high vaccum chamber ($< 5 \times 10^{-4}$ Pa) using thermal evaporation of $PbCl_2$ (SigmaAldirch 98%) powder. For each experiment a pristine 6 MHz Au covered QCM crystal was used while the deposition pressure was around 5×10^{-3} Pa. The initial experiment was conducted using the forward facing QCM, which was held at around 20 °C using cooling water. In order to get a stable MAI rate, the effusion cell was given 30 min to heat and stabilize before performing the experiment. To gauge the background rate of the chamber, the deposition rate was chopped in 10 min intervals using the effusion cell shutter. The experimental conditions were equivalent to the situation where the deposition rate of MAI is controlled using a QCM and thus served as a good starting point for the investigations. From the observation that the MAI would cover the entire deposition chamber it was expected, that the sticking coefficient of the compound was low. The fact that one is, however, able to grow perovskite using sequential deposition suggests that it can stick to $PbCl_2$ [42]. As a result the effect of adding a different surface than Au, or preexcisting MAI, onto which MAI could stick, was examined. This was done by using a crystal on which 20 nm of $PbCl_2$ had been deposited while again water cooling the QCM. From the work of Chen *et al.* [42], it was known that a substrate temperature of 75 °C was optimal for perovskite deposition when employing the sequential deposition method. As

the aim of the project was to determine why such high partial pressures of MAI were required for successful perovskite conversion, an experiment using a 20 nm $PbCl_2$ film and a sensor heated to 75 °C was conducted. Due to the fact that the resonance frequency of the QCM is temperature dependent, a special heating and thermalization routine was adopted. The water bath was given 20 min to reach the desired temperature and stabilize. Subsequently, the water was left running for an hour to allow the QCM to heat and stabilize. The frequency shift associated with heating a crystal to 85 °C using this protocol was roughly -125 Hz, as shown in Figure C.2. The resulting deposition rates are shown in Figure 4.2. In the figure, the rate observed when using a blank crystal and a QCM temperature of 65 °C is included for comparison.

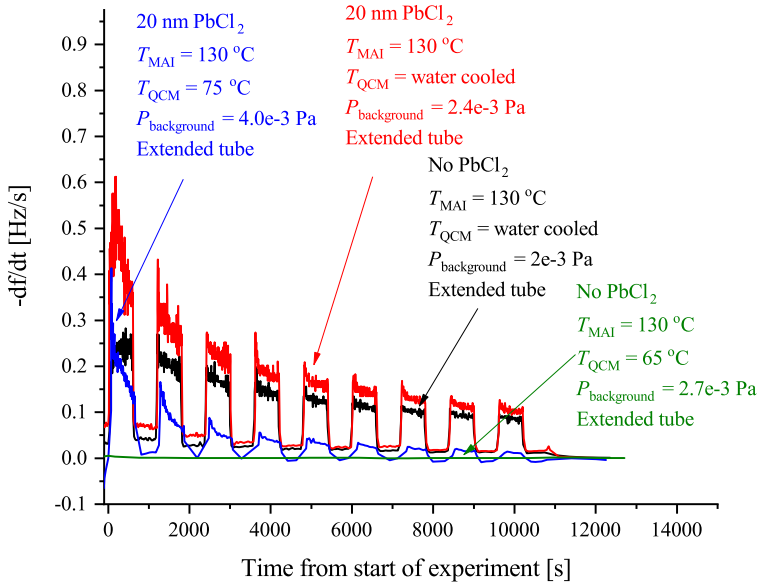

Figure 4.2: Deposition rates of the initial MAI sticking experiments using the forward facing QCM. The black curve shows the experiment where a blank crystal and water cooled QCM was used. The red curve is the case where a 20 nm $PbCl_2$ film and a water cooled sensor was used. The blue curve shows the rate using a QCM temperature of 75 °C with a 20 nm $PbCl_2$ film. Finally, the green curve shows the rate measured using a blank crystal and sensor heated to 65 °C. "Extended tube" means that the effusion cell was positioned 19.5 cm away from the QCM as compared to the 9.5 cm otherwise used. T_{MAI} is the evaporation temperature, T_{QCM} is the temperature of the QCM while $P_{\mathrm{background}}$ is the background pressure. In all cases the signals were chopped in 10 min intervals using the shutter.

The black curve shows the observed rate in the case where a blank crystal and a water cooled QCM were used, from which several interesting observations can be made. The rate decreases over time, which indicates that the sticking of the MAI decreases. The cause for this is not known, but a plausible explanation could

be that the surface of the deposited film is heated slightly over time by infrared radiation from the effusion cell. Given that the sticking coefficient is temperature dependent, this could explain the observed phenomenon. In addition to the overall drop-off, the rate does not vanish when the shutter is closed. The origin for this is believed to be MAI evaporating off the walls and the exterior of the effusion cell itself. The decrease in this background rate observed after the first shutter cycle is most likely caused by the effusion cell "cleaning" itself due to its elevated temperature.

As is evident from a comparison of the black and red curves, adding $PbCl_2$ to the crystal initially increases the sticking of the MAI. As explained, this was expected given that the possibility to form $CH_3NH_3PbI_{(3-x)}Cl_x$ should make sticking to the $PbCl_2$ easier. Upon heating the QCM, the initial rate is lower, while the drop-off happens much faster. An immediate explanation for this change is that all the $PbCl_2$ has been converted into perovskite. Upon examining the overall frequency drop observed during the experiment, this is, however, found not to be a valid hypothesis. As detailed in Appendix A, the total amount of deposited MAI is not sufficient to fully exhaust the supply of $PbCl_2$. The more probable explanation is consequently that the hotter surface severely diminishes the sticking coefficient of the MAI. This argument is supported by the fact that no rate is observed when a heated QCM and a blank crystal is used, as seen from the green curve. One would furthermore have expected the initial rates of the heated and unheated experiments using $PbCl_2$ films to be the same, as the pristine surfaces should be similar.

The fact that MAI is observed to stick everywhere in the deposition chamber is as mentioned curious when considering that one would expect near ballistic transport at the used background pressures. This indicates that the MAI has a low sticking and requires multiple collisions with the chamber walls before attaching itself, even at room temperature. Spurred by this observation, the effects of chamber geometry was examined further. To do so, measurements where the distance between the effusion cell and the forward facing QCM was either 9.5 cm or 19.5 cm, were conducted. In the experiment the sensor was water cooled and a blank crystal was used. All other experimental parameters were the same as before and the measurements yielded the rates shown in Figure 4.3. As can be observed, the rates are almost identical, which is baffling if the evaporation is thought of as a regular PVD process. In that case one would expect the rate to be highly dependent on the distance between the source and the substrate. To further examine this curiosity, a measurement using the reverse QCM was recorded, yielding the results shown in Figure 4.4. As is evident from the figure, the majority of the rate comes from the background, in stark contrast to what one would expect. If the transport of the MAI was near ballistic, the rate observed by the reverse facing QCM should be zero. It is thus clear that one does not need line of sight between the evaporation source and the sample to achieve a successful deposition. The drop-off in the rate over time is also seen in the reversed QCM experiment which suggests that heating from the source is less likely to be the origin of the phenomenon. Another possible explanation could be that the sticking of the MAI depends on the thickness of the layer already deposited. A concrete explanation was never obtained and remained an unanswered, as well as a somewhat frustrating, question throughout the project. From both of the geometry related experiments it is clear that thinking of MAI

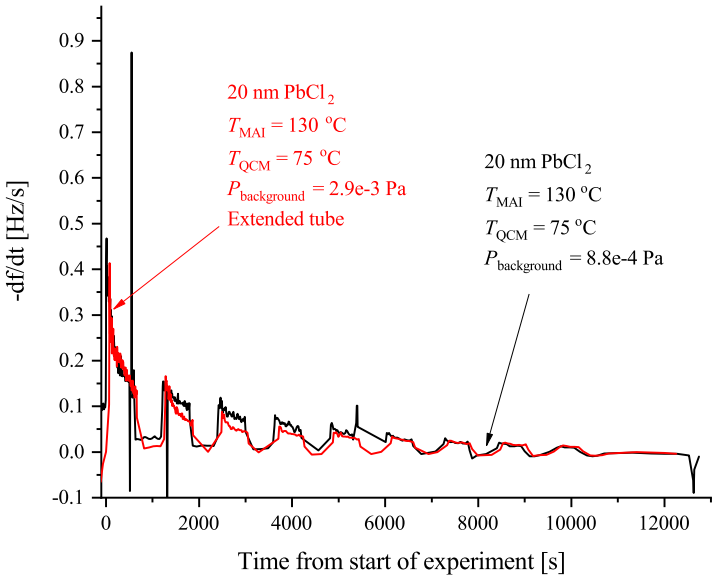

Figure 4.3: Deposition rates of the initial MAI sticking experiments using the forward facing QCM. The black curve shows the experiment where the distance from the effusion cell to the QCM was 9.5 cm while the red shows the experiment where the distance was 19.5 cm (extended tube). In both cases a water cooled QCM and a blank crystal was used. T_{MAI} is the evaporation temperature, T_{QCM} is the temperature of the QCM while $P_{\mathrm{background}}$ is the background pressure. In all cases, the signals were chopped in 10 min intervals using the shutter.

evaporation as a PVD process will lead to erroneous conclusions. Instead, the process should be treated more as a chemical vapour deposition (CVD), which alters the considerations of a deposition chamber design process.

The next parameter examined was the effect of the QCM temperature, and by extension, the effect of substrate temperature during perovskite deposition. To do so, two additional experiments were conducted where 20 nm $PbCl_2$ films and a sensor temperature of either 65 °C or 85 °C was used. The resulting rates are shown in Figure 4.5a. The initial rates are similar, but as the experiment progresses differences become apparent. The 65 °C rate (black curve) is seen to drop of slightly slower as compared to the 75 °C case shown in the blue trace. The rate observed in the 85 °C experiment, on the other hand, drops off much faster. The initial conclusion was that the $PbCl_2$ was simply being expended at a different pace, due to difference in MAI diffusion through the forming perovskite. As explained above this cannot, however, be the explanation, and examining the overall frequency change in the three experiments (seen in Figure 4.5b) further confirms it. As seen in the figure, about 155 Hz worth of additional mass per area has been deposited on the crystal in the 65 °C experiment as compared to the 85 °C measurement. The anticipation was that the amount would be the same, but that the 85 °C

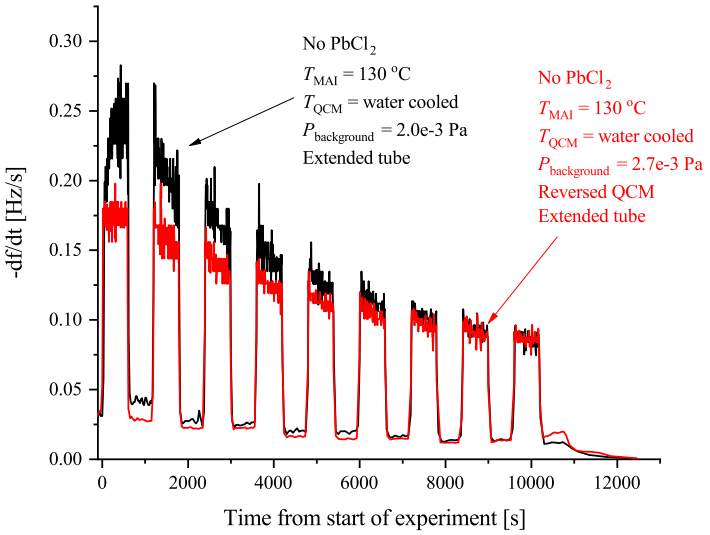

Figure 4.4: Deposition rates of the MAI sticking experiments using the forward or reverse facing QCM. The black curve shows the rate recorded by the forward QCM while the red curve is the rate measured by the reverse facing QCM. In both cases a water cooled QCM and a blank crystal was used. T_{MAI} is the evaporation temperature, T_{QCM} is the temperature of the QCM while $P_{\mathrm{background}}$ is the background pressure. In all cases, the signals were chopped in 10 min intervals using the shutter.

experiment should simply saturate faster. This discrepancy between the expected and the observed, further confirms that complete conversion into perovskite cannot be the explanation. The results do, however, explain why such high partial pressures of MAI are needed to deposit perovskite. Due to the low sticking of the compound, a large part of what is deposited onto the sample, simply re-evaporates before it can react with the $PbCl_2$. This is especially the case when the substrate is heated, and a high incident rate, and consequently a high partial pressure, of MAI is thus needed to have a net influx of reactants.

Having the overall frequency changes observed in Figure 4.5b ($\Delta f = -405$ Hz, -360 Hz and -250 Hz for the 65 °C, 75 °C and 85 °C case, respectively) allows one to make a more quantitative estimation of the MAI sticking coefficient, S_c. To do so one can use the concept of a Langmuir, which as a rule-of-thumb tells you that a monolayer of material is formed per second on a surface exposed to an atmosphere at a pressure of 1.33×10^{-4} Pa. This estimation is, however, only valid under the assumption that everything that hits the surface sticks (i.e. $S_c = 1$). By comparing the rate suggested by the partial pressure of MAI to the one observed by the QCM one is able to estimate the sticking coefficients. The detailed calculations can be seen in Appendix A, yielding the results that $S_c = 3.4 \times 10^{-4}, 3.0 \times 10^{-4}$ and 2.1×10^{-4} in the 65 °C, 75 °C and 85 °C case, respectively.

The final pertubation that was examined, was the effect of $PbCl_2$ film thickness

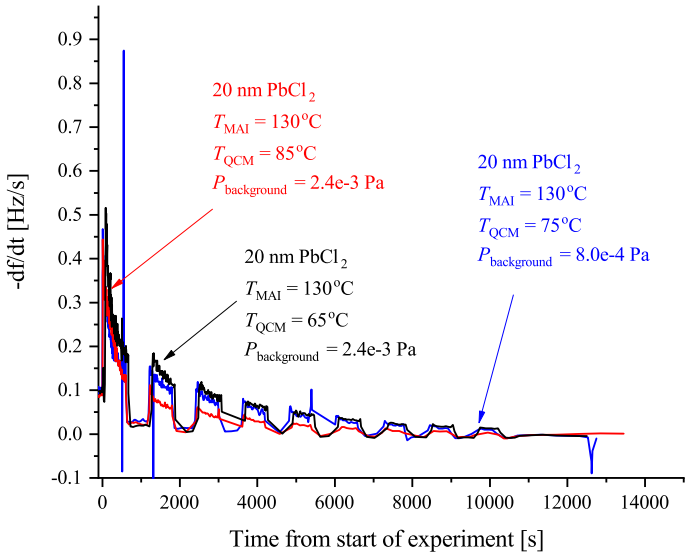

(a)

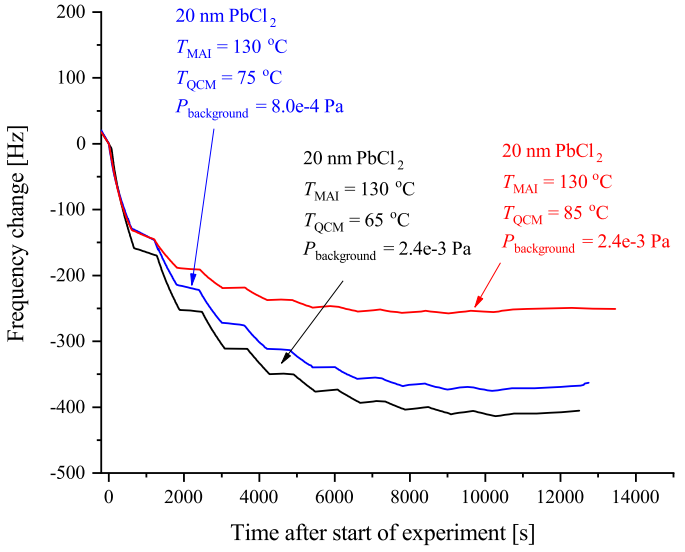

(b)

Figure 4.5: Results of the experiments using various QCM temperatures and a forward facing sensor. The black curve shows the data recorded at 65 °C while the red and the blue curves show the data observed using 85 °C and 75 °C, respectively. **(a)** shows the resultant rates while **(b)** shows the frequency change. T_{MAI} is the evaporation temperature, T_{QCM} is the temperature of the QCM while $P_{\mathrm{background}}$ is the background pressure. In all cases, the signals were chopped in 10 min intervals using the shutter.

on the observed deposition rate. To do so, additional measurements using $PbCl_2$ film thicknesses, of 40 nm and 150 nm were performed, yielding the results shown in Figure 4.6. The initial rates are again similar, which makes sense as the initial surfaces are the same. Furthermore, the drop-offs behaves in a similar manner to what was observed in the temperature experiments. Here, the thicker film is seen to progress slower towards saturation, while the drop-off is more rapid for the thinner films. As the saturation cannot be attributed to the $PbCl_2$ being depleated, another argument is needed. Given that it is known from the literature, that a 150 nm film of $PbCl_2$ could be fully converted into perovskite when using a substrate temperature of 75 °C, the diffusion of MAI through the film is expected to be fast [42]. Rather than a top down growth mechanism, the perovskite might, as a consequence, nucleate and grow throughout the $PbCl_2$ film. As the diffusion coefficient of the MAI will be dependent on the concentration of $PbCl_2$, this can explain the observed phenomenon. While the diffusion energy provided by the temperature would be the same in all cases, the thicker film would have a larger concentration of $PbCl_2$ to drive the reaction.

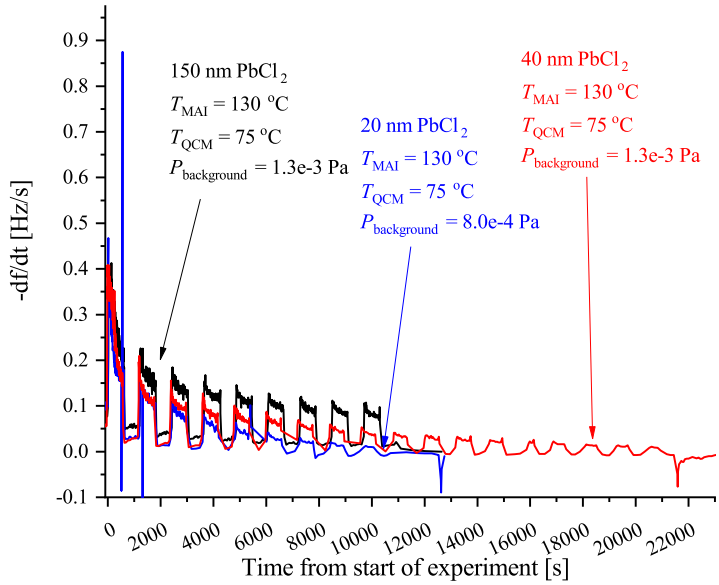

Figure 4.6: Deposition rates of the $PbCl_2$ film thickness experiments recorded using the forward facing QCM. The black trace shows the results of from the 150 nm experiment, while the red curve shows the 40 nm case and the blue shows the results for the 20 nm experiment. T_{MAI} is the evaporation temperature, T_{QCM} is the temperature of the QCM while $P_{\mathrm{background}}$ is the background pressure. In all cases, the signals were chopped in 10 min intervals using the shutter.

4.3 Mass spectrometry

From the QCM experiments an explanation for why such high MAI deposition pressures is needed for successful perovskite deposition could now be provided. The reason for the low MAI sticking was, however, still obscure. To elucidate the matter, the MAI was examined using mass spectrometry. Since the main interest was to study the MAI under deposition conditions a temperature window of 100 °C−130 °C was initially used, as it agreed well with what is normally employed in literature [21,37,39,41,42,121]. To record the mass spectra, the Waters VG AutoSpec sector magnet mass spectrometer was applied as mentioned in section 2.5. As described, this had the distinct advantage that it could measure up to high m/z ranges with an excellent mass resolution. For the experiments a m/z range of 0-380 AMU/e was used, and given that MAI should have a theoretical m/z of 159 AMU/e, the high mass range allowed for its direct detection. In addition, the possibility to change the ionization energy meant that the effects of this parameter could be studied. This feature is beneficial, as it allowes one to distinguish whether any observed decomposition was caused by thermal fracturing or through the ionization process. In the experiments ionization energies of 14 eV and 35 eV were used. 35 eV was selected as the high energy, as it was known from previous experiments to yield good signals. 14 eV, on the other hand, was the lowest ionization energy that still yielded useful signals, due to the sharp decrease in the ionization cross sections of many compounds around this energy [123]. The MAI was introduced into the mass spectrometer in solid form by loading it into a small Al cylinder, which could be inserted into a heatable sample holder. The sample holder could then be placed in the immediate vicinity of the ionization source and the inlet to the analyser. This feature meant that the time delay between the evaporating compounds leaving the source, being ionized and subsequently detected, was minimum. Consequently, the peaks observed in the mass spectra can readily be correlated to the temperature of the sample holder, which is a profound advantage. For all the presented data, MAI synthesised at DTU was used, and the background pressure was $< 5 \times 10^{-5}$ Pa in all cases.

Prior to initiating the MAI experiments, the mass axis was calibrated using PFK, as described in section 2.5. Subsequently, the system was evacuated for 50 min to remove any traces of the calibration compound. Following the purge procedure, background mass spectra using an ionization energy of either 14 eV or 35 eV were recorded at 130 °C, with an empty Al cylinder inserted in the sample holder. The sample holder was then allowed to cool, before the MAI was loaded, and the sample holder reintroduced into the system. Mass spectra were then recorded at ionization energies of 14 eV and 35 eV at a temperature of 100 °C. Finally, the temperature was raised, first to 110 °C and subsequently to 130 °C, where measurements were performed using both ionization energies at both temperatures.

To investigate the degree of fracturing related to the ionization process, the mass spectra recorded at 130 °C using the two different ionization energies are compared. The data is presented in Figures 4.7a and 4.7b. Looking first at the 35 eV spectrum, it is clear that the introduction of MAI gives rise to new peaks at m/z = 14, 15, 16, 27, 30, 31, 63.4, 64, 85, 127, 128, 129, 142 and 150 when comparing to the background measurement. Additionally, the peaks located at m/z = 17, 28, and

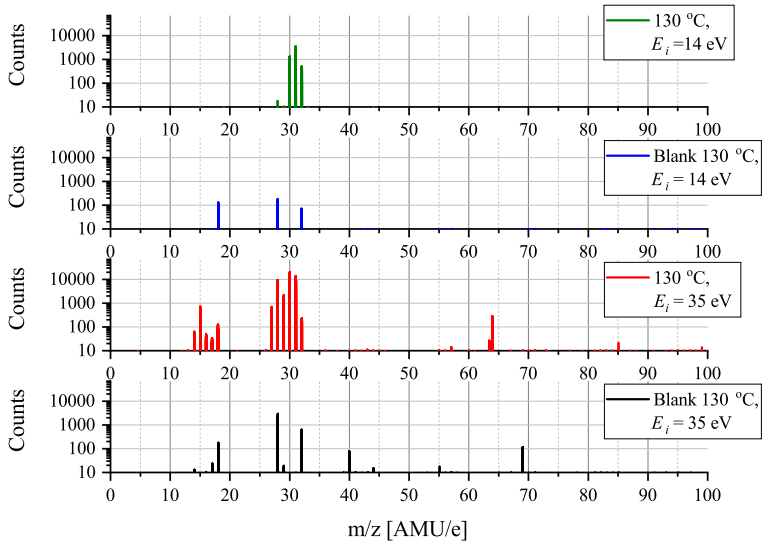

(a)

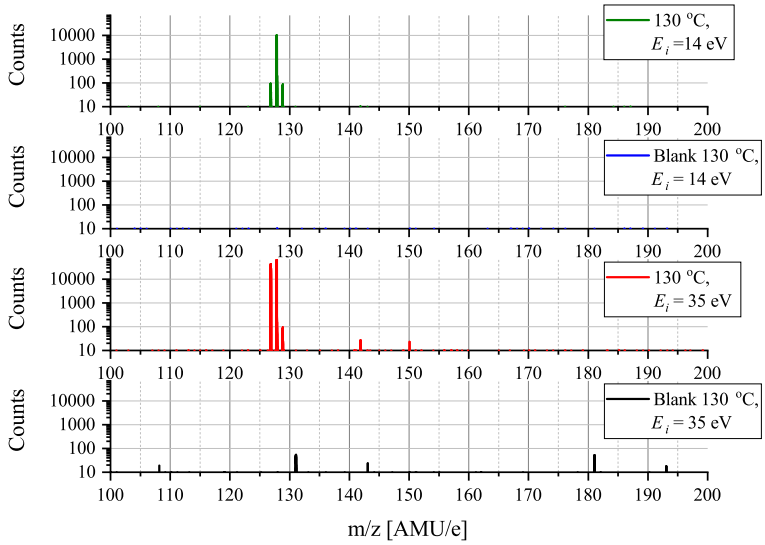

(b)

Figure 4.7: The mass spectra recorded at 130 °C using an ionization energy of either 14 eV or 35 eV. The "Counts" axes is logarithmic and starts at 10 as everything below was considered to be noise. E_i is the used ionization energy. **(a)** shows the 0-100 AMU/e range while **(b)** shows the 100-200 AMU/e range.

29 are seen to increase in magnitude, suggesting that these are also related to the MAI. The peak positions, as well as the compound they are associated with, are listed in Table 4.1. The major peaks are associated with CH_3NH, CH_3NH_2, I and HI, which suggests that the MAI is decomposing, primarily into these compounds. The prominent increases in the peaks at m/z = 28 and 29 additionally indicate that a substantial amount of the parent molecule decomposes further into N_2 and CNH. Small amounts appear to fracture even further into CH_3 and CH_4 which agrees well with the large amount of molecular nitrogen released. The absence of a peak at m/z = 159, which is associated with MAI, furthermore indicates that the compound evaporates entirely as its individual constituents.

Table 4.1: The peaks initially found in the mass spectra, the likely compound they are associated with and the parent molecule they stem from. The peak location of MAI is included for reference.

m/z [AMU/e]	Likely compound	Likely parent molecule
14	N^+	CH_3NH_2 or N_2 fragment
15	$CH_3{}^+$	CH_3NH_2 fragment
16	O^+ or $CH_4{}^+$	O_2 or CH_3NH_2 fragment
17	$NH_3{}^+$ or OH^+	CH_3NH_2 or H_2O fragment
18	H_2O^+	H_2O parent peak
27	CHN^+	CH_3NH_2 fragment
28	CH_2N^+	CH_3NH_2 fragment
29	CH_3N^+	CH_3NH_2 fragment
30	CH_3NH^+	CH_3NH_2 fragment
31	$CH_3NH_2{}^+$	CH_3NH_2 parent peak
32	$CH_3NH_3{}^+$ or $O_2{}^+$	MAI fragment or O_2 parent peak
63.4	I^{2+}	I parent peak
64	HI^{2+}	HI parent peak
85	C, N, H compound	CH_3NH_2 fragment
127	I^+	HI fragment
128	HI^+	HI parent peak
129	C, N, H compound	CH_3NH_2 fragment
142	CH_3I^+	MAI fragment
150	C, N, H, I compound	MAI fragment
159	$CH_3NH_3I^+$	MAI parent peak

Compared to the background, the peak at m/z = 32 decreases in magnitude, from which the immediate conclusion would be that the amount of O_2 (m/z = 31.97) in the system is decreasing. The peak associated with CH_3NH_3 is, however, expected to appear at m/z = 32.04, and a closer examination is thus warranted. Due to the high mass resolution of the spectrometer two peaks, positioned at m/z = 32.00 and 32.07, can be identified, as detailed in Figure C.3. Although the peak locations are not entirely correct, the spacing between the peaks fits the expected. The lowest peak is thus assigned to O_2, while the higher is associated with CH_3NH_3. The shift in the m/z axis can be explained by drift in the magnetic field happening over time. Since the calibration was done prior to the MAI experiments, this is not unexpected. The same drift was most likely also the cause for I^{2+} not being at m/z = 63.5 as expected. The O_2 peak is seen to drop from around 800 counts in the background to 30 in the MAI scan. The CH_3NH_3 peak, on the other hand, was not present at all in the background, but has an intensity of about 300 counts in the MAI scan. From this two things can be concluded, namely that the drop in intensity at m/z = 32 is due to O_2 being pumped away and that CH_3NH_3 also appears as a decomposition product of the MAI. The same approach can be used to discern if any NH_3 (m/z = 17.00) is evolved during MAI evaporation, or if the peak around m/z = 17 should be attributed to OH^- (m/z = 16.98) coming from water. Closer examination reveals that two peaks at m/z = 17.01 and 17.03 are present as detailed in Figure C.4. Once again the m/z axis is shifted while the spacing is correct. The increase in intensity of the NH_3 peak is, however, minuscule (25 to 32 counts) and the compound is thus not a major component of MAI decomposition at these temperatures. Several other peaks that appear in the background spectrum are seen to disappear in the MAI spectrum. The likely cause for this is that species associated with the peaks are evacuated between the recording of the background and MAI spectra.

The effects of fracturing due to the ionization process can be derived from a comparison of the 14 eV and 35 eV spectra. Due to the fact that the peak intensities are highly dependent on the lens and slit configuration of the mass spectrometer, the peak height found at different ionization energies are not directly comparable. The peak position and relative peak heights in each spectra are not affected by this and can thus be compared. The 14 eV spectra exhibit significantly fewer peaks, found at m/z = 28, 30, 31, 32, 127, 128 and 129. This phenomenon could be caused by the lower ionization cross sections due to the lower ionization energy, but there are indications that it is, at least partly, due to reduced fracturing. The major peaks are m/z = 30, 31 and 128, and comparing this to the 35 eV results, some clear differences appear. The most prominent of these is the sharp reduction of the I signal compared to the HI signal. While I was the dominating species in the 35 eV case, the iodide is now primarily released in the from of HI. This suggests that at least some decomposition should be attributed to the ionization process. Looking at the ratio between the m/z = 30 and 31 peaks, a similar conclusion is reached, as the dominate species is again found to be the one containing more hydrogen. A final indication that less ionization fracturing is transpiring is the fact that the m/z = 32 signal is seen to increase drastically compared to the background. Closer examination again reveals that the peak should be attributed to CH_3NH_3, which suggests that the compound is decomposing less than in the 35 eV case (see Figure

C.3). Even at the low ionization energy, no peak is present at m/z = 159, and one can thus conclude that MAI does not evaporate as a unified compound but rather decomposes, primarily into CH_3NH, CH_3NH_2 and HI.

Given the lower amount of ionization fragmentation in the 14 eV case this ionization energy is selected to study the effect of evaporation temperature in the full 0-380 AMU/e range. As explained earlier, spectra were also recorded using an ionization energy of 35 eV, which can be found in Appendix C, although no discussion of the results is included. The obtained 14 eV spectra are shown in Figures 4.8a, 4.8b, 4.9a and 4.9b. From the 0-200 AMU/e results it is evident that the only effect of increasing the temperature is an increase in peak intensity, as expected from an increased evaporation rate. This observation strongly supports that evaporating MAI as a single compound is not possible. In the 200-300 AMU/e range, only two very small peaks are detected at m/z = 254 and 275.1 in the 130 °C and 100 °C spectrum, respectively. The first of these is attributed to I_2 which is most likely not detected in the lower temperature spectra due to the even smaller amounts released. The origin of the peak at m/z = 275.1 is not immediately clear, but based on a search of the NIST database it can be attributed to $C_8H_{20}IO^-$ [124]. The quantity of the mystery compound is, however, petite and it disappears in the higher temperature experiments. In the 300-380 AMU/e range only a single peak is observed at m/z = 317.73 in the 100 °C spectrum. The peak is not very intense but it is close to where one would expect the MAI dimer to be located (m/z = 317.95). The discrepancy in the peak location could again be explained by a drift in the m/z axis and suggests that a tiny amount of $(CH_3NH_3I)_2$ is produced in addition to the aforementioned evaporating species. The full 200-300 AMU/e and 300-380 AMU/e range plots are shown in Figures C.5 and C.6, respectively, while the additional peaks are listed in Table 4.2.

Prior examples of mass spectrometry being used to examine MAI can be found in literature, and the results also indicate that MAI decomposes upon evaporation [125, 126]. The focus of both of the studies is on thermal stability of perovskite, and as a consequence, the MAI is subjected to temperatures up to 400 °C. Nenon *et al.* [125] observe peaks related to CH_3NH_2 when evaporating MAI at 110 °C. At temperatures above 160 °C, the fracturing pattern is seen to shift towards NH_3 and CH_3, which suggests a shift in the nature of the evaporation. Their findings thus seem to agree well with what was presented here. The shortcoming of their study is the fact that they do not scan above 100 AMU/e which means that they could not observe species containing I directly. Juarez-Perez *et al.* [126], on the other hand, record mass spectra in the 0-200 AMU/e range and are thus able to detect both I and HI. Contrary to the results presented here, and to those of Nenon *et al.* [125], they do not observe any species below 250 °C. Above this limit they detect strong signals originating from NH_3 and CH_3I. There thus seemed to be a substantial difference between what Juarez-Perez *et al.* [126] observed and what was found from the experiments presented above. To confirm that the MAI does indeed decompose primarily into CH_3NH, CH_3NH_2 and HI, and to better be able to compare the results with literature, a high temperature experiment in the 0-200 AMU/e range was performed. To do so, 1-2 mg of MAI was loaded into the chamber following the calibration of the m/z axis described in section 2.5. The temperature was then raised to 100 °C, and a spectrum using 14 eV as

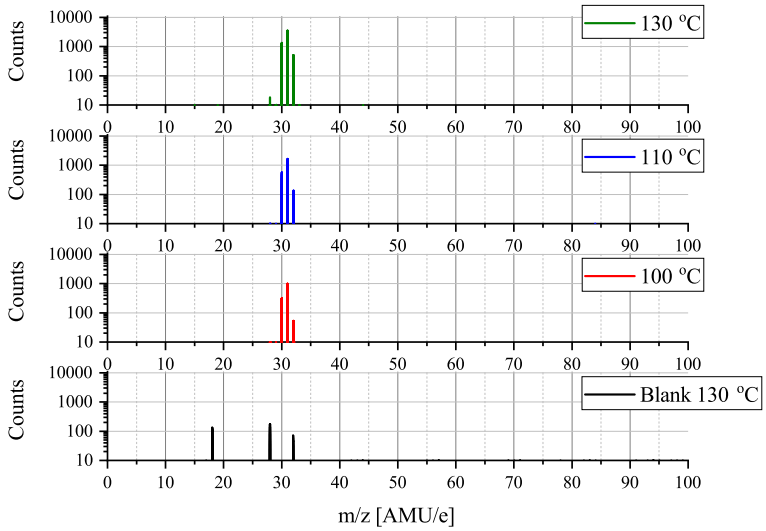

(a)

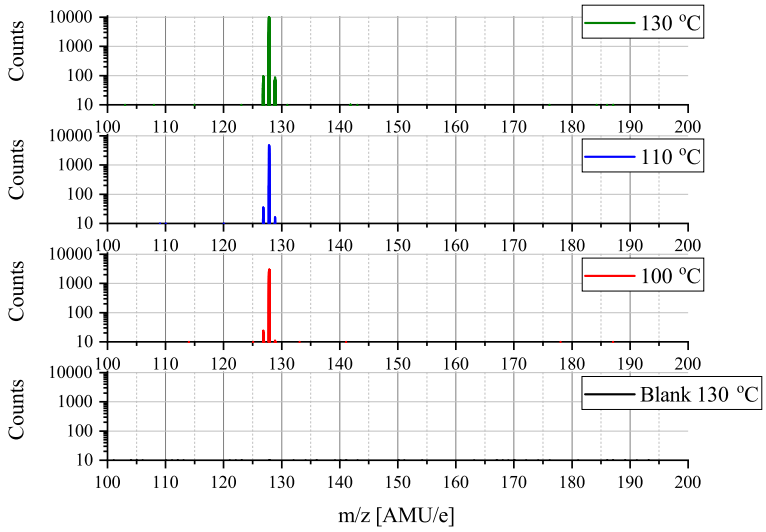

(b)

Figure 4.8: The mass spectra recorded using an ionization energy of 14 eV and a temperature of 100 °C, 110 °C or 130 °C. The "Counts" axes are logarithmic and starts at 10 as everything below was again considered to be noise. **(a)** shows the 0-100 AMU/e range while **(b)** shows the 100-200 AMU/e range.

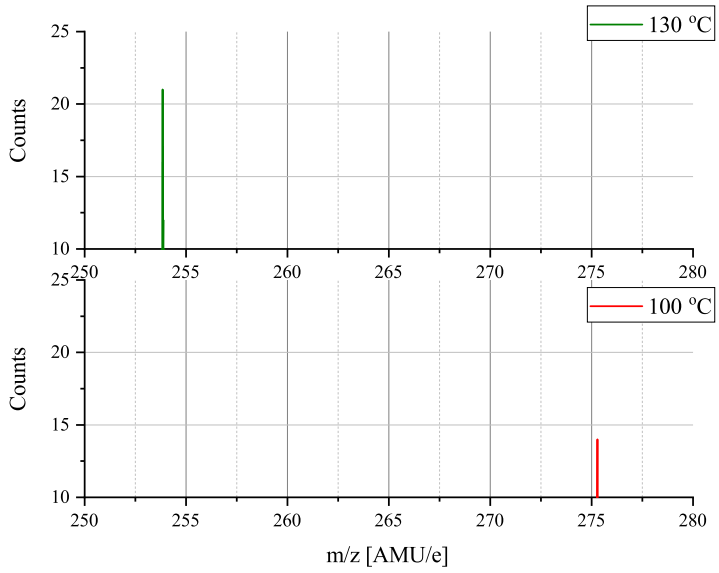

(a)

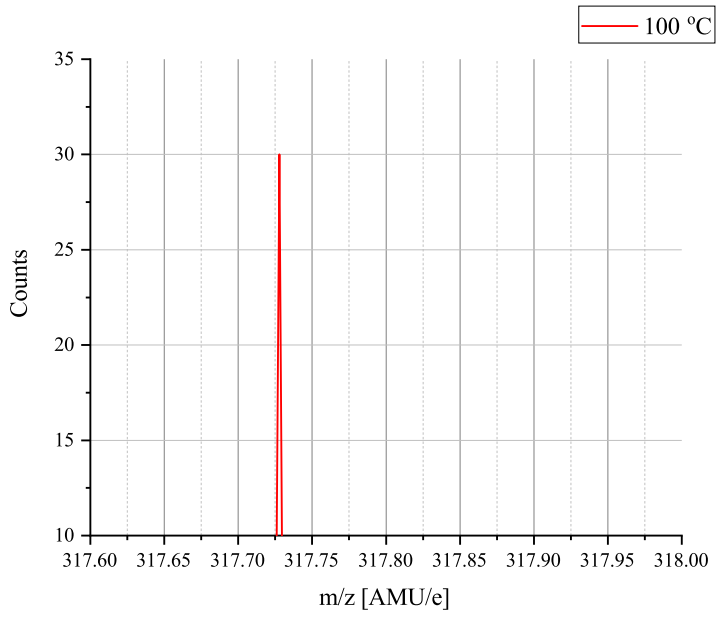

(b)

Figure 4.9: The mass spectra recorded using an ionization energy of 14 eV and a temperature of 100 °C or 130 °C. The "Counts" axes are linear and starts at 10 as everything below was again designated as noise. **(a)** shows the 250-280 AMU/e range while **(b)** shows the 317-318 AMU/e range.

ionization energy was recorded. The temperature was subsequently raised in steps of 10 °C up to 160 °C, where measurements were conducted at each temperature. The temperature step size was then increased to 20 °C until reaching 380 °C. Each measurement and temperature ramp sequence took approximately 12 min. By the end of the experiment, the Al cylinder was inspected visually and appeared to be empty, which strongly indicates that all the MAI had been evaporated during the measurements. The resulting mass spectra are shown in Figures 4.10a and 4.10b in the areas where peaks were observed. Since the main interest is the primary decomposition products, and thus the major peaks, only peaks with an intensity over 500 counts are included.

In good agreement with the previous results major peaks are observed at m/z = 30, 31 and 128 up until 240 °C. This confirms that CH_3NH, CH_3NH_2 and HI are major decomposition products at higher temperatures as well. Above 160 °C peaks at m/z = 15, 29, 28, 32, 142 and especially 127 are seen to become more prominent. This suggests an increase in the thermal decomposition of both the HI and the CH_3NH_2, although an increased evaporation rate will also serve to intensify the peaks. The latter explanation is the most likely cause for the increase in CH_3NH_3 content, as this cannot originate from CH_3NH_2. Due to the detector saturating at 65,000 counts, it was unfortunately not possible to observe if HI or I is the dominant species at higher temperatures. The increase in the amount of CH_3I does, however, suggest that substantial fracturing of the hydrogenated species is taking place. Above 180 °C additional small peaks appear at m/z = 17, 18, 44 and 45, where the last two can be attributed to C_2H_6N and C_2H_7N, respectively. Comparing this to what was observed in the 35 eV experiments (see Figures 4.7a and 4.7b) some insights can be gained. The results suggests that CH_3, NH_3 and CH_3I are primarily formed through the decomposition of CH_3NH_2 and HI happening thermally or through the ionization process. At 240 °C all peaks are seen to disappear. This phenomenon is most likely caused by the MAI source being expended and coincided with a rapid decrease in chamber pressure from 2×10^{-4} Pa to 2×10^{-5} Pa. Supporting the theory is the fact that the MAI source appeared empty after the experiments as mentioned earlier. The minor peaks found at elevated temperatures are summarized in Table 4.2, while the full range versions of Figures 4.10a and 4.10b are shown in Figures C.7 and C.8, respectively.

Although NH_3 and CH_3I are formed at higher temperatures, the main decomposition products of MAI remain CH_3NH, CH_3NH_2 and HI. The origin of the discrepancies between the results presented here and those of Juarez-Perez *et al.* [126] are most likely the differences in the experimental method. In their case the MAI is placed in a thermogravametric analyser and covered in alumina powder. To get the evaporating compounds to the mass spectrometer they furthermore use a carrier gas (He) to transport them through a capillary. Both the Al_2O_3 matrix and the helium will retard the diffusion of the gasses, and the experimental conditions are thus different from those presented here.

The dissociative nature of MAI evaporation, and the implications it has on perovskite fabrication, yields an explanation for the low sticking coefficients found in the QCM experiments. Since both CH_3NH_2 and HI need to be present at the surface at the same time, and in the same place, the perovskite formation probabil-

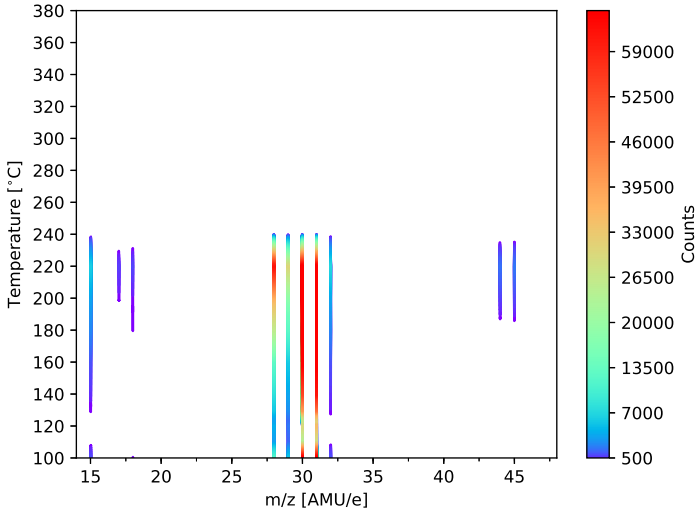

(a)

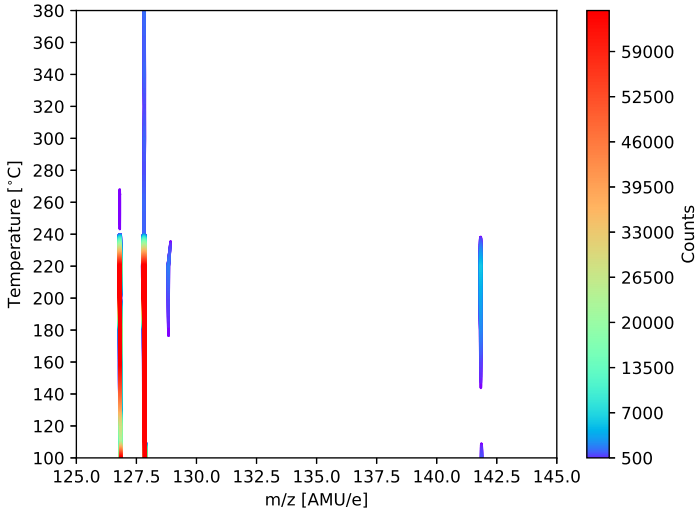

(b)

Figure 4.10: The mass spectra of the major peaks recorded using an ionization energy of 14 eV and an evaporation temperature between 100 °C and 380 °C. **(a)** shows the 14-48 AMU/e range while **(b)** shows the 125-145 AMU/e range.

Table 4.2: The additional peaks found in the mass spectra of Figures 4.9a- 4.10b, the likely compound they are associated with and the parent molecule they stem from.

m/z [AMU/e]	Likely compound	Likely parent molecule
44	$C_2H_6N^+$	CH_3NH_3I fragment
45	$C_2H_7N^+$	CH_3NH_3I fragment
254	$I_2{}^+$	I_2 parent peak
274.1	$C_8H_{20}IO^+$	CH_3NH_3I and O_2 fragment
317.73	$(CH_3NH_3I)_2{}^+$	$(CH_3NH_3I)_2{}^+$ parent peak

ity is severely reduced. Another possibility could be that the perovskite is formed solely from what appears to be the MAI dimer. The high pressure would in this scenario be needed due to the minuscule amounts of produced $(CH_3NH_3I)_2$. The dimer would, however, need to dissociate into MAI before it desorbs which again significantly lowers the reaction probability. Of the two explanations, the former thus seems the most likely. The results have some interesting implications when considering the design of an MAI deposition chamber. Due to the gaseous nature of the reactants it is better to treat the MAI evaporation as a CVD like process rather than a PVD one. This means that the volume and pumping speed of the chamber should be reduced to prevent undue loss of CH_3NH_2 and HI, while ensuring the required deposition pressure. Given that the MAI never evaporates as a unified compound another approach might also be possible, namely, to use CH_3NH_2 and HI as precursors in the first place. In this way, one would avoid the synthesis of MAI and mitigate the requirements of moisture free storage. The alternative approach is, however, not without complications (HI is for example toxic and highly corrosive), and further studies would be needed to determine its feasibility.

4.4 Conclusion and outlook

In this chapter I have presented the experiments and results of our project regarding evaporation of MAI. From the QCM experiments, it is clear that the required high deposition pressure of MAI is a consequence of its low sticking coefficient. Much of the evaporated MAI was found to simply reevaporate before forming the perovskite. It was furthermore found that line of sight is not needed for MAI deposition something that is paramount in PVD processes. As a consequence, MAI deposition behaves more like a CVD process in which the chamber dimensions should be kept small. From mass spectrometry measurements, we learned that the reason for the poor sticking was the fact that MAI does not evaporate as a unified compound but decomposes primarily into CH_3NH_2 and HI. The results presented herein have thus provided some fundamental insight into the nature of MAI evaporation as well as the kinetics of $CH_3NH_3PbI_{(3-x)}Cl_x$ formation. On a personal level, the results were very gratifying, as the difficulties producing perovskite in the large

PVD chamber could now be explained. Given that a large amount of time, as well as a new and completely redesigned effusion cell, had gone into the process it was a nice consolation for the lack of perovskite solar cells.

Based on the discoveries made in this project it would be interesting to construct a new deposition chamber, in which the above suggestions could be tested. Furthermore, the high temperature mass spectrometry experiment could be repeated using better slit settings to avoid saturating the detector. This way, one would be able to properly gauge the ratios between the various compounds. Finally, one could use Rutherford backscattering spectroscopy or depth profiling X-ray photoelectron spectroscopy to examine whether or not the perovskite grows from the top of the $PbCl_2$ or throughout the film.

Chapter 5

Investigations into the thermal stability of $CH_3NH_3PbX_3$ perovskite

In continuation of the MAI evaporation experiments, the approach of using QCM measurements and mass spectrometry was applied to study the thermal stability of $CH_3NH_3PbX_3$ perovskite. This subject has been the focus of a number of studies in literature, and the data presented here compliments many of the previously reached conclusions [58, 59]. Our motivation for performing the experiments, was to assess how much MAI leaves the perovskite at temperatures similar to those used during vacuum deposition. Significant reevaporation from already formed perovskite would naturally increase the needed influx of MAI, and consequently the partial pressure needed. As it was the case with the MAI experiments some data obtained during the project is mentioned but not discussed in detail. As previously, I have included the data for the benefit of readers wanting to carry out similar investigations in the future.

5.1 QCM experiments

For the QCM experiments the pure MAI LP-VASP perovskite was examined by depositing it on a pristine 6 MHz crystal using the fabrication procedure described in chapter 3. As with the MAI experiments the crystal was inserted into the QCM sensor after which the chamber was evacuated to a background pressure below 5×10^{-3} Pa. To test the thermal stability of the perovskite, two different QCM temperatures were used, namely 85 °C and around 102 °C. 85 °C was employed, as it was the highest temperature used in the MAI evaporation experiments, and additionally equal to what both Cornings *et al.* [58] and Fan *et al.* [59], used. In case of the first temperature, the same QCM heating and stabilization procedure used in the MAI experiments was employed. Originally, the high temperature was intended to be 120 °C but since glycol, rather than water, had to be used the QCM never got

above 102 °C. The issue was caused by the fact, that glycerol is much more viscous than water, which meant that pumping it through the system was problematic at room temperature. Consequently, the temperature of the exit tube from the QCM never exceeded 102 °C in spite of the fact, that the heat bath was set to 120 °C. Due to the circulation problems, the heating sequence became much longer, lasting for about 5400 s. The perovskite covered crystal was used in both experiments, with the 85 °C being conducted first. The crystal was visually inspected between the experiments, without any noticeable difference being detectable.

The results from the experiments can be seen in Figure 5.1a and 5.1b. The results of a blank experiment conducted using a QCM temperature of 85 °C is included in Figure 5.1a. From both figures a clear change in frequency is observed amounting to 100 Hz and 500 Hz in the 85 °C and 102 °C case, respectively. In case of the 102 °C experiment the first 600 s give rise to a sharp increase in frequency. A similar feature is observed when running a blank crystal at 85 °C and is expected to be caused by the temperature stabilizing (See Figure 5.1a). The frequency change observed in this region is thus not included in the 500 Hz. As dictated by equation (2.7.1) the positive frequency changes corresponded to something evaporating from the QCM. By a comparison with the blank experiment at 85 °C one can furthermore conclude that the frequency change is likely to originate from the perovskite. Using equations (2.7.1) and (2.7.2) one can estimate the amount of mass per area that has left the film to be $\Delta m_{85\ ^\circ\mathrm{C}} = 1.23 \times 10^{-6}\ \frac{\mathrm{g}}{\mathrm{cm}^2}$ and $m_{102\ ^\circ\mathrm{C}} = 6.14 \times 10^{-6}\ \frac{\mathrm{g}}{\mathrm{cm}^2}$. Assuming that the starting film thickness, T_s, was about 500 nm like the regular samples (see Figures 3.22a and 3.22a) the starting mass per area, m_s, was

$$m_s = \rho_{\mathrm{CH_3NH_3PbI_3}} T_s = 4.04\ \frac{\mathrm{g}}{\mathrm{cm}^3} \times 500 \times 10^{-7}\ \mathrm{cm} = 2.02 \times 10^{-4}\ \frac{\mathrm{g}}{\mathrm{cm}^2}, \quad (5.1.1)$$

where the density of pure $CH_3NH_3PbI_3$, $\rho_{\mathrm{CH_3NH_3PbI_3}} = 4.04\ \mathrm{g/cm^3}$ has been used. In the case the mass loss is purely associated with MAI evaporation, the fraction of the film that has decomposed can be estimated. The amount of MAI in the starting film, m_{MAI}, is given by

$$m_{\mathrm{MAI}} = \frac{M_{\mathrm{MAI}}}{M_{\mathrm{CH_3NH_3PbI_3}}} \times 2.02 \times 10^{-4}\ \frac{\mathrm{g}}{\mathrm{cm}^2} = 5.30 \times 10^{-5}\ \frac{\mathrm{g}}{\mathrm{cm}^2}, \quad (5.1.2)$$

where $M_{\mathrm{MAI}} = 159$ and $M_{\mathrm{CH_3NH_3PbI_3}} = 620$ are the molar weights of MAI and $CH_3NH_3PbI_3$, respectively. From this one can conclude that around 2.32% of the MAI is lost in the 85 °C case while approximately 11.6% evaporates in the 102 °C experiment. Using the same approach, as well as the time elapsed in the experiments (purple region), one can furthermore estimate the rate of film loss, r_d. Given that the 85 °C experiment ran for around 22,650 s while the 102 °C experiment lasted for about 19,490 s one arrives at $r_{\mathrm{d},85\ ^\circ\mathrm{C}} = 2.44 \times 10^{-4}$ nm/s and $r_{\mathrm{d},102\ ^\circ\mathrm{C}} = 1.42 \times 10^{-3}$ nm/s as detailed in Appendix A.

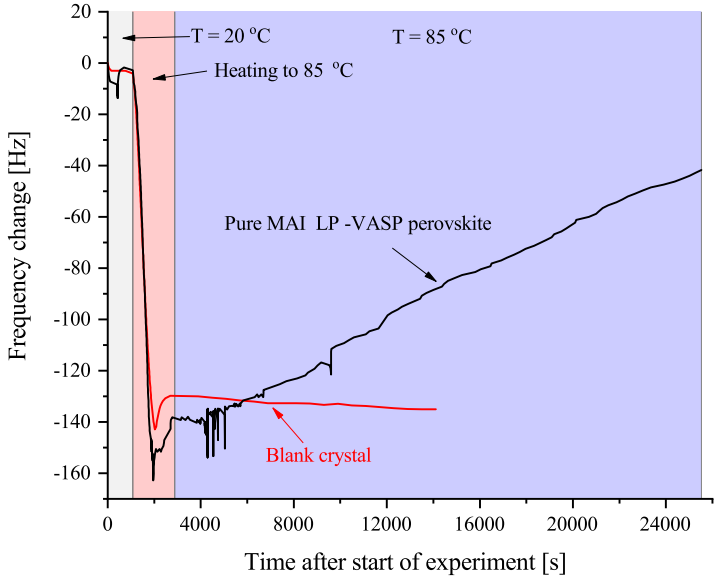

(a)

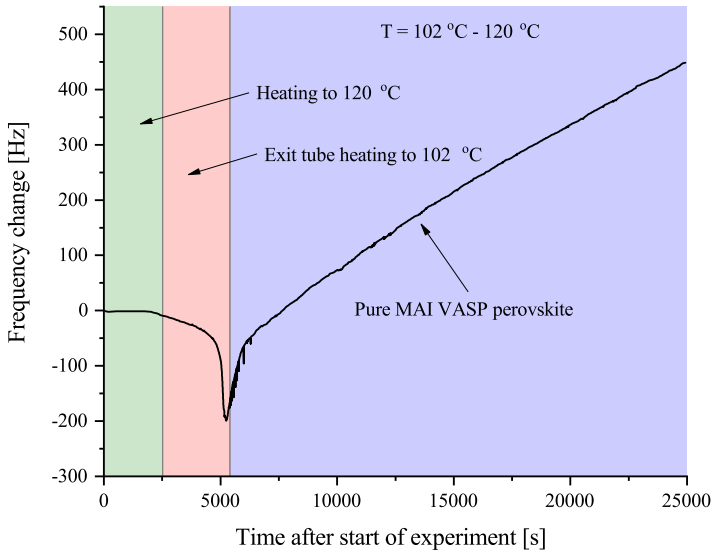

(b)

Figure 5.1: The frequency changes observed in the perovskite heating experiments. **(a)** shows the 85 °C results including those of a blank experiment. **(b)** shows the results from the 102 °C experiment. The different temperature zones were as labelled.

5.2 Mass spectrometry experiments

From the QCM experiments it was not evident if the evaporating species were indeed pure MAI constituents and if so, if they originated from the perovskite or from excess MAI remaining from the fabrication process. To provide clarification, mass spectrometry was used to study the evaporation of perovskite as a function of temperature. Though the QCM experiments had been conducted using perovskite containing Br (from the $PbI_2/PbBr_2$ precursor) the mass spectrometry was primarily done on pure $CH_3NH_3PbI_3$. This was done to ease the interpretation of the resulting mass spectra. Even though the perovskites used in the two characterization methods were not identical, the results are related. While the inclusion of Br might change the thermal stability of the perovskite slightly it has been found to still decompose when annealed at 85 °C in air [127]. The $CH_3NH_3PbI_3$ experiment thus serves as a baseline where the difference expected would be, that both MAI and MABr would evaporate rather than only the I containing compound. This was confirmed by low temperature experiments using the regular Br containing LP-VASP perovskites, recorded using a similar procedure as the MAI experiments described in the previous chapter and an ionization energy of 24 eV. The spectra can be seen in Figures D.9a and D.9b where peaks located at m/z = 80.0 and 82.0 can be observed. These peaks are associated with $H^{79}Br$ and $H^{81}Br$, respectively, and thus indicate that MABr related compounds have evaporated from the perovskite.

To produce the CH_3NH_3PbI, the LP-VASP method was employed, where a 1 M PbI_2 in DMF solution was used rather than the mixed precursor. Synthesised MAI was employed and all other process steps were as detailed in chapter 3. Two films were produced on 16×14 mm^2 substrates and subsequently scraped off to produce a powder. The powder was then loaded into the Al cylinder and introduced into the system following the PFK calibration routine. Due to the higher evaporation temperature of the PbI_2 an experiment similar to the high temperature experiment conducted with the MAI was carried out. The measurements were initiated at 100 °C and increased in steps of 10 °C up to 160 °C. The step size was then increased to 20 °C up to a maximum temperature of 380 °C. In all cases ionization energies of both 14 eV and 35 eV were used and the m/z range was extended up to 650 AMU/e to allow for detection of the $CH_3NH_3PbI_3$. The time spend at each temperature step was roughly 15 min.

As explained, both 35 eV and 14 eV measurements were conducted at each temperature step. In good agreement with what was observed in the MAI experiments, the 35 eV spectra feature more peaks suggesting a higher degree of fragmentation due to the ionization process. Consequently only the 14 eV data will be discussed in detail but the 35 eV data is included in Appendix D for completeness. The 14 eV spectra can be seen in Figures 5.2a - 5.4 in the m/z range surrounding the major peaks. No peaks were observed in the m/z = 470-650 range. Since the main interest of this study was the major decomposition products only peaks with a intensity above 250 counts (about 1% of the full range) are included. The observed peaks along with their associated compound are collected in Table 5.1. Looking at the major peaks of the spectra, it appears that CH_3NH, CH_3NH_2 are released from 110 °C to 160 °C, while HI is observed already at 100 °C. This indicates

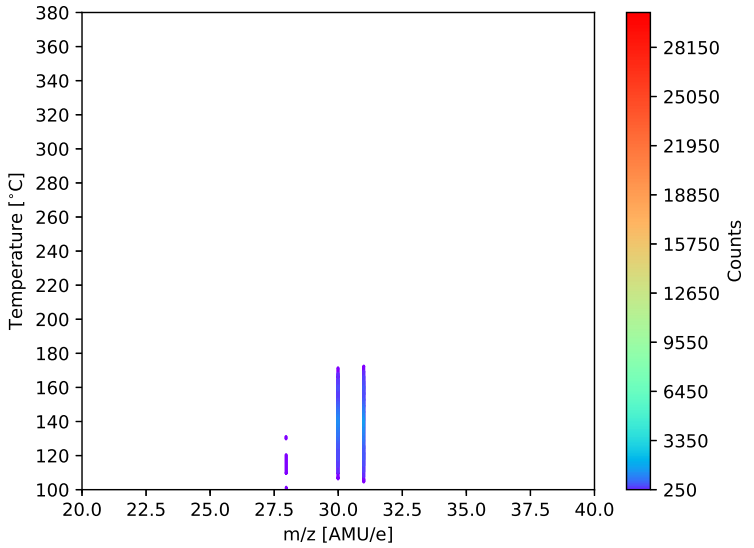

(a)

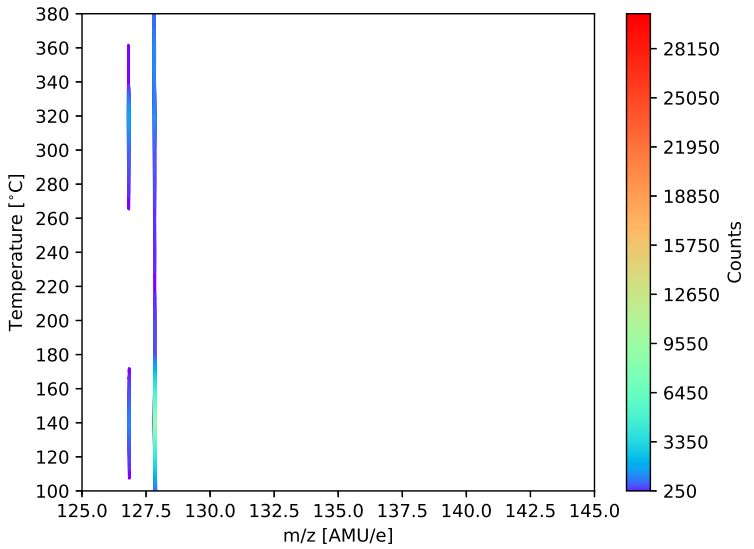

(b)

Figure 5.2: Mass spectra of the $CH_3NH_3PbI_3$ as a function of temperature in the area around the major peaks. **(a)** shows the 20-40 AMU/e region while **(b)** shows the 125-145 AMU/e region. The "Counts" axes starts at 250.

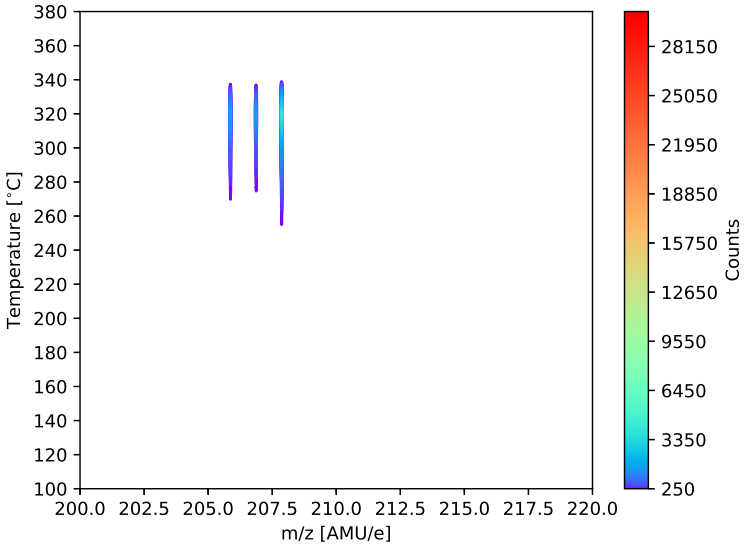

(a)

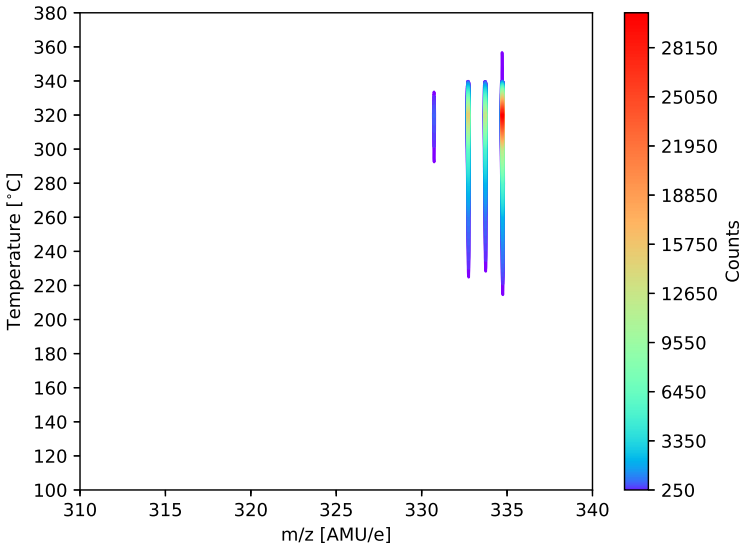

(b)

Figure 5.3: Mass spectra of the $CH_3NH_3PbI_3$ as a function of temperature in the area around the major peaks. **(a)** shows the 200-220 AMU/e region while **(b)** shows the 310-340 AMU/e region. The spectra were recorded using an ionization energy of 14 eV. The "Counts" axes again starts at 250.

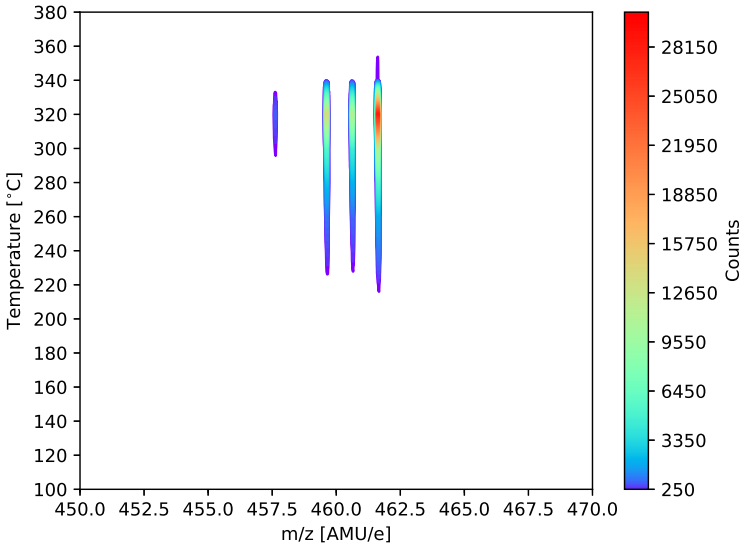

Figure 5.4: Mass spectra of the $CH_3NH_3PbI_3$ as a function of temperature in the 450-470 AMU/e region. The spectra were recorded using an ionization energy of 14 eV. The "Counts" axis again starts at 250.

that the MAI related compounds leaves the perovskite already at 100 °C, in good agreement with what was observed in literature and the MAI experiments [58, 59]. At 160 °C all of the peaks are diminished substantially indicating that all the organic compounds have evaporated. From 220 °C the first traces of PbI_2 related compounds are observed, primarily in the form of PbI and PbI_2 though some Pb is also seen. At 280 °C small amounts of I and HI reappear where the former most likely originates from the observed PbI and Pb. The latter could stem from small remnants of organic compounds bound more tightly to the PbI_2 or from a reaction between background H_2O and I. At 340 °C all the peak intensities, save for a small HI presence, are seen do drop radially suggesting that all the Pb compounds have been evaporated completely. Upon visually inspecting the Al cylinder after the experiment it appeared to be empty thus supporting the theory. The full 0-650 AMU/e range mass spectra are shown in Figures D.5a - D.8.

Table 5.1: The significant peaks found in the mass spectra, the likely compound they are associated with and the parent molecule they originate from.

m/z [AMU/e]	Likely compound	Likely parent molecule
28.0	N_2^+	N_2 parent peak
30.0	CH_3NH^+	CH_3NH_2 fragment
31.0	$CH_3NH_2^+$	CH_3NH_2 parent peak
126.8	I^+	HI fragment
127.8	HI^+	HI parent peak
205.9	$^{206}Pb^+$	$^{206}PbI_2$ fragment
206.9	$^{207}Pb^+$	$^{207}PbI_2$ fragment
207.9	$^{208}Pb^+$	$^{208}PbI_2$ fragment
330.7	$^{204}PbI^+$	$^{204}PbI_2$ fragment
332.7	$^{206}PbI^+$	$^{206}PbI_2$ fragment
333.7	$^{207}PbI^+$	$^{207}PbI_2$ fragment
334.7	$^{208}PbI^+$	$^{208}PbI_2$ fragment
457.6	$^{204}PbI_2^+$	$^{204}PbI_2$ fragment
459.6	$^{206}PbI_2^+$	$^{206}PbI_2$ parent peak
460.6	$^{207}PbI_2^+$	$^{207}PbI_2$ parent peak
461.6	$^{208}PbI_2^+$	$^{208}PbI_2$ parent peak

5.3 Discussion

The results of the QCM and mass spectrometry experiments suggests that a small amount of the MAI incorporated into the perovskites evaporates even at 85 °C. Over time the loss of the organic cation will undoubtedly lead to a decline in the efficiency of a solar cell. The phenomenon is seen to be highly dependent on temperature and even small increases in substrate heating during device fabrication might be detrimental for the resulting performance. The implication for the vacuum fabrication process is that the amount of MAI that is reevaporated of the sample increases. The temperatures used during deposition are, however, lower than 85 °C meaning that the effect is probably small. The fact that fully converted perovskite can be formed, nevertheless suggests that the formation and decomposition of the material is to some degree reversible. Capping the perovskite with a MAI impermiable layer might limit the decomposition and therefore serve to increase the perovskite lifetime, in good agreement with what has been suggested by Leijtens *et al.* [30].

Several other observations can be made from the mass spectrometry part of the study. The first of these is the fact that PbI_2 appears to fracture into Pb and especially PbI when evaporating from the "perovskite". Whether or not a similar mass spectrum would be observed if pure PbI_2 was evaporated is unclear and further investigations would be needed to clarify the matter. Though the observation of CH_3NH_3, CH_3NH, I and HI suggests that MAI is released from the perovskite their ratios are seen to be different when comparing to the pure MAI experiments at 130 °C. From Figures 4.8a and 4.8b as well as the intensities at 130 °C in Figures 5.2a and 5.2b (see Figure D.10) one gets the ratios seen in Table 5.2.

Table 5.2: The ratios between CH_3NH_2, CH_3NH, I and HI at 130 °C in the MAI and $CH_3NH_3PbI_3$ perovskite case.

Starting compound	CH_3NH_2/HI	I/HI	CH_3NH/CH_3NH_2
MAI	0.35	9.2×10^{-3}	0.38
$CH_3NH_3PbI_3$	0.17	0.14	0.87

Comparing the resultant ratios obtained for the two starting compounds a clear trend emerges. A large amount of the MAI related species appear in their more dehydrogenated form when evaporating from the perovskite, as oppose to from the MAI itself. This suggests that the decomposition process from perovskite is more violent than from MAI or that it proceeds through a different mechanism. The increase in I seen in the perovskite case could naturally also stem from PbI_2, something that could be investigated by conducting a similar experiment using pure PbI_2. The absence of a peak in the 600-650 AMU/e range (see Figure D.8), indicates that $CH_3NH_3PbI_3$ is not evaporated in large quantities. This observation suggests that evaporating the perovskite is difficult as the organic part of the compound will desorp long before the PbI_2 related species will. Consequently, single step deposition of $CH_3NH_3PbI_3$ by using thermal evaporation does not appear to be a viable deposition method.

As mentioned in the previous chapter, Juarez-Perez *et al.* [126] and Nenon *et al.* [125] also performed mass spectrometry on $CH_3NH_3PbI_3$. Though neither of their experiments include detection the Pb compounds they do observe MAI related species escaping from the perovskite. Juarez-Perez *et al.* [126] primarily observe CH_3I and NH_3 though not before a temperature of 350 °C. Given the differences in experimental approach discussed previously the discrepancy is, however, not surprising. Through a combination of thermogravemetric analysis and mass spectrometry, Nenon *et al.* [125] finds indications that MAI is released in a single step at 215 °C. Their perovskite is introduced through drop casting of a perovskite precursor solution containing DMF. Sadly, parts of the cracking pattern of DMF is similar to that of CH_3NH_2 which makes it difficult to conclude the origins of many of the peaks at low temperatures. Signals that they attribute uniquely to MAI are as a consequence not observed before they reach higher temperatures. Given that temperature can be surprisingly difficult to measure correctly, the inconsistencies between the experiments presented here and the literature ones might originate

from there. Regardless of the differences, the consensus is that the perovskite appears to decompose thermally. Initially this happens through the release of MAI related compounds, followed by the Pb species at higher temperatures.

5.4 Conclusion and outlook

From our QCM and mass spectrometry investigations I can conclude that $CH_3NH_3PbI_3$ does not appear to be thermally stable at temperatures above 100 °C. At these temperatures, the organic constituents of the material are observed to evaporate from the material, strongly suggesting that the decline in layer thickness observed from the QCM experiment, should be attributed to this phenomenon. Assuming that this is also the case in the 85 °C experiment, I have shown that one can calculate the rates of film loss of $r_d = 2.44 \times 10^{-4}$ nm/s and $r_d = 1.42 \times 10^{-3}$ nm/s in the 85 °C and 102 °C case, respectively. This indicates that the perovskites are ill-suited for high temperature annealing steps though the inclusion of a capping layer might mitigate the problem.

From the project several additional questions have emerged which would serve as good starting points for further investigations. Initially an experiment using a more well defined amount of $CH_3NH_3PbI_3$ should be conducted as it would allow one to better confirm that all the powder had been expended during the experiment. An experiment using PbI_2 should then be conducted to elucidate which signal originates from the compound. By using an equivalent amount of PbI_2 to what was incorporated into the calibrated perovskite experiment, a good compatibility would be ensured. Likewise, an experiment with a calibrated amount of MAI should be performed. Such an investigation would help shed light on the origin of the different decomposition product ratios observed. Finally, it would be very interesting to subject different types of organolead halide materials, such as the double or triple cation compounds, to the same investigations and compare them to the ones I have presented here.

Chapter 6

Thesis conclusion and outlook

The goal of this project was to produce efficient two-photon PEC devices to achieve unassisted water splitting by employing methylammonium lead halide perosvskite photoabsorbers. The work presented in the thesis has in some way all been related to the endeavours, though the included studies were very different in nature. In the chapters I have tried to present not only the successful discoveries, but also results that were slightly less useful. I have done so in the hope that these can be beneficial for future researchers, who want to dive into the field.

The work presented in chapter 3 were the efforts most directly aimed at producing solar cells. As a result optimization of the different fabrication processes was the main focus. As shown, the LP-VASP method can be used to successfully deposit high quality perovskite layers. By tuning the Br content in the $CH_3NH_3PbI_{3-x}Br_x$ structure, the band gap of the absorbers was varied and I found that a MAI/MABr ratio of 40/60 yielded a band gap energy around the desired 1.7 eV. These layers were used to produce fairly efficient solar cells by employing the normal device architecture, and yielded open circuit voltages over 1 V. In the chapter I furthermore presented, how ALD layers of TiO_2 were deposited on the perovskite cells and the beneficial effects they had on the device performance. Additionally, I have shown how to successfully deposit ITO layers using sputtering. The work presented in the final part of the chapter was aimed at making the perovskite cells useful as a PEC device by utilizing a special encapsulation strategy. Though water splitting using the devices was never achieved, I feel that it is currently the best approach for properly protecting perovskite based PEC devices.

In chapter 4 I showed how QCM measurements, coupled with mass spectrometry, were used to study the kinetics of perovskite formation and the nature of MAI evaporation. The results provided an explanation for the abnormally high deposition pressure of MAI required for successful perovskite deposition. The QCM measurements indicated that the sticking coefficient of MAI was extremely low, which caused most of the compound to reevaporate from the $PbCl_2$ surface before it could react. This was especially the case if the surface was heated. A substantial

incident flux density of MAI was consequently needed to ensure a net deposition rate of the compound. The mass spectrometry revealed that the cause for the low sticking was that the MAI evaporated exclusively as it constituents, primarily in the form of CH_3NH_2 and HI.

The approach of using QCM measurements and mass spectrometry was, additionally, used to study the thermal stabilities of $CH_3NH_3PbI_{3-x}Br_x$ and $CH_3NH_3PbI_3$ as presented in chapter 5. The investigations revealed that the organic parts of the perovskite appear to evaporate already at temperatures around 100 °C. The results have widespread implications for both device fabrication and lifetime. The fact that no high annealing steps can be included after the perovskite deposition steps severely limits the usefulness of thick protective layers like TiO_2, which require thermal treatment to crystallize properly.

Though the projects, sadly, never came together to yield a fully functioning PEC device, I have thoroughly enjoyed working with both the applied and fundamental aspects of the subject. Whether or not perovskite photoabsorbers will find their use in future PEC devices is an open question due to the serious stability challenges. In the short run, the PV plus electrolyzer configuration thus seem most attractive, though time will tell which approach comes out on top. Using sunlight to drive chemical reactions, nevertheless, has the potential to significantly impact the energy sector of tomorrow and I feel confident that it, in some form, will be widely applied in the future.

Outlook

Several of the projects that I started during my stay at LBNL have still not been concluded though especially the ALD TiO_2 work came close. It would naturally be a good continuation of the studies to further investigate the use of Ti contacts and TiO_2 layers. The feasibility of using the epoxy encapsulation of the perovskites also deserves further scrutiny, and it might help clarify if using perovskits in PEC devices is a viable approach. The use of organo lead halide perovskites for solar cells certainly holds great promise, and will more than likely find its commercial application in the future. It has, however, become clear that the metylammonium based materials suffer from a rather broad range of stability challenges. For future investigations it might, consequently, be more appropriate to employ the Fa-Cs perovskite.

Bibliography

[1] James Hansen, Makiko Sato, and Reto Ruedy. Perception of climate change. *Proceedings of the National Academy of Sciences of the United States of America*, 109(37):E2415–23, sep 2012.

[2] IPCC Contribution of Working Groups I II, III to the Fifth Assessment Report of the Intergovernmental Panel on Climate Change [Core Writing Team R.K. Pachauri, and L.A. Meyer (eds.)]. IPCC Geneva Switzerland 151 pp. Climate change 2014: Synthesis report. Technical report, Intergovernmental panel on climate change, 2014.

[3] US National Oceanic and Global Monitering Devision Atmospheric Administration, Earth System Research Laboratory. Full mauna loa co2 record. `https://www.esrl.noaa.gov/gmd/ccgg/trends/full.html`, 2018.

[4] Jet Propulsion Laboratory / National Aeronautics and Space Administration. Global climate change: Evidence. nasa global climate change and global warming: Vital signs of the planet. `https://climate.nasa.gov/evidence/`, 2018.

[5] BP Global. Bp statistical review of world energy 2017. `https://www.bp.com/en/global/corporate/energy-economics/statistical-review-of-world-energy.html`, 2018.

[6] Søren Dahl and Ib Chorkendorff. Solar-fuel generation: Towards practical implementation. *Nature Materials*, 11(2):100–101, jan 2012.

[7] Steven Chu, Yi Cui, and Nian Liu. The path towards sustainable energy. *Nature Materials*, 16(1):16–22, 2016.

[8] Blaise A. Pinaud, Jesse D. Benck, Linsey C. Seitz, Arnold J. Forman, Zhebo Chen, Todd G Deutsch, Brian D James, Kevin N Baum, George N Baum, Shane Ardo, Heli Wang, and Thomas F Jaramillo. Environmental Science Technical and economic feasibility of centralized facilities for solar hydrogen production via photocatalysis and photoelectrochemistry. *Energy & Environmental Science*, 6(7):1983–2002, 2013.

[9] Evgenii V. Kondratenko, Guido Mul, Jonas Baltrusaitis, Gastón O. Larrazábal, and Javier Pérez-Ramírez. Status and perspectives of CO2 conversion into fuels and chemicals by catalytic, photocatalytic and electrocatalytic processes. *Energy & Environmental Science*, 6(11):3112, 2013.

[10] Christina W. Li and Matthew W. Kanan. CO 2 reduction at low overpotential on Cu electrodes resulting from the reduction of thick Cu 2O films. *Journal of the American Chemical Society*, 134(17):7231–7234, 2012.

[11] Michael G. Walter, Emily L. Warren, James R. McKone, Shannon W. Boettcher, Qixi Mi, Elizabeth a. Santori, and Nathan S. Lewis. Solar water splitting cells. *Chemical Reviews*, 110(11):6446–6473, 2010.

[12] J Brillet, J H Yum, M Cornuz, T Hisatomi, R Solarska, J Augustynski, M Graetzel, and K Sivula. Highly efficient water splitting by a dual-absorber tandem cell. *Nature Photonics*, 6(12):823–827, nov 2012.

[13] Oscar Khaselev and John A Turner. A Monolithic Photovoltaic-Photoelectrochemical Device for Hydrogen Production via Water Splitting. *Science*, 280(5362):425–427, 1998.

[14] Brian Seger, Ivano E Castelli, Peter C K Vesborg, Karsten W Jacobsen, Ole Hansen, and Ib Chorkendorff. 2-Photon tandem device for water splitting: comparing photocathode first versus photoanode first designs. *Energy & Environmental Science*, 7(8):2397–2413, 2014.

[15] C. J. Dawson and J. Hilton. Fertiliser availability in a resource-limited world: Production and recycling of nitrogen and phosphorus. *Food Policy*, 36(SUPPL. 1):S14–S22, 2011.

[16] Charles C L McCrory, Suho Jung, Ivonne M. Ferrer, Shawn M. Chatman, Jonas C. Peters, and Thomas F. Jaramillo. Benchmarking Hydrogen Evolving Reaction and Oxygen Evolving Reaction Electrocatalysts for Solar Water Splitting Devices. *Journal of the American Chemical Society*, 137(13):4347–4357, 2015.

[17] Peter C. K. Vesborg and Thomas F. Jaramillo. Addressing the terawatt challenge: scalability in the supply of chemical elements for renewable energy. *RSC Advances*, 2(21):7933, 2012.

[18] E. Kemppainen, A. Bodin, B. Sebok, T. Pedersen, B. Seger, B. Mei, D. Bae, P. C. K. Vesborg, J. Halme, O. Hansen, P. D. Lund, and I. Chorkendorff. Scalability and feasibility of photoelectrochemical H ₂ evolution: the ultimate limit of Pt nanoparticle as an HER catalyst. *Energy Environ. Sci.*, 8(10):2991–2999, 2015.

[19] Bastian Mei, Anastasia A Permyakova, Rasmus Frydendal, Dowon Bae, Thomas Pedersen, Paolo Malacrida, Ole Hansen, Ifan E L Stephens, Peter C K Vesborg, Brian Seger, and Ib Chorkendor. Iron-Treated NiO as a Highly Transparent p - Type Protection Layer for Efficient Si-Based Photoanodes. *The Journal of Physical Chemistry Letters*, 5(20):3456–3461, 2014.

[20] Jeffrey A. Herron, Jiyong Kim, Aniruddha A. Upadhye, George W. Huber, and Christos T. Maravelias. A general framework for the assessment of solar fuel technologies. *Energy & Environmental Science*, 8(1):126–157, 2015.

[21] Mingzhen Liu, Michael B Johnston, and Henry J Snaith. Efficient planar heterojunction perovskite solar cells by vapour deposition. *Nature*, 501(7467):395–398, sep 2013.

[22] William Shockley and Hans J. Queisser. Detailed Balance Limit of Efficiency of p-n Junction Solar Cells *. *Journal of Applied Physics*, 1640:510–519, 1960.

[23] Martin Jesper Bækbo. Fabrication of perovskite tandem solar cells for photocatalytic water splitting. Master's thesis, Technical University of Denmark, 2015.

[24] Bastian Mei, Thomas Pedersen, Paolo Malacrida, Dowon Bae, Rasmus Frydendal, Ole Hansen, Peter C. K. Vesborg, Brian Seger, and Ib Chorkendorff. Crystalline TiO 2 : A Generic and Effective Electron-Conducting Protection Layer for Photoanodes and -cathodes. *The Journal of Physical Chemistry C*, 119(27):15019–15027, 2015.

[25] Brian Seger, Thomas Pedersen, Anders B Laursen, Peter C K Vesborg, Ole Hansen, and Ib Chorkendorff. Using TiO2 as a conductive protective layer for photocathodic H2 evolution. *Journal of the American Chemical Society*, 135(3):1057–1064, 2013.

[26] Dowon Bae, Thomas Pedersen, Brian Seger, Mauro Malizia, Andrej Kuznetsov, Ole Hansen, Ib Chorkendorff, and Peter C. K. Vesborg. Back-illuminated Si photocathode: a combined experimental and theoretical study for photocatalytic hydrogen evolution. *Energy Environ. Sci.*, 8(2):650–660, 2015.

[27] Juan-Pablo Correa-Baena, Antonio Abate, Michael Saliba, Wolfgang Tress, T. Jesper Jacobsson, Michael Grätzel, and Anders Hagfeldt. The rapid evolution of highly efficient perovskite solar cells. *Energy Environ. Sci.*, 10(3):710–727, 2017.

[28] Michael Saliba, Taisuke Matsui, Ji-Youn Seo, Konrad Domanski, Juan-Pablo Correa-Baena, Nazeeruddin Mohammad K., Shaik M Zakeeruddin, Wolfgang Tress, Antonio Abate, Anders Hagfeldt, and Michael Gratzel. Cesium-containing Triple Cation Perovskite Solar Cells: Improved Stability, Reproducibility and High Efficiency. *Energy Environ. Sci.*, 9(6):1853–2160, 2016.

[29] Martin a. Green, Anita Ho-Baillie, and Henry J. Snaith. The emergence of perovskite solar cells. *Nature Photonics*, 8(7):506–514, jun 2014.

[30] Tomas Leijtens, Kevin Bush, Rongrong Cheacharoen, Rachel Beal, Andrea Bowring, and Michael D. McGehee. Towards enabling stable lead halide perovskite solar cells; interplay between structural, environmental, and thermal stability. *J. Mater. Chem. A*, 5(23):11483–11500, 2017.

[31] Samuel D Stranks, Samuel D Stranks, Giles E Eperon, Giulia Grancini, Christopher Menelaou, Marcelo J P Alcocer, Tomas Leijtens, Laura M Herz, Annamaria Petrozza, and Henry J Snaith. Electron-Hole Diffusion Lengths Exceeding 1Micrometer in an Organometal Trihalide Perovskite Absorber. *Science*, 342(6156):341–344, 2013.

[32] Spencer T Williams, Fan Zuo, Chu-chen Chueh, Chien-yi Liao, Po-wei Liang, and Alex K Jen. Role of Chloride in the Morphological Evolution of Organo-Lead Halide Perovskite Thin Films. *ACS Nano*, 8(10):10640–10654, 2014.

[33] Hui Yu, Feng Wang, Fangyan Xie, Wenwu Li, Jian Chen, and Ni Zhao. The Role of Chlorine in the Formation Process of "CH 3 NH 3 PbI 3-x Cl x " Perovskite. *Advanced Functional Materials*, 24(45):7102–7108, 2014.

[34] M Ibrahim Dar, Neha Arora, Peng Gao, Shahzada Ahmad, Michael Grätzel, and Mohammad Khaja Nazeeruddin. Investigation regarding the role of chloride in organic-inorganic halide perovskites obtained from chloride containing precursors. *Nano Letters*, 14(12):6991–6996, 2014.

[35] Jun Hong Noh, Sang Hyuk Im, Jin Hyuck Heo, Tarak N Mandal, and Sang Il Seok. Chemical management for colorful, efficient, and stable inorganic-organic hybrid nanostructured solar cells. *Nano Letters*, 13(4):1764–1769, 2013.

[36] Carolin M. Sutter-Fella, Yanbo Li, Matin Amani, Joel W. Ager, Francesca M. Toma, Eli Yablonovitch, Ian D. Sharp, and Ali Javey. High Photoluminescence Quantum Yield in Band Gap Tunable Bromide Containing Mixed Halide Perovskites. *Nano Letters*, 16(1):800–806, 2016.

[37] Jun Yin, Hui Qu, Jing Cao, Huiling Tai, Jing Li, and Nanfeng Zheng. Vapor assisted crystallization control toward high performance perovskite photovoltaics with over 18% efficiency in open air. *J. Mater. Chem. A*, 4(34):13203–13210, 2016.

[38] Woon Seok Yang, Jun Hong Noh, Nam Joong Jeon, Young Chan Kim, Seungchan Ryu, Jangwon Seo, and Sang Il Seok. High-performance photovoltaic perovskite layers fabricated through intramolecular exchange. *Science*, 348(6240):1234–1237, jun 2015.

[39] Dong Yang, Zhou Yang, Wei Qin, Yuliang Zhang, Shengzhong Frank Liu, and Can Li. Alternating Precursor Layer Deposition for Highly Stable Perovskite Films Towards Efficient Solar Cells Using Vacuum Deposition. *J. Mater. Chem. A*, 3:9401–9405, 2015.

[40] Xiong Li, Dongqin Bi, Chenyi Yi, Jingshan Luo, Shaik Mohammed Zakeeruddin, and Anders Hagfeldt. A vacuum flash–assisted solution process for high-efficiency large-area perovskite solar cells. *Science*, 353(6294):58–62, 2016.

[41] Yanbo Li, Jason K. Cooper, Raffaella Buonsanti, Cinzia Giannini, Yi Liu, Francesca M. Toma, and Ian D. Sharp. Fabrication of planar heterojunction perovskite solar cells by controlled low-pressure vapor annealing. *Journal of Physical Chemistry Letters*, 6(3):493–499, 2015.

[42] Chang Wen Chen, Hao Wei Kang, Sheng Yi Hsiao, Po Fan Yang, Kai Ming Chiang, and Hao Wu Lin. Efficient and uniform planar-type perovskite solar cells by simple sequential vacuum deposition. *Advanced Materials*, 26(38):6647–6652, oct 2014.

[43] Han Chen, Fei Ye, Wentao Tang, Jinjin He, Maoshu Yin, Yanbo Wang, Fengxian Xie, Enbing Bi, Xudong Yang, Michael Grätzel, and Liyuan Han. A solvent- and vacuum-free route to large-area perovskite films for efficient solar modules. *Nature*, 550(7674):92–95, 2017.

[44] Bert Conings, Aslihan Babayigit, Matthew T. Klug, Sai Bai, Nicolas Gauquelin, Nobuya Sakai, Jacob Tse-Wei Wang, Johan Verbeeck, Hans-Gerd Boyen, and Henry J. Snaith. A Universal Deposition Protocol for Planar Heterojunction Solar Cells with High Efficiency Based on Hybrid Lead Halide Perovskite Families. *Advanced Materials*, pages 1–9, 2016.

[45] Michael Saliba, Taisuke Matsui, Konrad Domanski, Ji Youn Seo, Amita Ummadisingu, Shaik M. Zakeeruddin, Juan Pablo Correa-Baena, Wolfgang R. Tress, Antonio Abate, Anders Hagfeldt, and Michael Grätzel. Incorporation of rubidium cations into perovskite solar cells improves photovoltaic performance. *Science*, 354(6309):206–209, 2016.

[46] Rundong Fan, Yuan Huang, Ligang Wang, Liang Li, Guanhaojie Zheng, and Huanping Zhou. The Progress of Interface Design in Perovskite-Based Solar Cells. *Advanced Energy Materials*, 6(17):1–32, 2016.

[47] Zonglong Zhu, Yang Bai, Xiao Liu, Chu Chen Chueh, Shihe Yang, and Alex K Y Jen. Enhanced Efficiency and Stability of Inverted Perovskite Solar Cells Using Highly Crystalline SnO2 Nanocrystals as the Robust Electron-Transporting Layer. *Advanced Materials*, pages 6478–6484, 2016.

[48] Elham Halvani Anaraki, Ahmad Kermanpur, Ludmilla Steier, Konrad Domanski, Taisuke Matsui, Wolfgang Tress, Michael Saliba, Antonio Abate, Michael Grä, Anders Hagfeldt, and Juan-Pablo Correa-Baena. Highly efficient and stable planar perovskite solar cells by solution-processed tin oxide. *Energy Environ. Sci.*, 3128(9):3128–3134, 2016.

[49] Jingbi You, Lei Meng, Tze-Bin Song, Tzung-Fang Guo, Yang (Michael) Yang, Wei-Hsuan Chang, Ziruo Hong, Huajun Chen, Huanping Zhou, Qi Chen, Yongsheng Liu, Nicholas De Marco, and Yang Yang. Improved air stability of perovskite solar cells via solution-processed metal oxide transport layers. *Nature Nanotechnology*, 11(October):1–8, 2015.

[50] Niraj N. Lal, Yasmina Dkhissi, Wei Li, Qicheng Hou, Yi-Bing Cheng, and Udo Bach. Perovskite Tandem Solar Cells. *Advanced Energy Materials*, 7(18):1602761, 2017.

[51] Steve Albrecht, Michael Saliba, Juan Pablo Correa Baena, Felix Lang, Lukas Kegelmann, Mathias Mews, Ludmilla Steier, Antonio Abate, Joerg Rappich, Lars Korte, Rutger Schlatmann, Nazeeruddin Mohammad K., Anders

Hagfeldt, Michael Grätzel, and Bernd Rech. Monolithic Perovskite/Silicon-Heterojunction Tandem Solar Cells Processed at Low Temperature. *Energy Environ. Sci.*, 9(1):81–88, 2015.

[52] Bo Chen, Yang Bai, Zhengshan Yu, Tao Li, Xiaopeng Zheng, Qingfeng Dong, Liang Shen, Mathieu Boccard, Alexei Gruverman, Zachary Holman, and Jinsong Huang. Efficient Semitransparent Perovskite Solar Cells for 23.0%-Efficiency Perovskite/Silicon Four-Terminal Tandem Cells. *Advanced Energy Materials*, 6(19):1–7, 2016.

[53] The Duong, Yi Liang Wu, Heping Shen, Jun Peng, Xiao Fu, Daniel Jacobs, Er Chien Wang, Teng Choon Kho, Kean Chern Fong, Matthew Stocks, Evan Franklin, Andrew Blakers, Ngwe Zin, Keith McIntosh, Wei Li, Yi Bing Cheng, Thomas P. White, Klaus Weber, and Kylie Catchpole. Rubidium Multication Perovskite with Optimized Bandgap for Perovskite-Silicon Tandem with over 26% Efficiency. *Advanced Energy Materials*, 7(14):1700228, 2017.

[54] Jérémie Werner, Loris Barraud, Arnaud Walter, Matthias Bräuninger, Florent Sahli, Davide Sacchetto, Nicolas Tétreault, Bertrand Paviet-Salomon, Soo-Jin Moon, Christophe Allebé, Matthieu Despeisse, Sylvain Nicolay, Stefaan De Wolf, Bjoern Niesen, and Christophe Ballif. Efficient Near-Infrared-Transparent Perovskite Solar Cells Enabling Direct Comparison of 4-Terminal and Monolithic Perovskite/Silicon Tandem Cells. *ACS Energy Letters*, 1(2):474–480, aug 2016.

[55] Giles E. Eperon, Tomas Leijtens, Kevin A. Bush, Rohit Prasanna, Thomas Green, Jacob Tse-Wei Wang, David P. McMeekin, George Volonakis, Rebecca L Milot, Richard May, Axel Palmstrom, Daniel J. Slotcavage, Rebecca A. Belisle, Jay B. Patel, Elizabeth S. Parrott, Rebecca J. Sutton, Wen Ma, Farhad Moghadam, Bert Conings, Aslihan Babayigit, Hans-Gerd Boyen, Stacey Bent, Feliciano Giustino, Laura M. Herz, Michael B. Johnston, Michael D. McGehee, and Henry J. Snaith. Perovskite-perovskite tandem photovoltaics with optimized band gaps. *Science*, 354(6314):861–865, 2016.

[56] Adharsh Rajagopal, Zhibin Yang, Sae Byeok Jo, Ian L. Braly, Po Wei Liang, Hugh W. Hillhouse, and Alex K.Y. Jen. Highly Efficient Perovskite-Perovskite Tandem Solar Cells Reaching 80% of the Theoretical Limit in Photovoltage. *Advanced Materials*, 29(34):1702140, 2017.

[57] Taame Abraha Berhe, Wei-Nien Su, Ching-Hsiang Chen, Chun-Jern Pan, Ju-Hsiang Cheng, Hung-Ming Chen, Meng-Che Tsai, Liang-Yih Chen, Amare Aregahegn Dubale, and Bing-Joe Hwang. Organometal halide perovskite solar cells: degradation and stability. *Energy Environ. Sci.*, 9(2):323–356, 2016.

[58] Bert Conings, Jeroen Drijkoningen, Nicolas Gauquelin, Aslihan Babayigit, Jan D'Haen, Lien D'Olieslaeger, Anitha Ethirajan, Jo Verbeeck, Jean Manca, Edoardo Mosconi, Filippo De Angelis, and Hans Gerd Boyen. Intrinsic Thermal Instability of Methylammonium Lead Trihalide Perovskite. *Advanced Energy Materials*, 5(15):1–8, 2015.

[59] Zheng Fan, Hai Xiao, Yiliu Wang, Zipeng Zhao, Zhaoyang Lin, Hung-Chieh Cheng, Sung-Joon Lee, Gongming Wang, Ziying Feng, William A. Goddard, Yu Huang, and Xiangfeng Duan. Layer-by-Layer Degradation of Methylammonium Lead Tri-iodide Perovskite Microplates. *Joule*, 1(3):548–562, 2017.

[60] Severin N Habisreutinger, David P. McMeekin, Henry J Snaith, and Robin J. Nicholas. Research Update: Strategies for improving the stability of perovskite solar cells. *APL Materials*, 4(9):091503, sep 2016.

[61] Bart Roose, Karl C. Gödel, Sandeep Pathak, Aditya Sadhanala, Juan Pablo Correa Baena, Bodo D. Wilts, Henry J. Snaith, Ulrich Wiesner, Michael Grätzel, Ullrich Steiner, and Antonio Abate. Enhanced Efficiency and Stability of Perovskite Solar Cells Through Nd-Doping of Mesostructured TiO 2. *Advanced Energy Materials*, 6(2):1501868, jan 2016.

[62] Brian D. Viezbicke, Shane Patel, Benjamin E. Davis, and Dunbar P. Birnie. Evaluation of the Tauc method for optical absorption edge determination: ZnO thin films as a model system. *physica status solidi (b)*, 252(8):1700–1710, aug 2015.

[63] Mario Birkholz. *Thin Film Analysis by X-Ray Scattering.* WILEY-VCH Verlag GmbH & Co. KGaA, 2006.

[64] Ib Chorkendorff and J. W. Niemantsverdriet. *Concepts of modern catalysis and kinetics.* WILEY-VCH Verlag GmbH & Co. KGaA, second edition, 2007.

[65] Danial Abau-ras, Thomas Kirchartz, and Uwe Rau. *Advanced Characterization Techniques for Thin Film Solar Cells.* WILEY-VCH Verlag GmbH & Co. KGaA, 2011.

[66] Harland G. Tompkins and Eugene A. Irene. *Handbook of ellipsometry.* William Andrew publishing, 2005.

[67] Waters. Autospec nt user's guide.

[68] Robert F. Pierret. *Semiconductor device fundamentals.* Addison Wesly Longman, 1996.

[69] Angèle Reinders, Pierre Verlinden, Wilfried van Stark, and Alexandre Freundlich. *Photovoltaic Solar Energy.* Wiley, 2017.

[70] Stuart R. Wenham, Martin A. Green, Murial E. Watt, Richard Corkish, and Alistair Sproul. *Applied photovoltaics.* Earthscan, third edition, 2011.

[71] Günter Sauerbrey. Verwendung von Schwingquarzen zur Wägung dünner Schichten und zur Mikrowägung. *Zeitschrift für Physik*, 155(2):206–222, 1959.

[72] Stanford Reasearch Systems. Qcm100- quartz crystal microbalance theory and calibration.

[73] F. M. Smits. Measurement of sheet resistivities with the four-point probe. *Bell System Technical Journal*, 37(3):711–718, 1958.

[74] Irving Langmuir. The Vapor Pressure of Metallic Tungsten. *Physical Review*, 2(5):329–342, nov 1913.

[75] Amalie Dualeh, Peng Gao, Sang Il Seok, Mohammad Khaja Nazeeruddin, and Michael Grätzel. Thermal Behavior of Methylammonium Lead-Trihalide Perovskite Photovoltaic Light Harvesters. *Chemistry of Materials*, 26(21):6160–6164, nov 2014.

[76] Riikka L. Puurunen. Surface chemistry of atomic layer deposition: A case study for the trimethylaluminum/water process. *Journal of Applied Physics*, 97(12):121301, jun 2005.

[77] David B. Hall, Patrick Underhill, and John M. Torkelson. Spin coating of thin and ultrathin polymer films. *Polymer Engineering and Science*, 38(12):2039–2045, 1998.

[78] Qi Chen, Huanping Zhou, Ziruo Hong, Song Luo, Hsin-sheng Duan, and Hsinhua Wang. Planar heterojunction perovskite solar cells via vapor assisted solution process. *Journal of the American Chemical Society*, 136(2):622–625, 2014.

[79] Dowon Bae, Seyedmohammad Shayestehaminzadeh, Einar B. Thorsteinsson, Thomas Pedersen, Ole Hansen, Brian Seger, Peter C K Vesborg, Sveinn Ólafsson, and Ib Chorkendorff. Protection of Si photocathode using TiO2 deposited by high power impulse magnetron sputtering for H2 evolution in alkaline media. *Solar Energy Materials and Solar Cells*, 144:758–765, 2016.

[80] Kevin A. Bush, Colin D. Bailie, Ye Chen, Andrea R. Bowring, Wei Wang, Wen Ma, Tomas Leijtens, Farhad Moghadam, and Michael D. McGehee. Thermal and Environmental Stability of Semi-Transparent Perovskite Solar Cells for Tandems Enabled by a Solution-Processed Nanoparticle Buffer Layer and Sputtered ITO Electrode. *Advanced Materials*, 28(20):3937–3943, 2016.

[81] Matthew R. Leyden, Luis K. Ono, Sonia R. Raga, Yuichi Kato, Shenghao Wang, and Yabing Qi. High Performance Perovskite Solar Cells by Hybrid Chemical Vapor Deposition. *J. Mater. Chem. A*, 2(44):18742–18745, sep 2014.

[82] Matthew R. Leyden, Yan Jiang, and Yabing Qi. Chemical Vapor Deposition Grown Formamidinium Perovskite Solar Modules with High Steady State Power and Thermal Stability. *Journal of Materials Chemistry A*, 4(34):13203–13210, 2016.

[83] Yan Jiang, Matthew R. Leyden, Longbin Qiu, Shenghao Wang, Luis K. Ono, Zhifang Wu, Emilio J. Juarez-Perez, and Yabing Qi. Combination of Hybrid CVD and Cation Exchange for Upscaling Cs-Substituted Mixed Cation Perovskite Solar Cells with High Efficiency and Stability. *Advanced Functional Materials*, 28(1), 2017.

[84] Duyen H. Cao, Constantinos C. Stoumpos, Christos D. Malliakas, Michael J. Katz, Omar K. Farha, Joseph T. Hupp, and Mercouri G. Kanatzidis. Remnant PbI2, an unforeseen necessity in high-efficiency hybrid perovskite-based solar cells? *APL Materials*, 2(9):1–8, 2014.

[85] Qi Chen, Huanping Zhou, Tze Bin Song, Song Luo, Ziruo Hong, Hsin Sheng Duan, Letian Dou, Yongsheng Liu, and Yang Yang. Controllable self-induced passivation of hybrid lead iodide perovskites toward high performance solar cells. *Nano Letters*, 14(7):4158–4163, 2014.

[86] Lili Wang, Christopher McCleese, Anton Kovalsky, Yixin Zhao, and Clemens Burda. Femtosecond Time-Resolved Transient Absorption Spectroscopy of CH3NH3Pb3 Perovskite Films: Evidence for Passivation Effect of PbI2. *Journal of the American Chemical Society*, 136(35):12205–12208, 2014.

[87] Fangzhou Liu, Qi Dong, Man Kwong Wong, Aleksandra B. Djurišić, Annie Ng, Zhiwei Ren, Qian Shen, Charles Surya, Wai Kin Chan, Jian Wang, Alan Man Ching Ng, Changzhong Liao, Hangkong Li, Kaimin Shih, Chengrong Wei, Huimin Su, and Junfeng Dai. Is Excess PbI2 Beneficial for Perovskite Solar Cell Performance? *Advanced Energy Materials*, 6(7):1–9, 2016.

[88] Zafer Hawash, Luis K. Ono, and Yabing Qi. Photovoltaics: Moisture and Oxygen Enhance Conductivity of LiTFSI-Doped Spiro-MeOTAD Hole Transport Layer in Perovskite Solar Cells (Adv. Mater. Interfaces 13/2016). *Advanced Materials Interfaces*, 3(13):1–6, 2016.

[89] Rongrong Cheacharoen, Nicholas John Rolston, Duncan Harwood, Kevin Alexander Bush, Reinhold H. Dauskardt, and Michael D. McGehee. Design and understanding of encapsulated perovskite solar cells to withstand temperature cycling. *Energy Environ. Sci.*, 11:144–150, 2017.

[90] Jong Hoon Park, Jangwon Seo, Sangman Park, Seong Sik Shin, Young Chan Kim, Nam Joong Jeon, Hee Won Shin, Tae Kyu Ahn, Jun Hong Noh, Sung Cheol Yoon, Cheol Seong Hwang, and Sang Il Seok. Efficient CH3NH3PbI3 Perovskite Solar Cells Employing Nanostructured p-Type NiO Electrode Formed by a Pulsed Laser Deposition. *Advanced Materials*, 27(27):4013–4019, 2015.

[91] Jong H. Kim, Po Wei Liang, Spencer T. Williams, Namchul Cho, Chu Chen Chueh, Micah S. Glaz, David S. Ginger, and Alex K Y Jen. High-performance and environmentally stable planar heterojunction perovskite solar cells based on a solution-processed copper-doped nickel oxide hole-transporting layer. *Advanced Materials*, 27(4):695–701, 2015.

[92] Yuchuan Shao, Yongbo Yuan, and Jinsong Huang. Correlation of energy disorder and open-circuit voltage in hybrid perovskite solar cells. *Nature Energy*, 1(1):15001, 2016.

[93] Tanghao Liu, Ke Chen, Qin Hu, Rui Zhu, and Qihuang Gong. Inverted Perovskite Solar Cells: Progresses and Perspectives. *Advanced Energy Materials*, 6(17):1–17, 2016.

[94] Konrad Domanski, Juan Pablo Correa-Baena, Nicolas Mine, Mohammad Khaja Nazeeruddin, Antonio Abate, Michael Saliba, Wolfgang Tress, Anders Hagfeldt, and Michael Grätzel. Not All That Glitters Is Gold: Metal-Migration-Induced Degradation in Perovskite Solar Cells. *ACS Nano*, 10(6):6306–6314, 2016.

[95] Weibo Yan, Senyun Ye, Yunlong Li, Weihai Sun, Haixia Rao, Zhiwei Liu, Zuqiang Bian, and Chunhui Huang. Hole-Transporting Materials in Inverted Planar Perovskite Solar Cells. *Advanced Energy Materials*, 6(17):1–20, 2016.

[96] Jin Hyuck Heo, Hye Ji Han, Dasom Kim, Tae Kyu Ahn, and Sang Hyuk Im. Hysteresis-less inverted CH3NH3PbI3 planar perovskite hybrid solar cells with 18.1% power conversion efficiency. *Energy Environ. Sci.*, 8(5):1602–1608, 2015.

[97] Brian Seger, David S. Tilley, Thomas Pedersen, Peter C. K. Vesborg, Ole Hansen, Michael Grätzel, and Ib Chorkendorff. Silicon protected with atomic layer deposited TiO2: durability studies of photocathodic H2 evolution. *RSC Advances*, 3(48):25902, 2013.

[98] In Soo Kim, Richard T. Haasch, Duyen H. Cao, Omar K. Farha, Joseph T. Hupp, Mercouri G. Kanatzidis, and Alex B.F. Martinson. Amorphous TiO2 Compact Layers via ALD for Planar Halide Perovskite Photovoltaics. *ACS Applied Materials and Interfaces*, 8(37):24310–24314, 2016.

[99] Yongzhen Wu, Xudong Yang, Han Chen, Kun Zhang, Chuanjiang Qin, Jian Liu, Wenqin Peng, Ashraful Islam, Enbing Bi, Fei Ye, Maoshu Yin, Peng Zhang, and Liyuan Han. Highly compact TiO2 layer for efficient hole-blocking in perovskite solar cells. *Applied Physics Express*, 7(5):052301, 2014.

[100] In Soo Kim, Duyen H. Cao, D. Bruce Buchholz, Jonathan D. Emery, Omar K. Farha, Joseph T. Hupp, Mercouri G. Kanatzidis, and Alex B. F. Martinson. Liquid Water- and Heat-Resistant Hybrid Perovskite Photovoltaics via an Inverted ALD Oxide Electron Extraction Layer Design. *Nano Letters*, 16(12):7786–7790, 2016.

[101] Chunyan Jin, Ben Liu, Zhongxiang Lei, and Jiaming Sun. Structure and photoluminescence of the TiO2 films grown by atomic layer deposition using tetrakis-dimethylamino titanium and ozone. *Nanoscale Research Letters*, 10(1):95, 2015.

[102] Rajesh Katamreddy, Vincent Omarjee, Benjamin Feist, and Christian Dussarrat. Ti Source Precursors for Atomic Layer Deposition of TiO2, STO and BST. *ECS Transactions*, 16(4):113–122, 2008.

[103] Wolfgang Tress, Nevena Marinova, Thomas Moehl, Shaik M. Zakeeruddin, Nazeeruddin Khaja Mohammad, and Michael Grätzel. Understanding the rate-dependent J–V hysteresis, slow time component, and aging in CH 3 NH 3 PbI 3 perovskite solar cells: the role of a compensated electric field. *Energy Environ. Sci.*, 8(3):995–1004, 2015.

[104] Eric W. McFarland and Jing Tang. A photovoltaic device structure based on internal electron emission. *Nature*, 421(6923):616–618, 2003.

[105] N. Szydlo and R. Poirier. I-V and C-V characteristics of Au/TiO2 Schottky diodes. *Journal of Applied Physics*, 51(6):3310–3312, 1980.

[106] In Soo Kim and Alex B. F. Martinson. Stabilizing hybrid perovskites against moisture and temperature via non-hydrolytic atomic layer deposited overlayers. *J. Mater. Chem. A*, 3(40):20092–20096, 2015.

[107] Achilleas Savva, Ignasi Burgues-Ceballos, and Stelios A. Choulis. Improved Performance and Reliability of p-i-n Perovskite Solar Cells via Doped Metal Oxides. *Advanced Energy Materials*, 6(18):1–8, 2016.

[108] Changduk Yang, Jin Young Kim, Shinuk Cho, Jae Kwan Lee, Alan J Heeger, and Fred Wudl. Functionalized Methanofullerenes Used as n-Type Materials in Bulk-Heterojunction Polymer Solar Cells and in Field-Effect Transistors. *Journal of the American Chemical Society*, 130(20):6444–6450, 2008.

[109] Hobeom Kim, Kyung-Geun Lim, and Tae-Woo Lee. Planar heterojunction organometal halide perovskite solar cells: roles of interfacial layers. *Energy Environ. Sci.*, 9(1):12–30, 2016.

[110] Wei Chen, Yongzhen Wu, Jian Liu, Chuanjiang Qin, Xudong Yang, Ashraful Islam, Yi-Bing Cheng, and Liyuan Han. Hybrid interfacial layer leads to solid performance improvement of inverted perovskite solar cells. *Energy Environ. Sci.*, 8(2):629–640, 2015.

[111] Da-Xing Yuan, Xiao-Dong Yuan, Qing-Yang Xu, Mei-Feng Xu, Xiao-Bo Shi, Zhao-Kui Wang, and Liang-Sheng Liao. A solution-processed bathocuproine cathode interfacial layer for high-performance bromine–iodine perovskite solar cells. *Phys. Chem. Chem. Phys.*, 17:26653–26658, 2015.

[112] Heetae Yoon, Seong Min Kang, Jong-Kwon Lee, and Mansoo Choi. Hysteresis-free low-temperature-processed planar perovskite solar cells with 19.1% efficiency. *Energy Environ. Sci.*, 9(7):2262–2266, 2016.

[113] Lei Meng, Jingbi You, Tzung Fang Guo, and Yang Yang. Recent Advances in the Inverted Planar Structure of Perovskite Solar Cells. *Accounts of Chemical Research*, 49(1):155–165, 2016.

[114] F. Reinert, P. Steiner, S. Hüfner, H. Schmitt, J. Fink, M. Knupfer, P. Sandl, and E. Bertel. Electron and hole doping in NiO. *Zeitschrift für Physik B Condensed Matter*, 97(1):83–93, mar 1995.

[115] Guangda Niu, Siyu Wang, Jiangwei Li, Wenzhe Li, and Liduo Wang. Oxygen doping in nickel oxide for high efficient planar perovskite solar cells. *Journal of Materials Chemistry A*, 2018.

[116] M. Thirumoorthi and J. Thomas Joseph Prakash. Structure, optical and electrical properties of indium tin oxide ultra thin films prepared by jet nebulizer spray pyrolysis technique. *Journal of Asian Ceramic Societies*, 4(1):124–132, 2016.

[117] C. Guillén and J. Herrero. Influence of oxygen in the deposition and annealing atmosphere on the characteristics of ITO thin films prepared by sputtering at room temperature. *Vacuum*, 80(6):615–620, 2006.

[118] Karl A. Walczak, Gideon Segev, David M. Larson, Jeffrey W. Beeman, Frances A. Houle, and Ian D. Sharp. Hybrid Composite Coatings for Durable and Efficient Solar Hydrogen Generation under Diverse Operating Conditions. *Advanced Energy Materials*, 7(13), 2017.

[119] Luis K. Ono, Matthew R. Leyden, Shenghao Wang, and Yabing Qi. Organometal Halide Perovskite Thin Films and Solar Cells by Vapor Deposition. *J. Mater. Chem. A*, 4(18):6693–6713, 2016.

[120] Sheng Yi Hsiao, Hong Lin Lin, Wei Hung Lee, Wei Lun Tsai, Kai Ming Chiang, Wei Yu Liao, Chen Zheng Ren-Wu, Chien Yu Chen, and Hao Wu Lin. Efficient All-Vacuum Deposited Perovskite Solar Cells by Controlling Reagent Partial Pressure in High Vacuum. *Advanced Materials*, 28(32):7013–7019, 2016.

[121] Luis K. Ono, Shenghao Wang, Yuichi Kato, Sonia R. Raga, and Yabing Qi. Fabrication of semi-transparent perovskite films with centimeter-scale superior uniformity by the hybrid deposition method. *Energy Environ. Sci.*, 7(12):3989–3993, 2014.

[122] Joël Teuscher, Alexey Ulianov, Othmar Müntener, Michael Grätzel, and Nicolas Tétreault. Control and Study of the Stoichiometry in Evaporated Perovskite Solar Cells. *ChemSusChem*, 8(22):3847–3852, 2015.

[123] Y.-K. Kim, K.K. Irikura, M.E. Rudd, M.A. Ali, P.M. Stone, J. Chang, J.S. Coursey, R.A. Dragoset, A.R. Kishore, K.J. Olsen, A.M. Sansonetti, G.G. Wiersma, D.S. Zucker, and M.A. Zucker. Electron-impact cross sections for ionization and excitation database, December 2017.

[124] NIST Mass Spec Data Center and S.E. Stein. Mass spectra in nist chemistry webbook, nist standard reference database number 69, eds. p.j. linstrom and w.g. mallard, national institute of standards and technology, gaithersburg md, 20899 doi:10.18434/t4d303, December 2017.

[125] David P. Nenon, Jeffrey A. Christians, Lance M. Wheeler, Jeffrey L. Blackburn, Erin M. Sanehira, Benjia Dou, Michele L. Olsen, Kai Zhu, Joseph J. Berry, and Joseph M. Luther. Structural and chemical evolution of methylammonium lead halide perovskites during thermal processing from solution. *Energy & Environmental Science*, 9(6):2072–2082, 2016.

[126] Emilio J. Juarez-Perez, Zafer Hawash, Sonia R. Raga, Luis K. Ono, and Yabing Qi. Thermal degradation of CH 3 NH 3 PbI 3 perovskite into NH 3 and CH 3 I gases observed by coupled thermogravimetry–mass spectrometry analysis. *Energy Environ. Sci.*, 9(11):3406–3410, 2016.

[127] Rebecca J. Sutton, Giles E. Eperon, Laura Miranda, Elizabeth S. Parrott, Brett A. Kamino, Jay B. Patel, Maximilian T. Hörantner, Michael B. Johnston, Amir Abbas Haghighirad, David T. Moore, and Henry J. Snaith. Bandgap-Tunable Cesium Lead Halide Perovskites with High Thermal Stability for Efficient Solar Cells. *Advanced Energy Materials*, 6(8):1–6, 2016.

Appendix A
Supporting calculations

A.1 Depletion of $PbCl_2$ from QCM experiments

To calculate how much $PbCl_2$ one expect to remain on the QCM crystals one must look at the chemical reaction involved in the $CH_3NH_3PbI_{(3-x)}Cl_x$ formation. As mentioned earlier it is commonly believed that the amount of Cl left in the final structure is very small [32–34]. The resultant reaction thus becomes

$$3CH_3NH_3I + PbCl_2 \rightarrow CH_3NH_3PbI_3 + 2CH_3NH_3Cl. \tag{A.1.1}$$

As dictated by the equation one must supply 3 times more MAI than $PbCl_2$ to achieve a full conversion. Given that 20 nm of $PbCl_2$ was deposited one can calculate the amount supplied, Δm_{PbCl_2}, by using that the density of $PbCl_2$ is 5.85 $\frac{g}{cm^3}$. This yields

$$\Delta m_{PbCl_2} = 20 \times 10^{-7}\text{cm} \times 5.85\ \frac{g}{cm^3} = 1.17 \times 10^4\ \frac{ng}{cm^3}. \tag{A.1.2}$$

In the case that all the $PbCl_2$ is converted into perovskite and the MACl reevaporates, one can estimate the resultant mass per area by using that it is given by

$$\left(\frac{M_{CH_3NH_3PbI_3}}{M_{PbCl_2}} - 1\right) \times \Delta m_{PbCl_2}, \tag{A.1.3}$$

where $M_{CH_3NH_3PbI_3}$ and M_{PbCl_2} are the molar masses of $CH_3NH_3PbI_3$ and $PbCl_2$, respectively. This yields

$$\left(\frac{620\ \frac{g}{mol}}{278\ \frac{g}{mol}} - 1\right) \times 1.17 \times 10^4\ \frac{ng}{cm^2} = 1.44 \times 10^4\ \frac{ng}{cm^2}. \tag{A.1.4}$$

To estimate the maximum mass per area that has been deposited in the experiment one can use that a frequency change of -405 Hz was observed in the 65 °C case as seen in Figure 4.5b. From equations (2.7.1) and (2.7.2) one gets

$$\Delta m = -\frac{\Delta f}{C_f} = -\frac{\Delta f}{8.15 \times 10^7 \ \frac{\text{cm}^2 \ \text{Hz}}{\text{g}}}, \tag{A.1.5}$$

which yields

$$\Delta m = \frac{405 \text{ Hz}}{8.15 \times 10^7 \ \frac{\text{cm}^2 \ \text{Hz}}{\text{g}}} = 4.97 \times 10^3 \ \frac{\text{ng}}{\text{cm}^2}. \tag{A.1.6}$$

Since the deposited mass per area is much lower than what is needed for full conversion this cannot be the case. Should this have been the case the $PbCl_2$ film thickness would have to be no more than 6.90 nm thick which is unlikely.

A.2 MAI sticking coefficient calculations

As explained one can estimate the sticking coefficient, S_c, by assuming that an exposure of one Langmuir (i.e. a pressure of 1.33×10^{-4} Pa for 1 s) yields a deposition of 1 monolayer if $S_c = 1$. The exposure scales with pressure which means that a pressure of 1.33×10^{-3} will correspond to a deposition rate of 10 monolayers per second. Assuming that 1 monolayer has a thickness of about 0.3 nm the deposition rate at 10 Langmuir is 3 nm/s. The chamber pressure of a typical QCM experiment is shown in Figure A.1. From the figure it is clear that the partial pressure associated with MAI is around 2.6×10^{-3} Pa when the pressure stabilizes, thus yielding an expected deposition rate of 6 nm/s. The deposited mass per area can be calculated by

$$\Delta m = rtS_C\rho_{\text{MAI}}, \tag{A.2.1}$$

where r is the depoaition rate, t is the deposition time and ρ_{MAI} is the density of MAI. Assuming that $S_c = 1$ and using that $\rho_{\text{MAI}} = 2.22 \ \frac{\text{g}}{\text{cm}^3}$ [119] while t, from Figure A.1, is approximately 11,000 s one gets

$$\Delta m = 6 \times 10^{-7} \text{ cm/s} \times 11000 \text{ s} \times 2.22 \ \frac{\text{g}}{\text{cm}^3} = 1.47 \times 10^7 \ \frac{\text{ng}}{\text{cm}^2}. \tag{A.2.2}$$

The amount of MAI that sticks to the QCM can be found from equation (A.1.5) and the observed frequency changes of -405 Hz, -360 Hz and -250 Hz in the 65 °C, 75 °C and 85 °C case, respectively. This yields

$$\Delta m_{65 \ ^\circ\text{C}} = 4.97 \times 10^3 \ \frac{\text{ng}}{\text{cm}^2}, \ \Delta m_{75 \ ^\circ\text{C}} = 4.42 \times 10^3 \ \frac{\text{ng}}{\text{cm}^2} \tag{A.2.3}$$

and

$$\Delta m_{85 \ ^\circ\text{C}} = 3.07 \times 10^3 \ \frac{\text{ng}}{\text{cm}^2}. \tag{A.2.4}$$

The resultant sticking coefficients thus become

$$S_{c,65\ ^\circ\mathrm{C}} = 3.4 \times 10^{-4},\ S_{c,75\ ^\circ\mathrm{C}} = 3.0 \times 10^{-4} \tag{A.2.5}$$

and

$$S_{c,85\ ^\circ\mathrm{C}} = 2.1 \times 10^{-4}. \tag{A.2.6}$$

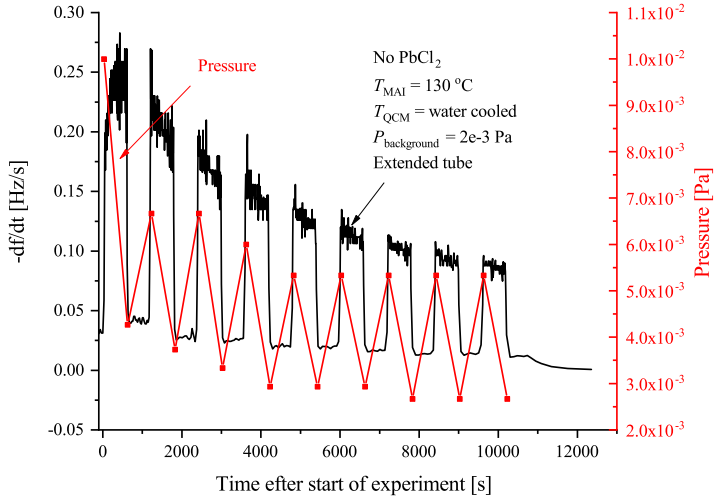

Figure A.1: The pressure recorded during as typical QCM experiment. The pressure measurements were conducted when the shutter was opened. T_{MAI} is the evaporation temperature, T_{QCM} is the temperature of the QCM while $P_{\mathrm{background}}$ is the background pressure. In all cases the signals were chopped in 10 min intervals using the shutter.

A.3 MAI desorption rate from perovkite

The film thickness T is related to the change in mass per area, Δm, by

$$T = \frac{\Delta m}{\rho}, \tag{A.3.1}$$

where ρ is the density of the film being deposited. The rate of film loss becomes

$$r_d = \frac{dT}{dt} \simeq \frac{1}{\rho}\frac{\Delta m}{\Delta t}, \tag{A.3.2}$$

where Δt is the time over which the the mass per area change occurs. Inserting equations (2.7.1) yields

$$r_d = \frac{1}{\rho C_f}\frac{\Delta f}{\Delta t}, \tag{A.3.3}$$

where the minus have been omitted since r_d is a rate of loss. Inserting equation (2.7.2), $\rho = 2.22\ \frac{\mathrm{g}}{\mathrm{cm}^3}$ as well as the appropriate Δf and Δt one arrives at

$$r_{d,85\ ^\circ\mathrm{C}} = 2.44 \times 10^{-4}\ \mathrm{nm/s}, \tag{A.3.4}$$

and

$$r_{d,102\ ^\circ\mathrm{C}} = 1.42 \times 10^{-3}\ \mathrm{nm/s}, \tag{A.3.5}$$

Appendix B

Additional figures for chapter 3

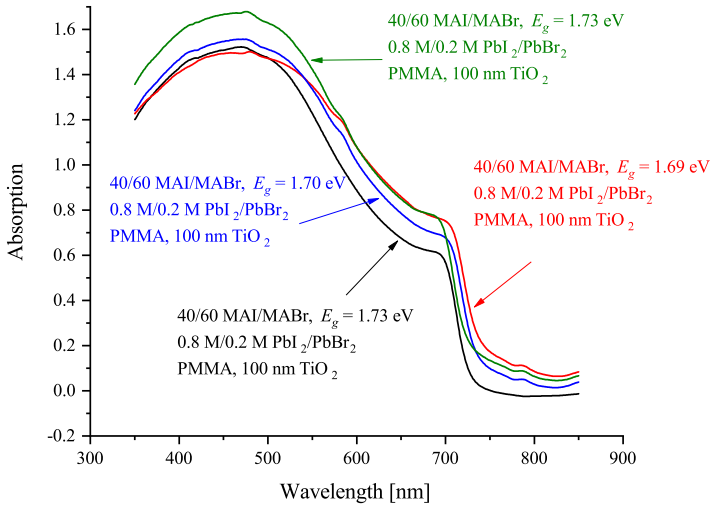

Figure B.1: The absorption spectra of the 4 additional 40/60 MAI/MABr perovskite samples. The band gaps were estimated using the Tauc plot method and in all cases the films were covered by a layer of PMMA to increase their resistance to moisture. The films were deposited on glass substrates coated with 100 nm of TiO_2.

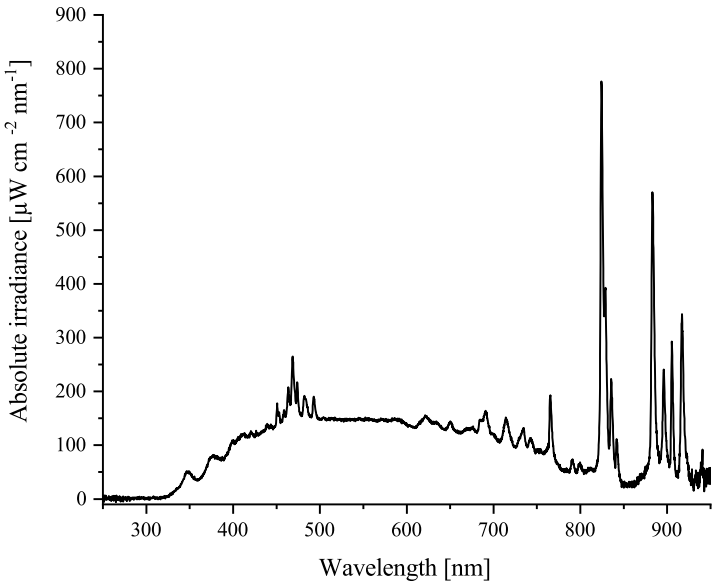

Figure B.2: An example of the calibrated Xe lamp spectrum using a AM1.5 filter. The spectrum was calibrated so that the intensity was 68.4 mW/cm^2 between 300 and 900 nm.

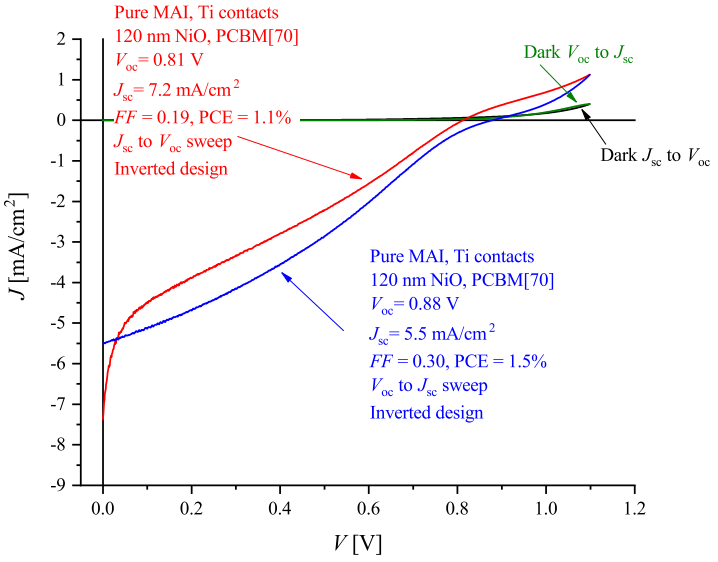

Figure B.3: The full J-V curves of the initial device using Ti contacts seen in Figure 3.18a. J_{sc} is the short circuit current density, V_{oc} is the open circuit potential, FF is the fill factor and PCE is the power conversion efficiency.

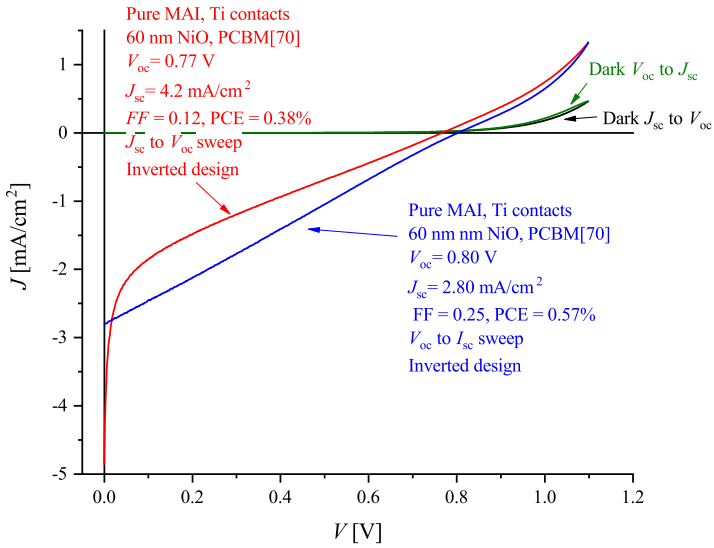

Figure B.4: The full J-V curves of the initial device using a NiO layer seen in Figure 3.18b. J_{sc} is the short circuit current density, V_{oc} is the open circuit potential, FF is the fill factor and PCE is the power conversion efficiency.

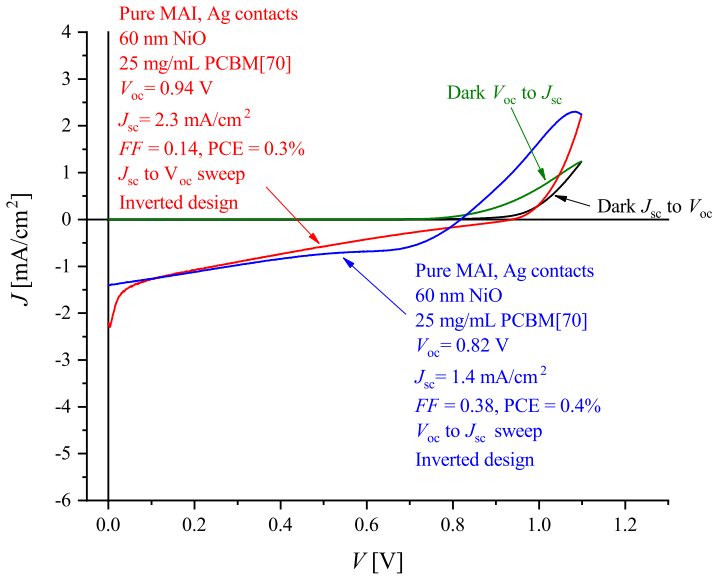

Figure B.5: The full J-V curves of the device using a PCBM[70] concentration of 25 mg/mL. J_{sc} is the short circuit current density, V_{oc} is the open circuit potential, FF is the fill factor and PCE is the power conversion efficiency.

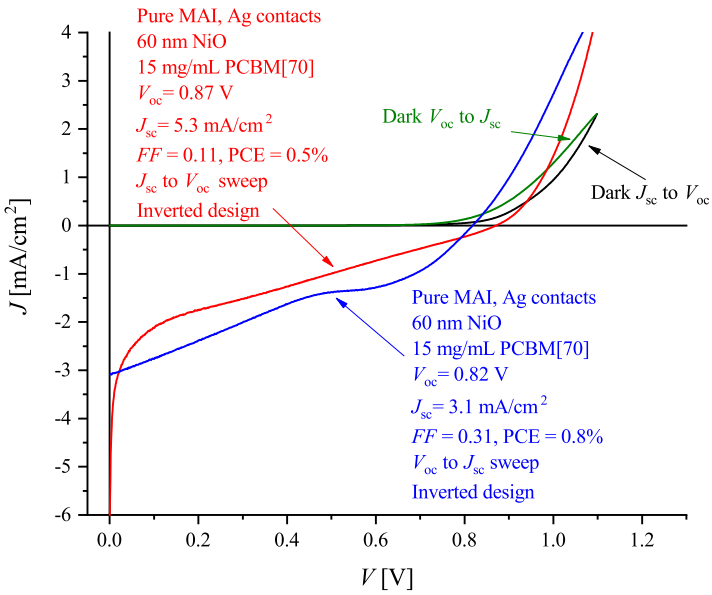

Figure B.6: The full J-V curves of the device using a PCBM[70] concentration of 15 mg/mL. J_{sc} is the short circuit current density, V_{oc} is the open circuit potential, FF is the fill factor and PCE is the power conversion efficiency.

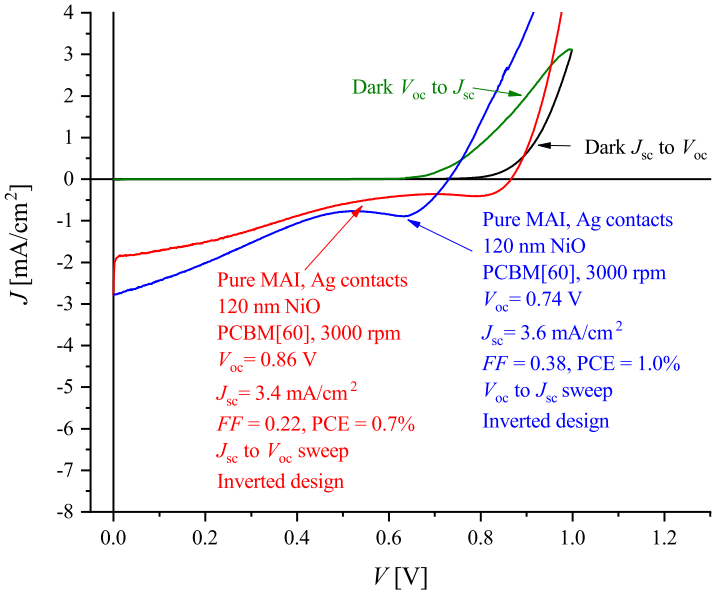

Figure B.7: The full J-V curves of the device using a spin speed of 3000 rpm when depositing the PCBM[60]. J_{sc} is the short circuit current density, V_{oc} is the open circuit potential, FF is the fill factor and PCE is the power conversion efficiency.

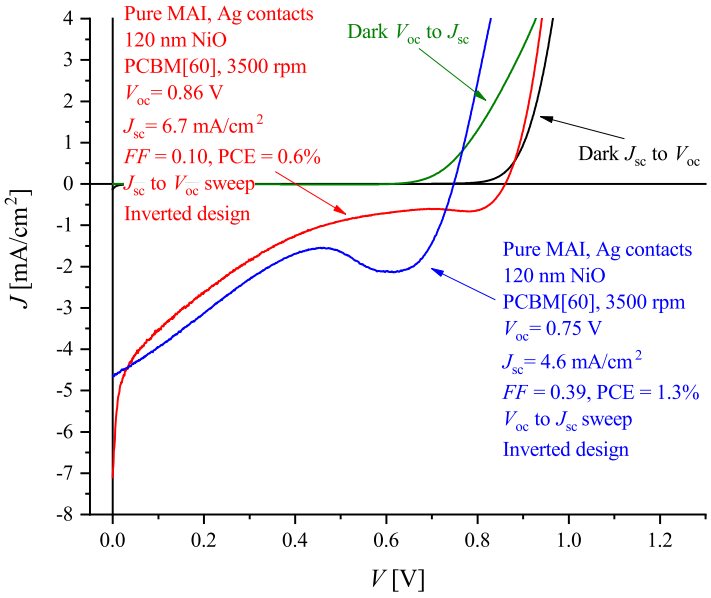

Figure B.8: The full J-V curves of the device using a spin speed of 3500 rpm when depositing the PCBM[60]. J_{sc} is the short circuit current density, V_{oc} is the open circuit potential, FF is the fill factor and PCE is the power conversion efficiency.

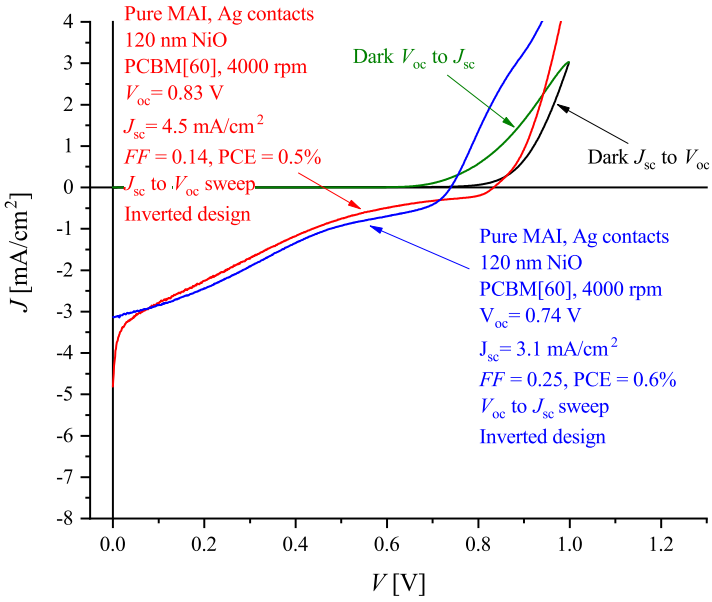

Figure B.9: The full J-V curves of the device using a spin speed of 4000 rpm when depositing the PCBM[60]. J_{sc} is the short circuit current density, V_{oc} is the open circuit potential, FF is the fill factor and PCE is the power conversion efficiency.

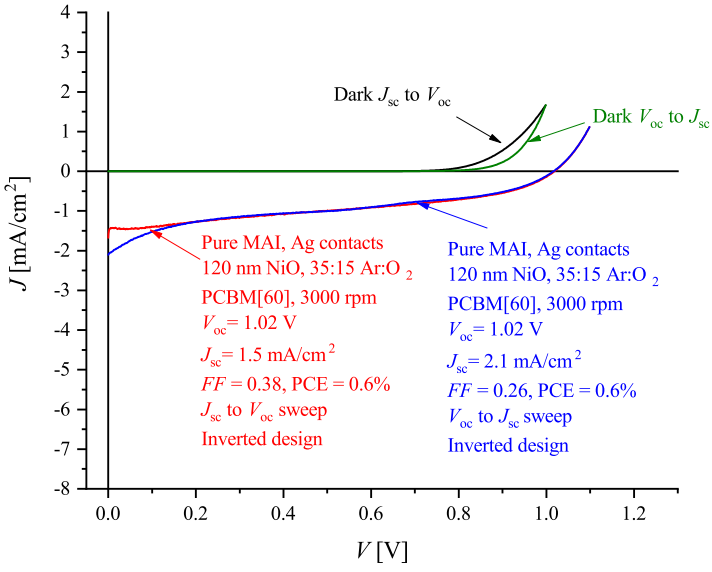

Figure B.10: The full J-V curves of the device using a 35:15 Ar:O_2 ratio when depositing the NiO. J_{sc} is the short circuit current density, V_{oc} is the open circuit potential, FF is the fill factor and PCE is the power conversion efficiency.

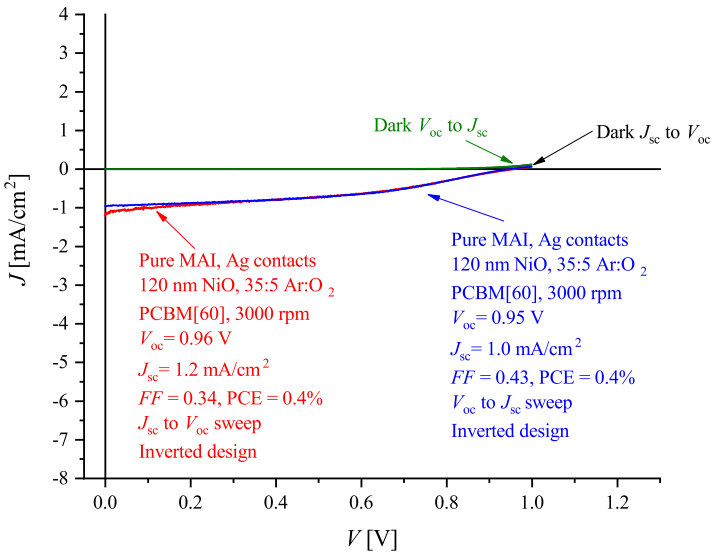

Figure B.11: The full J-V curves of the device using a 35:5 Ar:O_2 ratio when depositing the NiO. J_{sc} is the short circuit current density, V_{oc} is the open circuit potential, FF is the fill factor and PCE is the power conversion efficiency.

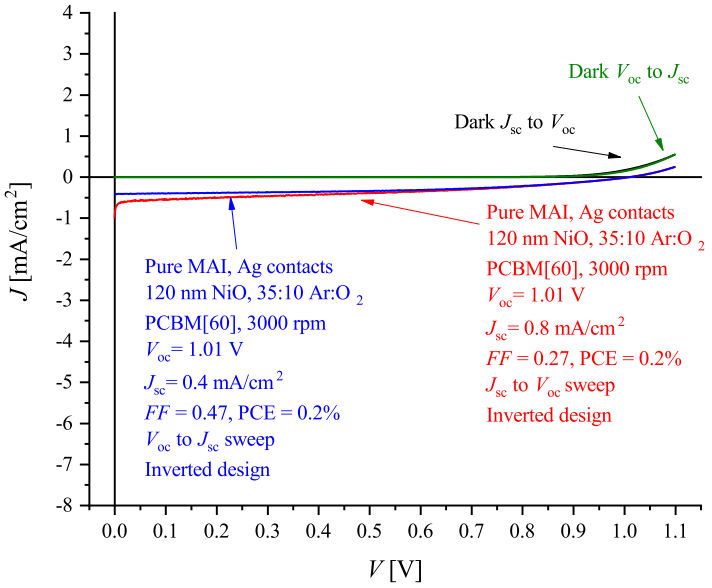

Figure B.12: The full J-V curves of the device using a 35:10 Ar:O_2 ratio when depositing the NiO. J_{sc} is the short circuit current density, V_{oc} is the open circuit potential, FF is the fill factor and PCE is the power conversion efficiency.

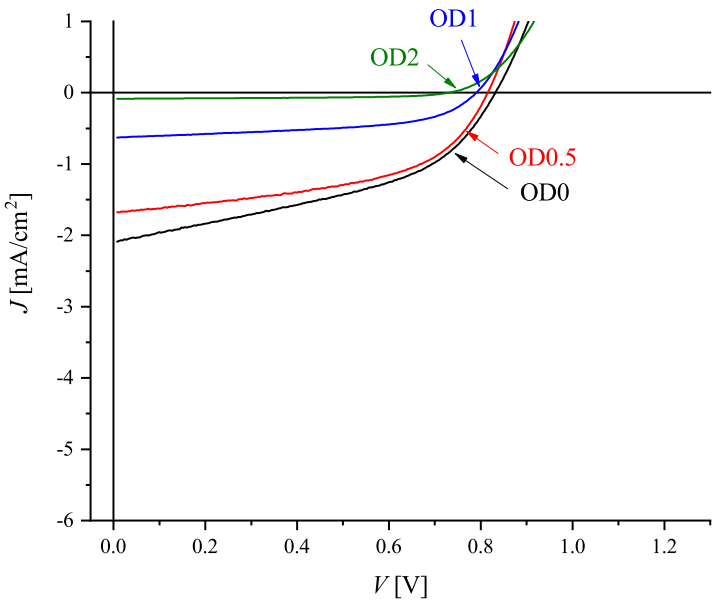

Figure B.13: The unscaled return J-V curves of the light intensity experiments.

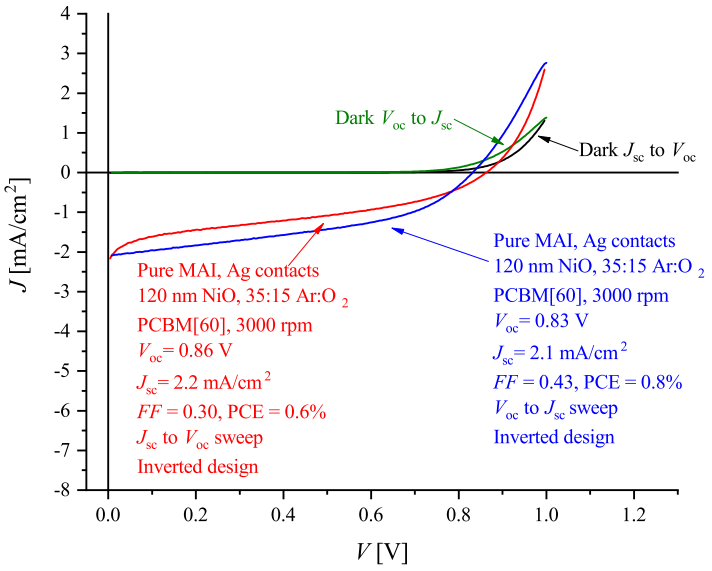

Figure B.14: The full J-V OD0 curves of the light intensity experiments. The area of the cell was defined by the back contact. J_{sc} is the short circuit current density, V_{oc} is the open circuit potential, FF is the fill factor and PCE is the power conversion efficiency.

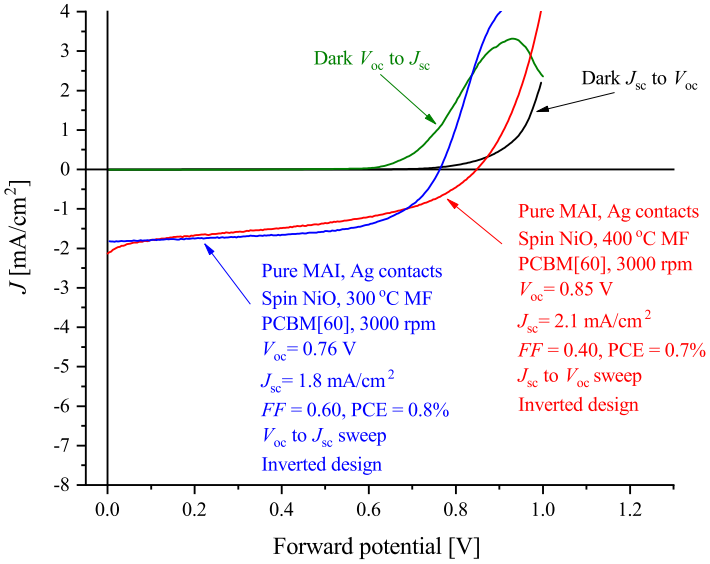

Figure B.15: The full J-V curves of the spin coated NiO annealing experiments using 300 °C on a hotplate. J_{sc} is the short circuit current density, V_{oc} is the open circuit potential, FF is the fill factor and PCE is the power conversion efficiency.

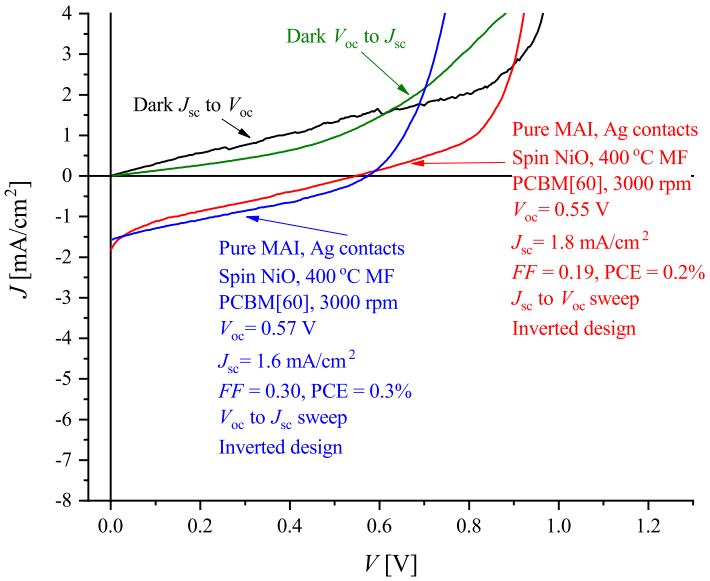

Figure B.16: The full J-V curves of the spin coated NiO annealing experiments using 400 °C in a muffle furnace. J_{sc} is the short circuit current density, V_{oc} is the open circuit potential, FF is the fill factor and PCE is the power conversion efficiency.

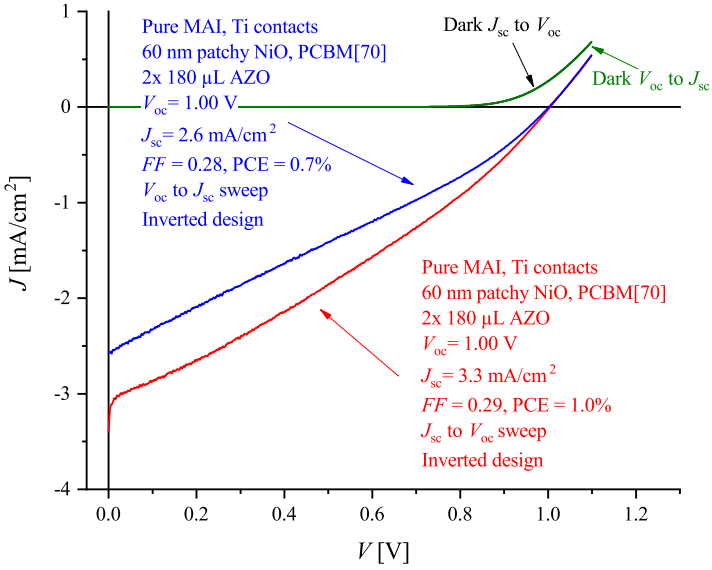

Figure B.17: The full J-V curves of the AZO experiment using 2×180 μL. J_{sc} is the short circuit current density, V_{oc} is the open circuit potential, FF is the fill factor and PCE is the power conversion efficiency.

Appendix C

Additional figures for chapter 4

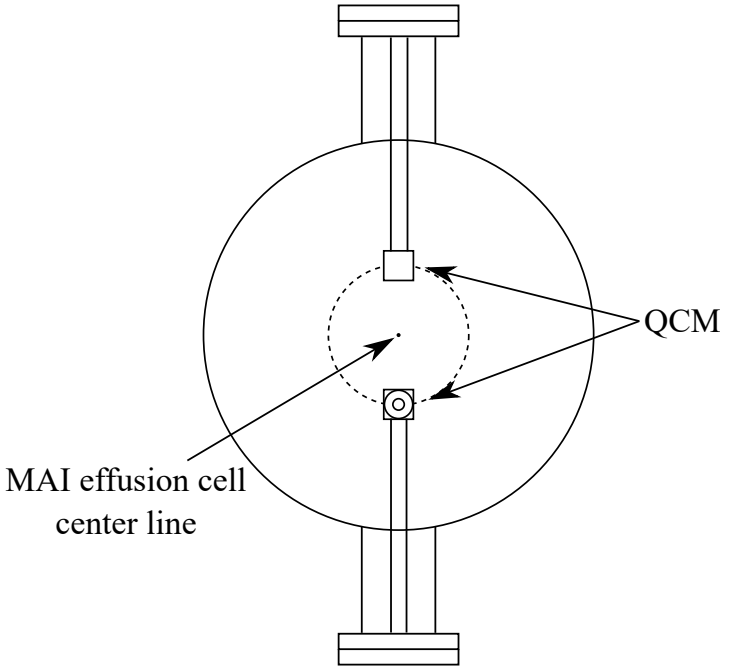

Figure C.1: Schematic drawing of the QCM set up seen from another angle.

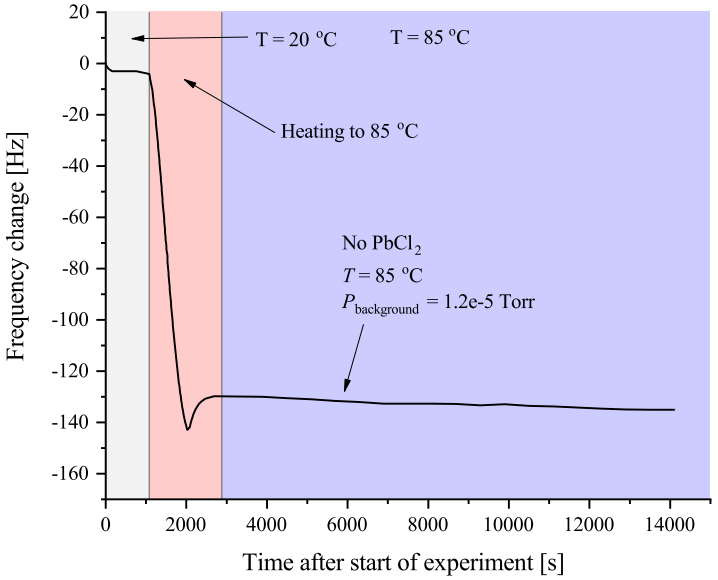

Figure C.2: Frequency change associated with the heating protocol when heating to 85 °C using a blank crystal. $P_{\text{background}}$ is the background pressure.

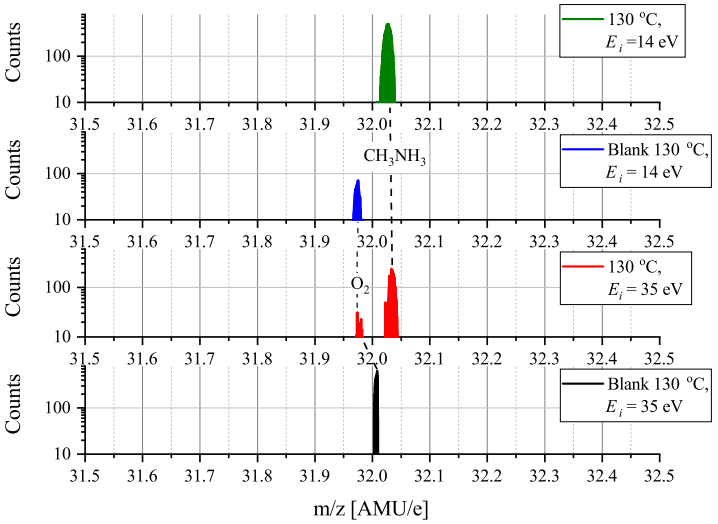

Figure C.3: Zoomed in version of Figure 4.7a in the 31-32 AMU/e range. The dotted lines are added to guide the eye while the compound associated to the peak is shown.

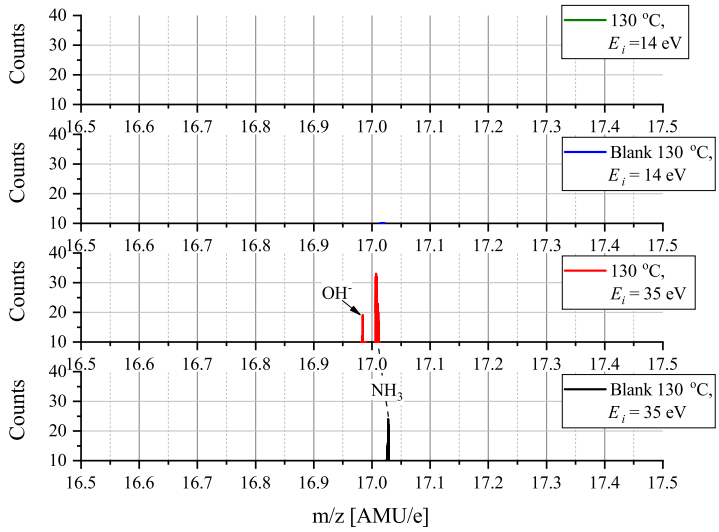

Figure C.4: Zoomed in version of Figure 4.7a in the 16-17 AMU/e range. The dotted lines are added to guide the eye while the compound associated to the peak is shown.

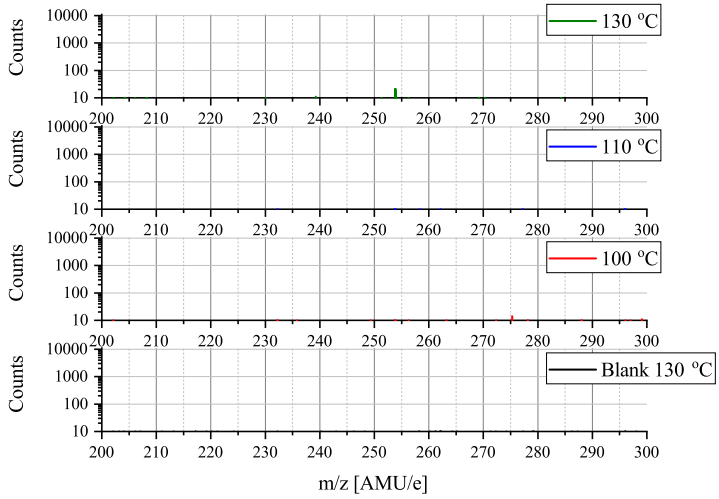

Figure C.5: The full 200-300 AMU/e range mass spectra recorded using an ionization energy of 14 eV and temperatures of either 100 °C, 110 °C or 130 °C. The "Counts" axis starts at 10 and is logarithmic.

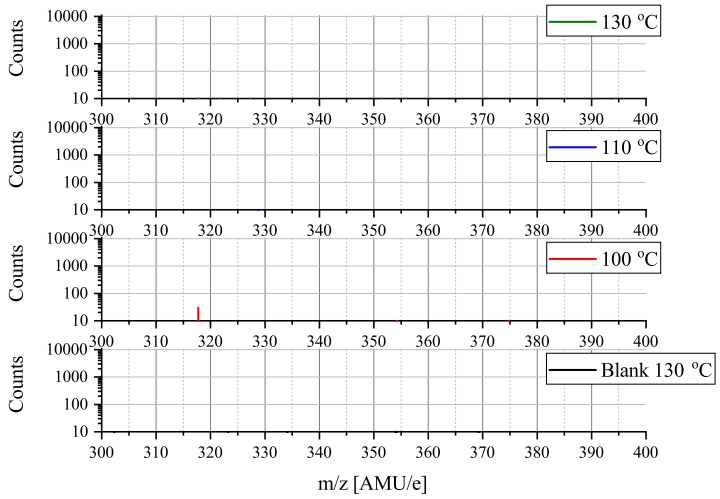

Figure C.6: The full 300-380 AMU/e range mass spectra recorded using an ionization energy of 14 eV and temperatures of either 100 °C, 110 °C or 130 °C. The "Counts" axis starts at 10 and is logarithmic.

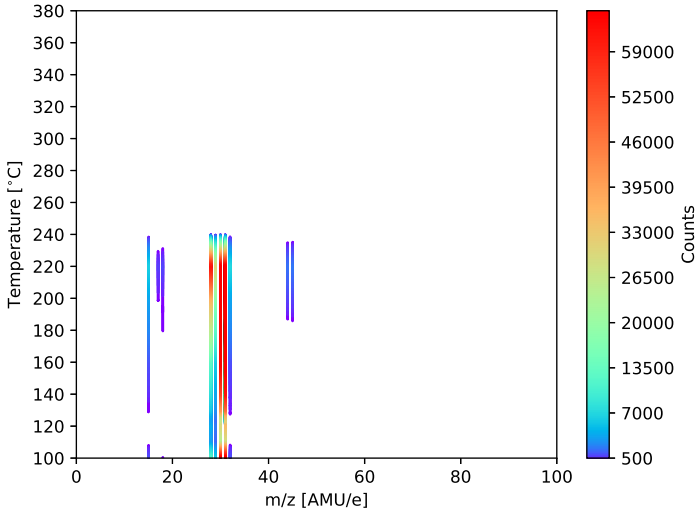

Figure C.7: The full 0-100 AMU/e range intensity plots from the high temperature experiments.

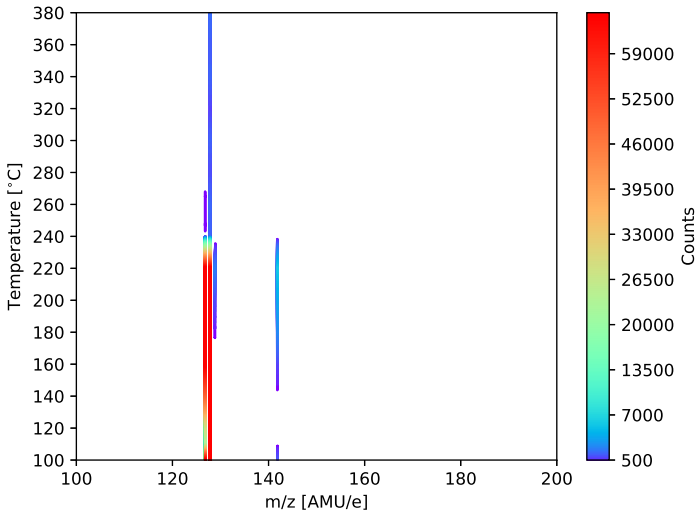

Figure C.8: The full 100-200 AMU/e range intensity plots from the high temperature experiments.

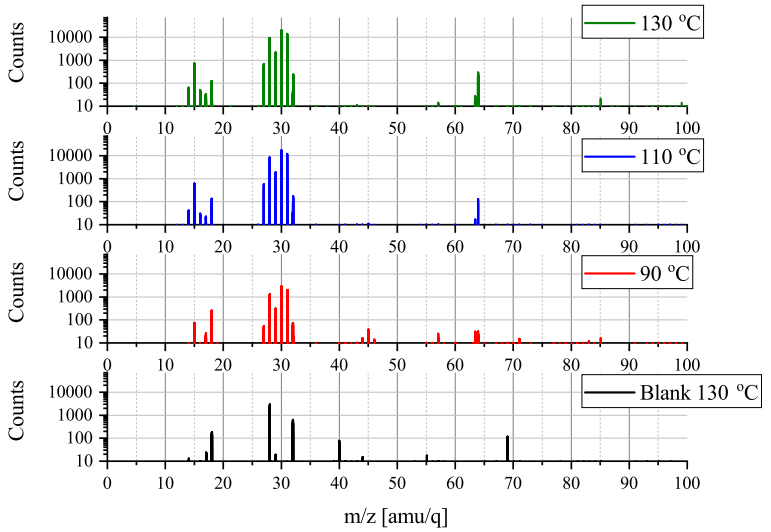

(a)

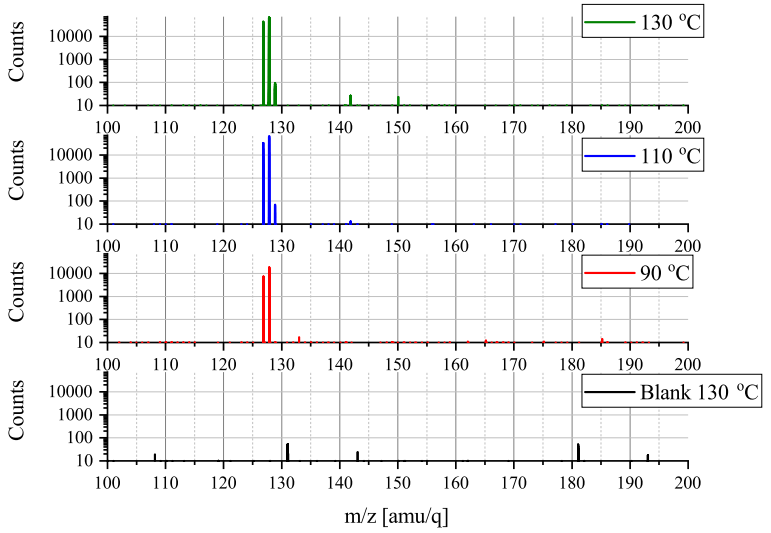

(b)

Figure C.9: The mass spectra recorded using an ionization energy of 35 eV and a temperature of 100 °C, 110 °C or 130 °C. The "Counts" axes are logarithmic and starts at 10 as everything below was considered to be noise. **(a)** shows the 0-100 AMU/e range while **(b)** shows the 100-200 AMU/e range.

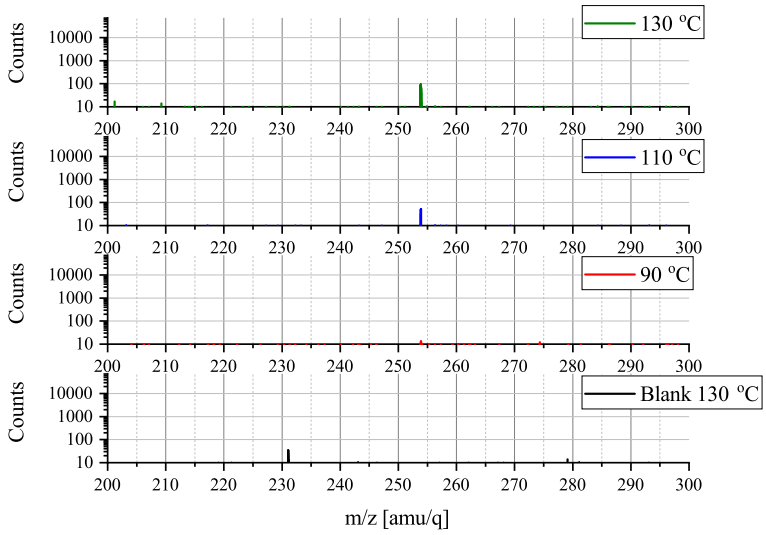

(a)

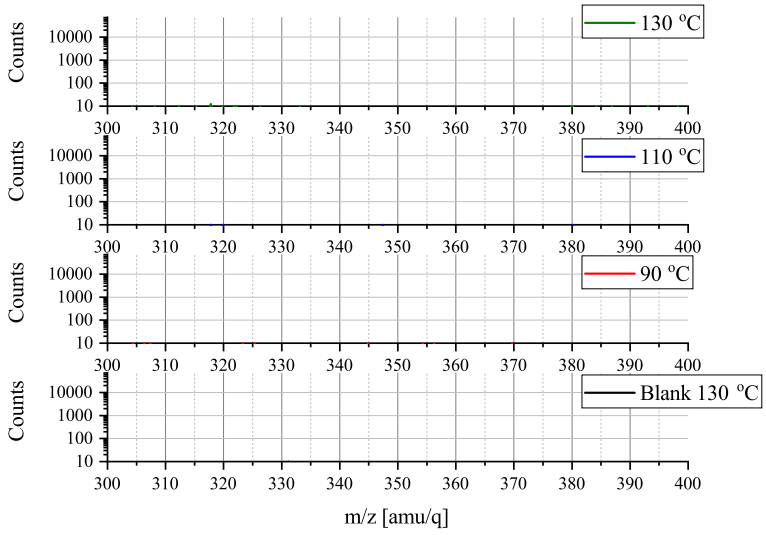

(b)

Figure C.10: The mass spectra recorded using an ionization energy of 35 eV and a temperature of 100 °C, 110 °C or 130 °C. The "Counts" axes are logarithmic and starts at 10 as everything below was again considered to be noise. **(a)** shows the 200-300 AMU/e range while **(b)** shows the 300-400 AMU/e range.

Appendix D

Additional mass spectra for chapter 5

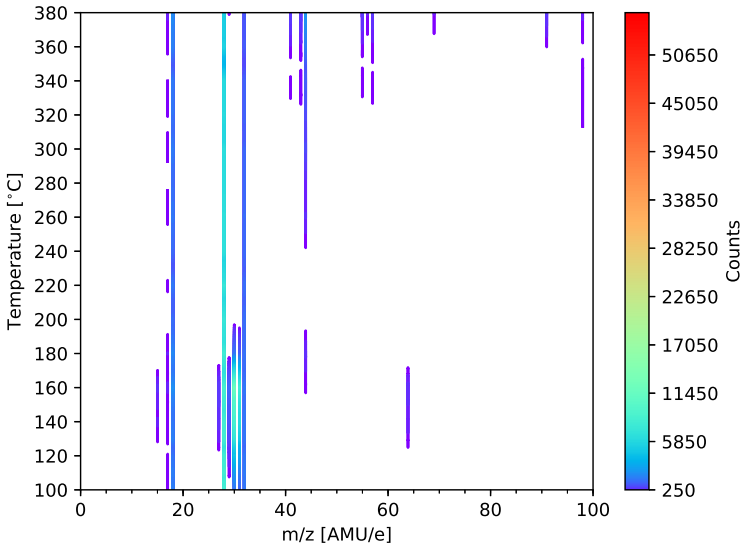

Figure D.1: Mass spectra of the $CH_3NH_3PbI_3$ as a function of temperature in the 0-100 AMU/e range recorded using an ionization energy of 35 eV. The "Counts" axis again starts at 250.

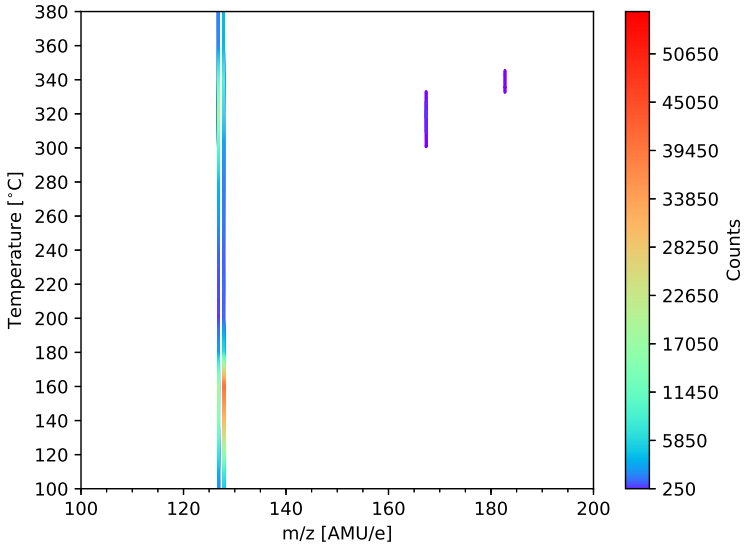

(a)

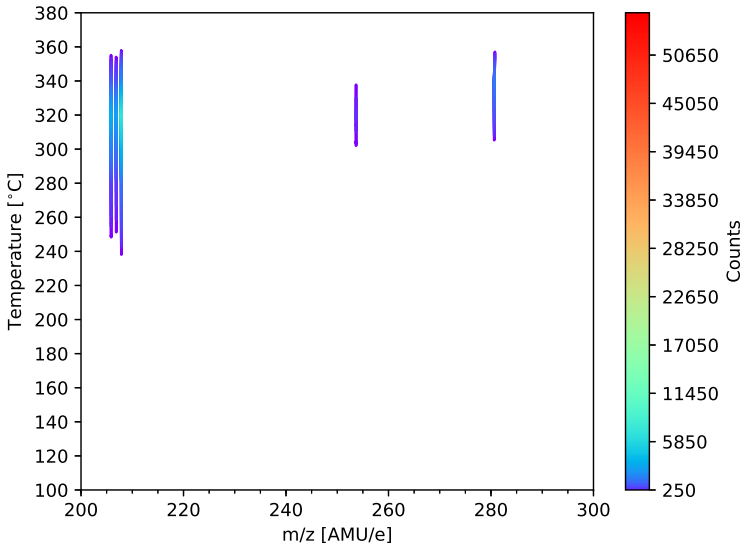

(b)

Figure D.2: Mass spectra of the $CH_3NH_3PbI_3$ as a function of temperature, recorded using an ionization energy of 35 eV. **(a)** shows the 100-200 AMU/e region while **(b)** shows the 200-300 AMU/e region. The "Counts" axes again starts at 250.

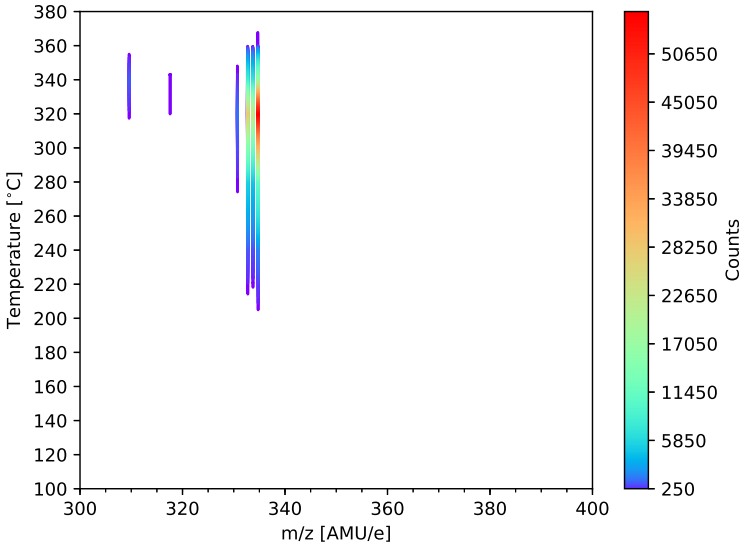

(a)

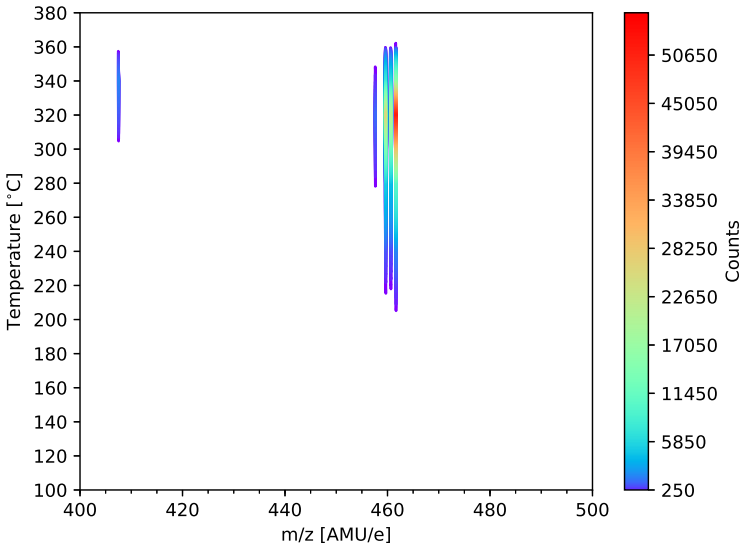

(b)

Figure D.3: Mass spectra of the $CH_3NH_3PbI_3$ as a function of temperature, recorded using an ionization energy of 35 eV. **(a)** shows the 300-400 AMU/e region while **(b)** shows the 400-500 AMU/e region. The "Counts" axes again starts at 250.

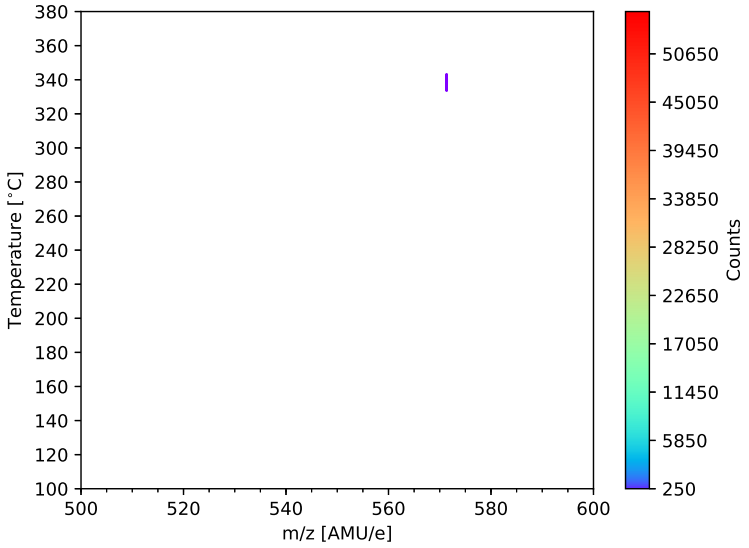

(a)

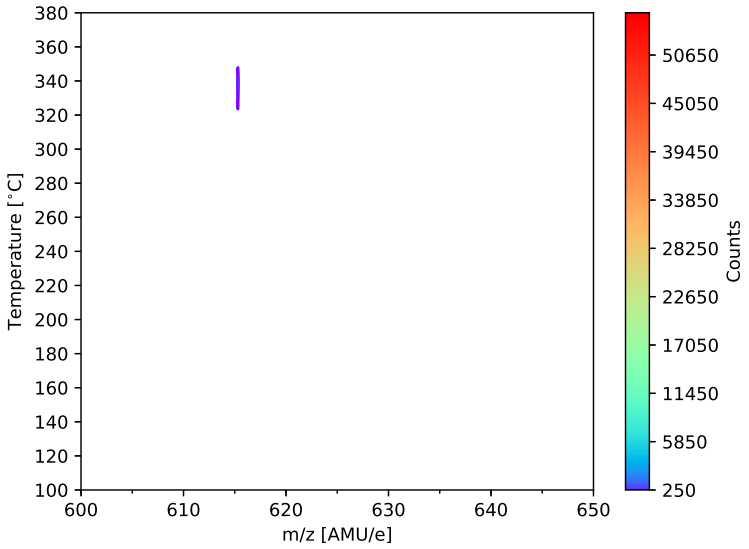

(b)

Figure D.4: Mass spectra of the $CH_3NH_3PbI_3$ as a function of temperature, recorded using an ionization energy of 35 eV. **(a)** shows the 500-600 AMU/e region while **(b)** shows the 600-650 AMU/e region. The "Counts" axes again starts at 250.

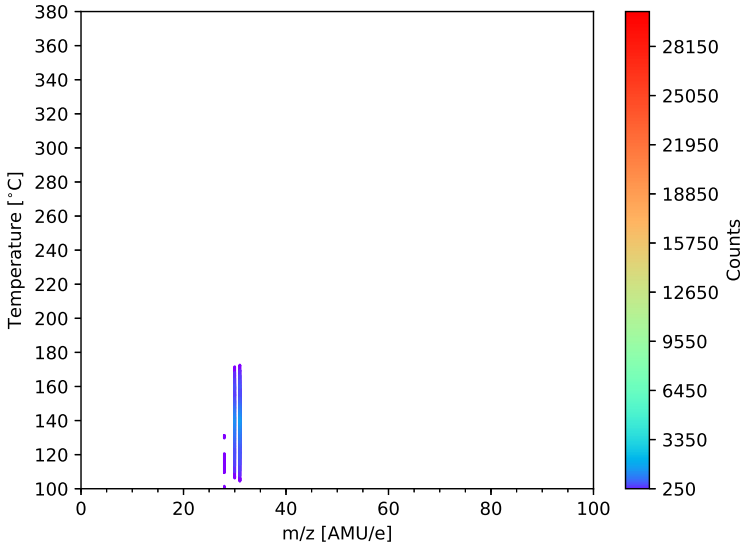

(a)

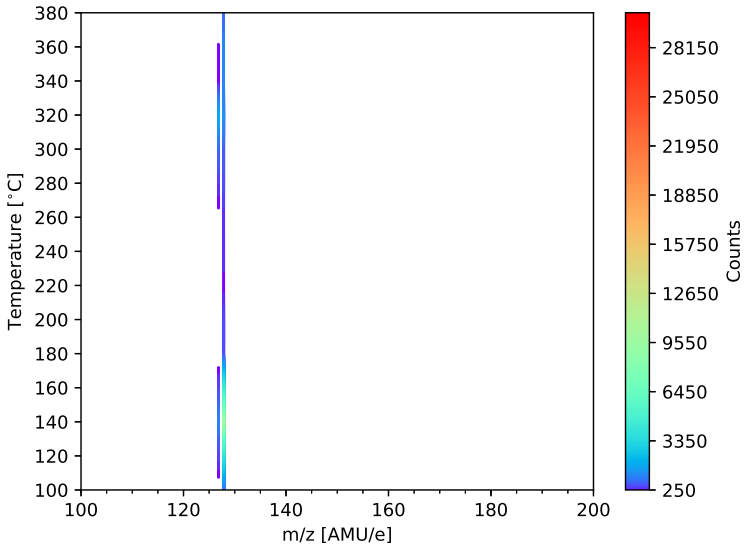

(b)

Figure D.5: Mass spectra of the $CH_3NH_3PbI_3$ as a function of temperature, recorded using an ionization energy of 14 eV. **(a)** shows the 0-100 AMU/e region while **(b)** shows the 100-200 AMU/e region. The "Counts" axes again starts at 250.

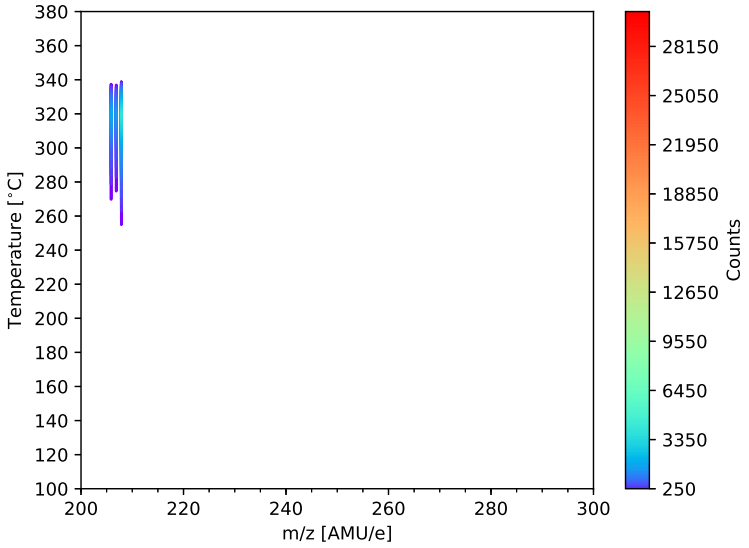

(a)

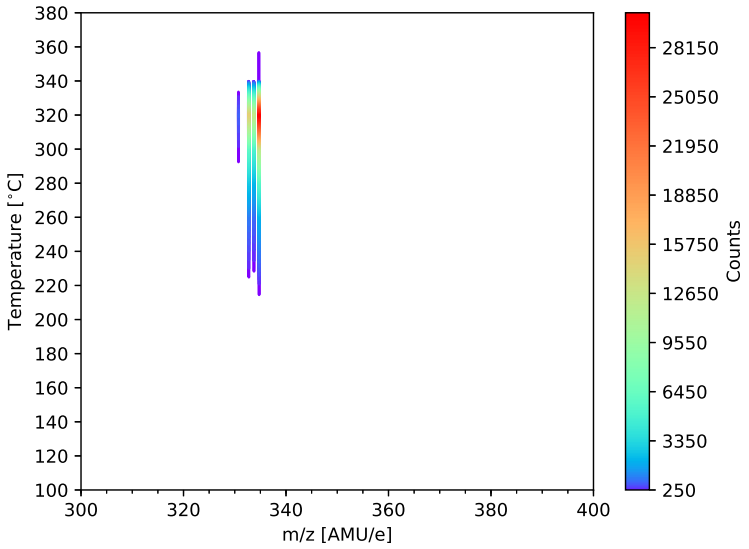

(b)

Figure D.6: Mass spectra of the $CH_3NH_3PbI_3$ as a function of temperature recorded using an ionization energy of 14 eV. **(a)** shows the 200-300 AMU/e region while **(b)** shows the 300-400 AMU/e region. The "Counts" axes again starts at 250.

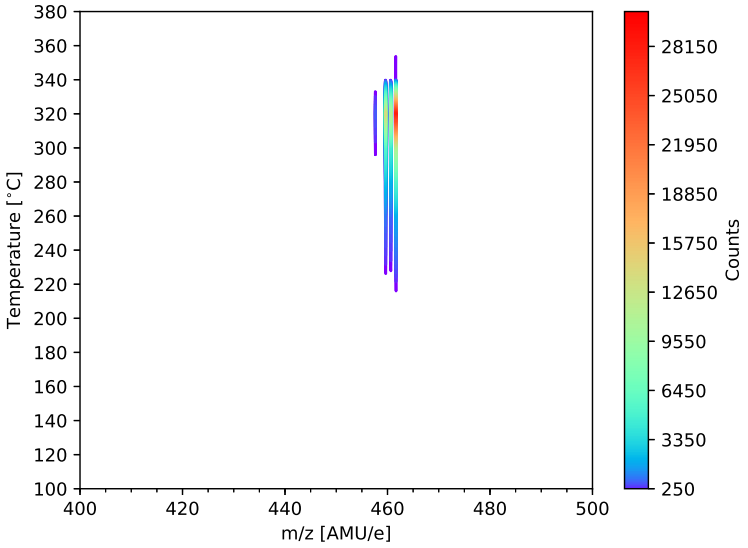

(a)

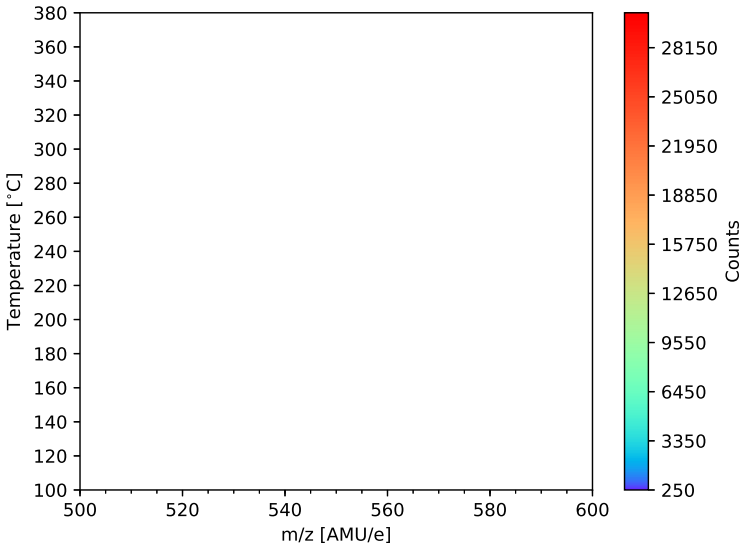

(b)

Figure D.7: Mass spectra of the $CH_3NH_3PbI_3$ as a function of temperature recorded using an ionization energy of 14 eV. **(a)** shows the 400-500 AMU/e region while **(b)** shows the 500-600 AMU/e region. The "Counts" axes again starts at 250.

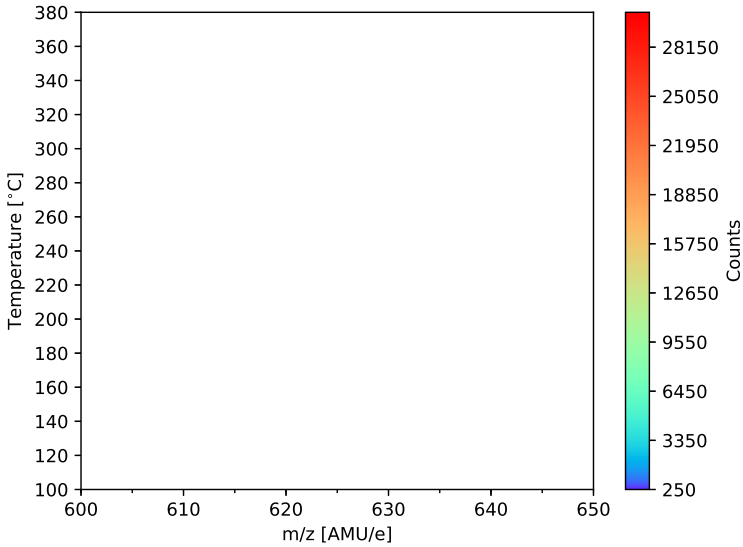

Figure D.8: Mass spectra of the $CH_3NH_3PbI_3$ as a function of temperature in the 600-650 AMU/e region. The spectra were recorded using an ionization energy of 14 eV, and the "Counts" axis again starts at 250.

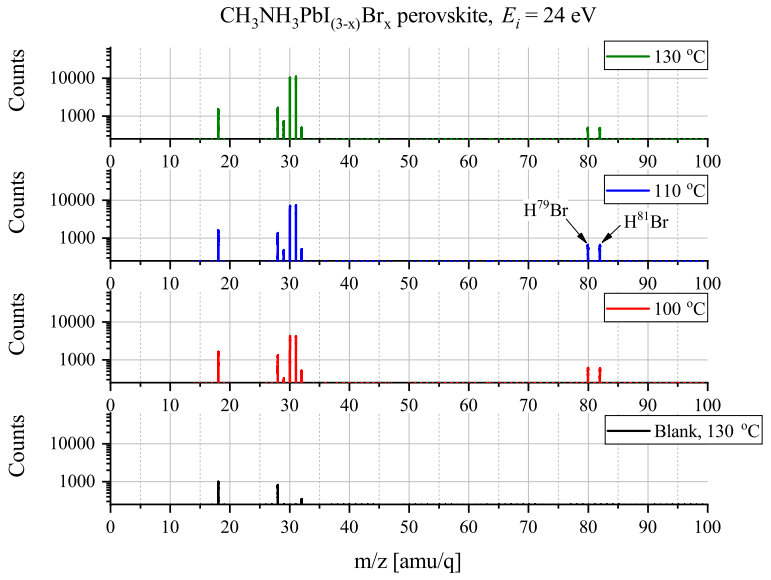

(a)

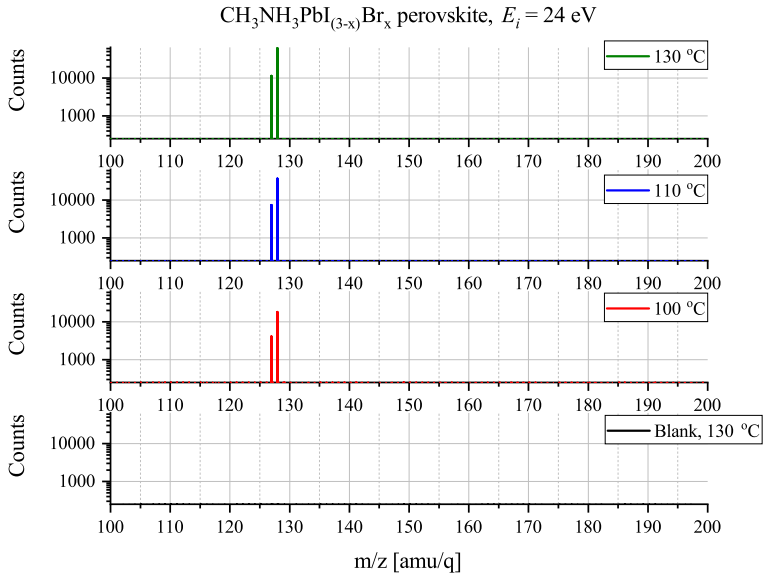

(b)

Figure D.9: Mass spectra of the $CH_3NH_3PbI_{(3-x)}Br_x$ recorded using a ionization energy of 24 eV. **(a)** shows the 0-100 AMU/e region while **(b)** shows the 100-200 AMU/e region. The "Counts" axes again starts at 250.

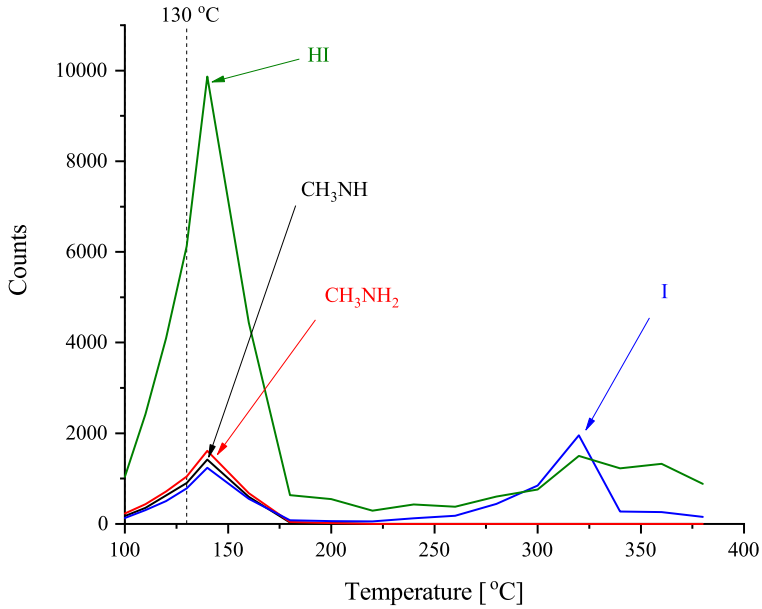

Figure D.10: Intensity as a function of temperature of the peaks associated with CH_3NH_2, CH_3NH, I and HI from Figures 5.2a and 5.2b. A line has been added at 130 °C to help guide the eye.

Appendix E
Appended publication

Paper I

Deposition of Methylammonium Iodide via evaporation - combined kinetic and mass spectrometric study

Martin J. Bækbo, Ole Hansen, Ib Chorkendorff, Peter C. K. Vesborg

Under review

Journal Name

ARTICLE TYPE

Cite this: DOI: 10.1039/xxxxxxxxxx

Deposition of Methylammonium Iodide via evaporation - combined kinetic and mass spectrometric study†

Martin J. Bækbo[a], Ole Hansen[b], Ib Chorkendorff[a] and Peter C. K. Vesborg*[a]

Received Date
Accepted Date

DOI: 10.1039/xxxxxxxxxx

www.rsc.org/journalname

Methylammonium lead halide perovskites have recently emerged as a very attractive and versatile material for solar cell production. Several different perovskite fabrication methods can be used though most of them involve either spin coating, evaporation under high vacuum or a combination hereof. In this study we focus on thermal evaporation of methylammonium iodide (MAI), or more specifically, why this process, in terms of a physical vapour deposition, requires such a high deposition pressure to be successful. We use quartz crystal micro balance (QCM) measurements as well as mass spectrometry. The results indicate that MAI has a very low sticking especially if the substrate is held at elevated temperatures and is furthermore observed to evaporate with disproportionation into primarily CH_3NH_2 and HI. Even when $PbCl_2$ is deposited on the QCM crystal, so that $CH_3NH_3PbI_{(3-x)}Cl_x$ perovskite can form, the MAI sticking remains low, possibly due to the requirement that both species be present on the film surface at the same time to form the perovskite. The results provide guidelines for designing a perovskite deposition chamber and additionally fundamental information about MAI evaporation.

Broader context

Methylammonium lead halide perovskite solar cells have gained a very high amount of attention due to the unprecedented increase in power conversion efficiency that have been obtained during a fairly short amount of time. Perovskite solar cells have now reached a point were the lab devices convert sunlight at efficiencies comparable to Si cells and therefore have the potential to significantly impact the worlds renewable energy production. The predicted low fabrication cost furthermore makes the technology more accessible and thus helps to pave the road towards a more sustainable future. Many avenues of fabrication techniques have been examined including spin coating, high vacuum evaporation or a combination hereof. In this paper we examine evaporation of methylammonium iodide under high vacuum conditions using quartz crystal micro balances and mass spectrometry to elucidate the underlying reasons for difficulties associated with this process. By combining the results of the two experimental methods we are able to give insights into the fundamental nature of MAI evaporation as well as $CH_3NH_3I_{(3-x)}Cl_x$ formation kinetics.

[a] *Surfcat, Technical University of Denmark, Fysikvej, Building 312, 2800 Kgs. Lyngby, Denmark ; E-mail: Peter.Vesborg@fysik.dtu.dk*

[b] *Department of Micro- and Nanotechnology, Technical University of Denmark, 2800 Kgs. Lyngby, Denmark*

† Electronic Supplementary Information (ESI) available: [details of any supplementary information available should be included here]. See DOI: 10.1039/b000000x/

1 Introduction

Methylammonium lead halide perovskites (CH_3NH_3PbX, X = I, Br, Cl) have received a massive amount of attention in recent years due to their very attractive material properties which make them highly efficient as the absorber in a solar cell[1]. These properties include good carrier mobility, a high defect tolerance, high absorbance in the visible range and, additionally, band gap tunability depending on the halides included. Furthermore a wellspring of different fabrication methods have been demonstrated in literature thus making the perovskites very flexible materials to work with[2–6]. Though the most common fabrication methods involve spin coating several groups have reported using high- or low vacuum deposition to fabricate devices. The advantage of using vacuum systems is the ability to control the fabrication environment to a much higher degree which normally results in a better reproducibility and a superior film quality. In spite of this, the reported power conversion efficiencies (PCEs) from studies using co-evaporation under high vacuum conditions are inferior to those obtained using either spin coating or sequential deposition[2,7–9]. As noted by Ono *et al.*[7] this shortcoming is often attributed to the difficulties controlling the rate of evaporation of methylammonium iodide (MAI), but the nature of these difficulties are not detailed.

The challenge posed has given rise to some clever deposition schemes which all rely on controlling the partial vapour pressure of the MAI rather than its rate[2,8,10,11]. Ono *et al.*[10] use a high vacuum system in which the perovskite is formed by co-evaporating

$PbCl_2$ and MAI while controlling the pressure of the later using the effusion cell temperature and a gate valve. Li *et al.*[8] demonstrates a sequential deposition method where the Pb-containing film is deposited by spin coating after which it is transferred to a test tube containing MAI. The tube is subsequently evacuated using a roughing pump and then heated by submerging it into an oil bath. In both cases the deposition pressure is much higher than what is usual for PVD processes (0.31 Pa and 40.0 Pa, respectively) which usually run at pressures below 5×10^{-4} Pa. At a pressure of 5×10^{-4} Pa one would expect that the (nearly) ballistic transport from the source to the target would give rise to a high incident flux density and good films. It is therefore peculiar that such high deposition pressures are needed for successful perovskite deposition.

In this study we combine quartz crystal microbalance (QCM) measurements of MAI deposition and evaporation with mass spectrometry to examine what transpires during MAI evaporation under vacuum conditions ($< 5 \times 10^{-3}$ Pa). The QCM experiments give information about MAI sticking to surfaces as a function of temperature and by depositing at layer of $PbCl_2$ on the crystal before initiating the experiment insight into the reaction kinetics of the perovskite layer is gained. Mass spectrometry complements the kinetics by elucidating which compounds evaporate when MAI is heated in a vacuum. The knowledge that may be gained from mass spectrometry, is the reason why it has been used in several previous studies[12,13]. The emphasis of these recent studies was mostly $CH_3NH_3PbI_3$ degradation and thus the applied temperature window is much wider than the 85°C−150°C, which is usually used when evaporating MAI[5,8–10,14,15]. In both papers the authors report that MAI appears to thermally decompose into its constituents upon evaporation. Nenon *et al.*[13] measures peaks associated with CH_3NH_2 at a temperature of around 110°C but observe a shift in the cracking pattern towards NH_3 and CH_3 at elevated temperatures. The fact that the mass range in their experiments does not extend above 100 AMU/e does, however, mean that they are not able to directly observe any species containing I. They are thus not able to give the full picture of MAI decomposition. Juarez-Perez *et al.*[12] show measurements with an extended mass range (up to 200 AMU/e) and report that MAI decomposes into CH_3I and NH_3 but do not observe any volatiles below 300°C in contrast to Nenon *et al.*[13]. Though it is certainly interesting to know what MAI decomposes into at 300°C it is, as mentioned, a much too high temperature for MAI deposition. In this work we therefore present mass spectrometry measurements of MAI in the relevant 100°C – 130°C deposition temperature range supported by high temperature (up to 380°C) experiments for completeness. By using a sector magnet mass spectrometer a highly increased mass resolution is obtained while the mass-range is, importantly, extended up to 380 AMU/e which allows us to detect I containing compounds. By changing the ionization energy we can, additionally, infer the effects of ionization fragmentation. This allows us elucidate if the MAI decomposition happens thermally or in the ionization process. By combining the results of both methods we suggest an explanation of the peculiar behaviour of evaporative deposition of MAI, which anyone designing an MAI evaporation system for perovskites or otherwise should take into consideration.

2 Experimental

2.1 Quartz crystal microbalance experiments

QCMs are routinely used in physical vapour deposition systems as they allow one to gauge the thickness of the layers being deposited by measuring the change of the resonance frequency of a piezoelectric quartz crystal as the film grows on it. The correlation between the frequency change Δf and the change in deposited mass per unit area Δm is given by Sauerbrey equation

$$\Delta f = -C_f \Delta m, \tag{1}$$

where C_f is called the sensitivity factor which depends on the type of crystal used[16]. From the equation it is clear that a drop in frequency corresponds to material being deposited on the crystal, and a positive deposition rate is correlated to a rate of frequency change. A schematic of the experimental set up used for the QCM measurements is shown in Figure 1.

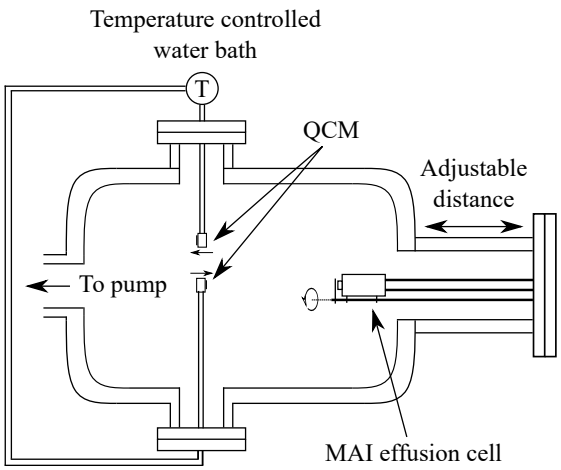

Fig. 1 Schematic drawing of the QCM set up which includes two QCMs, which can be cooled or heated using a water circulation bath, and an MAI effusion cell which can be closed with a shutter. The distance from the effusion cell to the QCM sensor can be varied by inserting a spacer on the chamber flange. The two QCMs sit with equal distance to the center line of the effusion cell at a 180° angle with respect to each other (see Figure S1) and with one facing the MAI source while the other faces away from it.

In the system two QCMs, connected to an Inficon SQM-160 control box, were installed with one facing the effusion cell and one rotated by 180° facing away from it. Both sensors were connected to a circulating water bath equipped with a thermostat to control the temperature of the crystal during the experiments. The effusion cell was an almost closed cell machined from copper with a small "chimney" in the top which could be closed off by a mechanical shutter. Using this system we measured the deposition rate of MAI with the forward-facing QCM either cooled to ca. 20°C or held at 65°C, 75°C or 85°C via the circulating water. For each experiment a fresh 6 MHz QCM crystal was used either as

delivered or with various layers of $PbCl_2$ (Sigma Aldrich 98%) deposited onto it prior to the experiment using thermal evaporation in a high vacuum chamber.

As the resonance frequency of the QCM changes with temperature a heating and thermalization procedure was employed to ensure that the sensor was stable before beginning the experiment. The water bath was run for 20 min to stabilize at the desired temperature after which the sensor was given an hour to stabilize with the water flowing. This procedure lead to a frequency change of roughly -125 Hz when heating to 85°C (see Figure S2 for details). Following the heating of the QCM, the MAI source was given 30 min to heat to 130°C and to stabilize. In order to gauge the background rate of the system (i.e. the deposition rate when the MAI source shutter is closed) the MAI deposition was chopped by opening and closing the shutter every 10 minutes (see Figure 2). The final two types of experiments were to 1) change the distance from the source to the QCM and 2) to measure the indirect (non ballistic) deposition by using the reverse-facing QCM. The MAI used in the QCM experiments was bought from Solaronix (lot number 24115).

2.2 Mass spectrometry experiments

The mass spectrometry experiments were carried out using a Waters VG AutoSpec sector magnet mass spectrometer, which ran at a background pressure below 5×10^{-5} Pa. To estimate the effects of ionization fragmentation two different ionization energies, namely 35 eV and 14 eV, were used. When comparing spectra captured at the two energies it is important to emphasize that count rate of any given compound depends on the lens and slit settings of the instrument and thus the intensities observed in the two experiments cannot be compared directly. Conversely, the relative heights in spectra taken at the same settings as well as peak occurrences may be compared. To calibrate the mass/charge axis the reference chemical perfluorokerosene (PFK) was injected through a septum and let into the analyser were a calibration scan could be recorded. By comparing the analyte scan with a PFK reference, as well as one for atmospheric air, the appropriate shift in the mass/charge axis could be identified and applied in subsequent data treatment. Following the calibration run the system was evacuated for approximately 50 min to remove any leftover PFK.

The MAI was introduced in solid form using a source in which a small Al cylinder carrying the powder could be inserted inside a heating stage located immediately adjacent to the ionization zone. To estimate the background signal of the system the source with the (empty) Al cylinder was inserted and heated to 130°C before a spectrum was recorded using either 14 eV or 35 eV as ionization energy. Then the source was allowed to cool before the MAI was loaded and the source reinserted. The source was then heated to 100°C and subsequently to 110°C where measurements using an ionization energy of 14 eV were performed at each temperature. Finally the source was heated to 130°C where measurements using both 14 eV and 35 eV as ionization energies, were conducted. For the high temperature experiments the equipment was initially calibrated in a similar manner as before. Following the calibration 1-2 mg of MAI was introduced and using an ionization energy of 14 eV a mass spectrum was recorded at 100°C. The temperature was then increased in steps of 10°C until reaching 140°C where mass spectra were recorded at each temperature. After 140°C the step size was increased to 20°C until a final temperature of 380°C was reached. Each temperature increase and measurement step took approximatly 12 min. The MAI used in the mass spectrometry experiments was synthesised in a similar manner as reported by Li *et al.*[8]. In short, methylamine (SigmaAldrich 33% in ethanol) was mixed with pure ethanol kept at 0°C using an ice bath. Afterwards HI (SigmaAldrich 57% in water) was added drop-wise while the solution was stirred vigorously using a stir bar and left to stir for 2h. The MAI powder was then reclaimed using a rotary evaporator before being recrystallized from pure ethanol and dried at 70°C in a tube furnace under an Ar flow.

3 Results and discussion

3.1 QCM experiments

Previous work has observed that MAI "seems to go everywhere" in the vacuum chamber during deposition suggesting that line of sight between the MAI source and the target is not needed[10]. The obvious implication is that MAI has very low sticking and bounces around in the chamber despite the chamber walls being at room temperature. We see a rather dramatic demonstration of this with the experiment using the reversed QCM where a substantial rate is observed even though there is no direct path from the source to the QCM surface. The same phenomenon explains that there is no apparent change in the deposition rate upon moving the source further away from the QCM (see Figures S3 and S4). It is important to underscore that under the experimental conditions used (i.e. a deposition pressure of 6.67×10^{-3} Pa) the mean free path is larger than the chamber dimensions and one would thus ordinarily expect that no rate would be observed when the QCM is reversed and cannot "see" the source directly. The inference is that MAI has a very low sticking coefficient, which also explains why high deposition pressures are needed to obtain proper perovskite deposition. To study this in more detail we performed a series of experiments to gain further insight into the kinetics of MAI deposition. In the first experiment a blank QCM crystal was used and the sensor was kept at cooling water temperature. Then a measurement using a water cooled sensor along with a crystal with a $PbCl_2$ layer was performed and finally a sensor held at 75°C also with a $PbCl_2$ layer was used. The first configuration mimics the situation where one controls the deposition by controlling the rate of MAI and thus serves as a reference for the rest of the experiments. The following two experiments are equivalent to the sequential deposition scheme performed at either room temperature or at an elevated temperature, which has been reported to be be optimal for perovskite conversion[15].

The results of the measurements are shown in Figure 2 along with the result of a running similar experiment but using a blank crystal. The black trace shows that the rate appears to decrease over time towards some steady state. The reason for the dropoff is not fully understood, but we speculate that it is caused by the

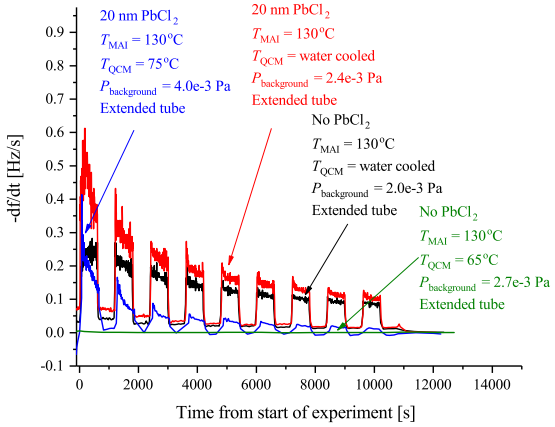

Fig. 2 The observed rates of the MAI sticking experiments using the forward facing QCM where T_{MAI} is the MAI source temperature, T_{QCM} is the QCM temperature, $P_{background}$ is the background pressure. Extended tube means that the distance from the source to the sensor was 19.5 cm as compared to the 9.5 cm used in Figure 3. The black curve shows the rate measured when the QCM crystal is water cooled and blank. The red curve shows the rate when the QCM crystal is water cooled and has 20 nm of $PbCl_2$ deposited on it. Finally the blue curve shows the rate when the QCM crystal is heated to 75°C and has 20 nm of $PbCl_2$ while the green curve shows the rate when a blank crystal heated to 65°C, is used. In all cases the signal was chopped using 10 min intervals.

topmost layers of the deposit being heated slightly over time due to infrared irradiance from the source. This lowers the sticking of the MAI and subsequently the observed rate. Comparing the red and the black traces it is clear that the addition of $PbCl_2$ initially increases the sticking of the MAI. This makes sense as the $PbCl_2$ should be reactive towards MAI, forming $CH_3NH_3I_{(3-x)}Cl_x$, which means that it is energetically more favourable to stick to the $PbCl_2$ surface as compared to the bare crystal or a pre-existing MAI layer. When the temperature of the QCM is increased the rate is seen to drop off much faster suggesting that all the $PbCl_2$ is converted which due to the increased diffusion of reactant species would happen faster. However, an estimation of the amount of $PbCl_2$ which has been converted into $CH_3NH_3I_{(3-x)}Cl_x$ from the amount of MAI that has been deposited, shows that a substantial amount of $PbCl_2$ should still be left unconverted (see the SI). The more likely explanation therefore seems to be that the sticking of the MAI is much diminished by the hotter surface. This is supported by the fact that no rate can be observed when running the same experiment using a blank crystal without a $PbCl_2$ layer (see Figure 2 and Figure S5). Supporting this further is the fact that the cooled crystal with $PbCl_2$ has a higher initial rate than when it is heated even though the starting surfaces are the same (compare red trace with the blue trace). In all the measurements it is evident that the rate does not go completely to zero when the shutter is closed. This is especially apparent in the experiments with the cooled QCM and during the first period with the shutter closed. The presence of a substantial background rate is likely caused by continuous evaporation of MAI from the walls of the chamber. The initially higher background rate, seen in the first shutter cycle, could be due to MAI sitting on the external surfaces of the source itself, which evaporates much faster than the MAI sitting on the chamber walls due to the higher temperature of the MAI source. This serves to "clean" the source of MAI causing the background rate to drop to what is delivered by the chamber.

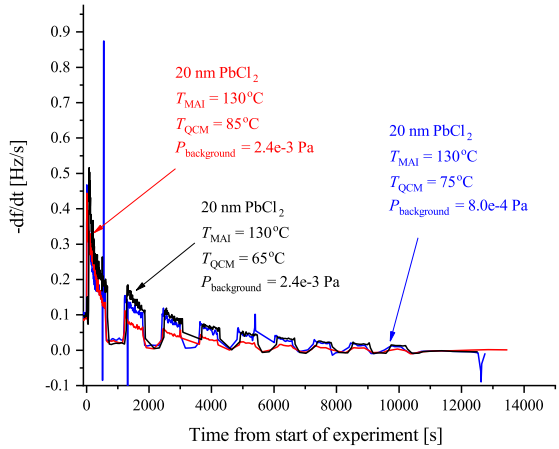

Fig. 3 QCM experiments using the forward facing QCM in which the sensor was heated to 65°C (black), 75°C (blue) or 85°C (red) where T_{MAI} is the MAI source temperature, T_{QCM} is the QCM temperature, $P_{background}$ is the background pressure. In all cases the crystal had 20 nm of $PbCl_2$ deposited on them and the signal was again chopped in 10 min intervals using the shutter on the MAI source.

To further examine the effect of substrate temperature we performed additional depositions with the QCM heated to 65°C and 85°C yielding the results shown in Figure 3. The initial rates are observed to be more or less the same in all cases but the 85°C rate is seen to drop of more rapidly while the 65°C rate drops off marginally slower when comparing to the 75°C rate. This supports the hypothesis that a too high substrate temperature is disadvantageous when considering MAI deposition isolated, as the rate is seen to drop off faster with increased temperature. Even postannealing a stack of $PbCl_2$ and MAI might prove problematic as a significant part of the MAI is likely to reevaporate especially if the annealing is done under vacuum. An elevated sample temperature has, however, been reported to be paramount for ensuring good perovskite crystallization and one therefore needs a very high deposition flux to compensate for the fast desorption[8,15]. In addition, the data in Figure 3 (see also Figure S6) also supports that the samples are not "running out" of $PbCl_2$ since if this were the case the total amount of deposited MAI, and thus the total frequency change, should be the same regardless of temperature. Instead a substantial difference in the terminal frequency is observed ($\Delta f = -250$ Hz, -360 Hz and -405 Hz for the 85°C, 75°C and 65°C cases, respectively). From these measurements one can additionally make an estimation of the sticking coefficient, S_c, of the MAI by comparing the incoming flux suggested by the chamber pressure to the amount of material observed to stick. The calculations in the SI yield the results that

$S_{c,85°C} = 2.1 \times 10^{-4}, S_{c,75°C} = 3.0 \times 10^{-4}$ and $S_{c,65°C} = 3.4 \times 10^{-4}$ which means that one can expect to loose a substantial amount of the evaporated MAI to pumping.

The final batch of experiments was conducted to elucidate the possible effect of the thickness of the $PbCl_2$ layer on the deposition rate. To do so we performed the same type of measurements as before, but using a crystal with either 150 nm or 40 nm $PbCl_2$ while keeping the QCM at 75°C in both cases. The results are displayed in Figure 4. It is evident that the initial rate is the same in all cases which is expected since the MAI being deposited sees the same surface. As the deposition progresses it, however, becomes clear that the rate saturates faster when a thinner $PbCl_2$ film is used. The reason for this is not clear but a plausible explanation could be that the diffusion rate of MAI depends on the concentration of $PbCl_2$ that is available for the MAI to react with. As reported by Chen *et al.*[15] MAI is able to completely convert a 150 nm film of $PbCl_2$ into perovskite which suggests that the MAI diffusion through the film is fast. This would mean that the MAI reacts throughout the $PbCl_2$ film and consequently that the $PbCl_2$ concentration in the thicker films will be higher for the same amount of deposited MAI. Supporting this hypotheses is the observation that the rate in the 40 nm $PbCl_2$ experiment reaches that of the 20 nm $PbCl_2$ experiment after twice as long deposition time.

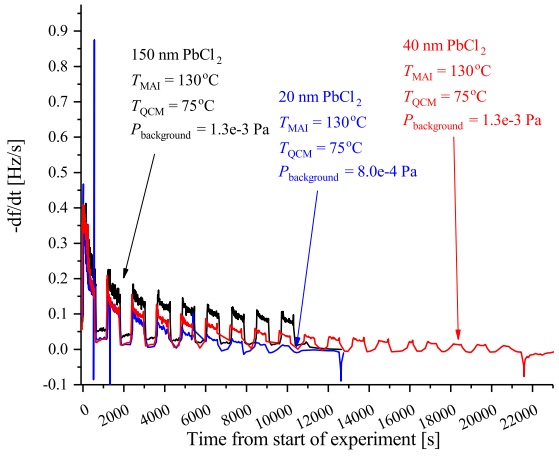

Fig. 4 QCM experiments using the forward facing QCM in which the crystal was covered with either 20 nm (blue), 40 nm (red) or 150 nm of $PbCl_2$ (black). Like previous T_{MAI} is the MAI source temperature, T_{QCM} is the QCM temperature, $P_{background}$ is the background pressure. In all cases the rate was again chopped in 10 min intervals using the shutter on the MAI source.

3.2 Mass spectrometry experiments

Having established that the sticking of MAI is generally very low and that depositing the compound on a substrate held at elevated temperatures as a result is difficult we turn to mass spectrometry to explain what is causing this phenomenon. In Figure 5 the mass scans from 0-200 AMU/e with an MAI source temperature of 130°C and ionization energies of either 35 eV or 14 eV are shown. Comparing the 35 eV plot with its background it is clear that many new peaks appear while some pre-existing peaks grow substantially. The most important peaks are summarised in Table 1 along with the most likely compounds they are associated with. The strong presence of CH_3, CH_3N, CH_3NH, CH_3NH_2, I and HI suggest that the MAI thermally decomposes into its components upon evaporation in vacuum which is further supported by the fact that no signal is detected at m/z = 159 where the parent compound should be. From the data it is not immediately clear whether or not NH_3 or CH_3NH_3 is produced as their m/z signal coincide with those of OH^- (coming from H_2O) and O_2, respectively. Closer examination of the peaks reveals that 4 peaks rather than 2 are observed, namely, at m/z = 16.98 (OH^-), 17.00 (NH_3), 31.97 (O_2) and 32.04 (CH_3NH_3) which suggests that all four compounds are present (see Figures S7 and S8 for details). Comparing the peak locations to the expected ones (m/z = 17.01, 17.03, 32.00 and 32.07 for OH^-, NH_3, O_2 and CH_3NH_3, respectively) it is clear that the m/z axis is shifted slightly but also that the spacing between the peaks are as expected. The slight shift can be explained by drift in the m/z axis which happens over time and since the MAI spectrum was recorded after the calibration file such a shift is reasonable. Though NH_3 is observed the N_2 signal is seen to drastically increase when evaporating MAI which suggests that a large part of the N from the MAI forms molecular nitrogen rather than NH_3 at the used temperatures. In addition to the intense peaks mentioned above several other substantial peaks are observed at m/z = 63.4, 64, 129, 142 and 150. The first two of these are most likely double charged I and HI which should be located at 63.5 AMU/e and 64 AMU/e, respectively. The peak at m/z = 142 most likely originates from CH_3I while the last two are believed to be some compound containing C, N and H and potentially I as well. The peaks that are present in the background spectrum but not in the MAI measurements are believed to be species that are pumped away between the recording of the background spectrum and the MAI spectrum as the later was recorded after the former. As always, when one is doing mass spectrometry, cracking of the analyte into fragments due to the ionization process is an important consideration and comparing the plots for 35 eV ionization with those for 14 eV ionization (which is very gentle and should suppress the cracking process) there are indeed some differences worthy of attention.

The 14 eV spectrum features substantially fewer peaks, which can partially be explained by the fact that the ionization cross sections of many of the compounds are very low at this gentle ionization energy[17]. This is clearly exemplified by the fact that the background spectrum measured at 14 eV only shows 3 peaks at m/z = 18, 28 and 32. In the green spectrum in Figure 5a, which shows the 14 eV ionization data, only three major peaks appear, namely, at m/z = 30, 31 and 32, along with a very small peak at m/z = 28. No peak at m/z = 18 is, however, observed and comparing to the background the peak at 28 AMU/e is seen to be drastically less intense. The explanation for this is again most likely that the background scan was done some time before the MAI scan which means that the H_2O and the N_2 has been evacuated. The fact that the peak at m/z = 32 is amplified substantially

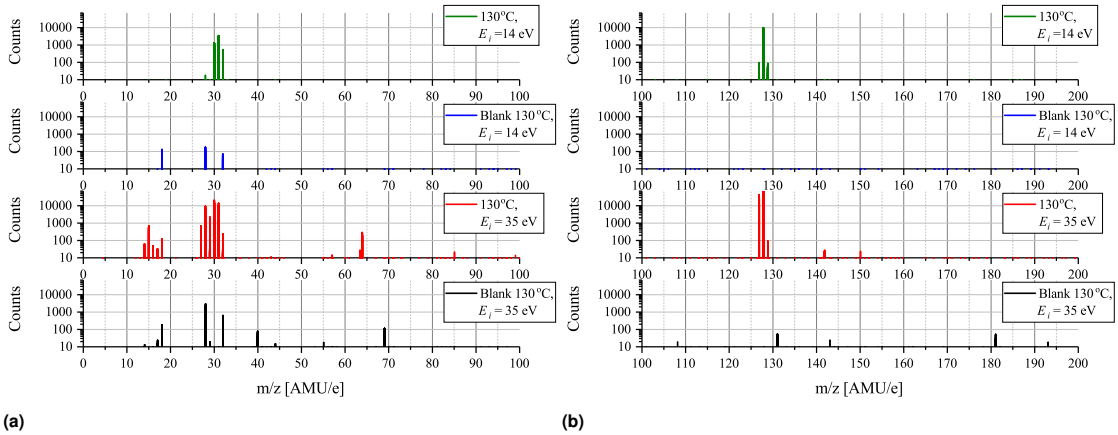

Fig. 5 Semi-log mass scans for MAI evaporated at 130°C recorded using an ionization energy, E_i, of 35 eV or 14 eV. **(a)** shows the m/z = 0-100 spectra while m/z = 100-200 spectra are shown in **(b)**. The Counts axis starts from 10 counts as everything below that is designated as noise.

Table 1 Table showing the relevant peaks, the compound giving rise to it and what parent molecule it might come from.

m/z	Compound	Likely parent molecule
15	CH_3^+	CH_3NH_2 fragment
16	O^+, CH_4^+	O_2 fragment, CH_3NH_2 fragment
17	NH_3^+, OH	CH_3NH_2fragment, H_2O fragment
18	H_2O^+	H_2O parent peak
27	CHN^+	CH_3NH_2 fragment
28	N_2^+	CH_3NH_2 fragment
29	CH_3N^+	CH_3NH_2 fragment
30	CH_3NH^+	CH_3NH_2 fragment
31	$CH_3NH_2^+$	CH_3NH_2 parent peak
32	O_2^+, $CH_3NH_3^+$	O_2 parent peak, CH_3NH_3I fragment
127	I^+	HI fragment
128	HI^+	HI parent peak
159	$CH_3NH_3I^+$	CH_3NH_3I parent peak

as compared to the background spectrum recorded under identical instrument settings strongly suggests that at least some of the peak at m/z = 32 should be attributed to CH_3NH_3 rather than O_2. This is supported by the fact that only one peak, coinciding with the one attributed to CH_3NH_3, is observed upon closer inspection (see Figure S8). The indication from the experiments is thus that MAI is thermally decomposed into CH_3NH_3, CH_3NH_2, CH_3NH and N_2 fragments. Comparing the ratio of the peaks at m/z = 30 and 31 for the 14 eV- and 35 eV spectra it is seen that the dominating peak shifts from CH_3NH_2 to CH_3NH as the ionization energy is increased. This increasing loss of hydrogen from the fragment with increasing ionization energy is expected and shows some ionization fracturing is indeed taking place - something which can also be concluded when examining Figure 5b. Here the peaks at m/z = 127 and 128 correspond to I and HI and once more the dominating peak is seen to switch from the the heavier compound to the dehydrogenated compound as the ionization energy is increased.

In order to minimize ionization cracking an ionization energy of 14 eV was used to study the effects of MAI evaporation temperature. From Figures 6a and 6b it is clear that up until 130°C temperature has no other apparent effect than to control the magnitude of the peak height. This is of course expected as a higher evaporation rate is obtained by increasing the source temperature, but it is important to note that the degree of thermal decomposition is not dependent on temperature in the 100°C – 130°C range. MAI appears to simply evaporate dissociatively as fragments as there is still no signal at m/z = 159 where the parent compound should be. In the m/z = 200-300 range only tiny peaks located at m/z = 275 and m/z = 254 are present in the 100°C and 130°C spectra as shown in Figure 6c. By consulting the NIST database[18] the m/z = 275 can be associated with $C_8H_{20}IO_2^-$ which appears to be thermally decomposing before 110°C as it does not show up in either of the elevated temperature spectra. The peak at 254 m/z can be attributed to I_2 and the explanation for why it is lacking in the two remaining spectra is most likely that the rates are not high enough for the peaks to emerge from the noise floor. In the final subfigure of Figure 6 another interesting feature appears in the 100°C spectrum, namely the presence of a, albeit tiny, peak at 317.72 AMU/e. This is very close the expected location of the MAI dimer, $(CH_3NH_3I)_2$, which should be located at 317.94 AMU/e and the discrepancy of 0.2 AMU/e can again be explained with drift in the magnet calibration. The lack of of the dimer in the 110°C and 130°C spectra suggests that it is not very thermally stable something which is supported by the fact that its observed intensity is minuscule compared to those of CH_3NH_2 and HI. The minor peaks of Figures 5 and 6 are summarized in Table 2 while the full m/z = 200-300 and 300-400 range plots are shown in Figures S9 and S10.

To further study the effects of the evaporation temperature mass scans were measured using temperatures of up to 380°C while again employing an ionization energy of 14 eV. The significant peaks (> 500 counts) of the resultant intensity plots are shown in Figures 7a and 7b. No significant peaks were found outside the m/z ranges indicated in the plots (m/z = 14-48 and 125-145) as seen in Figures S11 and S12 where the full m/z = 0-100 and 100-200 range spectra are shown. Initially peaks at m/z =

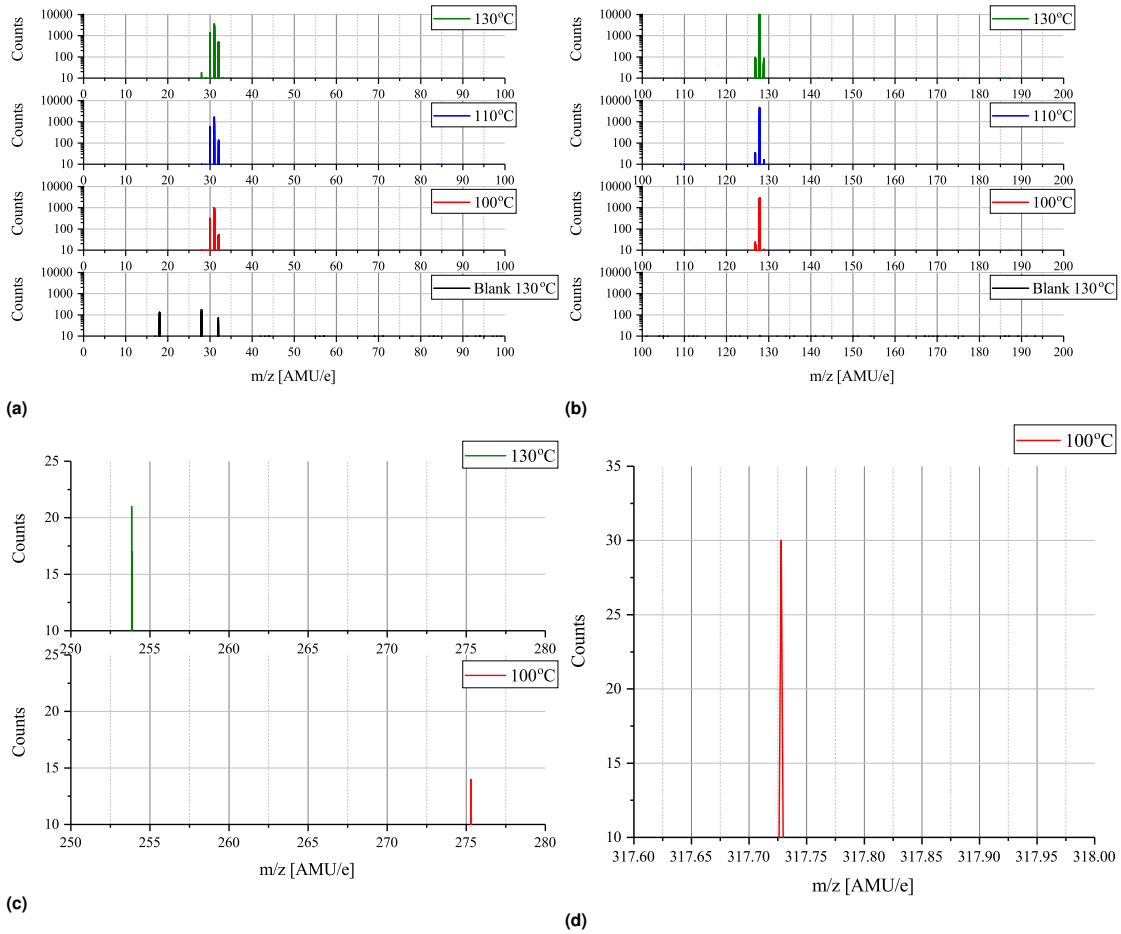

Fig. 6 Semi-log or linear plots showing the mass spectrometry data obtained using an ionization energy of 14 eV at an MAI source temperature of either 100°C, 110°C or 130°C. **(a)** shows the data in the 0-100 m/z range, **(b)** in the 100-200 m/z range, **(c)** in the 250-280 m/z range and **(d)** in the 317.6-318 m/z range. The Counts axis again starts from 10 which defines the noise floor.

28, 29, 30, 31, 127 and 128 are clearly observed which is in good agreement with what was found previously. As temperature increases these peaks become more intense and especially the peak at m/z = 127 is seen to be drastically elevated. This suggests that HI thermally decomposes into I and H at 160°C as the signals are seen to be equally strong. Due to detector saturation at 65000 counts it is not clear whether or not HI or I is the dominant species at these temperatures. At around 160°C several additional peaks located at m/z = 15, 32, 129, 142 as well as very faint peaks at m/z = 17, 18, 44 and 45, appear. The explanation for the appearance of the new peaks is to some degree the increased evaporation rate that one expect with increased temperatures. This is most likely the case with the m/z = 32 peak which also appear in the more zoomed plots in Figures 6a and 6b. In case of the remaining peaks another factor might, however, come in to play, namely thermal fracturing of the CH_3NH_2. As previously found when comparing the 14 eV and the 35 eV spectra m/z = 142 and 15 are observed in the later case which suggests that CH_3NH_2 suffers from increased ionization decomposition when using the higher ionization energy. Considering this observation, together with what was observed in literature, it thus seem likely that CH_3 and CH_3I are predominately formed from CH_3NH_2 and HI decomposition products originating from either thermal or ionization fracturing[12,13]. This could also be the explanation for the peaks at m/z = 44 and 45 which are attributed to C_2H_6N and C_2H_7N, respectively. Increased thermal decomposition is, however, less likely to be the cause for the increase in m/z = 32 as CH_3NH_3 fractures into CH_3NH_2 and one would thus expect a decreasing presence of CH_3NH_3 as the temperature increases. At 240°C all the peaks are seen to be severely diminished which strongly suggests that the supply of MAI ran out. This hypotheses is supported by the fact that the chamber pressure was observed to drop from

2.0×10^{-4} Pa to 5.0×10^{-5} Pa. In addition the Al sample container appeared empty when it was visually inspected after the experiment. Finally the fact that the MAI ran out agrees well with our experience from $CH_3NH_3PbI_{(3-x)}Cl_x$ fabrication in a PVD set up where several grams of MAI was found to be expended in an hour at this evaporation temperature. The additional peaks observed in the experiment are again shown in Table 2.

From the mass spectrometry data we can conclude that MAI does not actually evaporate as a compound, but dissociatively as mainly CH_3NH_2 and HI when using a source temperature of 130°C. The only "MAI-like" compound which is observed is a very small amount of the MAI-dimer when using lower evaporation temperatures. Taking this into account offers an explanation as to why one needs high MAI evaporation pressures for successful perovskite deposition: No MAI arrives at the sample and therefore, both a HI and a CH_3NH_2 molecule need to be present at the same time and place on the surface of the $PbCl_2$. This means that the conversion probability becomes much smaller and that the net rate is more likely to scale with the square of the chamber pressure rather than linearly with the direct flux like regular evaporative PVD. This issue naturally becomes substantially worse as one starts to heat the substrate since the vapour pressure of both compounds will increase significantly with temperature. An alternative explanation is that all the HI and CH_3NH_2 goes to waste and that only the MAI-dimer reacts with the $PbCl_2$, but this scenario is also rather problematic as the amount of dimer evaporated is, first of all, very low, but also because it requires that the dimer dissociate on the surface before it reevaporates. With this in mind it is clear that one needs to think carefully when designing an MAI evaporation chamber as the high deposition pressure needed is contradictory to common PVD design guidelines. Rather than having a big chamber which is pumped at a high pumping speed it appears to be much better to reduce both pumping speed and chamber dimensions, to minimize the waste of the evaporated MAI. Due to these facts MAI might be better suited for a CVD, rather than a PVD, process which has also been demonstrated to be a viable deposition strategy in literature[9]. Taking this line of thought a bit further one could imagine using HI and CH_3NH_2 as precursors rather than MAI which has the benefit that one avoids synthesis and storage of the notoriously moisture sensitive MAI. Whether or not this is feasible is, however, unclear and a study would need to be performed to provide clarification on the matter.

Table 2 Table showing the minor peaks of Figure 5-7, the compound giving rise to it as well as what parent molecule it might come from.

m/z	Compound	Likely parent molecule
44	$C_2H_6N^+$	CH_3NH_3I fragment
45	$C_2H_7N^+$	CH_3NH_3I fragment
63.4	I^{2+}	HI fragment
64	HI^{2+}	HI parent peak
129	C, H, N, I compound	CH_3NH_3I fragment
142	CH_3I^+	CH_3I parent peak
150	C, H, N, I compound	CH_3NH_3I fragment
254	I_2^+	I_2 parent peak
317.7	$(CH_3NH_3I)_2^+$	$(CH_3NH_3I)_2$ parent peak

3.3 Discussion

As mentioned in the introduction other groups have performed mass spectrometry on MAI and upon comparing the results obtained here with these some similarities, but also some discrepancies, emerge. Nenon *et al.*[13] use thermogravimetric analysis coupled with temperature programmed XRD and mass spectrometry to gauge the stability of various perovskite species and their precursors. At a temperature of 110°C they observe small amounts of m/z = 15, 17, 18, 26, 27, 28, 29 and 31 which are indicative of CH_3NH_2 evaporation and agrees well with what was observed here. Additionally they observe peaks in the 42-48 AMU/e range some of which are present in our experiments but not in large quantities before 200°C. As the temperature increases they observe an increase in peak intensity which is in good agreement with what one would expect, namely, that the evaporation rate is increased. At approximately 170°C primarily m/z = 15, 16 and 17 are observed suggesting that CH_3NH_2 is completely fractured into CH_3 and NH_3 above these temperatures. The increased amount of observed CH_3 fits well which our measurements but the lack of the parent peak, CH_3NH_2, is peculiar. From their collective results they additionally conclude that MAI begins to evaporate from $CH_3NH_3PbI_{(x-3)}Cl_x$ at around 100°C which again agrees well whith what we have observed. Juarez-Perez *et al.*[12] likewise perform thermogravimetric analysis coupled with mass spectrometry and additionally show first principle calculation to analyse the exhaust gas of thermally decomposing $CH_3NH_3PbI_3$. Like Nenon *et al.*[13] they go from room temperature up to 400°C but use a mass spectrometer with a wider mass range enabling them to measure up to 200 AMU/e. This allows them to observe both I, CH_3I, NH_3 and CH_3 evaporating off MAI at around 300°C. They conclude that MAI is thermally cracked primarily into CH_3I and NH_3 which agrees with what was observed by Nenon *et al.*[13] at temperatures above 170°C given that Nenon *et al.*[13] did not measure masses above 100 AMU/e. Considering this information together with the results obtained here, it suggests that MAI evaporates mainly as CH_3NH_3I and HI at lower temperatures but shifts cracking pattern towards CH_3I and NH_3 at temperatures above 170°C. In contrast to what was observed here and by Nenon *et al.*[13] Juarez-Perez *et al.*[12] do not measure any significant peaks at lower temperatures which means that they do not observe this shift in their experiments. They do, however, mix their sample with an alumina powder for their TGA experiments and use a carrier gas (He) to transport the evaporants to their mass spectrometer. Both the alumina matrix and the He will likely slow the diffusion of the decomposition gasses away from their sample holder. Their experimental approach is thus different from ours and the one employed by Nenon *et al.*[13] which is likely the cause for the discrepancies. The high temperature regime is not immediately relevant for MAI deposition as the frequently used evaporation temperatures are, as mentioned earlier, somewhat lower than 170°C in most cases. It is, however, very useful in the case of perovskite degradation as it provide insight into what one could expect from a high temperature annealing which is routinely used when depositing protection layers like TiO_2[19].

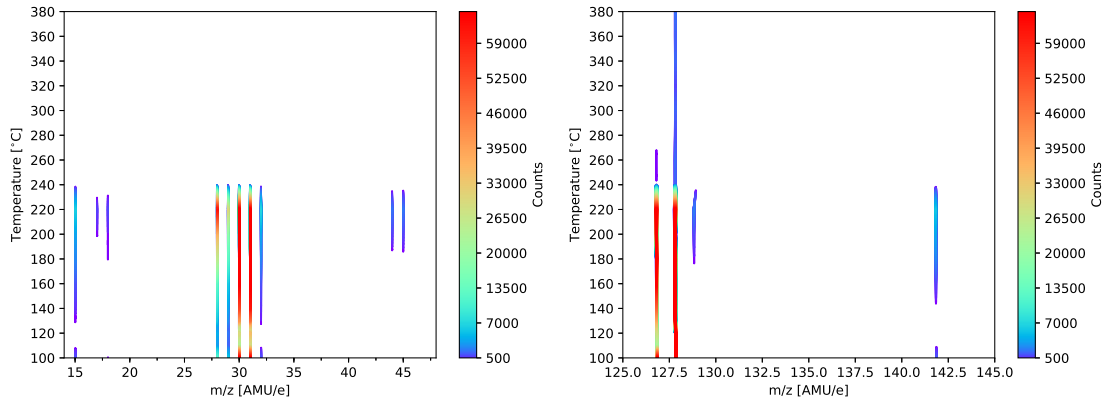

Fig. 7 Intensity plots showing the significant peaks (> 500 counts) of the mass scans of MAI as a function of temperature. The measurements were done using an ionization energy of 14 eV.**(a)** shows the m/z = 14-48 spectra while m/z = 125-145 is shown in **(b)**. The full m/z = 0-100 and 100-200 spectra are shown in Figures S11 and S12, respectively.

4 Conclusion

We can conclude that MAI suffers from a very low sticking coefficient which results in low deposition rates under typical PVD chamber pressures. Furthermore the majority of the observed deposition rate is indirect which has the consequence that MAI goes everywhere in the deposition chamber. This means that a direct line of sight from the source to the target is not needed - something which is paramount in PVD chambers. The initial MAI sticking can be improved by providing a film of $PbCl_2$ for it to land on and subsequently react with. When heating the target containing the $PbCl_2$ film to regular substrate temperatures the observed rate is, however, much diminished as the vapour pressure of the MAI is increased. By varying the $PbCl_2$ film thickness we can conclude that the rate saturates faster the thinner the film. This phenomenon can be explained by the diffusion rate being $PbCl_2$ concentration dependent with the result that the diffusion rate of the thicker films is higher. From the QCM results we can conclude that high MAI pressures are needed for the diffusion rate of the MAI, through the forming perovskite film, to outweigh its desorption rate especially if the target is held at elevated temperatures. The mass spectrometry explains the underlying cause for this behaviour as the MAI is observed not to evaporate as a compound but rather dissociatively (primarily as HI and CH_3NH_2) or in small amounts as an MAI-dimer ($((CH_3NH_3I)_2)$). When making perovskite films, this has the consequence that both CH_3NH_2 and HI need to be present at the same time in order for $PbCl_2$ to be converted into perovskite which lowers the reaction probability. One therefore needs relatively high pressures of the two species in order for the incoming flux to surpass the simultaneous re-desorption and allow for proper conversion to the perovskite. These results provide fundamental insight into the nature of MAI evaporation and should be taken into account when designing an MAI vacuum deposition chamber since parameters such as pumping speed and chamber dimensions needs to be more like those of a CVD system as opposed to those of a typical PVD system.

Acknowledgement

This work was supported by a research grant (DFF-4005-00463) from Danmarks frie forskningsfond and by a research grant (9455) from VILLUM FONDEN.

Conflict of interest

There are no conflicts of interest to declare.

References

1 J.-P. Correa-Baena, A. Abate, M. Saliba, W. Tress, T. Jesper Jacobsson, M. Grätzel and A. Hagfeldt, *Energy Environ. Sci.*, 2017, **10**, 710–727.

2 S. Y. Hsiao, H. L. Lin, W. H. Lee, W. L. Tsai, K. M. Chiang, W. Y. Liao, C. Z. Ren-Wu, C. Y. Chen and H. W. Lin, *Advanced Materials*, 2016, **28**, 7013–7019.

3 H. Chen, F. Ye, W. Tang, J. He, M. Yin, Y. Wang, F. Xie, E. Bi, X. Yang, M. Grätzel and L. Han, *Nature*, 2017, **550**, 92–95.

4 X. Li, D. Bi, C. Yi, J. Luo, S. M. Zakeeruddin and A. Hagfeldt, *Science*, 2016, **353**, 58–62.

5 D. Yang, Z. Yang, W. Qin, Y. Zhang, S. F. Liu and C. Li, *J. Mater. Chem. A*, 2015, **3**, 9401–9405.

6 Q. Lin, A. Armin, R. C. R. Nagiri, P. L. Burn and P. Meredith, *Nature Photonics*, 2015, **9**, 106–112.

7 L. K. Ono, M. R. Leyden, S. Wang and Y. Qi, *J. Mater. Chem. A*, 2016, **4**, 6693–6713.

8 Y. Li, J. K. Cooper, R. Buonsanti, C. Giannini, Y. Liu, F. M. Toma and I. D. Sharp, *Journal of Physical Chemistry Letters*, 2015, **6**, 493–499.

9 J. Yin, H. Qu, J. Cao, H. Tai, J. Li and N. Zheng, *J. Mater. Chem. A*, 2016, **4**, 13203–13210.

10 L. K. Ono, S. Wang, Y. Kato, S. R. Raga and Y. Qi, *Energy Environ. Sci.*, 2014, **7**, 3989–3993.

11 J. Teuscher, A. Ulianov, O. Müntener, M. Grätzel and N. Tétreault, *ChemSusChem*, 2015, **8**, 3847–3852.

12 E. J. Juarez-Perez, Z. Hawash, S. R. Raga, L. K. Ono and Y. Qi, *Energy Environ. Sci.*, 2016, **9**, 3406–3410.

13 D. P. Nenon, J. A. Christians, L. M. Wheeler, J. L. Blackburn, E. M. Sanehira, B. Dou, M. L. Olsen, K. Zhu, J. J. Berry and J. M. Luther, *Energy & Environmental Science*, 2016, **9**, 2072–2082.

14 M. Liu, M. B. Johnston and H. J. Snaith, *Nature*, 2013, **501**, 395–398.

15 C. W. Chen, H. W. Kang, S. Y. Hsiao, P. F. Yang, K. M. Chiang and H. W. Lin, *Efficient and uniform planar-type perovskite solar cells by simple sequential vacuum deposition*, 2014, http://doi.wiley.com/10.1002/adma.201402461.

16 G. Sauerbrey, *Zeitschrift für Physik*, 1959, **155**, 206–222.

17 Y.-K. Kim, K. Irikura, M. Rudd, M. Ali, P. Stone, J. Chang, J. Coursey, R. Dragoset, A. Kishore, K. Olsen, A. Sansonetti, G. Wiersma, D. Zucker and M. Zucker, *Electron-Impact Cross Sections for Ionization and Excitation Database*, 2017, https://physics.nist.gov/PhysRefData/Ionization/molTable.html.

18 NIST Mass Spec Data Center and S. Stein, *Mass Spectra in NIST Chemistry WebBook, NIST Standard Reference Database Number 69, Eds. P.J. Linstrom and W.G. Mallard, National Institute of Standards and Technology, Gaithersburg MD, 20899 doi:10.18434/T4D303*, 2017, http://webbook.nist.gov/chemistry/.

19 B. Seger, T. Pedersen, A. B. Laursen, P. C. K. Vesborg, O. Hansen and I. Chorkendorff, *Journal of the American Chemical Society*, 2013, **135**, 1057–1064.

Deposition of Methylammonium Iodide via evaporation - combined kinetic and mass spectrometric study

Supporting information

Martin J. Bækbo, Ole Hansen, Ib Chorkendorff, Peter C. K. Vesborg

Technical University of Denmark, Fysikvej, Kgs. Lyngby, Denmark

1 Additional figures

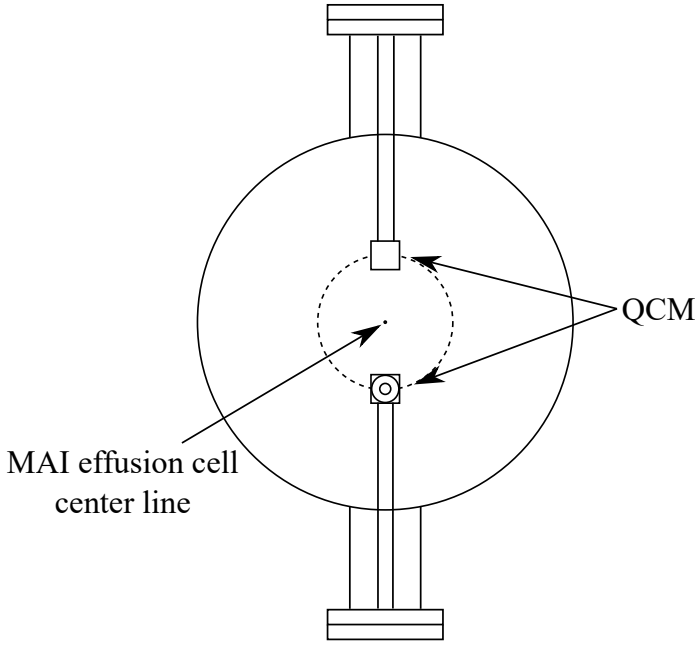

S 1 Schematic drawing of the QCM set up shown from a different angle compared to Figure 1.

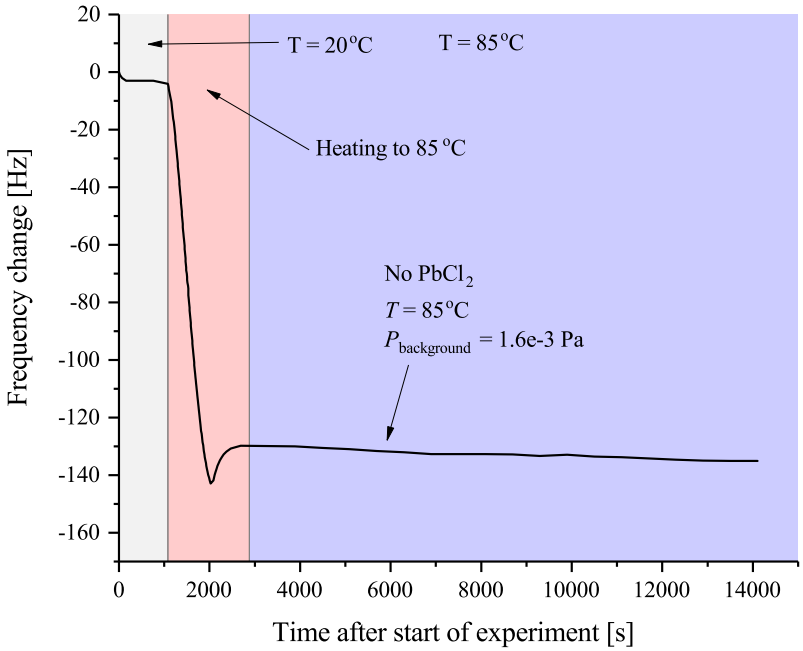

S 2 QCM experiment using the forward QCM in which a blank crystal was heated to 85°C without any MAI being deposited. The different zones define different temperature regions: the gray is 20°C, the red is heating to 85°C and the blue is 85°C. Like the experiments in the main paper the temperature was controlled using a heat bath.

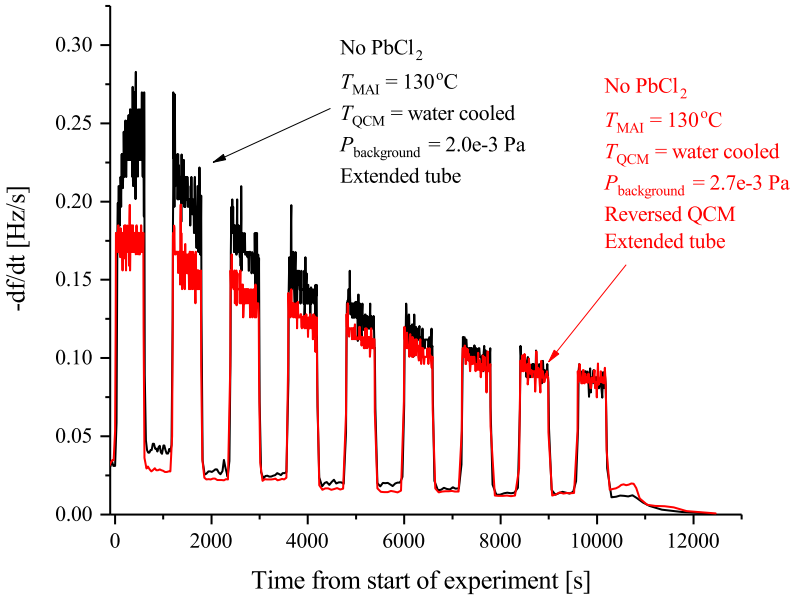

S 3 QCM experiment using the reverse QCM showing the effect of having line of sight from the MAI effusion cell and the sensor. T_{MAI} is the MAI source temperature, T_{QCM} is the QCM temperature, $P_{background}$ is the background pressure. The signal was again chopped in 10 min intervals using the shutter on the MAI source.

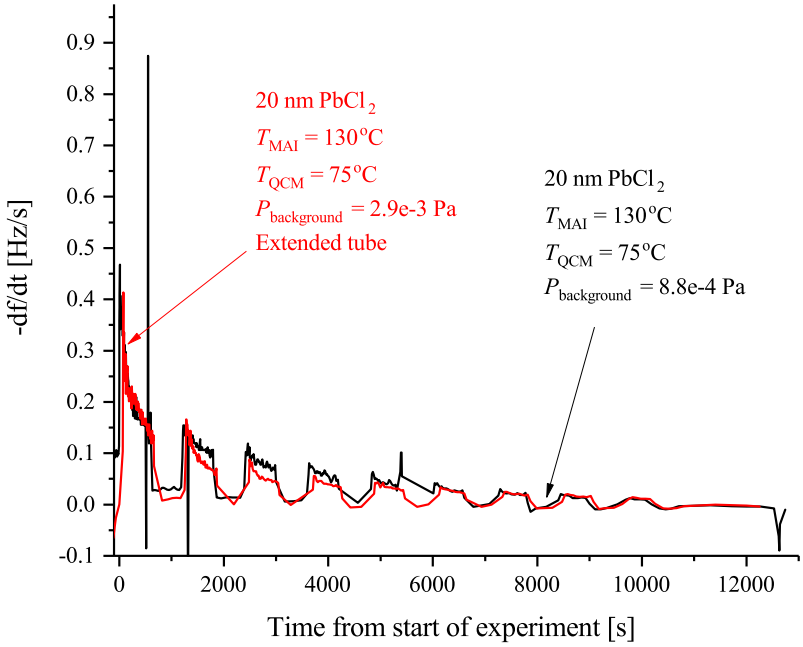

S 4 QCM experiment using the forward QCM showing the effect of moving the MAI effusion cell 10 cm further away from the sensor. T_{MAI} is the MAI source temperature, T_{QCM} is the QCM temperature, $P_{background}$ is the background pressure. The signal was again chopped in 10 min intervals using the shutter on the MAI source.

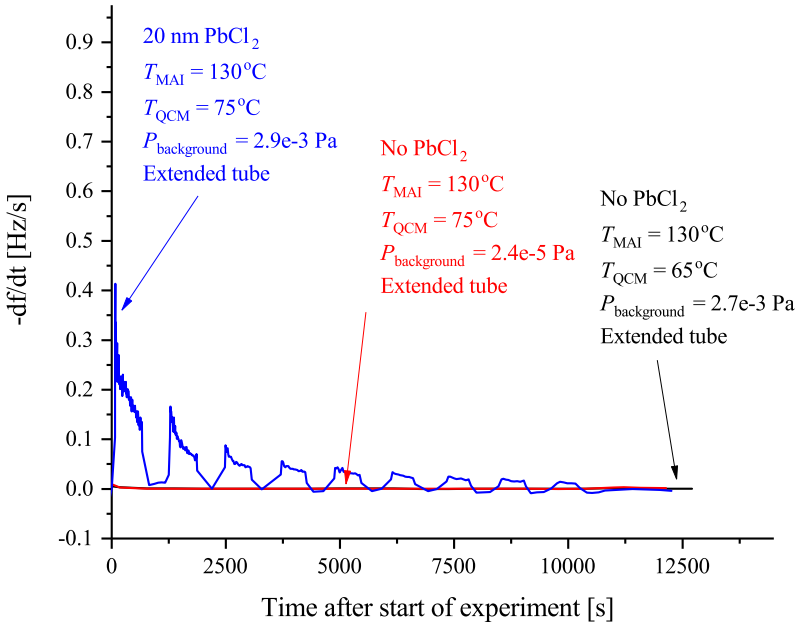

S 5 QCM experiment using the forward QCM showing the effect of having $PbCl_2$ predeposited on the QCM crystal. The 65°C and 75°C blank plot are hard to distinguish as they are more or lest identical. T_{MAI} is the MAI source temperature, T_{QCM} is the QCM temperature, $P_{background}$ is the background pressure. The signal was again chopped in 10 min intervals using the shutter on the MAI source.

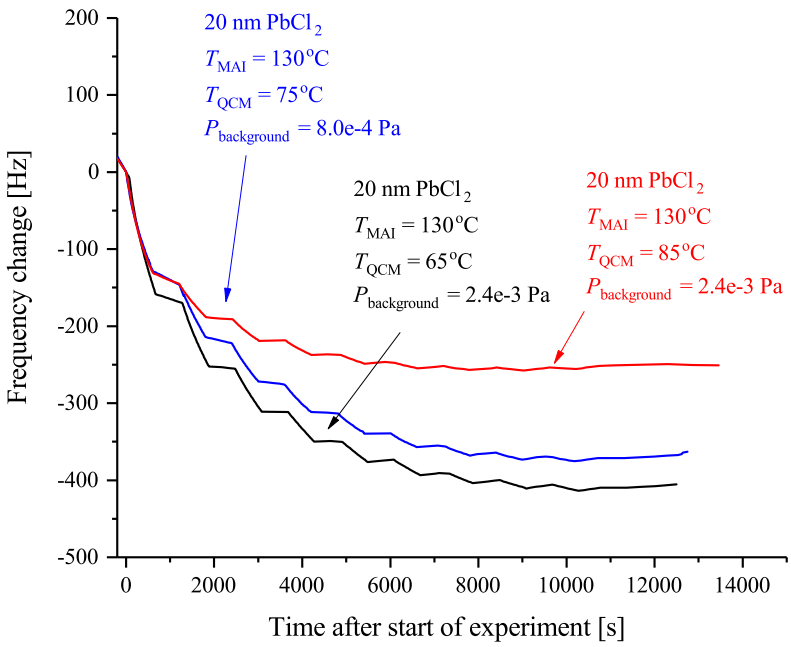

S 6 QCM experiment using the forward QCM showing the corresponding frequency change of the observed rate shown in Figure 3 of the main paper. T_{MAI} is the MAI source temperature, T_{QCM} is the QCM temperature, $P_{background}$ is the background pressure. The signal was again chopped in 10 min intervals using the shutter on the MAI source.

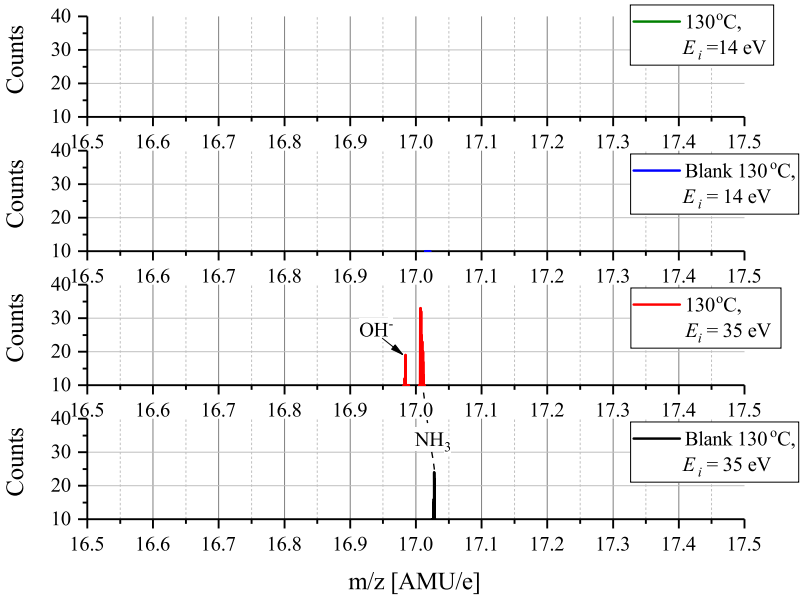

S 7 Mass scans in the m/z = 16.5-17.5 range for MAI evaporated at 130°C recorded using an ionization energy, E_i, of 35 eV or 14 eV. The dashed lines indicate peaks originating from the same species (OH^- or NH_3) indicated in the label. The Counts axis starts from 10 counts as everything below is designated as noise.

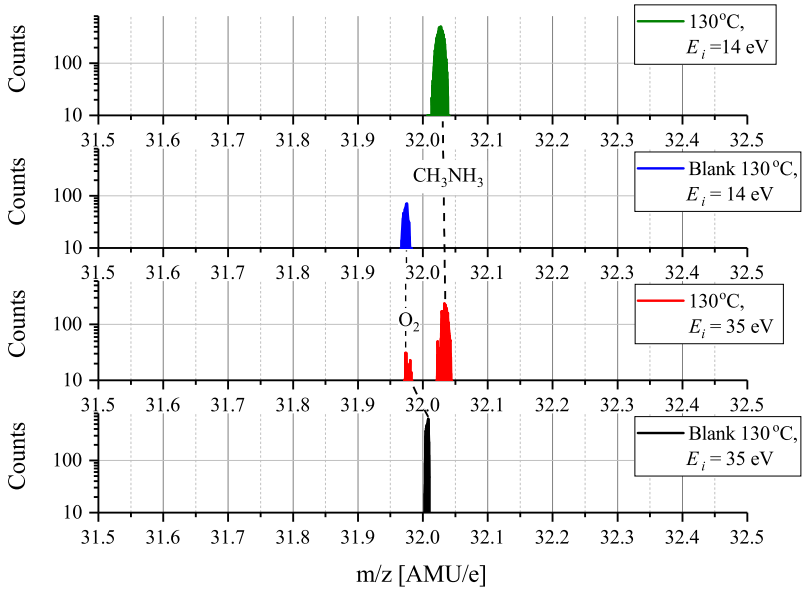

S 8 Mass scans in the m/z = 31.5-32.5 range for MAI evaporated at 130°C recorded using an ionization energy, E_i, of 35 eV or 14 eV. The dashed lines indicate peaks originating from the same species (O_2 or CH_3NH_3) indicated in the label. The Counts axis starts from 10 counts as everything below is designated as noise.

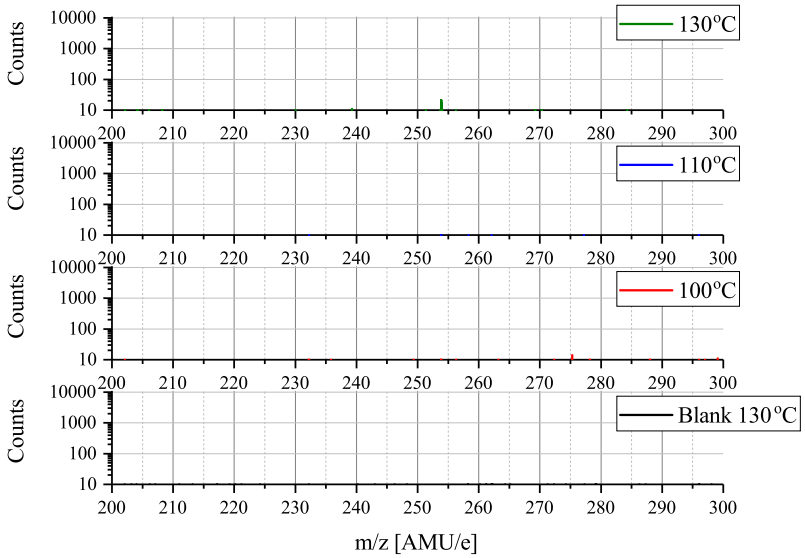

S 9 Mass scans in the m/z = 200-300 range for MAI evaporated at 130°C recorded using an ionization energy, E_i, of 14 eV. The Counts axis starts from 10 counts as everything below is designated as noise.

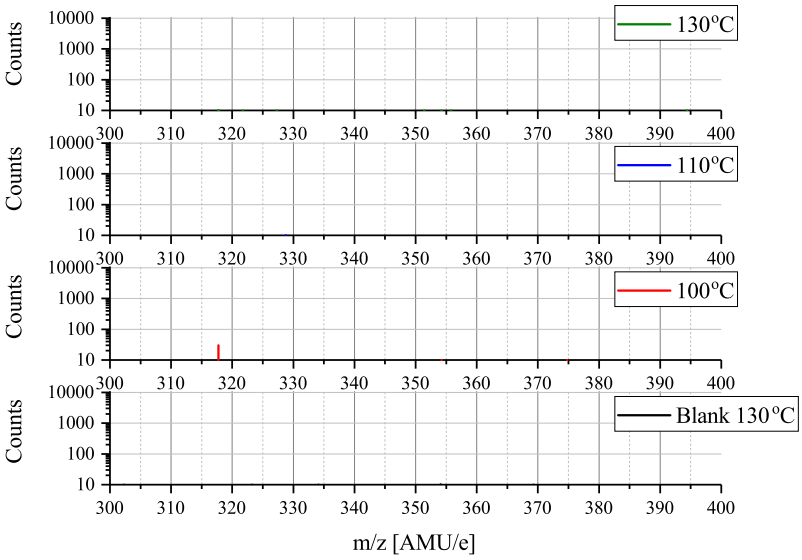

S 10 Mass scans in the m/z = 300-400 range for MAI evaporated at 130°C recorded using an ionization energy, E_i, of 14 eV. The Counts axis starts from 10 counts as everything below is designated as noise.

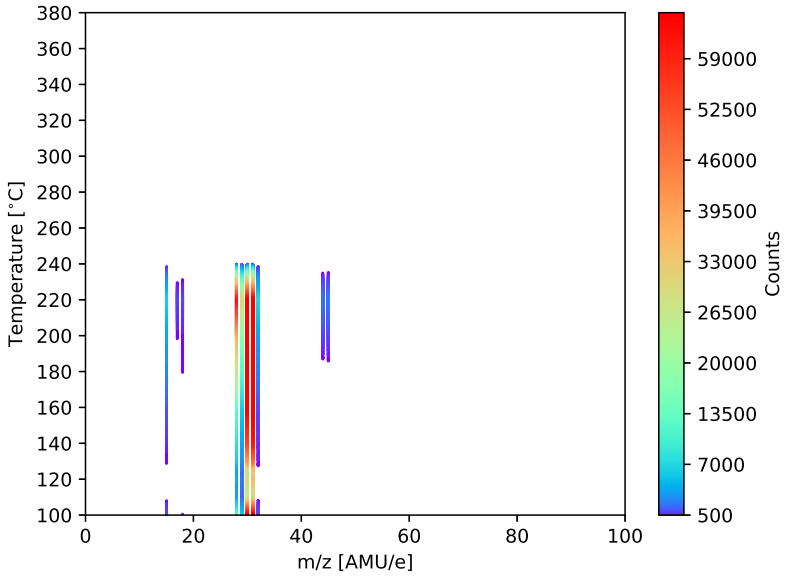

S 11 Intensity plot of the significant peaks (> 500 counts) in the m/z = 0-100 range for MAI evaporated at temperatures of up to 380°C. The data was recorded using an ionization energy of 14 eV.

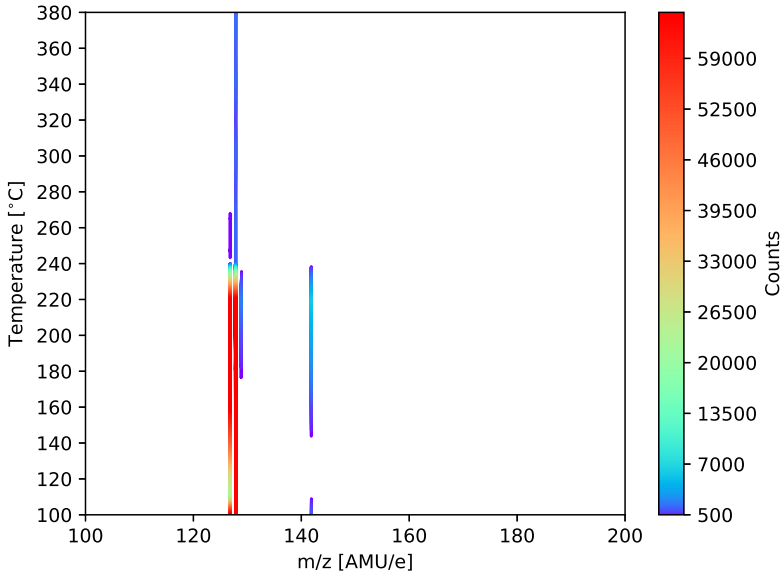

S 12 Intensity plot of the significant peaks (> 500 counts) in the m/z = 100-200 range for MAI evaporated at temperatures of up to 380°C. The data was recorded using an ionization energy of 14 eV.

2 $PbCl_2$ depletion calculations

The reaction expected to take place is

$$PbCl_2 + 3CH_3NH_3I \rightarrow CH_3NH_3PbI_3 + 2CH_3NH_3Cl, \tag{1}$$

from which one would anticipate that the amount of MAI that needs to be deposited is 3 times the amount of $PbCl_2$. The amount of $PbCl_2$ per area can be estimated by using that the density of $PbCl_2$ is 5.85 $\frac{g}{cm^3}$ which yields

$$20 \text{ nm} \times 5.85 \frac{g}{cm^3} = 1.17 \times 10^4 \ \frac{ng}{cm^2}. \tag{2}$$

From this the mass of the fully converted perovskite can be estimated by using the molar masses of $PbCl_2 = 278$ $\frac{g}{mol}$ and $CH_3NH_3PbI_3 = 620$ $\frac{g}{mol}$ which yields

$$\frac{620}{278} \times 1.17 \times 10^4 \ \frac{ng}{cm^2} = 2.61 \times 10^4 \ \frac{ng}{cm^2}. \tag{3}$$

The mass increase that one would expect for full conversion if all the MACl reevaporates is thus

$$2.61 \times 10^4 \ \frac{ng}{cm^2} - 1.17 \times 10^4 \ \frac{ng}{cm^2} = 1.44 \times 10^4 \ \frac{ng}{cm^2}. \tag{4}$$

To estimate the highest amount of MAI deposited we use that the maximal frequency change observed in Figure 6 is about 405 Hz (the 65°C plot). From equation (1) in the main paper one gets

$$\Delta f = -C_f \Delta m \Leftrightarrow \Delta m = -\frac{\Delta f}{C_f}. \tag{5}$$

By using that C_f is given by[1]

$$C_f = \frac{2nf_0^2}{(\rho_q \mu_q)^{1/2}}, \tag{6}$$

where n is the number of the harmonic at witch the crystal is driven, f_0 is the resonant frequency of the fundamental mode of the crystal, $\rho_q = 2.648$ $\frac{g}{cm^3}$ is the density of quartz, $\mu_q = 2.947 \times 10^{-11}$ $\frac{g}{cms^2}$ is the shear modules of quartz, that $n = 1$, $f_0 = 6 \times 10^6$ Hz and inserting the $\Delta f = 405$ Hz one gets

$$C_f = 8.15 \times 10^7 \ \frac{cm^2 Hz}{g} \Rightarrow \Delta m = \frac{405 \text{ Hz}}{8.15 \times 10^7 \ \frac{cm^2 Hz}{g}} = 4.97 \times 10^3 \ \frac{ng}{cm^2}. \tag{7}$$

This is obviously a much lower number than what one would expect and the $PbCl_2$ would needed to be no thicker than 6.90 nm for full conversion.

3 Sticking coefficient calculations

To estimate the sticking coefficient, S_c, from the pressure one can use the concept of Langmuir (L) where one Langmuir corresponds to an exposure of 1.33×10^{-4} Pa of gas for one second. By assuming a S_c of 1 one can show that an exposure of 1 L corresponds to a deposition of about 1 monolayer per second and since a monolayer is roughly 0.3 nm one expects a deposition rate of 0.3 nm/s for a 1 L exposure. The number of Langmuir scales with pressure meaning that a deposition pressure of 1.33×10^{-3} Pa gives rise to an exposure of 10 L or a rate of 3 nm/s. The chamber pressure during a typical experiment is shown in Figure 7 from which one can deduce that the partial pressure associated with MAI evaporation is roughly 2×10^{-3} Torr or a rate of 6 nm/s when the pressure change stabilizes.

Using a MAI density of 2.22 $\frac{g}{cm^3}$ [2] one can calculate the amount of MAI that would have been deposited during the approximately 11000 s the experiments shown in Figure 6 takes which is given by

$$\Delta m = S_c R t \rho_{\text{MAI}}, \tag{8}$$

where R is the rate, t is the exposure time, ρ_{MAI} is the MAI density and S_c is assumed to be 1. This yields

$$\Delta m = 6 \times 10^{-7} \text{ cm/s} \times 11000 \text{ s} 2.22 \ \frac{g}{cm^3} = 1.47 \times 10^{-2} \ \frac{g}{cm^2} = 1.47 \times 10^7 \ \frac{ng}{cm^2}. \tag{9}$$

By using equation (7) and that the frequency change observed in Figure 6 is $\Delta f = 250$ Hz, 360 Hz and 405 Hz for the 85°C, 75°C and 65°C case, respectively one can calculate the deposited mass per area to be

$$\Delta m_{85^\circ C} = 3.07 \times 10^3 \ \frac{ng}{cm^3}, \Delta m_{75^\circ C} = 4.42 \times 10^3 \ \frac{ng}{cm^3} \text{ and } \Delta m_{65^\circ C} = 4.97 \times 10^3 \ \frac{ng}{cm^3}. \tag{10}$$

From this one gains the sticking coefficients

$$S_{c,85^\circ C} = 2.095 \times 10^{-4} \simeq 2.1 \times 10^{-4}, S_{c,75^\circ C} = 3.017 \times 10^{-4} \simeq 3.0 \times 10^{-4} \text{ and } S_{c,65^\circ C} = 3.392 \times 10^{-4} \simeq 3.4 \times 10^{-4}, \tag{11}$$

in the 85°C, 75°C and 65°C case, respectively.

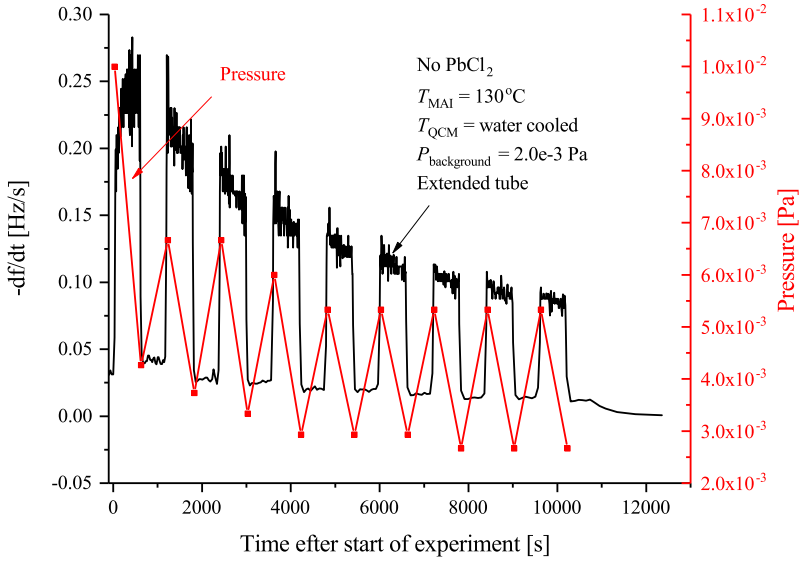

S 13 QCM experiment showing the change in chamber pressure observed when operating the shutter together with the observed deposition rate on a blank crystal. T_{MAI} is the MAI source temperature, T_{QCM} is the QCM temperature, $P_{background}$ is the background pressure. The signal was again chopped in 10 min intervals using the shutter on the MAI source.

References

[1] Stanford Reasearch Systems, *QCM100- Quartz Crystal Microbalance Theory and Calibration*, `http://www.thinksrs.com/downloads/PDFs/ApplicationNotes/QCMTheoryapp.pdf`.

[2] L. K. Ono, M. R. Leyden, S. Wang and Y. Qi, *J. Mater. Chem. A*, 2016, **4**, 6693–6713.